

PFC/RR-91-16

**Plasma and Neutral Gas Jet Interactions
in the Exhaust of a
Magnetic Confinement System**

Warren Allyn Krueger

June 1990

Plasma Fusion Center
Massachusetts Institute of Technology
Cambridge, MA 02139 USA

This work was supported by NASA under Contract No. NAS-9-18372, NASA/JPL under Contract No. 958265 and AFOSR under Contract No. AFOSR-89-0345.

Reproduction, translation, publication, use, and disposal, in whole or in part, by or for the US Government is permitted.

**Plasma and Neutral Gas Jet Interactions
in the Exhaust of a
Magnetic Confinement System**

by

Warren Allyn Krueger

B.A., Colby College (1982)

Submitted to the Department of Nuclear Engineering
in partial fulfillment of the requirements for the degree of

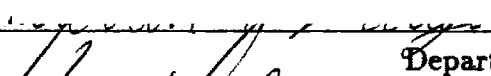
Doctor of Philosophy

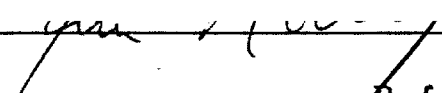
at the

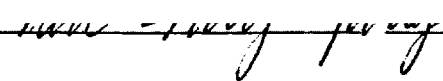
MASSACHUSETTS INSTITUTE OF TECHNOLOGY

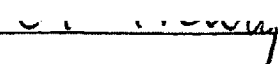
June 1990

© Massachusetts Institute of Technology 1990

Signature of Author  _____
Department of Nuclear Engineering
May 18, 1990

Certified by  _____
Kim Molvig
Professor, Department of Nuclear Engineering
Thesis Supervisor

Certified by  _____
Tien-Fang Yang
Staff Scientist, Plasma Fusion Center
Thesis Supervisor

Accepted by  _____
Allan F. Henry
Chairman, Departmental Committee on Graduate Students

**Plasma and Neutral Gas Jet Interactions
in the Exhaust of a
Magnetic Confinement System**

by
Warren Allyn Krueger

Submitted to the Department of Nuclear Engineering
on May 14, 1990, in partial fulfillment of the
requirements for the degree of
Doctor of Philosophy

Abstract

A general purpose 2 - 1/2 dimensional, multifluid, time dependent computer code has been developed. This flexible tool models the dynamic behavior of plasma/neutral gas interactions in the presence of a magnetic field. The simulation has been used to examine the formation of *smoke ring* structure in the plasma rocket exhaust by injection of an axial jet of neutral gas. Specifically, the code was applied to the special case of attempting to couple the neutral gas momentum to the plasma in such a manner that plasma smoke rings would form, disconnecting the plasma from the magnetic field. For this scenario several cases were run scanning a wide range of neutral gas input parameters. In all the cases it was found that after an initial transient phase, the plasma eroded the neutral gas and after that followed the original magnetic field. From these findings it is concluded that smoke rings do not form with axial injection of neutral gas. Several suggestions for alternative injection schemes are presented.

Thesis Supervisor: Kim Molvig
Title: Professor, Department of Nuclear Engineering

Thesis Supervisor: Tien-Fang Yang
Title: Staff Scientist, Plasma Fusion Center

Acknowledgments

This work was supported by NASA and Dr. Franklin Chang through the Flight Crew Operations Directorate of the Lyndon B. Johnson Space Center, Houston, TX. I would like to thank Franklin not only for supporting my graduate study at M.I.T., but also for getting me VIP passes to the space shuttle launch. I also would like to thank Dr. Tien-Fang (Ted) Yang, for putting up with me on a day to day basis as my thesis advisor. And Professor Kim Molvig, who agreed to be my departmental sponsor of my thesis work.

I would like to thank my parents, for all the obvious reasons, but also for whatever they did in my childhood that would eventually lead me to college and then graduate study. I would like to thank my father for all the stimulating mathematical discussions we had, usually at the dinner table, and for my mother's patience in putting up with them.

This entire thesis is typeset using the \LaTeX document preparation system. \LaTeX is based on the computer typesetting system \TeX developed by Donald Knuth. Thanks to their work, my work in preparing this thesis was greatly simplified. I also would like to thank Mark London, system programmer at the Plasma Fusion Center, for ETEK, a Tektronix graphics editor. All the figures in this thesis were prepared using ETEK. Mark also modified the printer driver for \TeX files to allow Tektronix plots to be automatically included in a document. Thanks to the above work, no cutting or pasting was done at any point in the development of this thesis.

I also would like to thank various friends that helped me get through various times of my stay at M.I.T. It started with Paul Gierszewski, who helped me get through my first year here. Then there was Mark Sands and Eric Esarey, who were both somehow convinced to share an apartment with me. I repaid Mark by driving his truck into a river and destroying his engine. About the same time there was John Petillo, who tried to burn up his car one night. I'll never forget his reaction when we took the general exam together. Dave Humphreys I meet through Aikido, and it turned out he had an office upstairs from me. We had many stimulating discussions of plasma physics and car crashes. Finally, there is Bill (Jim) Stewart, who helped me get through most of the technical details of turning in this thesis that I always managed to forget.

Finally I would like to thank my wife, Lisa. We were married when I thought I was close to graduating, which turned out not to be the case. Lisa has put up with many lonely nights and living on a student salary with hardly a complaint. The birth of our daughter Caitlin was the most wonderful experience in my life.

Contents

Table of contents	7
List of Tables	11
List of Figures	13
Abstract	3
Acknowledgments	5
1 Introduction	17
1.1 Fusion applications	18
1.2 Space propulsion applications	18
1.2.1 Specific Impulse	19
1.2.2 Magnetic nozzle	20
1.3 Hybrid Plume Plasma Rocket	20
2 Numerical Code	23
2.1 History	23
2.1.1 One dimensional radial code	23
2.1.2 1-1/2 Dimensional code.	24
2.1.3 First two-dimensional code	25
2.1.4 Full 2-1/2 dimensional code	25
2.2 Geometry	26
2.3 Equations	27
2.3.1 Ion quantities	27
2.3.2 Electron quantities	28

2.3.3	Field quantities	28
2.3.4	Neutral quantities	30
2.4	Forms for the Source Terms.	30
2.5	Solution Techniques	34
2.5.1	Fluid equations	34
2.5.2	Second order equations	35
2.6	Outline of Code sequence	36
2.7	Subroutine Descriptions	36
2.7.1	Fluidi	37
2.7.2	Cpara	39
2.7.3	Field	41
3	Axial Injection	43
3.1	Motivation	44
3.2	Magnetic Field Geometry	48
3.3	Code results, Static Magnetic Field	50
3.3.1	Reference Case: No reactions	51
3.3.2	Equal plasma and neutral gas densities.	70
3.3.3	High beta	95
3.3.4	Gas density ten-times the plasma density.	112
3.3.5	Equal plasma and neutral gas momentum.	127
3.3.6	Gas density one hundred times the plasma density.	140
3.3.7	Wide neutral jet injection.	162
3.4	Code Results, Dynamic Magnetic Field	178
3.4.1	Thirty percent beta	179
3.4.2	One-hundred percent beta case	181
3.5	Discussion	185
3.6	Conclusion	190
4	Recommendations	191
4.1	Hybrid Plume Possibilities	191
4.1.1	Auxiliary Heating	191
4.1.2	Radial Injection of Neutral Gas	192
4.2	Possible Code Improvements	193

4.2.1	Outflow Boundary Condition	193
4.2.2	Particle-In-Cell Simulation	193
Appendixes		194
A General Equations		195
A.1	Derivation of Transport Equations	196
A.1.1	Density	197
A.1.2	Momentum	198
A.1.3	Energy	198
A.2	Velocity Decomposition Transformation	199
A.2.1	Momentum Transport Equation	199
A.2.2	Energy Transport Equation	202
A.3	The Heat-Balance Equation	204
B Code Listing		207
B.1	Fluidi	207
B.2	Field	215
B.3	Cpara	219
Bibliography		235

List of Tables

2.1	Flow chart of primary code sequence.	37
3.1	Input parameters for reference case. No interactions.	54
3.2	Input parameters for case with equal plasma and neutral gas density.	75
3.3	Input parameters for the high beta case.	96
3.4	Input parameters for neutral gas density ten times that of the peak plasma density.	113
3.5	Input parameters for neutral gas momentum equal to that of the plasma.	130
3.6	Input parameters for neutral gas density one hundred times that of the peak plasma density.	141
3.7	Input parameters for wide neutral gas injection.	166
3.8	Simple table depicting relationships between magnetic Reynolds number and Magnetic interaction parameter.	186
3.9	Full table depicting relationships between magnetic Reynolds number, Magnetic interaction parameter, and ram pressure ratio.	188

List of Figures

3.1	Possible disconnection sequence for hybrid plume rocket.	47
3.2	Magnetic field geometry for Axial Injection cases.	49
3.3	Plasma density at two microseconds for the reference case.	56
3.4	Ion Velocity plot at two microseconds for the reference case.	57
3.5	Reaction rate plots case at two microseconds for reference case.	59
3.6	Momentum ratio and Coupling coefficient at two microseconds for reference case.	61
3.7	Ion temperature at two microseconds for reference case.	65
3.8	Neutral density at two microseconds for reference case.	67
3.9	Neutral Velocity plot at two microseconds for reference case.	68
3.10	Neutral temperature at two microseconds for reference case.	69
3.11	Plasma density at three microseconds for reference case.	71
3.12	Reaction rate plots at three microseconds for reference case.	72
3.13	Plasma Velocity plot at three microseconds for reference case.	73
3.14	Plasma Temperature at three microseconds for reference case.	74
3.15	Comparison of plasma density at two microseconds for reference case and even injection case.	76
3.16	Comparison of plasma temperature at two microseconds for reference case and even injection case.	77
3.17	Reaction rates plots at two microseconds for even injection case.	81
3.18	Coupling Coefficient at two microseconds for even injection case.	82
3.19	Comparison of neutral gas density at two microseconds for reference case and even injection case	84
3.20	Comparison of neutral gas velocity plots at two microseconds for reference case and even injection case.	85

3.21 Comparison of plasma density plots at three-microseconds for reference case and even injection case.	86
3.22 Reaction rate plots at three microseconds for even injection case.	87
3.23 Coupling Coefficient at three microseconds for even injection case.	89
3.24 Comparison of plasma velocity plots at three microseconds for reference case and even injection case.	90
3.25 Comparison of neutral gas densities at three microseconds for reference case and even injection case.	91
3.26 Plasma density plot at four microseconds for even injection case.	92
3.27 Reaction rates at four microseconds for even injection case.	93
3.28 Plasma velocity plot at four microseconds for even injection case.	94
3.29 Comparison of plasma density at two microseconds (low beta/high beta)	97
3.30 Comparison of reaction rate plots at two microseconds. (low beta/high beta)	98
3.31 Comparison of coupling coefficients at two microseconds. (low beta/high beta)	99
3.32 Comparison of plasma velocity plots at two microseconds. (low beta/high beta)	101
3.33 Comparison of plasma density plots at three microseconds. (low beta/high beta)	102
3.34 Comparison of reaction rate plots at three microseconds. (low beta/high beta)	103
3.35 Comparison of coupling coefficients at three microseconds. (low beta/high beta)	104
3.36 Comparison of plasma velocity plots at three microseconds. (low beta/high beta)	106
3.37 Comparison of neutral density plots at three microseconds. (low beta/high beta)	107
3.38 Comparison of plasma density plots at four microseconds. (low beta/high beta)	108
3.39 Comparison of reaction rate plots at four microseconds. (low beta/high beta)	109

3.40 Comparison of coupling coefficients at four microseconds. (low beta/high beta)	110
3.41 Comparison of plasma velocity at four microseconds. (low beta/high beta)	111
3.42 Comparison of plasma density at two microseconds. (even/10x)	114
3.43 Comparison of reaction rate plots at two microseconds. (even/10x) . .	115
3.44 Comparison of coupling coefficients at two microseconds. (even/10x) .	117
3.45 Comparison of plasma temperature at two microseconds. (even/10x) .	118
3.46 Comparison of neutral density at two microseconds. (even/10x)	120
3.47 Comparison of plasma density at three microseconds. (even/10x) . . .	121
3.48 Comparison of reaction rate plots at three microseconds. (even/10x) .	122
3.49 Comparison of coupling coefficients at three microseconds. (even/10x)	124
3.50 Comparison of plasma density at four microseconds. (even/10x)	125
3.51 Comparison of reaction rate plots at four microseconds. (even/10x) . .	126
3.52 Comparison of plasma velocity plots at four microseconds. (even/10x)	128
3.53 Comparison of neutral density at four microseconds. (even/10x)	129
3.54 Comparison of plasma density at two microseconds. Even density/Even momentum cases.	132
3.55 Comparison of reaction rate plots at two microseconds. Even density/Even momentum cases.	134
3.56 Comparison of coupling coefficients at two microseconds. Even density/Even momentum cases.	136
3.57 Comparison of neutral density at two microseconds. Even density/Even momentum cases.	137
3.58 Comparison of plasma density at three microseconds. Even density/Even momentum cases.	138
3.59 Comparison of neutral density at three microseconds. Even density/Even momentum cases.	139
3.60 Comparison of plasma density at two microseconds. (Even/100x) . . .	142
3.61 Comparison of reaction rate plots at two microseconds. (Even/100x) .	143
3.62 Comparison of coupling coefficients at two microseconds. (Even/100x)	145
3.63 Comparison of plasma velocity plot at two microseconds. (Even/100x)	146
3.64 Comparison of plasma temperature at two microseconds. (Even/100x)	147
3.65 Comparison of neutral density at two microseconds. (Even/100x) . . .	148

3.66	Comparison of neutral velocity plot at two microseconds. (Even/100x)	150
3.67	Comparison of plasma density at three microseconds. (Even/100x)	151
3.68	Comparison of reaction rate plots at three microseconds. (Even/100x)	153
3.69	Comparison of coupling coefficients at three microseconds. (Even/100x)	155
3.70	Comparison of plasma density at four microseconds. (Even/100x)	156
3.71	Comparison of reaction rate plots at four microseconds. (Even/100x)	158
3.72	Comparison of coupling coefficients at four microseconds. (Even/100x)	159
3.73	Comparison of neutral density at four microseconds. (Even/100x)	160
3.74	Plasma density at five microseconds. One hundred times neutral injection case.	161
3.75	Neutral density at five microseconds. One hundred times neutral injection case.	163
3.76	Plasma density at six microseconds. One hundred times neutral injection case.	164
3.77	Neutral density at six microseconds. One hundred times neutral injection case.	165
3.78	Comparison of plasma density at three microseconds. (even/wide)	167
3.79	Comparison of reaction rate plots at three microseconds. (even/wide)	168
3.80	Comparison of coupling coefficients at three microseconds. (even/wide)	170
3.81	Comparison of neutral density at three microseconds. (even/wide)	171
3.82	Comparison of plasma density at four microseconds. (even/wide)	172
3.83	Comparison of reaction rate plots at four microseconds. (even/wide)	174
3.84	Comparison of neutral density at four microseconds. (even/wide)	175
3.85	Plasma density at five microseconds for wide injection.	176
3.86	Neutral density at five microseconds for wide injection.	177
3.87	Magnetic field time evolution for thirty percent beta case. Reference case.	180
3.88	Magnetic field time evolution for thirty percent beta case. With Reactions.	182
3.89	Magnetic field time evolution for one-hundred percent beta case. Reference Case.	183
3.90	Magnetic field time evolution for one-hundred percent beta case. With reactions.	184

Chapter 1

Introduction

The main goal of this thesis is to study the interactions of a plasma with an intense source of neutral gas in the form of a jet. Specifically, the concentration will be on the generation of *smoke-ring* phenomena as the result of pure axial injection of the neutral gas jet. This analysis will be accomplished through the numerical simulation of the region of interest with a computer code that has been designed for this purpose. The code was designed as a general tool to study plasma neutral gas interactions. As such, it can be used in the future to study a wide variety of injection geometries. The outline of the thesis is as follows:

Chapter 1 Motivation behind the study of plasma/neutral gas interactions. Description of device that will be modeled in the thesis.

Chapter 2 Description of the numerical technique and the equations used in the simulation will be presented. An outline of the code with a description of major subroutines also included.

Chapter 3 Numerical results for the modeling of the hybrid plume plasma rocket concept are presented. Conclusions as to the viability of the hybrid plume plasma rocket are addressed in the last section of this chapter.

Chapter 4 Recommendations for future work in this area and suggestions for improvements to the numerical code.

1.1 Fusion applications

Plasma neutral gas interactions are of interest for several reasons. One of the first interests in plasma neutral gas interactions was the protection of the first wall in toroidal devices [1,10,2,18] This concept was known as a gas blanket. The idea here was to have a neutral gas blanket surrounding the plasma to reduce the heat and particle flux to the first wall. An obvious consideration was the impact of the neutral gas on the performance characteristics of the device.

An extension of this concept was proposed in the conceptual design of the Princeton Reference Tokamak [11]. Here the neutral gas was confined to the divertor region of the device. This limited the impact of the neutral gas on the performance of the device. In both of these concepts relatively low density neutral gas levels were considered and the gas was introduced as a blanket that was designed not to interact directly with the plasma.

In this thesis I will consider neutral gas levels equal to or higher than the plasma density. Also, I will consider neutral gas jets that interact directly with the plasma. This has the benefit of possibly reducing the back flow of neutral gas into the region of plasma creation, as well as providing a suitable heat removal scheme for scrape-off layers in magnetic divertors [6].

1.2 Space propulsion applications

With these parameters for the neutral gas quantities a new area of interest develops. The idea is plasma propulsion for space travel. The idea of *electric* or *ion* propulsion is not new [8,7,5]. This thesis attempts to extend these concepts to use plasma parameters in the regime of fusion devices (low density, very high temperatures). Typical ion propulsion schemes are designed having a plasma temperature of a few electron Volts (eV). Here it is proposed to use plasma parameters on the order of current day fusion devices (thousands of eV).

This parameter regime gives rise to several benefits if it can be achieved. These benefits will now be discussed.

1.2.1 Specific Impulse

Specific impulse is defined as the mass averaged velocity of a specified rocket:

$$I_{sp} = \frac{\int \dot{m}V}{\int \dot{m}g} \quad (1.1)$$

Here g is the force of gravity at the earth's surface and is a constant (i.e., it is not the local gravity). The units are seconds. For comparison purposes, the specific impulse of the solid rocket boosters of the space shuttle is approximately 300seconds. The specific impulse of a plasma rocket would be on the order of 1000 to 5000seconds. High specific impulse is desirable for rocket engines which are not power limited because it correlates directly to fuel efficiency. For a given amount of thrust, a rocket that had a high specific impulse would use less mass than a rocket with a low specific impulse. It is this extra mass of propellant that must be carried which leads to the efficiency loss. For rockets that are power limited it is also desirable to modulate the specific impulse at constant power to achieve optimum propulsive efficiency, as defined by

$$\eta_{\text{rocket}} = \frac{2\frac{v}{u}}{1 + \left(\frac{v}{u}\right)^2}. \quad (1.2)$$

Here v is the velocity of the ship and u is the exhaust velocity. The idea is that one would like to match the exhaust speed of the plasma to the speed of the ship relative to the specific frame of reference from which the ship departed (i.e., the earth). If this condition were satisfied, then in that frame of reference the exhaust gases would be at rest. From an energy standpoint this is desirable. Any extra velocity in the exhaust gas translates into wasted energy taken from the ship, which presumably has a fixed amount of total energy available for the trip.

The optimum characteristics for a rocket depend on more than the specific impulse of the exhaust, the details of which are beyond the scope of this thesis. The exact trip must be specified and the distance and payload parameters all come into play. In general, however, a high specific impulse device is desirable.

It should be noted that high specific impulse devices generally are low thrust devices. They get their desired performance characteristics by being able to maintain their thrust over a significant portion of the trip. This is in contrast to a low specific impulse device that burns all its fuel quickly, and then coasts most of the way to its destination. The

high specific impulse device may have low thrust (small acceleration) but it maintains it over a much longer time and can eventually obtain much higher vehicle velocities. It is obvious from this consideration that there is some cutoff point at which a low specific impulse rocket would be a better choice (say, for minimizing trip time) than a high specific impulse rocket. In general, low thrust, high specific impulse devices are desirable for very long distance (interplanetary) trips.

1.2.2 Magnetic nozzle

One major difference between a conventional rocket engine and a plasma rocket engine is that the working fluid in a plasma rocket is subject to electromagnetic forces. The most obvious force to consider is that of the guiding magnetic field. In the proposed plasma rocket, the plasma is created in some type of fusion device. It could be a mirror machine, tokamak, etc. The important point is that the plasma that is created be magnetically isolated from the containment device. It is this magnetic field that must guide the plasma out of the device. This magnetic field in the region of interest is known as a magnetic nozzle. In a conventional rocket, internal (thermal) energy is converted to directed energy through interactions of a physical nozzle. The nozzle shape is designed to continuously trade off random thermal motion for directed motion. Once the working fluid has passed the exit plane of the nozzle, the nozzle (and ship) no longer has an effect on the flow. Once the fluid has left the nozzle it cannot act back on the ship to produce drag.

This is not the case for a magnetic nozzle. The magnetic field that produces the nozzle continues to expand past the physical end of the device. These magnetic field lines must close back on themselves and theoretically fill all space. It is this magnetic field that can lead to thrust degradation (drag) and thus the effect of the magnetic field on the flow must be carefully considered.

1.3 Hybrid Plume Plasma Rocket

A design has been proposed that utilizes the benefits of a high specific impulse device. It is the *Hybrid Plume Plasma Rocket*. Its goal is to combine the basic plasma output of a fusion type machine with some type of neutral gas injection to provide usable thrust. The neutral gas in this device serves several purposes. One purpose is to help detach

the plasma from the magnetic field lines. This is necessary with a magnetic nozzle and the plasma parameters considered in the device. A second purpose of the neutral gas is protection of the walls of the physical nozzle from the heat of the plasma. The magnetic field provides most of the insulation needed. However, as the magnetic field lines diverge, they can pass through the wall of the physical nozzle. Even relatively cool plasma interacting directly with the wall could lead to undesirable erosion.

The exact design of a Hybrid Plume Plasma Rocket device depends on a complicated combination of all the above considerations. A specific trip must be proposed and the ship designed around such a trip. This analysis is beyond the scope of this thesis and will not be addressed. The goal of this thesis is to study the conditions necessary for the formation of the hybrid plume plasma rocket, in one particular injection geometry. It is desired to understand the principle physical processes at work in this configuration and the ramifications they would have on the the design of a Hybrid Plume Plasma Rocket.

The following chapters will describe the code that was developed (Chapter 2), present a detailed description of the injection geometry and specific detachment process that is to be studied in this thesis (Chapter 3) and present the results of the simulation of this case. Chapter 4 will suggest alternative geometries that may be of interest.

Chapter 2

Numerical Code

The numerical code which was developed is called PGaS, for **Plasma Gas Simulation**. It models the interactions between a plasma and neutral gas. The code is written in FORTRAN, and was developed using the computers at the Magnetic Fusion Energy Computer Center at Lawrence Livermore National Laboratory. The code is the cumulation of many years of work. Not all the work from these years are directly included in PGaS. A brief history of the developments that led to the creation of PGaS will now be presented.

2.1 History

2.1.1 One dimensional radial code

The first code that was written was a one dimensional code to study the dynamics of the radial interactions between a plasma and a neutral gas jet. Because of the simplicity of the one dimensional code, many species were included on the analysis. These included H , H_2 , H^+ , H_2^+ and the various interactions between these species. The magnetic field was assumed to be only in the axial direction and constant in time.

No conclusive results were obtained from these simulations. A shooting method was used to solve the resulting system of equations. The results of the simulations showed that one of the densities would go negative. It was concluded that the code was too simple and needed to be improved to better model the axial flow.

2.1.2 1-1/2 Dimensional code.

The next step was the creation of a $1 - \frac{1}{2}$ dimensional code. The dimension of the code was obtained by modeling two space dimensions, but only one velocity component of the flow. In this case the axial velocity of the fluid was included. The radial dynamics were assumed to be of a certain type and modeled out of the problem. In this case, the flow was assumed to be predominately in the axial direction and diffusing radially. The magnetic field was assumed to be straight (only B_z). The code solved the steady-state fluid equations.

These assumptions greatly simplified the problem and led to the development of a code that *marched* in the axial direction solving for the radial dynamics at each step. Each fluid conservation equation could be cast in terms of a second order diffusion equation. At each axial position a tridiagonal matrix would be inverted that would provide the solution at that particular location. The axial step size was determined by the condition that the plasma temperature must remain positive. As the two fluids started to interact, this condition on the plasma temperature mandated an extremely small time step. This presented no insurmountable obstacle because the code would later attempt to increase the time step. The code continued to march down the duct until a predetermined distance was reached.

An approximation to include the effects of the radial expansion of the magnetic field was attempted. It allowed parameters that depended on the magnetic field (e.g., the plasma diffusion coefficient) to have some prescribed axial variation. This crudely modeled the change of the magnetic field strength that would result from an expanding magnetic field. This approximation grossly underestimated the effect that the radial expansion of the magnetic field had on the dynamics of the interactions. Instead of allowing the plasma to expand on the the streaming time scale, these approximations only allowed the plasma to expand on the slow diffusion time scale of the plasma. This allowed the formation of steady state boundary layers between the plasma and the neutral gas to develop. As one will see in the full two dimensional model, these structures do not exist in the steady state solution.

The primary short coming of this code was that it did not address the issue of the disconnection of the plasma from the magnetic field. With such a simple assumption for the magnetic field, one could not see the true effect of the magnetic field on the interactions. It was decided to develop a full two dimensional time dependent code to

study the full dynamics of the plasma and magnetic field.

2.1.3 First two-dimensional code

The first two dimensional code was two dimensional in space, and included all the velocity components. A full time dependent magnetic field was included. The plasma consisted of an ideal MHD fluid. This code was never fully developed into a working version with both plasma and neutral gas effects. To develop the code it chosen to simulate a theta pinch implosion. This would test the algorithms of both the field and plasma time advance. The code would run for a short period of time when a numerical instability would occur at the plasma/vacuum boundary that was being formed by the implosion. The source of this numerical instability was never determined. It was decided to use a code that had demonstrated that it could model the full time dynamics of a plasma simulation. This is when it was decided to adapt the numerical code ZEMER to the simulation of the plasma/neutral gas interactions

2.1.4 Full 2-1/2 dimensional code

PGaS is based on the numerical code ZEMER written by Dennis Hewett [9]. ZEMER was created to model macroscopic phenomena in magnetic fusion devices. The simulation technique is based on the particle-in-cell (PIC) simulation method. The PIC method is a simulation technique using particles where one follows the particles in a Lagrangian sense. The macroscopic quantities of interest are then transformed back to a fixed Eulerian grid via linear interpolation. From these macroscopic quantities on the grid the force terms for the equation of motion are calculated (in the case of the plasma this force is the Lorentz force). These force terms then advance the particles in time using the equation of motion, and the cycle repeats. PIC can be a very accurate plasma simulation method.

The ZEMER ions are modeled using a PIC technique. To obtain better electron response information, a hybrid model was formed using a zero-electron mass electron fluid. The zero electron inertia assumption lessens the time step limit imposed by the Courant-Friedrichs-Lewy (CFL) stability constraint.

It was decided to run PGaS in a simple fluid mode for several reasons. One reason was because of the CPU time and code size that would be required to run PGaS in

PIC mode. More importantly, ZEMER was not designed with neutral gas interactions. The arbitrary location of the source terms needed for plasma/neutral gas interactions would require the modification of the PIC algorithm used. Though not impossible, it is difficult. It was decided to use the simpler fluid model to get the initial information for the system to be studied. The extension of PGaS to a full PIC implementation would be a wonderful project for the future.

PGaS is an extension of ZEMER in several areas. The most obvious is the inclusion of the neutral gas species. Also included are the source terms required for the plasma/gas interactions that are being studied. The algorithm used to advance the field quantities was also modified to include the ability to vectorize an arbitrary combination of Neumann/Dirichlet boundary conditions. A Neumann boundary condition is a boundary condition on the derivative of the variable. A Dirichlet boundary condition is a boundary condition on the value of the variable. The design of ZEMER obtained much of its speed from the vectorization of the field advance algorithm. Any modification of this algorithm that prohibited it from being vectorized would greatly increase the CPU time required for a run.

2.2 Geometry

PGaS is a 2-1/2 dimensional code. The two refers to two space dimensions that PGaS models (r, z). All quantities will be described on a two-dimensional grid. As mentioned before, PGaS models an axisymmetric cylinder. The radial and axial directions are modeled directly, and all information in the theta direction is assumed to be axisymmetric; that is, that is no variation of a quantity in the theta direction ($\partial/\partial\theta = 0$). Thus for a scalar quantity, like density (n), the code will calculate $n(i, j)$. Here the i refers to the radial grid location and j refers to the axial grid location. The 1/2 dimension applies to vector quantities. In general for a vector quantity, say velocity (V), the components would be V_r, V_θ and V_z . A pure 2 dimensional code would calculate only two of the velocity components, say V_r and V_z . A 2 - 1/2 dimensional code, as PGaS, calculates both V_r and V_z , but also V_θ . The only restriction on V_θ (or for that matter on all the quantities) is that it does not vary in the theta direction. Thus, each grid location (i, j) will have an associated $V_\theta(i, j)$.

For comparison, a full 3-dimensional code would allow quantities to vary in all

directions. Density would be represented as $n(i, j, k)$, and allowed to vary in the theta direction.

In this configuration (r - z being modeled) a $2 - 1/2$ dimensional code could model a kink-instability, for example, but a full 3-dimensional code would be required to model a flute instability (a flute instability has density variations along θ). On the other had, the $2 - 1/2$ dimensional code could model column rotation, and it would not be limited to rigid-rotor rotation. It should be pointed out that not all $2 - 1/2$ dimensional codes need model the r - z plane. If one wanted to study the flute instability, for example, a $2 - 1/2$ dimensional code could be written for the r - θ plane.

The dimension of a code and its particular implementation are important because, as shown above, it directly effects the physics that can be represented by the code. In this case, for the study of the Hybrid Plume plasma rocket, one is primarily interested in flow along z , expanding in radius. Thus the choice of the r - z plane is obvious.

2.3 Equations

The form of the equations PGaS solves will now be presented. PGaS solves for the ion quantities, the electron quantities, the neutral quantities, and finally for the electric and magnetic fields.

2.3.1 Ion quantities

Ion density is solved via the fluid representation of the continuity equation:

$$\frac{\partial n_i}{\partial t} + \nabla \cdot (n_i \mathbf{u}_i) = S_{pi}. \quad (2.1)$$

Here n_i is the ion density, \mathbf{u}_i is the ion fluid velocity, and S_{pi} is the source of particles, to be described later.

In PGaS quasi-neutrality is assumed so $n_i \sim n_e = n$. The notation n_i will be kept to differentiate ion density from neutral density.

The ion velocity is given by the ion momentum equation:

$$\frac{\partial}{\partial t} (m_i n_i \mathbf{u}_i) + \nabla \cdot (m_i n_i \mathbf{u}_i \mathbf{u}_i) + \nabla p_i - en_i \left(\mathbf{E} + \frac{1}{c} \mathbf{u}_i \times \mathbf{B} \right) = \mathbf{S}_{mi}. \quad (2.2)$$

Here m_i is the ion mass per particle. \mathbf{E} is the electric field, \mathbf{B} is the magnetic field and c is the speed of light. p_i is the pressure, and \mathbf{S}_{m_i} is the ion momentum source, to be described later.

The final ion quantity is the ion temperature. This is given by the ion energy equation:

$$\frac{3}{2} \frac{\partial n_i T_i}{\partial t} + \nabla \cdot \left(\frac{3}{2} n_i T_i \mathbf{u}_i \right) + n_i T_i \nabla \cdot \mathbf{u}_i + \nabla \cdot \mathbf{q} = Q_i \quad (2.3)$$

2.3.2 Electron quantities

Since quasi-neutrality is assumed, the only electron quantities that are needed are the electron velocities and the electron temperature. The electron temperature is determined via an energy equation similar to the one used for the ions. To obtain the electron velocities, the fluid description of the current is used:

$$\mathbf{J} = en(\mathbf{u}_i - \mathbf{u}_e). \quad (2.4)$$

Substituting the field information for the plasma current, one obtains

$$u_{er} = u_{ir} + \frac{c}{4\pi e\rho} \frac{\partial B_\theta}{\partial z}, \quad (2.5)$$

$$u_{e\theta} = u_{i\theta} + \frac{c}{4\pi e\rho} \nabla^2 A|_\theta, \quad (2.6)$$

$$u_{ez} = u_{iz} - \frac{c}{4\pi e\rho r} \frac{\partial r B_\theta}{\partial r}. \quad (2.7)$$

Here \mathbf{A} is the magnetic vector potential in the Coulomb gauge. Since $\mathbf{B} = \nabla \times \mathbf{A}$, one can use A_θ to obtain both B_r and B_z . This reduces the number of equations that need to be solved by one. Now all that is needed are the equations to advance A_θ and B_θ in time.

2.3.3 Field quantities

The theta component of the magnetic vector potential will be obtained from the electron momentum equation.

For zero electron mass, the electron momentum equation reduces to

$$\mathbf{E} = -\frac{\nabla n k T_e}{en} - \frac{1}{c} \mathbf{u}_e \times \mathbf{B} + \eta \mathbf{J}. \quad (2.8)$$

This can be thought of as the Ohm's Law for the model. One can use Maxwell's equations to transform this equation into expressions for A_θ and B_θ .

The radiation-free limit of Ampere's law is

$$\nabla \times \mathbf{B} = \frac{4\pi}{c} \mathbf{J}, \quad (2.9)$$

and Faraday's law is

$$\nabla \times \mathbf{E} = -\frac{1}{c} \frac{\partial \mathbf{B}}{\partial t}. \quad (2.10)$$

Since one needs only the theta component of the magnetic vector potential, axisymmetry simplifies the transformation of the electron momentum equation presented in Equation 2.8. Using Maxwell's equations and substituting in the form $\mathbf{B} = \nabla \times \mathbf{A}$, the electron momentum equation reduces to

$$\dot{A}_\theta = \mathbf{u}_e \times (\nabla \times \mathbf{A})|_\theta + \frac{c^2}{4\pi} \eta \left(\nabla \times (\nabla \times \mathbf{A}) \right)|_\theta. \quad (2.11)$$

Expanding the operators one gets a second order equation of the form

$$\dot{A}_\theta + \frac{\partial}{\partial r} \left(\frac{1}{r} \frac{\partial r A_\theta}{\partial r} \right) + \frac{\partial^2 A_\theta}{\partial z^2} + u_{er} \frac{1}{r} \frac{\partial r A_\theta}{\partial r} + u_{ez} \frac{\partial A_\theta}{\partial z} = 0. \quad (2.12)$$

This gives the equation for the time advance of the magnetic vector potential, from which B_r and B_z can be derived.

All that is left is to obtain a form for the time advance of B_θ . This is obtained by first taking the curl of Equation 2.8. Substituting $\nabla \times \mathbf{E} = -\dot{\mathbf{B}}/c$ from Faraday's law gives an equation for the time advance of the magnetic field. Keeping only the theta component and grouping terms in the unknown B_θ on the left hand side, one obtains

$$\dot{B}_\theta - \frac{c^2}{4\pi} \left[\frac{\partial}{\partial r} \eta \frac{\partial (r B_\theta)}{r \partial r} + \frac{\partial}{\partial z} \eta \frac{\partial B_\theta}{\partial z} \right] + \frac{\partial (u_{er} B_\theta)}{\partial r} + \frac{\partial (u_{ez} B_\theta)}{\partial z}$$

$$= \frac{\partial(u_{e\theta} B_r)}{\partial r} + \frac{\partial(u_{e\theta} B_z)}{\partial z} + \left(\nabla \times \left(\frac{c \nabla \rho T_e}{e \rho} \right) \right) \Big|_{\theta}. \quad (2.13)$$

This is similar in form of the equation of the time advance of A_{θ} . Both equations require a more sophisticated algorithm to efficiently advance the quantities in time. The B_r and B_z terms on the right hand side of Equation 2.13 couple the two equations together. It turns out that both equations will be advanced in time together to maintain stability of the overall algorithm. This is discussed in more detail below.

The final field quantity that one needs is the electric field. This can be obtained directly from the electron momentum equation, Equation 2.8. Note that this is a simple algebraic relationship, assuming that the quantities on the right hand side are known.

2.3.4 Neutral quantities

The neutral quantities are similar to the fluid plasma quantities. There are corresponding equations for density, momentum, and energy conservation:

$$\frac{\partial n_n}{\partial t} + \nabla \cdot (n_n \mathbf{u}_n) = S_{pn}. \quad (2.14)$$

$$\frac{\partial}{\partial t} (m_n n_n \mathbf{u}_n) + \nabla \cdot (m_n n_n \mathbf{u}_n \mathbf{u}_n) + \nabla p_n = S_{mn}. \quad (2.15)$$

$$\frac{3}{2} \frac{\partial n_n T_n}{\partial t} + \nabla \cdot \left(\frac{3}{2} n_n T_n \mathbf{u}_n \right) + n_n T_n \nabla \cdot \mathbf{u}_n = Q_n \quad (2.16)$$

In all, PGaS advances the following 20 quantities in time: $n_i, n_n, T_i, T_n, T_e, u_{ir}, u_{i\theta}, u_{iz}, u_{er}, u_{e\theta}, u_{ez}, u_{nr}, u_{n\theta}, u_{nz}, E_r, E_{\theta}, E_z, B_r, B_{\theta}$ and finally B_z ,

2.4 Forms for the Source Terms.

To complete the description of the equations used in PGaS the specifications of the source terms that appear in the fluid conservation equations must be determined. The reactions between the plasma and neutral gas will be considered first.

The following reactions are modeled:

Electron impact ionization:



Resonant charge-exchange:



Three body recombination:



And finally, elastic collisions.

The source of particles for a species is sum of the individual contributions from each particular reaction. That is

$$S_{pj} = S_{ion,j} + S_{cx,j} + S_{rec,j}. \quad (2.20)$$

The terms *ion*, *cx*, and *rec* refer to the individual contributions due to ionization, charge-exchange, and recombination, respectively. The *j* subscript denotes the species. In this case the subscript will either be *i* for the ions or *n* for the neutral gas.

The individual source terms have the form, for some reaction *rx*,

$$S_{rx} = R_{rx} = n_1 n_2 \langle \sigma v \rangle_{rx}. \quad (2.21)$$

Here n_1 and n_2 are the two species involved in the reaction and v is the relative speed difference between the particles. The notation $\langle \cdot \rangle$ denotes an average. The term R_{rx} is called the reaction rate. It has units of particles per unit volume per second.

Conservation of particles might lead one to assume that $S_{pi} = -S_{pn}$. Though this is certainly true in the global sense, it may not be correct given certain assumptions about the interactions. For the charge-exchange reaction, the hot charge exchange neutral is assumed lost from the system. This is based on the assumption that the charge-exchanged neutral will be at the typical plasma temperature, and hence its thermal velocity will be very large. For this fast charge-exchanged neutral to be thermalized in the background neutral gas, it would have to undergo several scattering events with the background neutral gas. Since the fast charge exchange neutral is assumed to be at near

the plasma thermal velocity, the mean free path between collisions will be very large, usually greater than the characteristic length of the system. This neutral gas particle would stream out of the system without any interaction with the background neutral gas. In this case it would be a bad assumption to thermalize these fast charge-exchange neutrals into the background fluid.

For the ions, charge-exchange is not a source of particles ($S_{cx_i} = 0$). One hot ion is replaced by a cold ionized neutral. For neutrals, assuming that the hot charge exchange neutral is lost, this one to one replacement does not take place, and charge-exchange is a source of particles ($S_{cx_n} < 0$). In general, $S_{pi} \neq S_{pn}$ in the code.

The form of the source term must be consistent with the form of the conservation equation that is being used. For the particle conservation equation, this is never an issue because there is generally only one form of this conservation. For the momentum and energy equation, this is not the case. The momentum equation can either be expressed in terms of the variable (nu) , or simply in term of the variable u . Here (nu) is considered a single variable. The first form is the true conservation form, conservation of momentum. The second form is sometimes called the equation of motion for the system. The form of the source term for each equation will be different.

An example of this difference is the ionization of the neutral gas. The velocity of the neutral gas is not expected to change because of the ionization process. If the momentum equation is cast in terms of (nu) , then the ionization reaction would be a source for this equation ($S_{mn} < 0$). If the momentum equation is cast in terms of u , then the ionization reaction would not be a source for this equation ($S_{mn} = 0$). In both cases, the velocity of the gas is unchanged. This is obvious for the case when $S_{mn} = 0$. For the case when the variable is (nu) , the velocity is recovered by dividing (nu) by the density, which has also been reduced by the ionization process. The ratio of the decrease in (nu) and the decrease of n would be the same (in this simple scenario) and the resultant u would be unchanged.

The source term for the energy equation has the same concern. The energy equation can be cast in either total energy, or internal energy. The source term must reflect this choice.

The momentum source terms for the ionization, charge-exchange and recombination reactions are similar to the form for the particle source. The general form for the total momentum source term is:

$$S_{mj} = \sum_{rx} (mV)_{rx} R_{rx} \quad (2.22)$$

Here R_{rx} are the reaction rates for the individual reactions being considered. The term $(mV)_{rx}$ is the amount of momentum appropriate for reaction rx , keeping in mind the above discussion of the consistency of the source term to the form of the equation. In the code, the momentum equation is cast in terms of (nu) , so the source terms must reflect this.

For the ions, ionization is a source of momentum, so $(mV)_{ion} = m_n u_n$. The subscripts on the right hand side indicates that it is the neutral particle that is ionized into the ions. The opposite type of reaction is the recombination reaction. In this case, there is a net momentum loss from the ions, and $(mV)_{rec} = -m_i u_i$. The charge-exchange reaction is a combination of events. The plasma loses the momentum associated with the plasma particle, but gains the momentum associated with the neutral component. This gives $(mV)_{cx} = m(u_n - u_i)$. Here it was assumed that $m_i = m_n$, as is the case in these simulations. The form can be checked by noting that if the neutrals are moving slower than the ions, this will be a negative source of momentum for the ions and their velocity will be reduced. If the neutral particle is moving faster than the ion, this will be a positive source of momentum, and the ion velocity will increase.

One must then account for the momentum transfer in elastic collisions. The momentum transfer for elastic collisions has the form

$$S_{m_{elastic}} = m_1 n_1 \nu_{21} (u_2 - u_1), \quad (2.23)$$

where ν_{21} is the collision frequency of particles of type 1 with particles of type 2. Here it was assumed that $m_1 = m_2$.

For the energy source terms, the atomic reactions lead to energy source terms similar in form to the source terms for momentum:

$$Q_j = \sum_{rx} (E)_{rx} R_{rx}. \quad (2.24)$$

Here $(E)_{rx}$ is the energy brought in per reaction. For the ions, $(E)_{ion} = 3/2 n_n T_n$, $(E)_{rec} = -3/2 n_i T_i$, and $(E)_{cx} = 3/2 n_i (T_n - T_i)$.

Finally, a form for the resistivity, η , is needed for the field equations. For a simple plasma with no electron-neutral collisions, the resistivity is assumed to be the classical resistivity of Spitzer and Härm [17]. To include the effect of the elastic scattering of electrons on neutrals, the following form is used for the conductivity [12]:

$$\sigma \simeq \frac{n_e e^2}{m_e \nu_{eH}}. \quad (2.25)$$

Here ν_{eH} is the scattering frequency from all heavy particles. That is, $\nu_{eH} = \nu_{ei} + \nu_{en}$. The resistivity is the inverse of Equation 2.25. In the limits of a fully ionized plasma Equation 2.25 is off by about a factor of two. In these cases, when the neutral density is very small or zero, the code uses Spitzer and Härm conductivity, given by

$$\sigma_{SH} = 1.975 \frac{n_e e^2}{m_e \nu_{ei}}. \quad (2.26)$$

2.5 Solution Techniques

2.5.1 Fluid equations

For all of the fluid equations, the conservation equation takes on the form

$$\frac{\partial Q}{\partial t} + \nabla \cdot (Qu) = S. \quad (2.27)$$

Here Q is whatever quantity one is computing; it may or may not be a vector. The finite difference form of this equation becomes

$$Q^{n+1} = Q^n - dt \left(\frac{\partial}{\partial r} (rQu_r) + \frac{\partial}{\partial z} (Qu_z) - S \right). \quad (2.28)$$

The partial derivatives on the right hand side of this equation are evaluated using Donor Cell differencing. This is a common finite-difference technique that takes into account some of the physics of the flow. It is equivalent to the *Upwind* differencing method (referred to as the second upwind method by Roache[16, page 73]). It appeals to the physics of the flow to difference (in space) in the direction from where the information for this particular cell is coming from. *Upwind*, if you will. In general, this direction can be different for each cell. A benefit of this scheme is that it is

both conservative and transportive. A difference scheme is said to be *conservative* if it preserves certain conservation relations of the continuum equation. A difference scheme is said to be *transportive* if any errors associated with the scheme are convected in the direction of the flow. Both these properties are beneficial for an algorithm to have, although not absolutely required.

2.5.2 Second order equations

The equations for the time advance of A_θ and B_θ are second order partial differential equations. As mentioned previously, these equations must use a finite difference technique that is different from the upwind method used for the conservation equations. The method that will be used is called the Alternating Direction Implicit method [14], or ADI.

A generic form of a two-dimensional second order partial differential equation is the heat equation

$$\frac{\partial Q}{\partial t} = \alpha \left(\frac{\partial^2 Q}{\partial x^2} + \frac{\partial^2 Q}{\partial y^2} \right) \quad (2.29)$$

This particular form is in cartesian coordinates, but no generality is lost in this form. To finite difference this equation using ADI techniques, one would obtain the following two step process:

$$\begin{aligned} \frac{Q_{i,j}^{n+1/2} - Q_{i,j}^n}{\Delta t/2} &= \alpha \left(\frac{Q_{i+1,j}^{n+1/2} - 2Q_{i,j}^{n+1/2} + Q_{i-1,j}^{n+1/2}}{(\Delta x)^2} + \frac{Q_{i,j+1}^n - 2Q_{i,j}^n + Q_{i,j-1}^n}{(\Delta y)^2} \right) \\ \frac{Q_{i,j}^{n+1} - Q_{i,j}^{n+1/2}}{\Delta t/2} &= \alpha \left(\frac{Q_{i+1,j}^{n+1/2} - 2Q_{i,j}^{n+1/2} + Q_{i-1,j}^{n+1/2}}{(\Delta x)^2} + \frac{Q_{i,j+1}^{n+1} - 2Q_{i,j}^{n+1} + Q_{i,j-1}^{n+1}}{(\Delta y)^2} \right). \end{aligned} \quad (2.30)$$

The idea is to preserve the tridiagonal system of simple algebraic equations that result when differencing each second order operator. A tridiagonal system of equations can be inverted very efficiently. If one were to finite difference the second order partial differential equation in a straight forward implicit manner, the resultant matrix that would have to be inverted would no longer be tridiagonal. The matrix would still be

band limited, but would not be as efficient to invert as a tridiagonal matrix. The idea in Equation 2.31 is to implicitly difference only one part of the multi-dimensional operator in each step (the method extends to three dimensions). The information solved for in the first step are the quantities at some fractional time step $n + 1/2$. If the first equation in Equation 2.31 is rewritten with all quantities at time level $n + 1/2$ on the left hand side, then the information on the right hand side is at time level n , and is known. This can be thought of as doing an implicit finite difference on the x component of the two dimensional operator, and an explicit finite difference on the y component. In the second step the operator which is differenced implicitly is switched (or cycled in a three dimensional problem), so that the information on the right hand side is known at time level $n + 1/2$ and again is an explicit difference. In this case, the left hand side solves implicitly for the quantities at time level $n + 1$, and the time step is complete.

When a more general form of a second order equation is solved, care must be given to the determination of the coefficients of the operators. In general these coefficients can be time dependent. The *time level* of the coefficients on each side of equation play a role in determining the truncation error of the scheme, and a crucial role in the overall stability of the algorithm. For a discussion of these considerations see Anderson [3, page 167] or Peyret [15, page 66].

2.6 Outline of Code sequence

The code sequence is outlined in Table 2.1. It consists of a main driver program that executes a loop for each time step that is desired. In this loop the separate subroutines are called that advance the quantities in time. The first subroutine that is called is FLUIDI. This subroutine advances the fluid quantities (e.g., n_i, u_i). The next subroutine that is called is FIELD. This in turn calls CPARA, which advances the magnetic field. Finally, FIELD calculates the electric field at time level $n + 1$, and the sequence is complete. These subroutines are discussed in further detail in the following section.

2.7 Subroutine Descriptions

In this section the details of the subroutines used in PGaS will be presented. Specifically, the following three subroutines will be described: FLUIDI, CPARA, and FIELD. These three subroutines represent the bulk of the work that is done in PGaS. These subroutines

-
-
- Main calling loop. Time is advanced from $t \rightarrow t + \Delta t$
 - Calls subroutine FLUIDI. Explicitly advances fluid quantities from n to $n + 1$
 - Calls FIELD to advance field quantities.
 - * FIELD calls CPARA. Advances \mathbf{B} to $n + 1$.
 - * Calculates \mathbf{E} at $n + 1$ via Ohm's Law.
 - FIELD returns.
 - Loops to top of Main loop for another time step.
-
-

Table 2.1: Flow chart of primary code sequence.

are listed in Appendix B. The other subroutines in PGaS provide support services (e.g., diagnostics) and are not discussed.

The subroutines will not be described line-by-line. Rather, the outline of the implementation of the algorithm will be explained. For instance, in some places an average density is used instead of an actual cell density. This is a particular detail that is obvious from the source listing, but does not directly effect the implementation of the algorithm. Most of the algorithms used in PGaS are all described in detail elsewhere, and the reader will be referred to suggested texts.

2.7.1 Fluidi

Subroutine FLUIDI advances the ion and neutral fluid quantities in time. Of all the quantities in the code, only the density, n , and the particle fluxes, nu , are true second order quantities in time. A second order quantity means one in which the truncation error goes as $(\Delta t)^2$.

The density, temperature and velocities are advanced from time level n to $n + 1$ in this subroutine. The fluxes (nu) are calculated at half increments, so the fluxes are advanced from time level $n - 1/2$ to $n + 1/2$. The reason for the fluxes being at half integral time steps compared to the density is in the historical development of PGaS. It was originally written as a PIC code and the fluid routine was included to provide a fast mode to run the code to debug the field advance. In the PIC algorithm, the flux is

required to be at half integral time steps for stability, so this requirement was carried over into FLUIDI.

FLUIDI implements a clever algorithm that maintains second-order accuracy in time by center-differencing (in time) the fluid quantities. The quantities are second-order in time but they are not time reversible. A scheme is time reversible if one can set $dt = -dt$ and run the algorithm and recover the exact value at time level n from the information at time level $n + 1$. The reason the time advance is not time reversible is because the algorithm uses a one-sided difference to get the estimate at the center point. For example, to advance the density from time level n to $n + 1$, one first gets an estimate of all the quantities at time level $n + 1/2$. (By all the quantities I mean everything used on the right hand side of the equation.) The algorithm gets the estimate at time level $n + 1/2$ by doing a one-sided difference from time level n . If dt was set to $-dt$ and the algorithm run from time level $n + 1$, the information used to obtain the center estimate would now come from a one sided difference from time level $n + 1$. The center point estimates will in general not be the same, and thus the algorithm will not be exactly time reversible. This is not to imply that the information is meaningless. It will not be time reversible in the exact sense (to machine precision). It will be accurate to the truncation limit of the algorithm being used, in this case dt^2 . For a true time reversible algorithm, one could advance from time level n to $n + 1$, and then back to n , and get the exact answer back for the information at time level n (to machine precision).

The algorithm is explicit and thus uses information only at old (known) time steps. Passed into FLUIDI are the values of n^n , T^n , E^n , B^n , and the particle fluxes, ($flx = nu$), $flx^{n-1/2}$ and flx^n . The particle flux at time n is recovered from n^n and u^n . The algorithm loops through the same finite-difference loop twice, each time advancing different quantities to different time levels. The loop being referred to here is the loop defined by the FORTRAN label 120 and the goto 120 statement as seen in the appendix. The density and temperature are advanced by a time step $dt1$, and the fluxes are advanced by a time step $dt2$. The first time through the loop $dt1 = dt/2$ and $dt2 = dt$. What is happening here is as follows: the fluxes are being advanced from $n - 1/2$ to $n + 1/2$ in a time centered fashion. This is achieved by the fact the all the quantities being used to advance the fluxes are at time level n . Even the fluxes that are use during this time advance are at time level n because the fluxes at time level n

were recovered from the information stored in n^n and u^n .

At the same time, during the first loop, the density and temperature are advanced to a provisional time level $n + 1/2$. These provisional quantities at $n + 1/2$ will be used with the fluxes calculated during the first pass, which are now also at time level $n + 1/2$, during the second pass.

The second pass sets $dt1 = dt$ and $dt2 = dt/2$. This is because the density and temperature (which use $dt1$) will be advanced from time level n to $n + 1$ using all the quantities (density, temperature, velocities, and fluxes) that are currently at time level $n + 1/2$. This maintains the time-centered advancement of density and temperature.

The fluxes (which use $dt2$) will be advanced another $dt/2$. This is to provide the information needed to extract the velocities at time level $n + 1$. After the second pass through the loop, all the fluid quantities are advanced to the desired time level.

2.7.2 Cpara

The CPARA subroutine advances both A_θ and B_θ to time level $n + 1$. It does this implicitly using an ADI method (Alternating Direct Implicit) described earlier. The particular implementation of the ADI method used in CPARA was designed by Dennis Hewett[9]. It was carefully designed to vectorize on CRAY computers, and is unique in that it advances both A_θ and B_θ at the same time.

The description that follows refers to loop numbers in the subroutine listing in the appendix.

The purpose of CPARA is to advance the magnetic field information from time level n to $n + 1$. It does this by advancing A_θ (Equation 2.12), which gives B_r and B_z , and B_θ (Equation 2.13). As was noted in the discussion that followed Equation 2.13, these two equations are coupled together. The fact that they are second order requires that some type of implicit method be used to remove the stringent time step requirements that the CFL condition would impose on an explicit method. To ensure the overall stability properties of the time advance, some clever way must be developed to advance these quantities. Such an algorithm is implemented in CPARA.

The algorithm has the following general outline:

1. The first half of the ADI advance is performed for A_θ . This pass does r implicitly. This takes A_θ from A_θ^n to $A_\theta^{n+1/2}$.

2. A *temporary* second half ADI advance is performed for A_θ . This brings A_θ to a temporary value $\overline{A_\theta^{n+1}}$. This value is used only to obtain estimates of B_r , B_z and $u_{e\theta}$ at time level $n + 1$. All these quantities depend on A_θ and they appear on the right hand side of the equation for B_θ (Equation 2.13).
3. The first half of the ADI advance for B_θ is then performed. This pass does r implicitly. After this step, an estimate of u_{ez} is obtained with the current values of B_θ . This electron velocity component is about to appear in the implicit z advance for B_θ , so it is updated now.
4. The second half of the ADI advance is done on B_θ . This half does z implicitly. B_θ is now at time level $n + 1$.
5. The final ADI advance is performed for A_θ . This half advances A_θ from time level $n + 1/2$ to time level $n + 1$.
6. The vacuum field is cleaned up.
7. The new values of B_r , B_z and $u_{e\theta}$ are calculated. All the information for these quantities are now at time level $n + 1$. This completes the time advance for the magnetic field.

Loops 5, 7, 25 and 30 do book keeping that sets up the boundary condition information in the appropriate arrays. It seems overly complicated but it was done in this manner to ensure that the main loops that follow could be vectorized, and to minimize the number of arrays that need to be passed to CPARA. The boundary values of A_θ and B_θ are passed in the ghost cells of arrays `saq` and `sq`, which hold A_θ^n and B_θ^n , respectively. From these boundary values and knowing what boundary conditions are desired at the boundaries, interpolation factors can be determined. Once these interpolation factors are determined, the appropriate values of A_θ and B_θ are returned to the ghost cells.

In loop 105 the most recent u_{er} is calculated. This quantity will appear on the implicit side of the equation, as discussed earlier. The other components of the electron velocity appear on the explicit right hand side and are left at their current values.

In loop 150 the first of four ADI passes will be set up. All of the ADI set-ups have the same form. The first ADI pass will do the r component implicitly (the r derivatives

are on the left hand side of the equation, and the z derivatives are explicitly calculated on the right hand side). This loop will be described in greater detail, and the following will just be called the ADI setup.

Loop 150 sets up the coefficients for the tridiagonal inversion of the set of equations for a particular row j in the z direction. It runs from $i = 2$ to $i = nr1$. The inner loop, loop 140, sets up the coefficients for every row j . All the axial rows will be inverted with one call to a specialized tridiagonal subroutine, VTRIR. The arrays $tp()$, $tc()$, and $tm()$ hold the coefficients for the $i + 1$, i , and $i - 1$ values of $A_\theta^{n+1/2}$. The right hand side of the equation is the explicit approximation for the axial derivatives. These are stored in the array $t0()$.

Loop 160 passes the desired boundary value to VTRIR in the associated ghost cells of array $t0()$. The call to VTRIR is made and the first half of the ADI advance, in this case $A_\theta^{n+1/2}$, is returned in array $t0()$. The boundary conditions in the axial directions are set (VTRIR sets the radial boundary conditions) and then the vacuum magnetic field is cleaned up. This step ensures that $\nabla \times \mathbf{B} = 0$ in the vacuum.

Now the temporary second half of the A_θ ADI is preformed (loop 350). It is set up the same as for the r implicit pass, but this time z is implicit and the r derivatives appear explicitly on the right hand side of the equations.

The full ADI advance for B_θ is now performed. As noted above, u_{ez} is updated between the r implicit (loop 250) and z implicit pass (loop 450).

To complete the time advance, the final z implicit ADI advanced is performed for A_θ (loop 750). This advances A_θ to time level $n + 1$.

Before returning, the current values for B_r , B_z and $u_{e\theta}$ are calculated. This completes CPARA and it returns to FIELD.

2.7.3 Field

The FIELD subroutine gets its name because it advances the fields (\mathbf{E} and \mathbf{B}) in time.

FIELD first calls the subroutine CPARA, described above, which advances both A_θ and B_θ to time level $n + 1$. A_θ can be used to obtain both B_r and B_z .

FIELD then advances the electric field to time level $n + 1$. It advances the electric field by solving the electron momentum equation (the Ohm's law for the model) for \mathbf{E} . At this point in the cycle all quantities except \mathbf{E} are known at time level $n + 1$. The solution for \mathbf{E} is a simple algebraic step, but it is essentially implicit because all

quantities used to calculate E are now at time level $n + 1$.

Chapter 3

Axial Injection

In this chapter the results for the axial injection of a neutral gas jet will be presented. The title *Axial Injection* is chosen because the injection of the neutral gas is only in the axial direction. In the summary chapter, Chapter 4, alternative methods are presented that could be utilized in the creation of the hybrid plume plasma rocket. This chapter will focus on the axial injection method for forming a smoke ring structure that will act as the detachment process of the plasma from the magnetic field.

The results from these simulations are divided into two groups. The first group are those simulations performed with a static magnetic field. It was decided to use a static magnetic field for two reasons. First, the amount of CPU time involved with each run is very large. This is partly due to the fact that the outflow boundary had to be sufficiently far away from the prime area of interest to prevent numerical instabilities from terminating the simulation. The second reason for using a static magnetic field is that it allowed the simulation to continue to a further time. Even with the outflow boundary moved away from the interaction region, the plasma flow across this boundary is unavoidable. The code was much more robust in the stability of the outflow boundary when the magnetic field was static. This allowed one to run the code further out in time, seeing more of the interactions that one desired. With the full time dependent magnetic field the code terminated approximately one microsecond after the interactions started. This did not allow one to develop a good intuition about the reactions being studied. By using a static field, a longer period of the interactions could be examined, giving one a better understanding of the physics involved. The method envisioned to capitalize on the strengths of both simulation procedures was as follows. The static magnetic field cases would be carried out initially. The speed of the code would allow

one to do a detailed parameter scan of the interactions. The long simulation periods would allow one to develop a good intuition of the dynamics of the interactions. From these runs one could analyze the results and look for indications that the dynamics of the field behavior was important. One indication would be the resultant plasma velocity vectors. If there was significant cross-field flow, the response of the magnetic field to that flow would probably be important. For the cases that are selected, the full time dependent simulations could be performed. From the knowledge that was gained through the static field results, one would have a good idea of what to look for and on what time scale. Consequently, even though the static magnetic field simulations do not include all of the physical phenomena of the full time dependent simulations, the two simulation techniques used together form a powerful method for analyzing systems of interest. Because of the longer interaction period, the static field cases will be presented first.

3.1 Motivation

For high temperature plasmas, the plasma will tend to expand along the magnetic field lines. In the limiting case of ideal MHD, the conductivity is considered infinite (zero resistivity). In this limit the plasma and field lines are *frozen* together. Since the resistivity goes inversely as the temperature to the three-halves power, even a moderately high temperature plasma will tend to cling to the field lines. As the field lines expand, the axially directed momentum (the thrust one wants) will be redirected in the radial direction. Since the field lines are axisymmetric, there will be no net radial force, the momentum is just lost in terms of z directed thrust.

One must come up with some way to allow the plasma to detach itself from the magnetic field lines. The magnetic field lines are generated by the ship, thus any drag the plasma has while crossing the field lines will be felt by the ship. In the scenario above, the plasma never actually crosses the field lines, but the magnetic field bends the plasma in the radial direction. There is a force in the negative z direction (the positive z direction is defined as going away from the ship) slowing the plasma down, and simultaneously a positive force in the r direction accelerating the plasma radially. Since the magnetic field can do no net work on the particle (it is simply applying a torque on the particle), the total energy of the plasma remains the same, it is just

redirected radially. Actually there can be a transfer of perpendicular energy to parallel energy (perpendicular and parallel in reference to the magnetic field), but energy is still conserved; this is a detail of the interaction, and not important in what is considered here. In ideal MHD, the radial and axially forces just described are such that the particle remains on the field line. It is the coils in the device creating the magnetic field that also feel these forces. The axial force will tend to slow the ship down, so this drag is important.

What was described above holds for a low beta plasma. Beta is the ratio of plasma pressure to magnetic field pressure.

$$\beta \equiv \frac{\sum nKT}{B_G^2/8\pi} \quad (3.1)$$

Here n is the particle density, K is Boltzman's constant, and T the particle temperature. B_G is the magnetic field in units of Gauss (1 Telsa= 10,000 Gauss). Beta is an indication of the relative importance of the two different pressure components. In low-beta plasmas (e.g., $\beta \sim 1\%$), the magnetic field dominates and one would expect the plasma to have little effect on the magnetic field (i.e., the plasma will follow the field lines). With a high beta plasma ($\beta \sim 1.$), the two pressures are almost equal and thus the plasma won't obviously be dominated by magnetic forces. In this regime the plasma could deform the magnetic field.

Another indication of which effect will dominate the interaction is balance of energy density. For the plasma this is the directed energy density, or *ram pressure*. Ram pressure is defined as:

$$p_{ram} = \frac{1}{2}\rho v^2 \quad (3.2)$$

Here it can be seen that even a low-beta plasma (e.g., small thermal pressure due to a low temperature), can have a high ram pressure if it has a high directed velocity, e.g., a beam. One must compare the plasma ram-pressure against the magnetic field energy density ($\sim B^2$).

The idea behind axial injection is for the neutral gas to provide a mechanism to drive the disconnection of the plasma from the field lines. This disconnection process would be the generation of something like a smoke ring. If this smoke ring could be magnetically disconnected from the field of the ship, the smoke ring would cause little

drag on the ship as the ring leaves.

A particular process that is the focus of this thesis for the detachment of the plasma from the field lines is as follows. The plasma begins expanding along the magnetic field. The neutral gas is introduced at some radius so as to interact with the plasma in a region of reduced magnetic field strength. Here the neutral gas imparts momentum to the plasma preferentially in the z direction. Under ideal MHD conditions, the plasma and field lines would be frozen together. If the inertia of the newly created plasmoid structure is large compared to the magnetic field force, the magnetic field would be elongated in the z direction. Under ideal MHD there would be no mechanism for the field lines to reconnect and the elongation would continue until there was a balance between input momentum and the magnetic field tension. At this point a second role of the neutral gas becomes important. The neutral gas, through collisions with the plasma, will increase the resistivity of the plasma locally in the region of interaction. This added resistivity gives the magnetic field a channel in which the plasmoid structure could detach itself from the field lines of the ship and limit the continued stretching that would happen under ideal MHD. The field structure just before reconnection is envisioned to be like that of a droplet of water breaking away from a faucet. After reconnection the plasmoid structure would continue to stream away from the nozzle. The field lines within the plasmoid are now detached from the ship. It is this plasmoid structure that is referred to as a smoke ring (all this is happening symmetrically in the θ direction).

A possible method for this disconnection process is depicted in Figure 3.1. This is a non self consistent result in that the reactions between the plasma and neutral gas are assumed, and not calculated. Hence the resulting density, velocity, and temperature variations are not considered. The magnetic field response is accurate given the assumed plasma parameters, it is just that the plasma parameters are not physically consistent.

The simulation uses a extremely rapid magnetic field expansion in order to observe the result of the added axial momentum. The figure presents a time sequence of plots depicting the magnetic field structure. The time series progresses from left to right, top to bottom. Each subplot is labeled with an iteration number IT . In this figure, the z axis of each plot is the horizontal axis in the figure. The r axis is the vertical axis. The point $r = 0$ is at the top of each plot and $z = 0$ is at the left hand side of each plot. *This is the only figure in this chapter to use this geometry.* Other figures

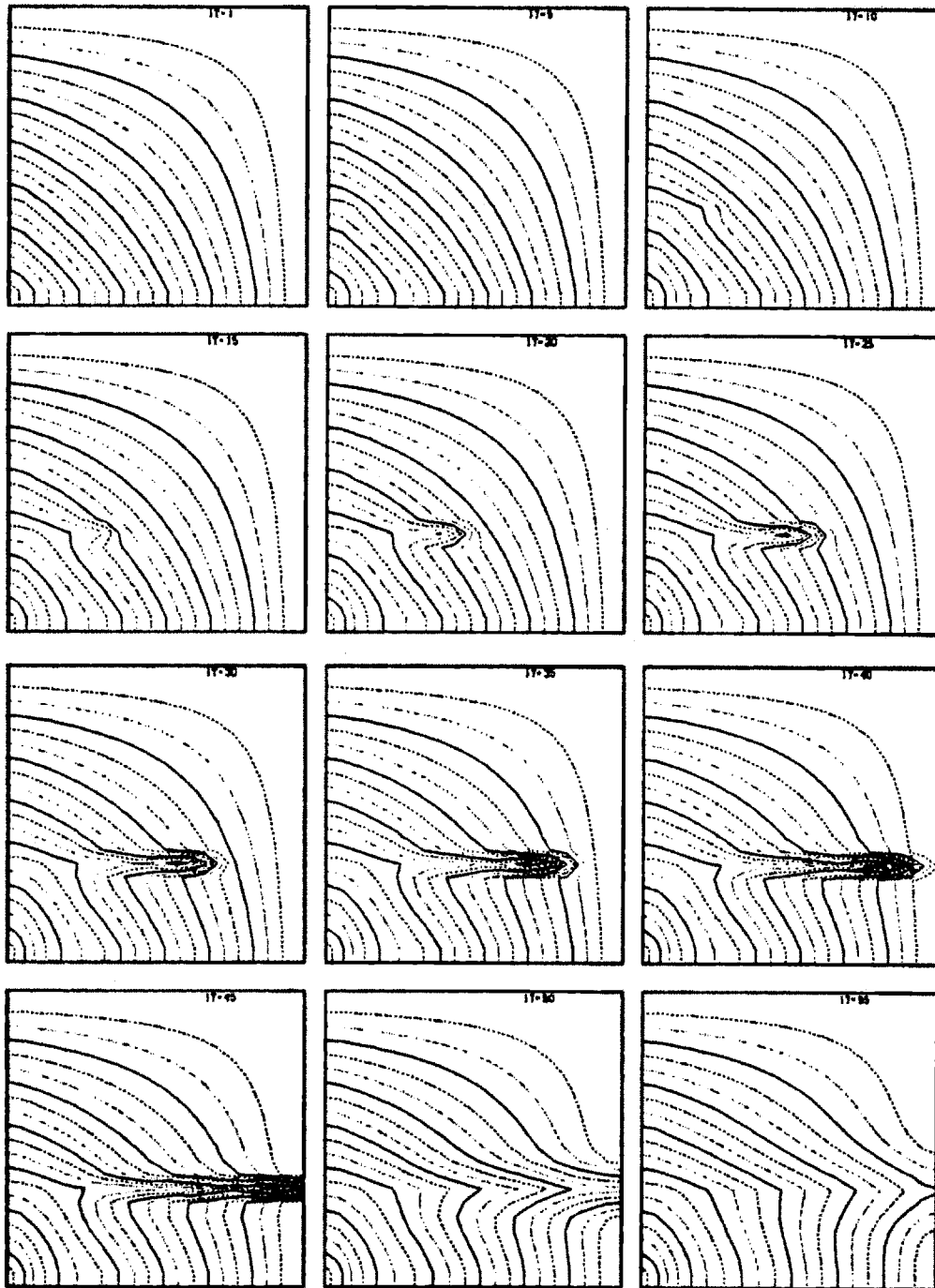


Figure 3.1: Non self-consistent simulation of smoke ring detaching from magnetic field lines via the axial injection of a neutral gas jet.

will have the radial axis the horizontal axis, and the vertical axis will be the z axis. In this figure the neutral gas jet is flowing from left to right. The other plots the neutral gas jet will flow from bottom to top.

The upper left hand plot shows the field configuration at approximately $t = 0$. This is the background or vacuum field. The neutral gas jet is being introduced at the left hand side approximately one third the way the axis. In the middle plot in the top row is the field configuration at five iterations. The field can just be seen deforming under the influence of the added plasma momentum.

As the time sequence progresses, the formation of the smoke ring is seen. It is deforming the field and pulling some of the field with it. Starting at $it = 40$ the resistivity behind the plasma structure is increased. The field lines deformed by the exiting smoke ring snap back, and the plasmoid structure is free to leave the rocket.

For the smoke ring to disconnect in this manner, two conditions must be satisfied. First, the neutral gas must couple its axial momentum to the plasma flow to give the plasma a cross field flow. Second, the neutral gas must increase the local resistivity sufficiently so that the magnetic field can move through this region and disconnect. If either of these conditions are not met, the disconnection process as outlined above will fail. Thus, in analyzing the results of the various runs, careful consideration will be given to these points.

3.2 Magnetic Field Geometry

The magnetic field is shown in Figure 3.2 As can be seen, the magnetic field falls off quite rapidly in the z direction. In this case, the field on axis at $z = 0$ is approximately 15,000 Gauss. At the exit plane, ($z = 40\text{cm}$), the field strength is approximately 150 Gauss. This is a reduction in field strength by a factor of one hundred, and a reduction in magnetic energy density of a factor of ten-thousand!

The field was chosen in this way to assist the plasma leaving the device. If one can generate the smoke rings described above, the smoke rings will undoubtedly be unstable, and will break up at some point down stream of the rocket nozzle. It is thought that the formation of the smoke ring will allow for the macroscopic plasma parameters (density, temperature, velocity) to be transported into a region of significantly reduced field. Here the local beta and ram pressure will be greatly different from where the plasma

B Field

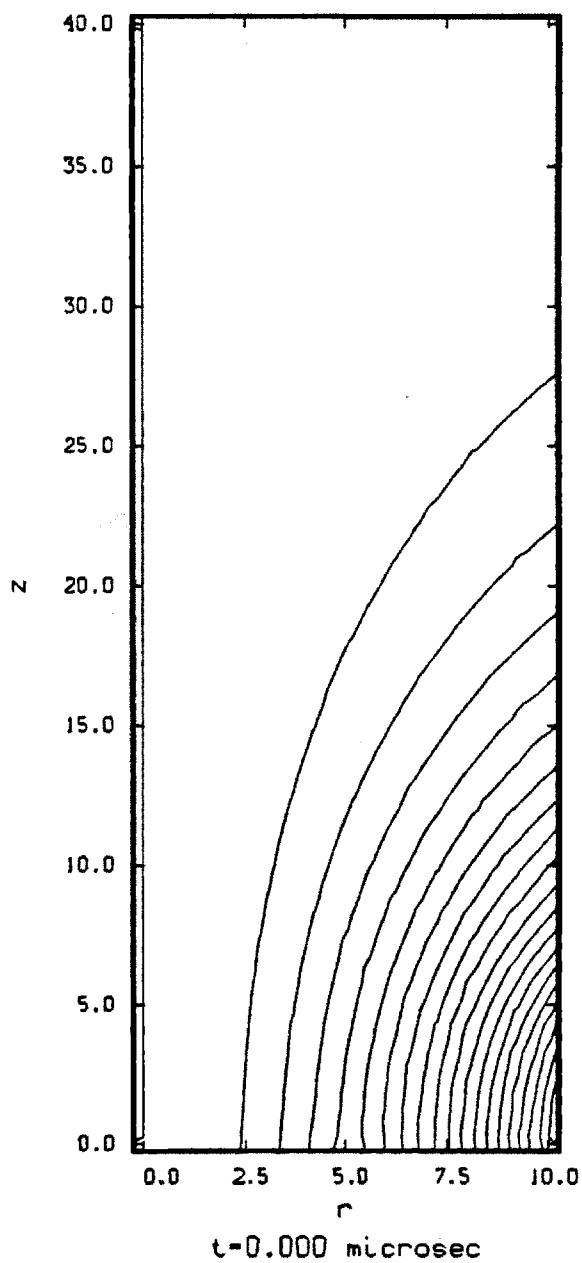


Figure 3.2: Magnetic field geometry for Axial Injection cases.

was created, and the exhaust can continue to exit from the nozzle with little more effect on the ship. For the field described above, this would be a reduction of field energy by a factor of 10,000, while the plasma parameters (ideally) remain unchanged. The details of stability of the smoke ring are beyond the scope of this thesis. The analysis will concentrate on whether the creation of such smoke rings (the prerequisite for the instability to be a concern) is possible.

3.3 Code results, Static Magnetic Field

The bulk of the code results will now be presented. The following cases will be considered:

1. Reference Case. Plasma neutral case system with all reactions between the plasma and neutral gas turned off.
2. Standard Case. Basic reactions turned on. Neutral gas density equal to plasma density. Gas injected at Mach seven.
3. High Beta Case. Same as the standard case but plasma beta increased to 50% (standard case beta is about 1%). Fluid parameters remain unchanged, beta increase is due to a lower magnetic field. Field fall off remains the same (magnitude scaled down).
4. High Density Case. Neutral gas jet injected at ten times the plasma density. Neutral jet Mach number remains at seven.
5. Matched Velocity Case. Neutral gas jet injected with initial velocity equal to that of the plasma. At Mach seven ($t_n = .025eV$), the neutral gas is moving almost a factor of ten slower than the plasma. In the Matched Velocity Case, gas is injected at an artificially high Mach number to match the axial velocities at $t = 0, z = 0$.
6. Super High Density Case. Neutral gas density is increased to a factor of one hundred over the plasma density. Mach number remains the same as standard case.

7. Wide Jet Case. Width of neutral gas jet increased. In all previous cases the width of neutral gas jet was kept small to provide a highly localized flux of momentum. In this case the jet width is increased to see how results scale with jet width.

Most of the specific details of the code (e.g., boundary conditions) will be presented under the reference case. All the graphs that will be used to analyze the flow will be presented and described, though most of the graphs will contain trivial data (all zero). In all subsequent cases, it will be assumed that the section for the reference case has been read and completely understood.

3.3.1 Reference Case: No reactions

The first case to be considered will be the reference case. This is the case when no reactions are turned on. The code still solves for both the plasma behavior and the neutral behavior, but the two fluids do not interact in any way; it was as if each were flowing into a vacuum. The reference case is important because it shows the natural behavior of the stand alone plasma. If this behavior is to expand and follow the field lines, one knows that something must be done if one wants to use this device as a plasma thruster. It also defines the baseline for which all the other results will be compared against to judge if they have had any real effect on the plasma.

The initial conditions used for the reference case will now be presented. Only the plasma properties will be referred to. Unless specifically stated otherwise, the same boundary conditions can be applied for the neutral component. The initial conditions for the plasma are also boundary conditions for the plasma at $z = 0$. That is, the plasma conditions at $z = 0$ and time $t = 0$ are held fixed throughout the simulation ($0 < t \leq t_{end}$). This boundary condition is fine as long as there is no information propagating upstream in the solution. This will be the case for supersonic flow. The plasma flow velocity is slightly subsonic at $z = 0$. The fixed boundary conditions are still used for simplicity and for numerical robustness (a Dirchlet boundary condition will tend not to blow up numerically). One must carefully watch the simulation develop and look for counter-streaming information. If it is observed that there is plasma streaming toward $z = 0$ and piling up, for instance, one must assume that the fixed boundary conditions there are inappropriate and are affecting the computational results. This has rarely been observed.

The initial conditions are described qualitatively as a central core of hot plasma with a density falling off exponentially. The peak density is specified as with the scale length for the fall off of density. The temperature is assigned in a similar fashion, with the same scale factor for the fall off as for the density. The velocity is a *constant* in radius and is chosen such that the bulk plasma velocity, V_b , is equal to the density weighted local thermal velocity. In other words

$$V_b = \frac{\sum n_i V_{th}}{\sum n_i}. \quad (3.3)$$

It was chosen to initialize the plasma velocity in this manner partly due to the physics of the flow, and to avoid the (physical) shear instability that such a flow can support.

The neutral gas velocity is a constant across the jet, as is the temperature. The velocity is set at the thermal velocity times a desired Mach number. Generally the Mach number should be kept high to minimize gas backflow; in this example it has been set to seven. However, the Mach number is varied in different cases.

The boundary conditions at $r = 0$ are set as Neumann zero. This is a consequence of the axisymmetry assumed in the problem. The radial components of the velocities (u_r) are set to zero. This is also consistent with axisymmetric flow. The boundary conditions at the wall, $r = r_{wall}$, are a bit more complicated. The radial components of the velocities are again set to zero, but this time because the flow is assumed to be running into a physical wall. The axial components are set as Neumann zero. This is known as a *slip* condition, and is consistent with a viscous free simulation. (If the axial flow is set to zero at the wall, this will tend to set up large radial gradients in that quantity. The only consistent way to model the problem is then to include viscous effects; they will be important in regions of large gradients. Since one does not expect that flow parallel to the wall to play a dominate role in the physics that is desired to be simulated, it was decided to use the simpler slip model.) The density is also set to Neumann zero. This allows the density to float to any value. The temperature boundary condition is the hardest to set. A Neumann zero boundary condition is used for the temperature. It is hard to justify this boundary condition because in reality the wall temperature should be some relatively fixed value (it can only be as high as the melting point of the surface). The problem with setting the boundary

condition on the wall to a specific value is that unless this value is self consistent, this boundary condition will support non-physical pressure gradients, which will tend to make the density (because it can float) blow up. A self consistent temperature boundary condition means that the temperature at the wall could be calculated in terms of the heat capacity of the wall and the heat flux into the wall. If this was done, whatever the side effects of maintaining this temperature (in terms of pressure gradients) should be physical and somehow self-limiting (after all, the density should not go to infinity). The temperature boundary condition is primarily a concern for the neutral gas. The plasma is never expected to be in contact with the wall, so the choice of boundary conditions for the plasma temperature is not important. After all, if the plasma is contacting into the wall, the insulating properties of the gas are lost. In terms of the neutrals, calculating the wall temperature self consistently could be done, but it adds complexity to the code in a situation that one is not really interested in. The prime concern is not the detailed effects of the neutral/wall interactions but the neutral/plasma interaction. Consequently, a Neumann zero boundary condition was chosen for the temperature. It is slightly non-physical, but the benefits gained in terms of numerical robustness far out weigh the slight inaccuracies of the boundary condition.

All quantities in the duct are assumed to be zero at $t = 0$, except for the neutral gas. The neutral gas is started *prestreamed* some distance down the duct. This would correspond physically to turning on the neutral gas for some time before the plasma. Because of the relative speed difference between the plasma and neutral gas, this prestreaming avoids the computation of the initial *start-up* phase of the device, where nothing is happening (in terms of interaction of the plasma and neutral gas). The length of this prestreamed neutral gas can be varied.

With this description of the input parameters and boundary conditions used, the specific plasma and neutral gas parameters are listed in Table 3.1.

An important number to note is the difference in mass flow rate (\dot{m}). The mass flow rate of the neutral gas is almost an order of magnitude less than that of the plasma. The neutral gas velocity corresponds to a Mach number of seven. The specific impulse (I_{sp}) is shown for each fluid, and then the combined specific impulse for the device. It is important to note here that this specific impulse is measured at $z = 0$. The specific impulse will vary depending on the exact location that it is measured at. The specific impulse reported here is measured at $z = 0$ and represents the best that can

Item	Ions	Neutrals
mass flow rate (\dot{m}), kg/sec	2.87e - 04	3.86e - 05
Thrust, Newtons	32.47	0.6
Power, MWatts	1.83	0.005
Temperature, eV	100.0	0.025
Density, part/cm ³	1.0e+15	1.0e+15
Velocity, cm/sec	1.13e+07	1.5e+06
I_{sp} , sec	11,500	1,600
I_{sp} net, sec	10,350	

Table 3.1: Input parameters for reference case. No interactions.

be hoped for from the device. The number is presented here as an optimum that the machine could be expected to achieve. The specific impulse will degrade due to plasma expansion and the neutral gas slowing down the plasma. The specific impulse could increase if there is a significant exchange of internal plasma energy (temperature) into directed energy (velocity). It is important to remember that specific impulse in this context is the mass averaged velocity. In other words, you want your mass where your velocity is. If most of the mass flow is from the relatively slow neutral gas, this will lower the overall specific impulse of the device. This is an important figure of merit for a plasma thruster, and must be considered carefully.

The actual results of the reference case will now be presented. The conditions at several time steps will be shown, and several different types of plots will be presented. Though nothing exciting is happening in this run, the plots will be presented so that one may become familiar with the form of the graphs that will be used to present later results. Without any reactions between the fluids, some graphs that are about to be presented will be empty. They are presented to form a complete description of the upcoming analysis. Then when there are reactions between the fluids, the graphs should then be easier to understand. The field used in this run (and all the following in this chapter) was shown in Figure 3.2 on page 49. With no interactions, one expects the plasma to expand and follow the field lines, and the neutral gas to expand slowly (due to the small thermal pressure) and stream down the duct. This is what one sees.

In Figure 3.3 the plasma density at two microseconds is presented. The front of the plasma has streamed out to about 30cm. Some detail along the leading edge of the plasma can be seen in this plot. This is a consequence of the finite grid of the computa-

tional domain. The grid is 20×80 (r and z respectively), making $dr = dz = .5cm$. If the exact nature of this expansion front was the prime concern of the simulation, one would have to refine the grid in both the z direction and r direction. The price one would pay is in the computer time needed to generate the same results. A doubling of the number of grids in both r and z would quadruple the amount of computations involved. On a vectorized computer such as a CRAY, this does not immediately translate into a factor of four increase in CPU time involved in the simulation, but it does significantly increase the running time of the code. The current grid parameters were chosen as a compromise between resolution and CPU time.

At the top of the figure are listed the maximum and minimum contours. The labels on each contour have been omitted for readability. The number on the left is the minimum contour level and the number on the right is the largest contour plotted. These numbers may not always be present. If the information being plotted does not have an easily understood macroscopic realization, they are not presented. Such a case is the magnetic field lines. The magnetic field lines are contours of constant ψ ($\psi = rA_\theta$). The values of ψ itself are not that important, but the plot of the values of constant ψ are conceptually meaningful.

From this figure of plasma density one can see that plasma has streamed partway into the duct. From the contours shown and the knowledge that the plasma started peaked at $r = 0$, one can tell that the plasma is falling off radially and axially. One might think that because the plasma is initialized with a constant velocity in radius, that the plasma should stream down the duct with a constant rate. This would be the case without axial pressure gradients. Since both the temperature and density vary as a function of r , the axial pressure gradient ($\nabla p_z = \partial nT / \partial z$) is also a function of radius. The maximum pressure gradient exists at $r = 0$ and thus the plasma at $r = 0$ will experience the largest force due to this pressure gradient, and in turn be accelerated to a higher velocity, and therefore stream further into the duct than the plasma further out in radius in a given time.

The next figure that will be analyzed is the velocity flow field. This graph is important because with a single graph, it gives a good qualitative feel of the nature of the flow (i.e., is the flow expanding along the field lines).

The arrows point in the direction of the flow, with the length of the arrow proportional to the local velocity relative to the maximum velocity of the current graph. The

Ion Density

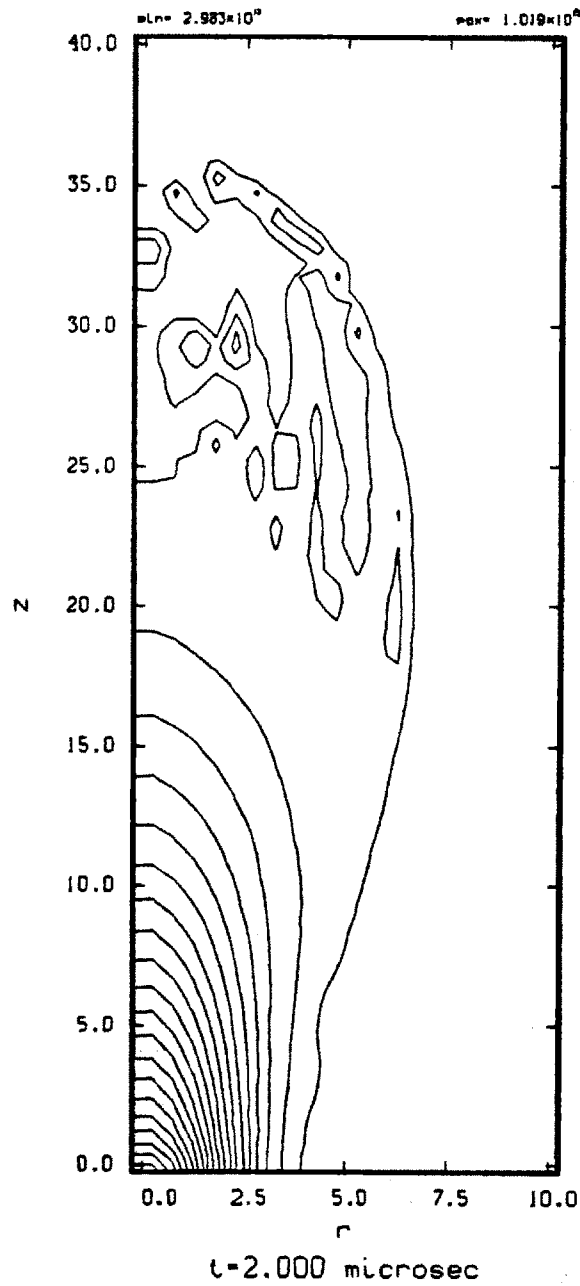


Figure 3.3: Plasma density at two microseconds for the reference case.

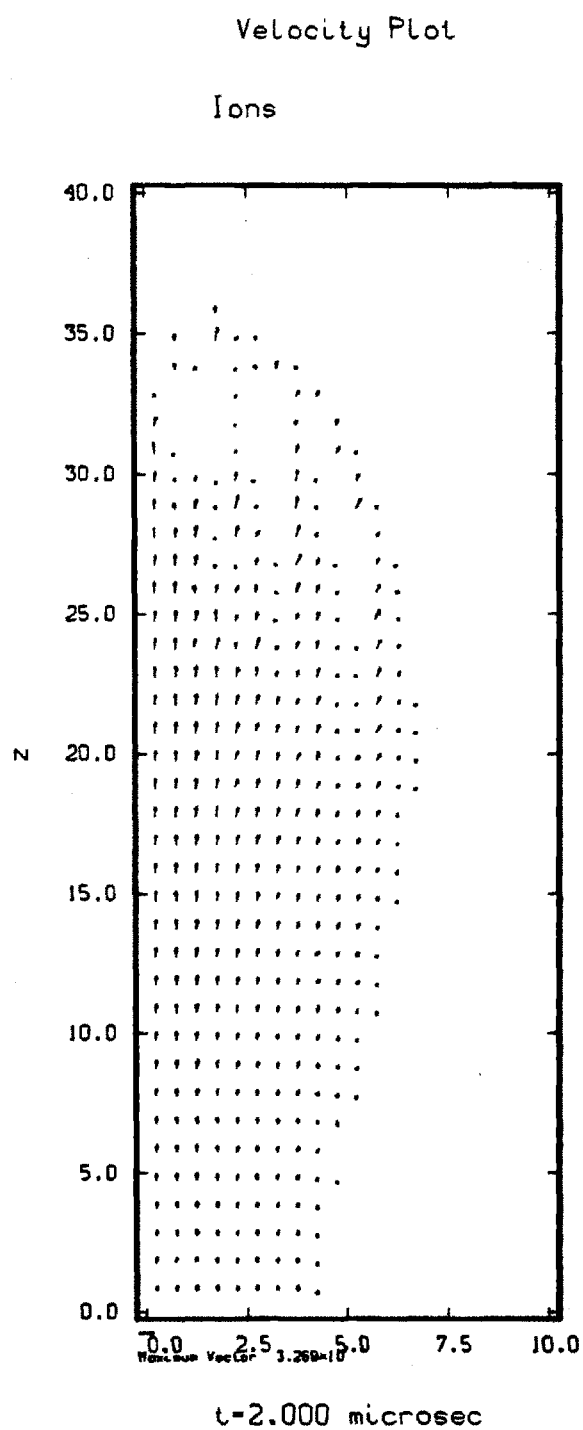


Figure 3.4: Ion Velocity plot at two microseconds for the reference case.

length of the maximum vector and its numerical equivalence is shown at the bottom of the graph.

In the velocity graph, one can see that the flow field has been accelerated by the axial pressure gradient. From the direction of the vectors one can tell that the plasma is starting to expand along the diverging field.

The next two graphs to be presented are the main diagnostic graphs. These will let one better understand the dynamics of the interactions that are happening and whether the interactions are sufficient for the operation of a plasma thruster.

The first of these graphs is shown in Figure 3.5. It is a series of three plots of the densities and reaction rates plotted as a function of z . The plot can be generated at any particular radius, but the obvious choice is to generate the plot at the radius of the neutral gas injection. This will give one a spatial trace of the interaction parameters that govern the dynamics of the system. The particular radius used is displayed above the second subplot.

The top plot in Figure 3.5 is a graph of the ion and neutral density, and their product. The neutral scale is on the left and the neutral trace is represented by a dashed line. The ion scale is on the right hand side and the ion trace is represented by a dotted line. The product ($n_n n_i$) is plotted as a thick solid line; its scale is not displayed. If the radius of the graph is the jet radius ($r = r_{jet}$), the neutral density information will be visible even from $t = 0$, unless the neutral gas has not been prestreamed (see description of prestreaming on pg. 53). The plasma density will be zero on this graph until the plasma passes through the plane defined by this radius (actually the cylinder of this radius). When the plasma does first appear on this graph, it will be some distance down in z . This distance is governed by how fast the magnetic field expands.

The second and third plots are the reaction rates for the interactions involved in the simulation. The reactions considered will be ionization and charge-exchange, but they do not necessarily have to be turned on for each simulation. The definition of the reaction rate for some process p between type-1 particles and type-2 particles is

$$R_{12}^{(p)} = n_1 n_2 \langle \sigma v \rangle_{(p)}. \quad (3.4)$$

In our case the species are usually the plasma density ($n_i \sim n_e$) and the neutral gas density (n_n). The process will be one of ionization, charge-exchange or recombination.

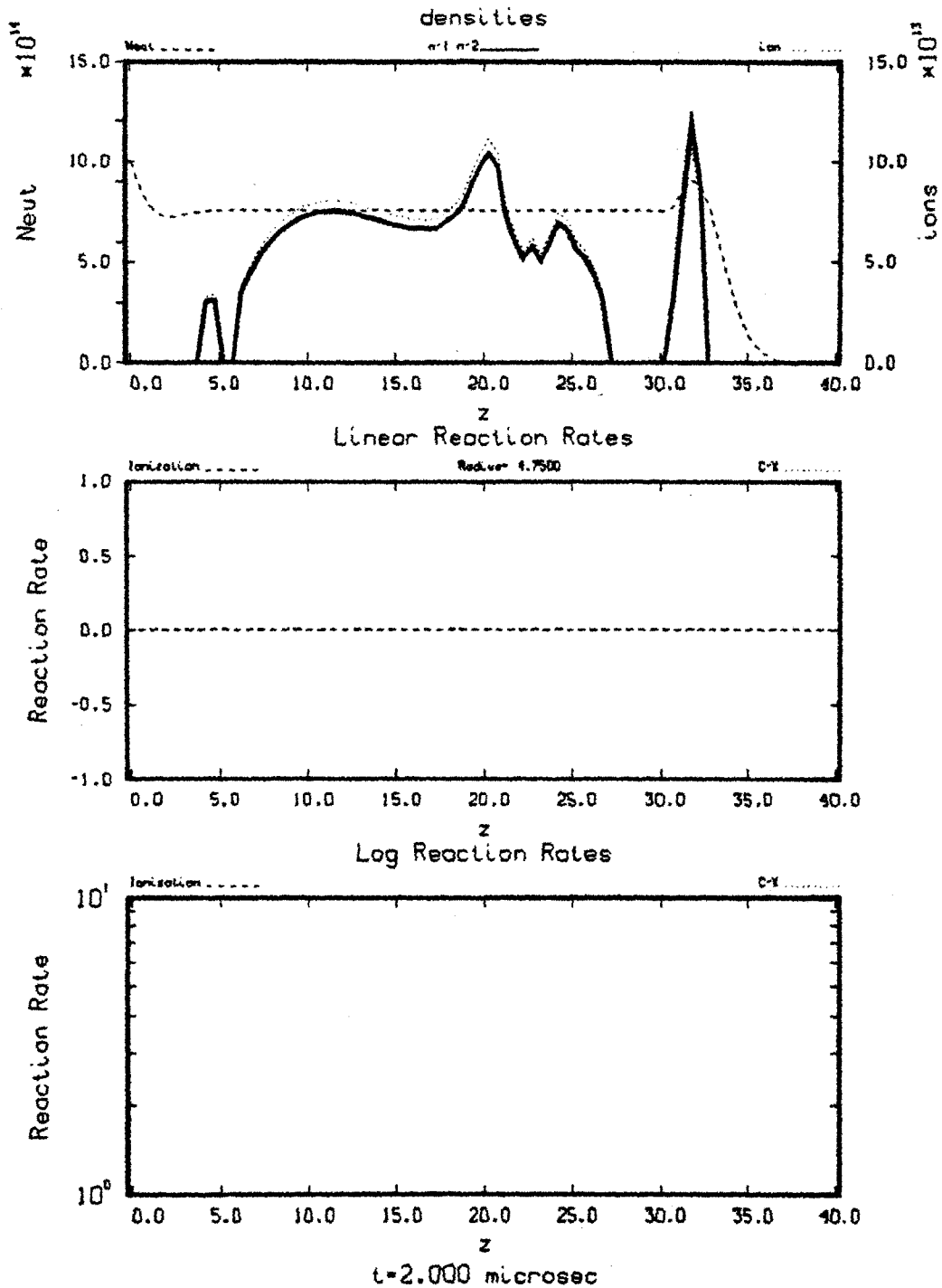


Figure 3.5: Reaction rate plots at two microseconds for reference case. See text for description of individual subplots.

The only difference between the second and third plot is that the second plot uses a linear scale while the third plot uses a log scale. The ionization reaction usually dominates and its reaction rate can be several orders of magnitude higher than that for ionization.

It is the information in the reaction rate plots that one is really after. The source terms in the fluid equations are proportional to these reaction rates. Thus, the reaction rates govern the dynamics of the interactions. By comparing the density profiles, especially the product $n_1 n_2$, and the form of the (linear) reaction rate, one can infer whether it is the change in density that is causing the change in the reaction rate or whether the cross-section itself is changing. If the reaction rate trace is similar to the product of the densities, then one knows that the cross-section for this reaction is relatively constant in this region. Then by comparing the relative density contributions to $n_1 n_2$, one can deduce the cause of the reaction rate change (e.g., is the reaction rate dropping because all the neutral gas is already ionized ($n_n \rightarrow 0$) or because ionization has lowered the plasma temperature and the cross-section is dropping ($\sigma \rightarrow 0$)). With a little practice, a lot of information can be extracted from these plots.

In these particular plots, one can see that the neutral gas jet has expanded slightly at the front (it was a sharp drop off at $t = 0$). The reaction rate plots are all zero, since there are no reactions turned on and because no plasma has reached this radius yet.

Figure 3.6 will be the figure used to determine if neutral gas is affecting the plasma flow. This figure has three subplots. The first is the *Momentum Ratio* and the second *Coupling Coefficient*. Both these plots are really just an extension of the previous reaction rate information, just in different forms.

The momentum ratio plot is provided to indicate the total amount of momentum that is coupled to the ion species for all the reactions being considered. Specifically, it looks at only z -directed momentum. It is a ratio that compares the amount of momentum in a computational cell at times t , and $t + dt$. For clarity I label time level t as *old* and time level $t + dt$ as *new*. The *rate* at which momentum is added to the computational cell at (i, j) is governed by

$$S_m(i, j) = R_m^{(T)} \Delta V(i, j) \quad (3.5)$$

S_m is the source term that appeared on the *r.h.s.* of the momentum conservation

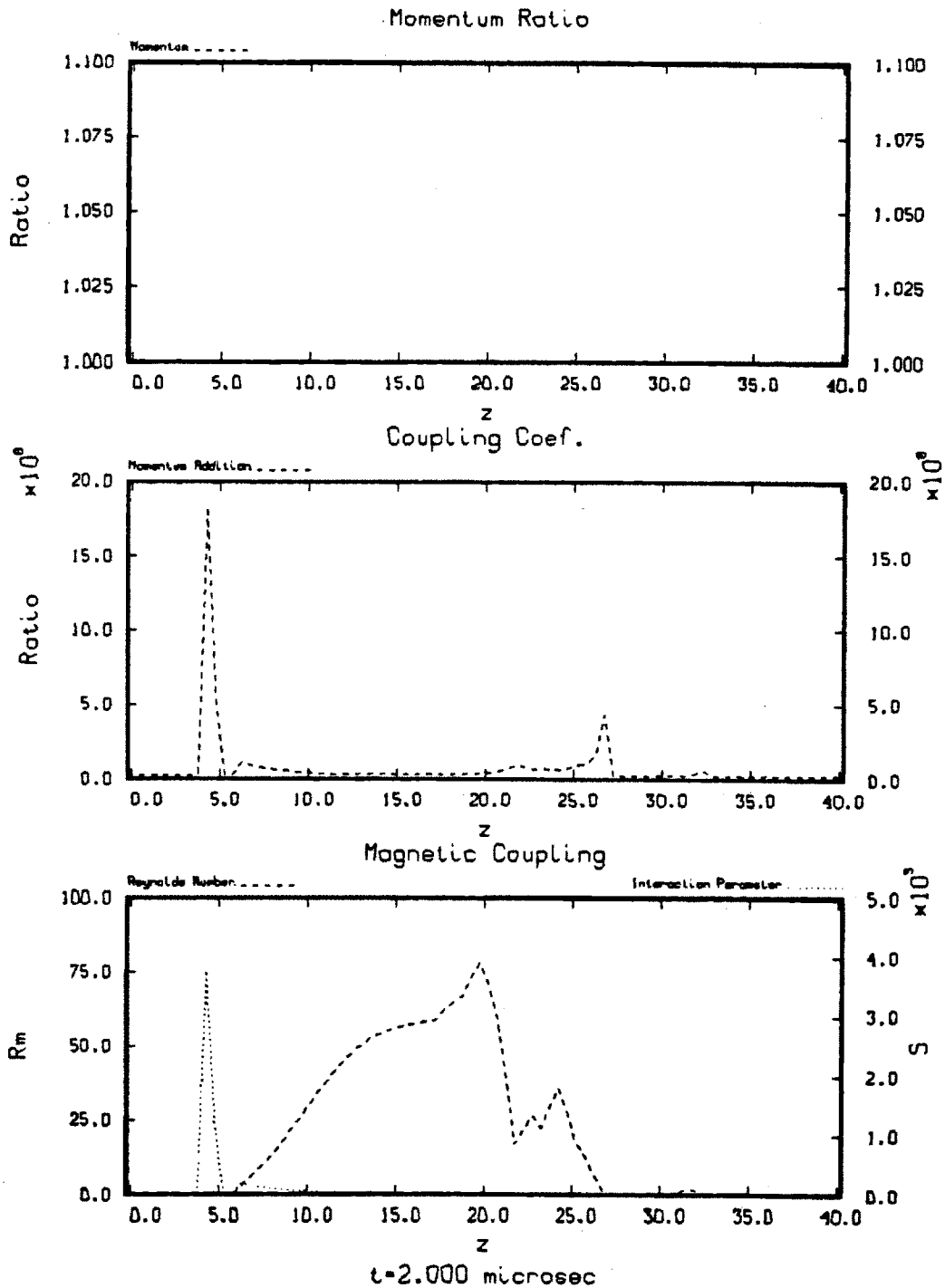


Figure 3.6: Momentum ratio and Coupling coefficient at two microseconds for reference case.

equation. The superscript (T) on the reaction rate is an indication that one wants the total source of momentum from all reactions. ΔV is the amount of momentum being brought in. Equation 3.5 formally is not correct. The term represented by ΔV is in general different for each process represented by the term $R^{(T)}$. This term can represent the reaction rates for ionization and charge-exchange. For ionization, ΔV is just v_n . For charge-exchange, $\Delta V = (v_n - v_i)$ because charge-exchange is adding particles at velocity v_n and removing particles at velocity v_i . The simple form of Equation 3.5 is used to describe the concept of the diagnostic that is being used. The subtleties just distract from the point that is being made.

Equation 3.5 is the rate of momentum addition into the cell at (i, j) . To determine the total momentum added between t and $t + dt$, one must multiply Equation 3.5 by dt . The *new* momentum is

$$nV_{new} = nV_{old} + R_{in}^{(T)} \Delta V dt. \quad (3.6)$$

Dividing by the *old* momentum one gets an equation for the momentum ratio,

$$\mathcal{R}_p = 1 + \frac{R_{in}^{(T)} \Delta V dt}{nV_{old}}. \quad (3.7)$$

The Coupling Coefficient is the ratio of the characteristic time of the flow through the cell, τ_{flow} , and the characteristic time for momentum addition, τ_{add} . τ_{add} is the inverse of the total frequency of momentum adding events. In other words

$$\tau_{add} = \frac{1}{\nu^{(T)}}, \quad (3.8)$$

where

$$\nu^{(T)} = \nu^{(ion)} + \nu^{(cx)}. \quad (3.9)$$

The quantities $\nu^{(ion)}$ and $\nu^{(cx)}$ are just the frequency of ionization events and charge-exchange events, respectively. Each frequency is defined as

$$\nu_{in}^{(p)} = \frac{R_{in}^{(p)}}{n_i} = n_n \langle \sigma v \rangle_p. \quad (3.10)$$

The characteristic time for the flow through the cell, τ_{flow} , can be approximated as

$$\tau_{flow} = \text{amin1} \left(\frac{dr}{v_{ir}}, \frac{dz}{v_{iz}} \right). \quad (3.11)$$

The coupling ratio is defined as τ_{flow}/τ_{add} . This implies that the faster the plasma is flowing through the cell, (small τ_{flow}) one would need a correspondingly small τ_{add} to affect the flow in that cell. In cells where there is little or no interaction between the plasma and neutral gas, $\tau_{add} \rightarrow \infty$, and the coupling ratio goes to zero; there is little time for the neutral gas to affect the plasma flow. For the plasma rocket to work one needs to have *large* coupling coefficients.

Having a large coupling coefficient is a necessary condition for the plasma rocket concept to work. If the plasma flows out of the cell where the neutral gas is interacting with it on a time scale faster than the neutral gas can act on the plasma, one wouldn't expect too much to happen. Having a high coupling coefficient is a necessary but not sufficient condition for the successful operation of the plasma rocket. This can be seen in the following scenario. Assume that the coupling coefficient is large, implying that the neutral gas jet is acting on the plasma on a time scale short compared to the plasma transient time. Also, assume that the velocity of the neutral gas is zero (or sufficiently small compared to the plasma velocity). Though the coupling coefficient is large, what is being *coupled* is infinitely small, so the neutral gas will have no effect on the plasma. It may modify the resistivity profile, but that alone is not enough to make the plasma thruster work. The mechanism for the plasma to leave the field lines through resistivity (via the diffusion of the field lines through the plasma) happens on too long of time scale to be useful for a high specific impulse plasma thruster.

The final subplot on this graph show the magnetic Reynolds number and the magnetic interaction parameter. Both these parameters help judge the effect of the magnetic field strength on the plasma flow.

The magnetic Reynolds number is defined as

$$R_m \equiv \frac{uL}{(\mu_0\sigma)^{-1}} = uL\sigma\mu_0. \quad (3.12)$$

Here L is the characteristic length of macroscopic change that one is interested in, and u and σ are the characteristic velocity and conductivity of the fluid. The magnetic

Reynolds number gains its name from the classical fluid mechanics counterpart. The Reynolds number characterizes the effects of convection to diffusion in a flow. In the magnetic case, it is the diffusion of the magnetic lines of force through the plasma that is being considered. For $R_m \gg 1$ transport of the lines of force with the fluid dominates over diffusion. In other words, there is *frozen flow*. Frozen flow implies that the lines of force and the fluid move as one. This does not mean that the fluid follows the original field configuration, just that the fluid must bend or stretch the magnetic field, and therefore do work against the field, in order to distort it. If $R_m < 1$, the resistive time scale is large enough that the fluid can diffuse across the lines of force on the time scale of interest. Resistivity (η) is the inverse of conductivity (σ) and conductivity goes like temperature to the three-halves power. For diffusion effects to dominate one must have a cold fluid. If the fluid should leave the field lines only through diffusion, the fluid would have to be very cold. For the plasma rocket this effect has to remain highly localized in order to still preserve the bulk energy and momentum of the flow.

The other quantity plotted here is the magnetic interaction parameter, S . The magnetic interaction parameter is defined as

$$S \equiv \frac{L\sigma B^2}{\rho u}. \quad (3.13)$$

It is the ratio of the $J \times B$ force to the inertia force. It is an indication of the effect of B on the flow. If $S \gg 1$, the effect of the magnetic field on the flow would be very large compared to the plasmas' inertia force, and one would expect the flow primarily to follow the magnetic field.

The first two graphs in Figure 3.6 for the reference case are both zero. This is because with the reference case, all reactions are turned off. The magnetic Reynolds number and interaction parameter are defined independent of the reactions, so the final plot can be non-zero even in the reference case. At this time step, the flow has not expanded to this radius, so in the final plot both quantities are also zero.

The final graph to be displayed for the plasma at this time step is Figure 3.7, the plasma temperature. The plot has the same general characteristics as the contour plot for density (Fig. 3.3).

The temperature plot is important in determining the amount of energy lost due to the interactions with the neutral gas. The neutral gas can lower the plasma tempera-

Ion Temperature

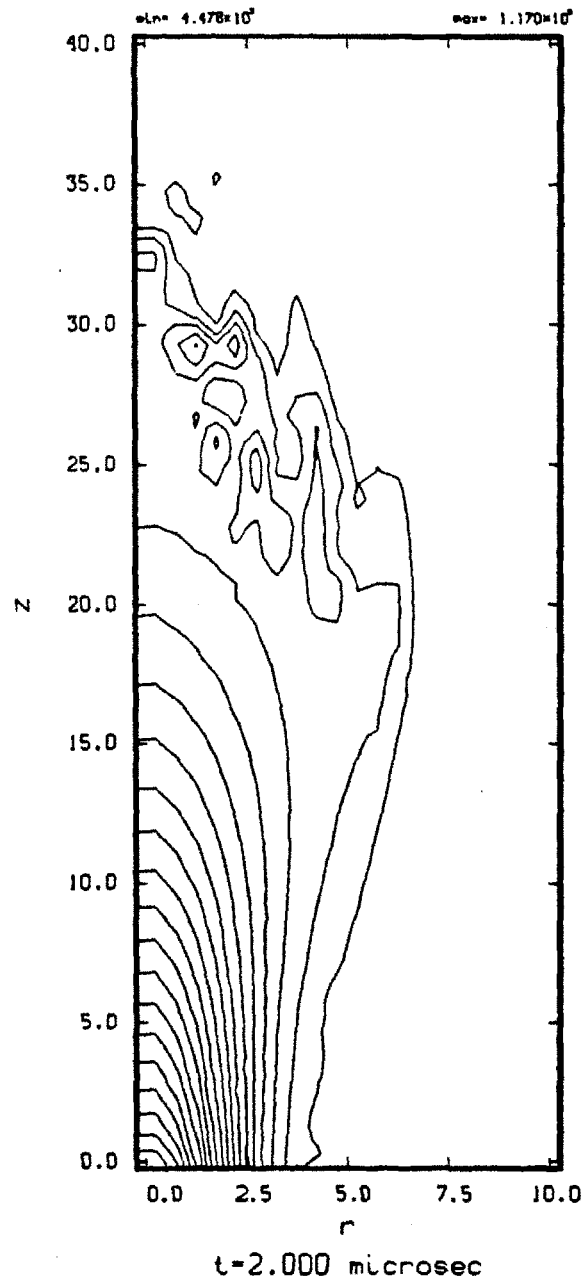


Figure 3.7: Ion temperature at two microseconds for reference case.

ture in two different ways. The first is through the ionization of the neutral gas. Some energy will be lost in the actual ionization event. This energy is lost from the electron fluid, but the electron and ion temperatures equilibrate. The main mechanism for ionization to lower the plasma temperature is through the thermalization of the neutral fluid (that has just become part of the plasma fluid). Unlike the electron/ion equilibration that takes place on some finite time-scale, the neutral thermalization happens instantaneously. This is a consequence of the fluid approximation. Whatever came into a computational cell during a given time step, at the beginning of the next time step all quantities are assumed to be uniform throughout the cell. An improvement to this situation (even within the fluid description) is to have many species of ions, all at different temperature ranges. The different species would tend to equilibrate among themselves in some specified characteristic time. This greatly adds to the complexity of the code and was not done.

The next three figures, Figure 3.8-Figure 3.10, are the neutral density, velocity, and temperature plots. They complete the description of the system at two microseconds.

One point to notice is that the neutral density was started prestreamed into the duct. Both the neutral density and temperature are constant across the jet. The density and temperature contour plots look very wide when in reality the jet is only one grid wide ($dr = .5cm$). This is because the contour algorithm is trying to plot many field lines in a very narrow area. To get the proper idea of the width of the neutral jet look at the neutral velocity plot. From the neutral velocity plot (Figure 3.9 one can see that the neutral gas is slowly starting to expand due thermal pressure. From the size and direction of the velocity vectors it shows that the bulk motion is along z .

This concludes the information for the reference case at two microseconds. Additional information is provided at one microsecond intervals. The next figures to be presented will be at three microseconds. From these figures one can conclude that the plasma does expand and follow the field lines. One point that needs to be made here is that the plasma in this reference case (and in several cases that are to follow) runs into the wall at r_{max} . Because of the previous discussion of wall boundary conditions (see discussion on the temperature boundary condition on pg. 52), a numerical instability develops that disrupts the code. One will see in the figures that the plasma properties are building up along the wall. This case terminated in about another half microsecond. This is acceptable because by this time level the answer that one was after has been

Neutral Density

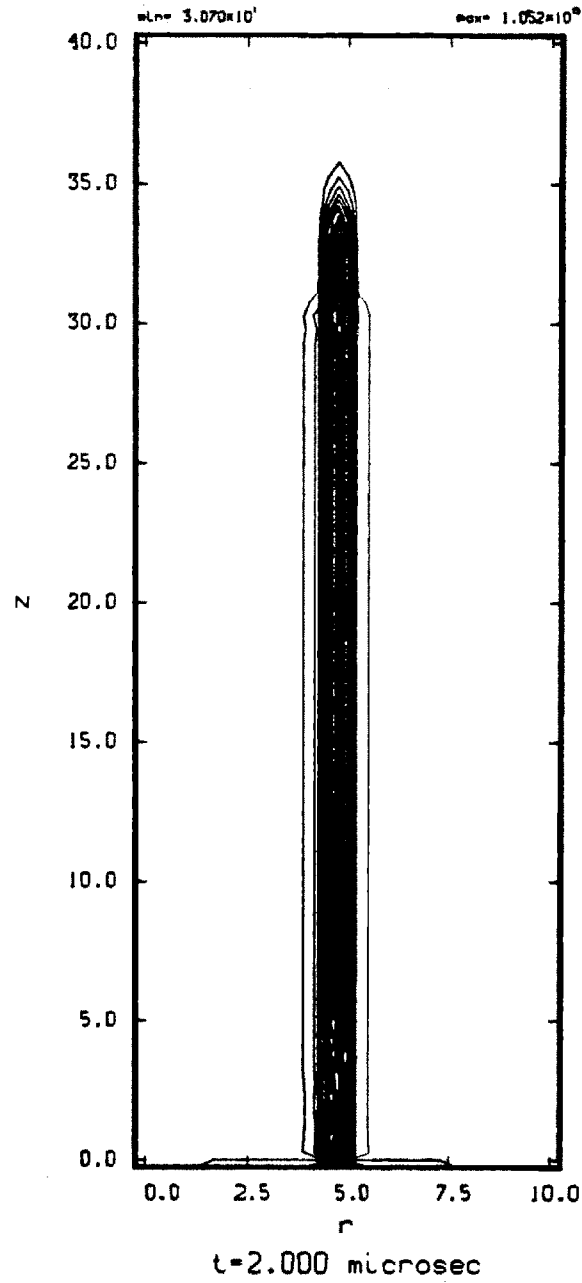


Figure 3.8: Neutral density at two microseconds for reference case.

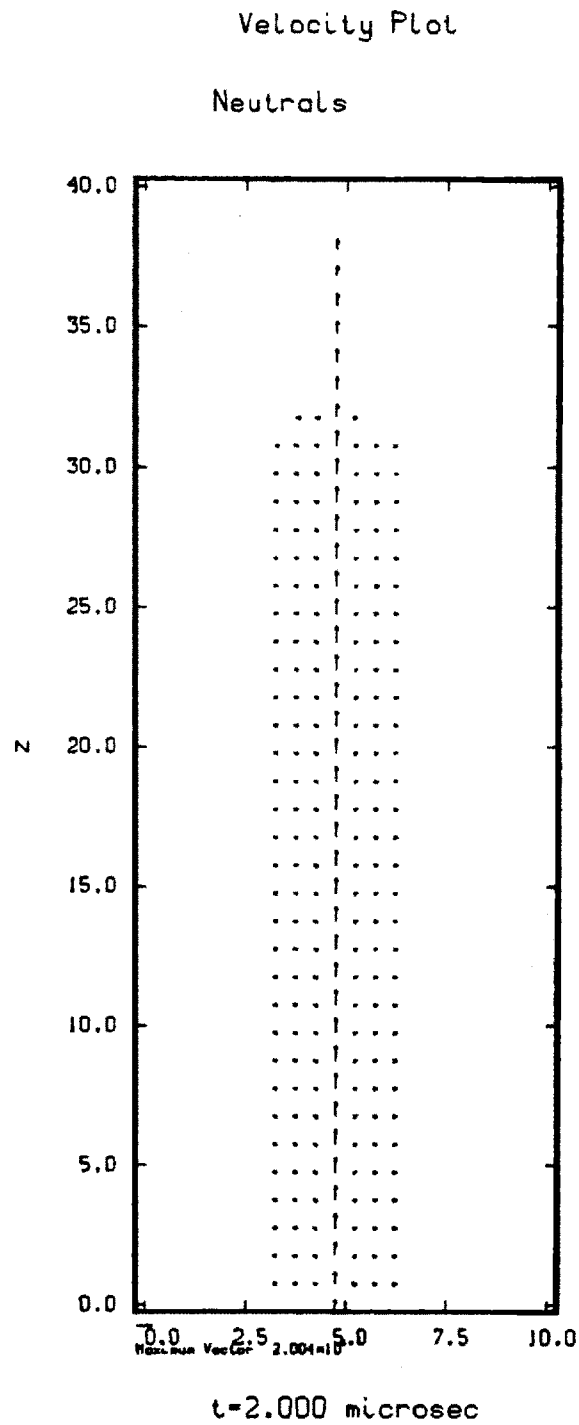


Figure 3.9: Neutral Velocity plot at two microseconds for reference case.

Neut Temperature

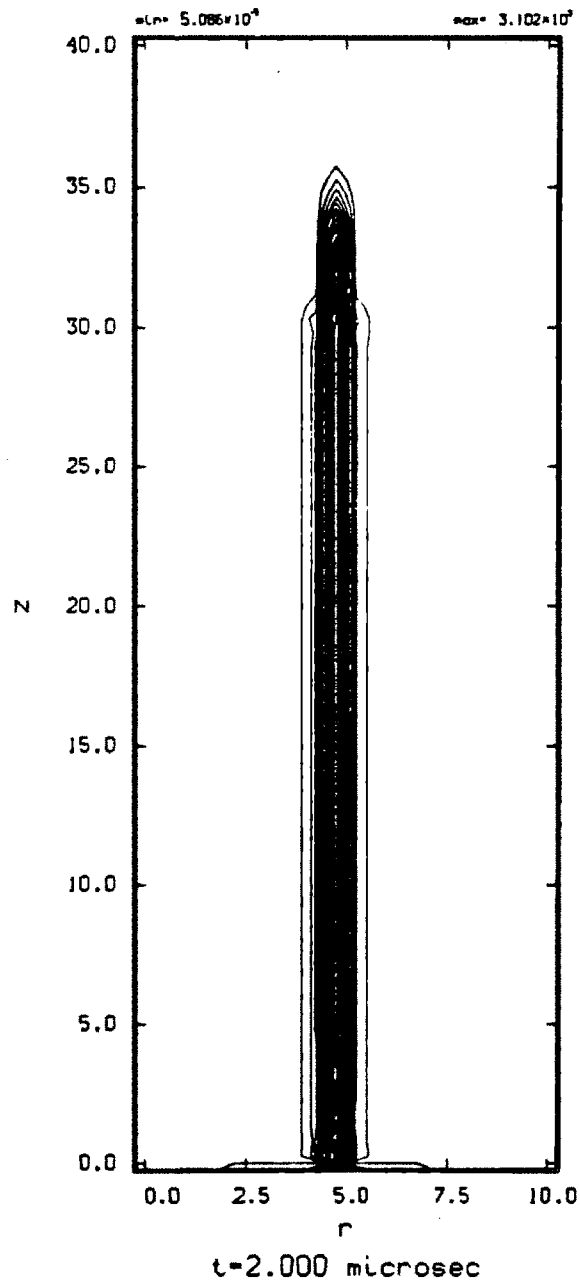


Figure 3.10: Neutral temperature at two microseconds for reference case.

achieved. To study simulations to a longer time, the radial boundary of the computational domain would have to moved further out in radius, or better boundary conditions at r_{max} would have to be implemented.

The plasma density is shown in Figure 3.11. One can see the plasma starting to build up at r_{max} starting at $z \sim 25cm$.

The next figure, figure 3.12, has the reaction rate information graphs. One can now see the plasma density profile on the top graph. The product $n_i n_n$ closely follows the ion density because the neutral gas is fairly constant in this region. The narrow spikes that form near $z = 30cm$ are a consequence the previously mentioned non-physical buildup of plasma against the wall.

The reference case plasma velocity plot, Figure 3.13, definitely shows the plasma expanding along the field lines. This situation would be very poor for a plasma thruster configuration.

The final plasma plot is the plasma temperature and it, too, has freely expanded along the field lines and has run into the wall.

3.3.2 Equal plasma and neutral gas densities.

The first case to be considered will be for the injection of the neutral gas jet at a density equal to the plasma density, $n_n = n_i$. Choosing the neutral gas density equal to the plasma density was chosen as a starting point in the analysis of the hybrid plume concept because one wants to keep the injected \dot{m} as small as possible. If the amount of thrust injected via the neutral gas to obtain the formation of the hybrid plume by this injection method is on the same order as the potential thrust from the plasma component, the hybrid plume concept via this injection method would be unattractive. In this particular case the neutral gas will be injected at a radius of $5cm$ at Mach seven. The input parameters for this case are given in Table 3.2. The input parameters are the same as for the reference case, the table is presented for completeness.

At one microsecond the plasma has not expanded enough to interact with the plasma jet. This time step will not be shown.

By two microseconds the interactions have begun. Figure 3.15 shows the plasma density at two microseconds compared to the reference case. The reference case is on the left. The right plot shows that the plasma density is peaking downstream of the neutral injection. This increase in density has two causes. The first reason is that there

Ion Density

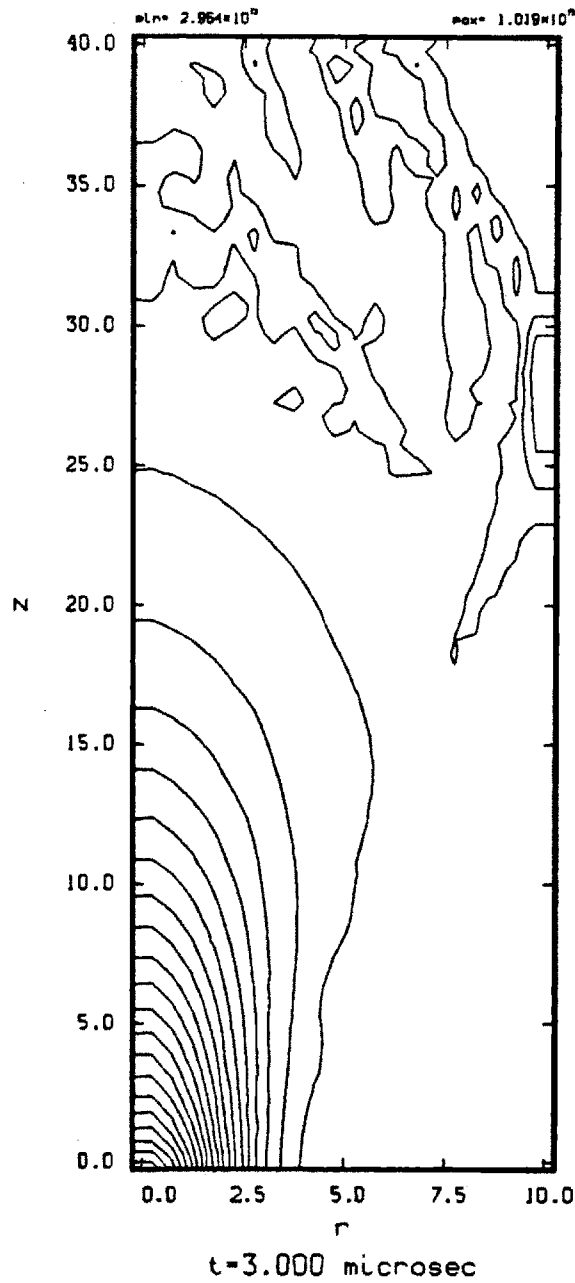


Figure 3.11: Plasma density at three microseconds for reference case. Note interaction of plasma with wall.

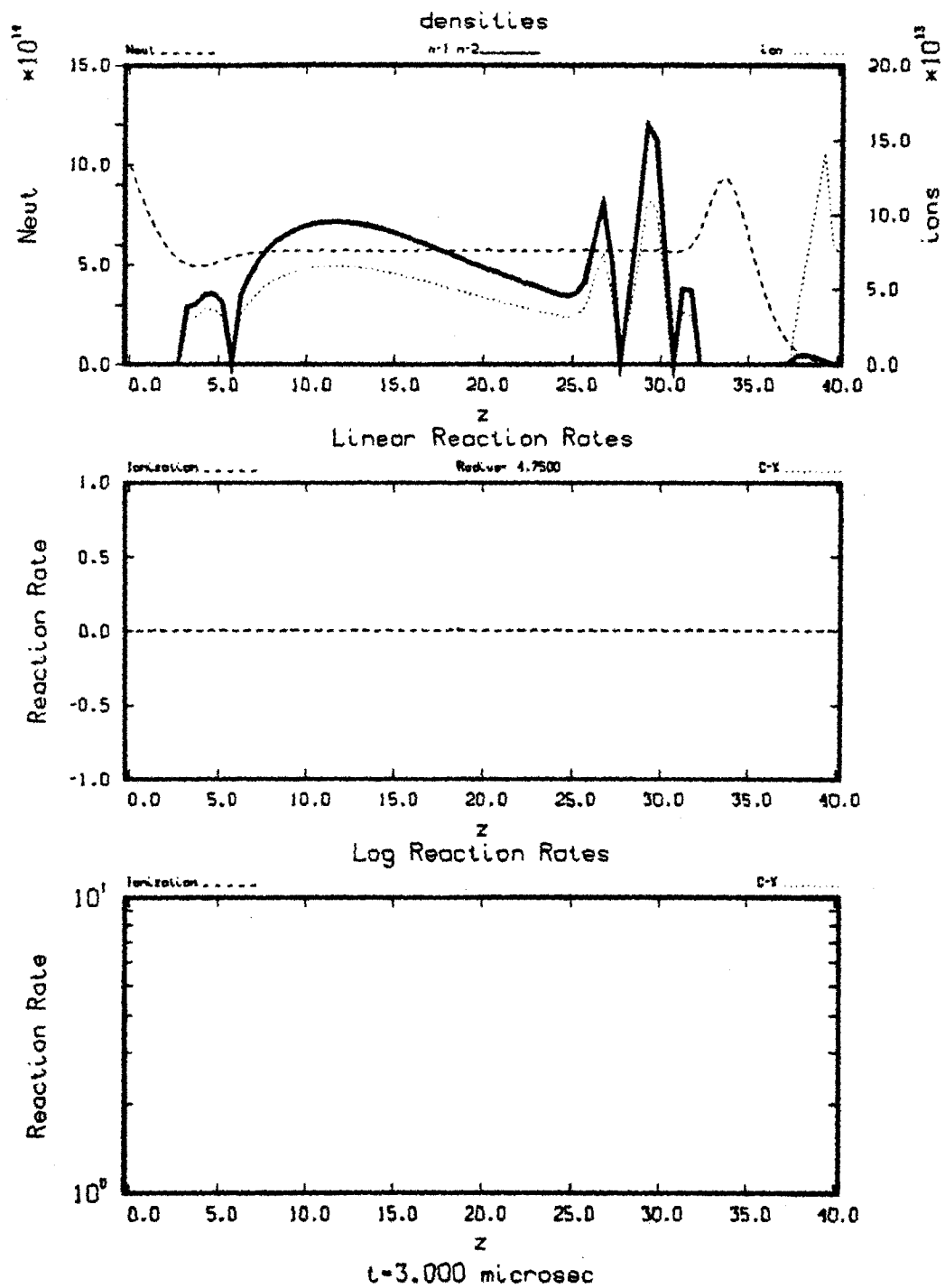


Figure 3.12: Reaction rate plots at three microseconds for reference case.

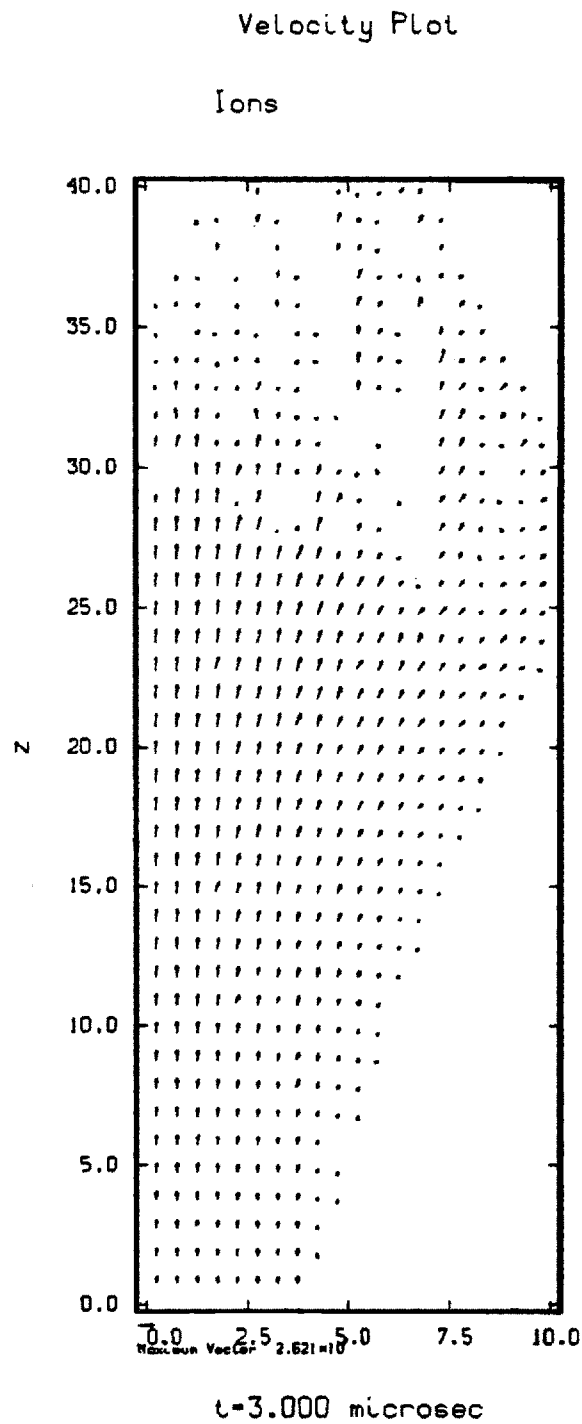


Figure 3.13: Plasma Velocity plot at three microseconds for reference case.

Ion Temperature

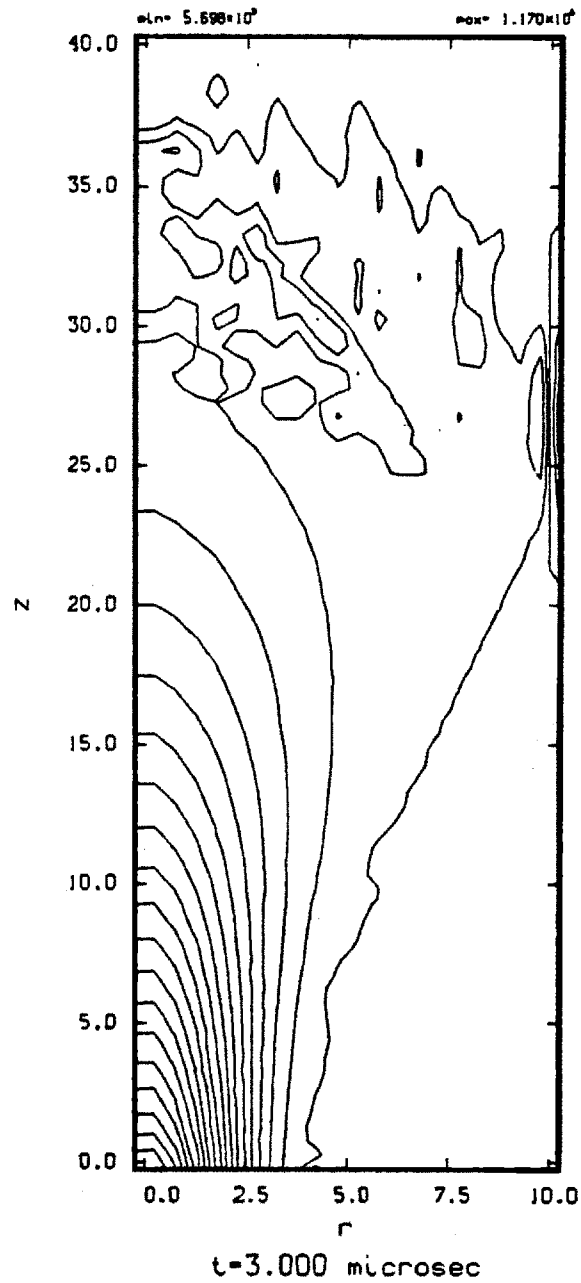


Figure 3.14: Plasma Temperature at three microseconds for reference case.

Item	Ions	Neutrals
mass flow rate (\dot{m}), kg/sec	$2.87e - 04$	$3.86e - 05$
Thrust, Newtons	32.47	0.6
Power, MWatts	1.83	0.005
Temperature, eV	100.0	0.025
Density, part/cm ³	$1.0e+15$	$1.0e+15$
Velocity, cm/sec	$1.13e+07$	$1.5e+06$
I_{sp} , sec	11,500	1,600
I_{sp} net, sec	10,350	

Table 3.2: Input parameters for case with equal plasma and neutral gas density.

is actually a source of plasma density from the ionization reaction. The second reason, which is not as obvious, is that the plasma is being cooled by the charge exchange reaction. The charge exchange reaction is not a source of particles, it simply replaces a plasma particle with what was a neutral particle. Since in general the neutral fluid is at a lower temperature than the plasma fluid, the plasma fluid temperature will be lowered. This cooling tends to increase the density. It can be demonstrated that this cooling takes place by shutting off the ionization reaction. There is then *no* source of plasma, but the plasma density still peaks downstream of the neutral jet.

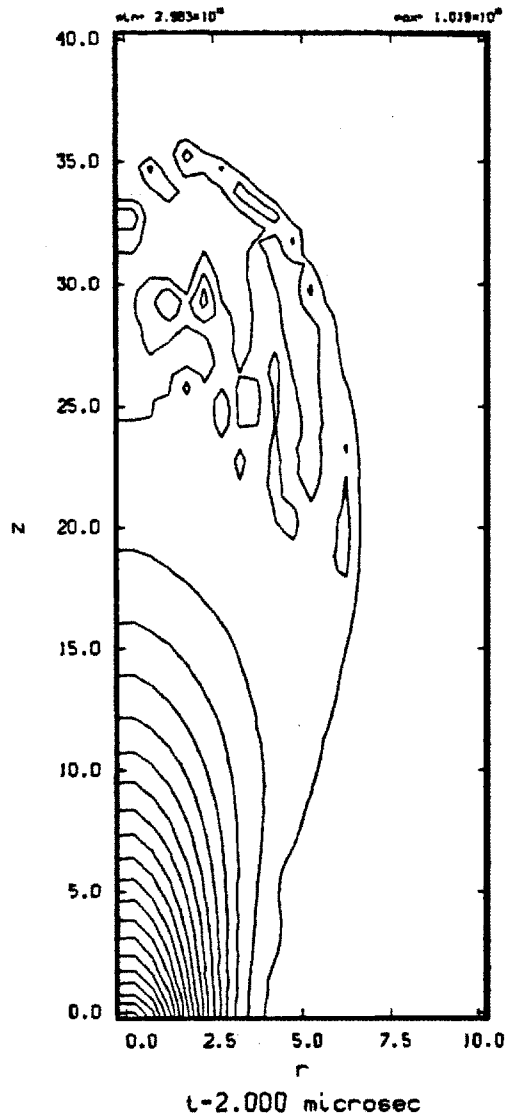
Figure 3.16 compares the ion temperature at two microseconds to the reference case. As can be seen, the plasma temperature is reduced downstream of the neutral jet. The temperature reduction also has two causes. One cause was mentioned above when describing the plasma density increase. Namely, that the charge exchange reaction is bringing in cold neutral gas (that is now an ion) and the remaining ion particles have to equilibrate with these particles. The second cause is that the ionization reaction is also bringing in cold neutrals, and the bulk ions must equilibrate with these new particles. Though both the ionization process and the charge-exchange process both have the same net effect, that of lowering the local ion temperature, the physics behind the two reactions is significantly different.

The ionization reaction is a source of internal energy. That is

$$\left(\frac{3}{2}nT\right)_{new} = \left(\frac{3}{2}nT\right)_{old} + \left(\frac{3}{2}nT\right)_{ionization} \quad (3.14)$$

Both terms on the right hand side are positive and the internal energy increases

Ion Density



Ion Density

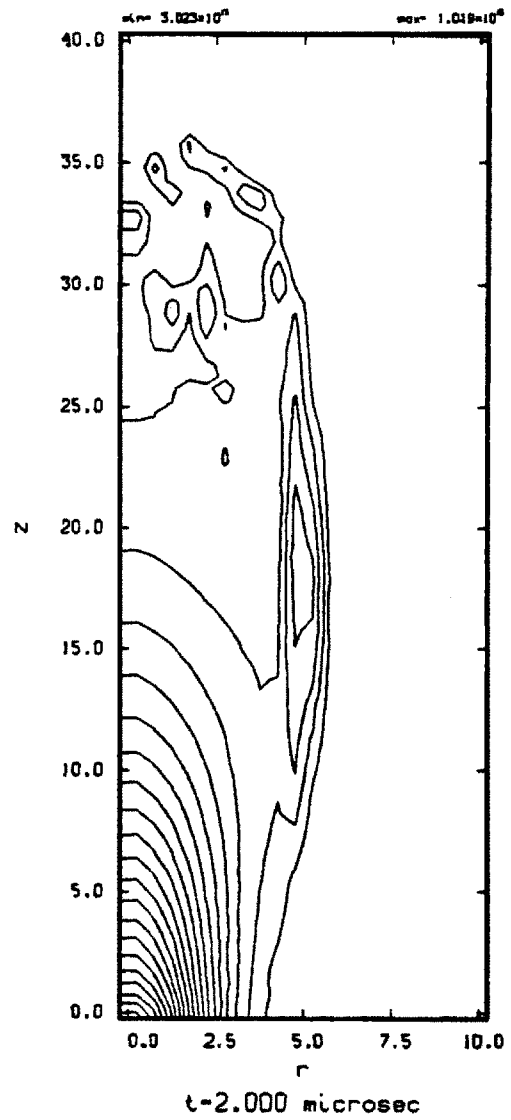
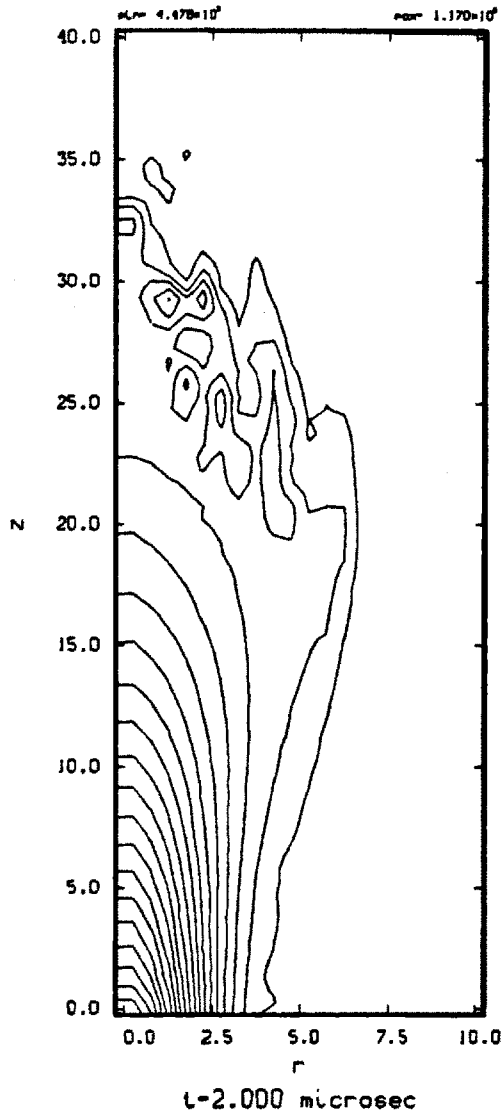


Figure 3.15: Comparison of plasma density at two microseconds for reference case and even injection case.

Ion Temperature



Ion Temperature

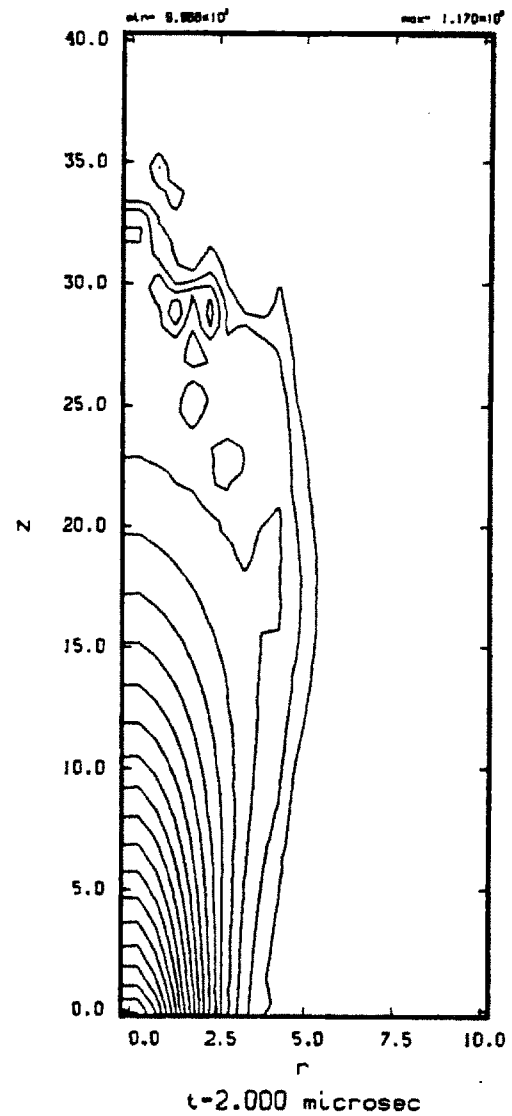


Figure 3.16: Comparison of plasma temperature at two microseconds for reference case and even injection case.

(these are actually energy *densities* and are needed to be integrated over some volume to obtain the actual energy). The local temperature can decrease because the temperature is defined as

$$T = \frac{I.E._{new}}{n_{new}}, \quad (3.15)$$

where *I.E.* is internal energy. If the increase in the density is not proportional to the increase in internal energy, the temperature will change. Whether the temperature increases or decrease depends on whether the density change is greater or less than the internal energy change. If you bring in particles colder than the background particles, the temperature will decrease. If you bring in particles hotter than the background particles, the temperature will increase. In both cases the total internal energy will *increase*. It has to increase because one has brought in a finite positive source of internal energy. For the neutral fluid, both nT and n decrease proportionally, so their temperature remains unchanged. This is all intuitively obvious; it is mentioned just to emphasize that the temperature can decrease even with a net increase in internal energy, and more importantly to highlight the difference between internal energy and temperature. Depending on how one has the differential equations cast (the differential equations can be in terms of either energy *or* temperature), the source terms will be different.

The charge-exchange reaction is fundamentally different. Because the fast charge-exchange neutrals created by the charge-exchange event are assumed lost, charge-exchange is a sink of neutrals, as is the ionization reaction. The charge-exchange reaction can also lead to a cooling of the plasma, but for a different reason. Whereas the ionization reaction cools the plasma because it brings in cold neutral gas, the charge-exchange reaction is actually a sink of internal energy (remember that the ionization reaction is a source of internal energy). If the neutral that is brought in by the charge-exchange event is at the same temperature as the background plasma, the plasma temperature will remain constant. If the neutral is at a lower temperature, the plasma temperature will drop. More importantly, the plasma energy will have decreased. This is to be compared with the ionization reaction. With the ionization reaction the total internal energy of the plasma increased, only the temperature decreased. With the charge-exchange reaction, the plasma internal energy decreases. If

the fast charge-exchange neutrals are lost, as is assumed in these runs, this is a net loss of energy from the system. This is an important point to consider when designing a rocket. One doesn't want a significant fraction of the energy of the system to be lost unnecessarily. In particular, one does not want to deposit this energy on the walls of the nozzle.

In reality, the fast neutrals will tend to thermalize with the bulk neutrals of the neutral jet, and the energy would not be lost. If one considers the mean-free-path of a warm neutral (say 10eV) and the typical scale length of 10cm for the rocket radius, it can be seen that assuming that fast neutrals leave is a good assumption (remember that it would take *several* collisions to thermalize with the background gas). The energy lost attributed to the fast charge-exchange neutrals must be considered in a bit more detail. Any charge-exchange neutral hitting the wall will obviously be a loss to the system, and possibly pose a material constraint on the system if the heat flux is too great. However, not all the charge-exchange neutrals will interact with the wall. In fact, the fraction of momentum in the z direction that these particles have when they leave the system can be considered 100% thrust. That is, the particle is detached from the field line and no longer acts back on the ship. If one could somehow collimate the fast-charge exchange neutrals in the z direction and charge-exchange *all* the plasma, one would have a 100% efficient plasma rocket. Unfortunately, that is not the case. It is not as bad as losing all the momentum to the walls, either. If the particles were simply flowing along the magnetic field when the plasma particle was instantaneously neutralized by the charge exchange event, it would continue to flow in the direction that it was traveling before the collision, i.e., along the magnetic field. One could calculate the solid angle that the field makes with respect to the nozzle at the point of separation, and if it intersects with the nozzle, the particle should be assumed lost. If this trajectory does not intersect the nozzle, the z directed momentum should be accounted as pure thrust. The radial component would cancel by symmetry and would be lost. This is far better than counting all the momentum as lost. However, the particles are not flowing simply along the magnetic field. The particles are in a gyro-orbit about the magnetic field line that they are following. The particles have a microscopic v_θ that needs to be accounted for. The principle in calculating the solid angle to intercept the nozzle is the same, it just yields a slightly less optimistic thrust contribution from the charge-exchange particles.

The next plots to consider are the reaction rate plots and the momentum coupling plots. These figures (Figures 3.17 and Figure 3.18) will indicate whether the neutral gas is having a significant enough effect on the plasma to detach the plasma from the field lines.

In Figure 3.17 are the reaction rate plots. In the top plot one can see the plasma profile as it looks as it crosses the plane (or cylinder) at $r = r_{jet}$. It can be seen that the plasma is eroding the neutral gas (both ionization and charge-exchange are a sink of neutral particles). It is important to remember that the scales for the ion density and neutral density are different in the top plot. The neutral scale is on the left and the plasma scale is on the right. For example, at approximately $z = 15cm$ the plasma density is about the same magnitude as the neutral density. The following two plots are the reaction rate plots. These plots show that the charge-exchange reaction dominates the overall interaction, usually by an order of magnitude.

The next figure, Figure 3.18 will tell us if the neutral gas is expected to have a significant effect on the plasma. From the top plot we can see that the change in momentum of the plasma at this radial location is very small. More importantly the second plot shows that the coupling coefficient is typically less than one. This implies that the plasma is streaming through the jet on a faster time scale than the ionization/charge-exchange process can add momentum to the plasma. The third plot shows the effect of the magnetic field. The magnetic Reynolds numbers are high, implying that the time scale for the diffusion of the field lines through the plasma is long. The magnetic interaction parameters are very much greater than one, indicating that the magnetic field will strongly affect the plasma flow. From this information, one wouldn't expect the jet to have a significant effect on the plasma flow, and it doesn't.

That the jet does not have a significant effect on the plasma at these early time steps suggests that via this injection method the jet will never have a significant effect. When the reactions first start out, the plasma density at the radial jet location there is also low, and thus the plasma axially directed momentum is low (mnV_z). The neutral axially directed momentum is high, as high as it is going to be. If the momentum ratio at this point is too low, as the plasma expands and the plasma density decreases, the momentum ratio would just be expected to get smaller. It is not clear from the coupling coefficient what to expect from the interactions at the early time steps. The coupling coefficient is the ratio of the time scales involved. The time scale for momentum

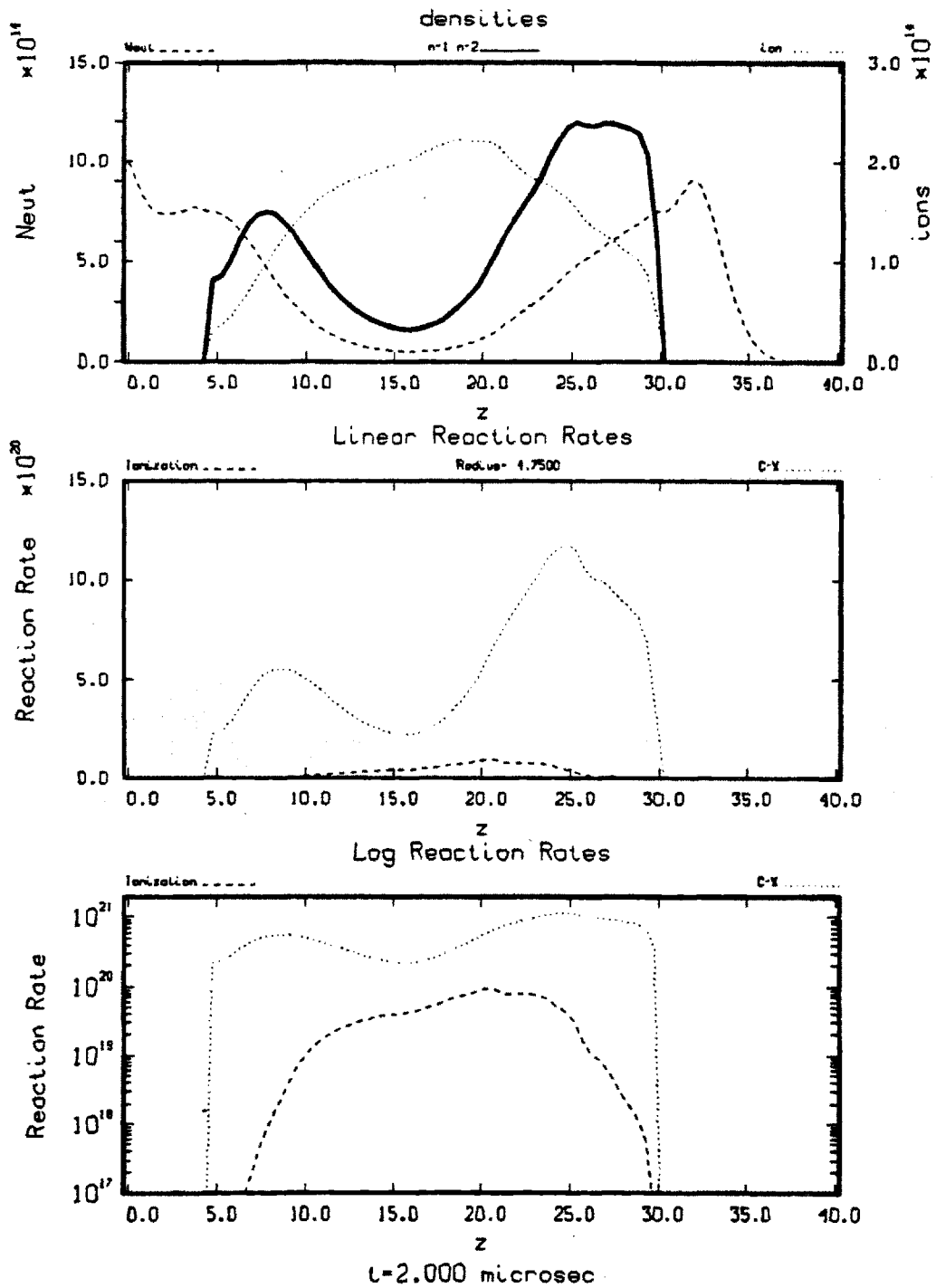


Figure 3.17: Reaction rates plots at two microseconds for even injection case.

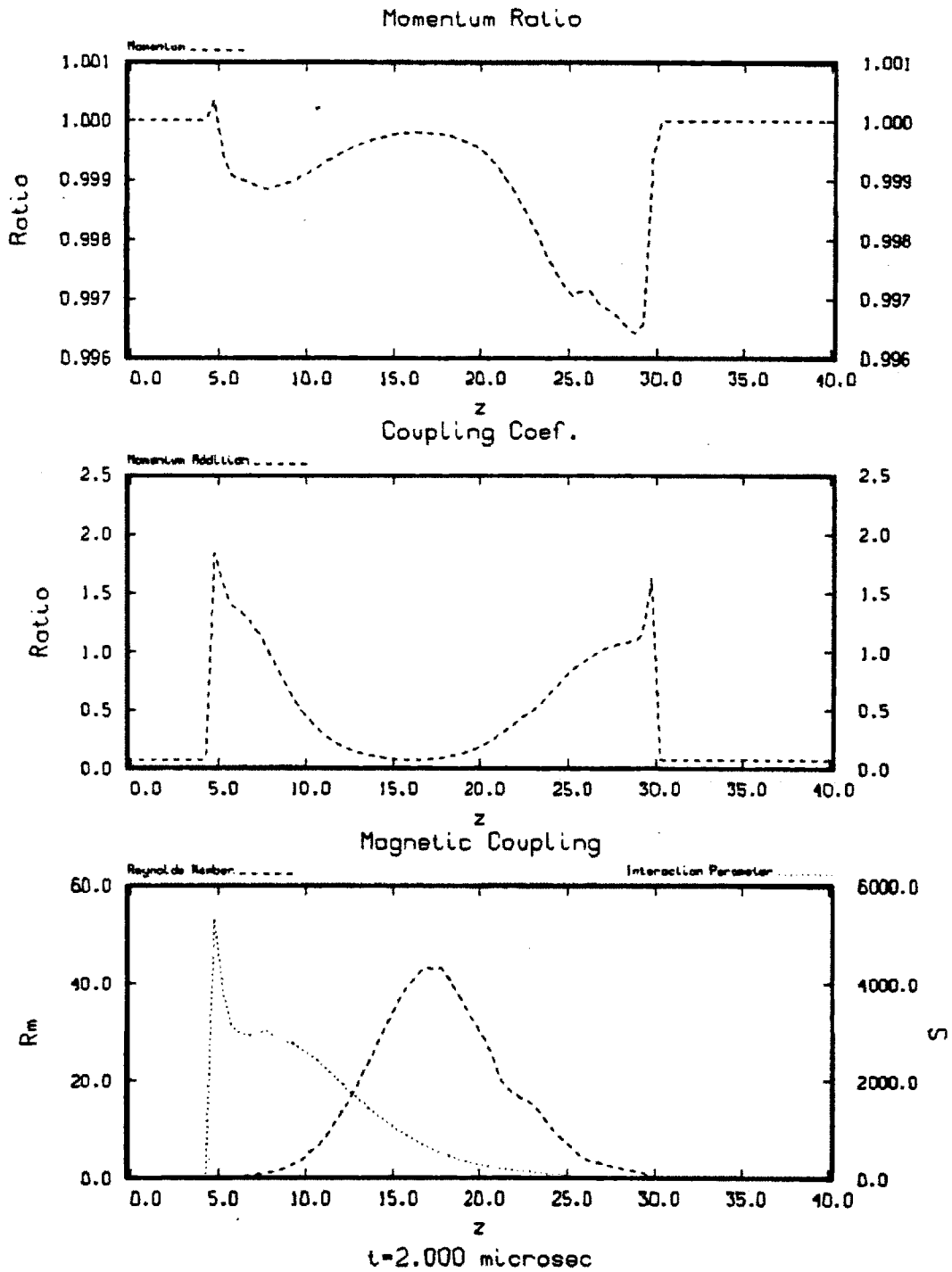


Figure 3.18: Coupling Coefficient at two microseconds for even injection case.

addition (or more precisely events that lead to a change in momentum of the plasma) goes inversely as the product of the densities ($n_i n_n$). One could hope that as the plasma density increased, the time scale for momentum addition would decrease enough such that the coupling ratio would become significantly greater than one. As will be seen, this does not happen.

Looking at the graph of the neutral density contour plots at two microseconds, Figure 3.19, the erosion of the neutral gas is seen more clearly. The gas at approximately $z = 15\text{cm}$ is being eaten away. The neutral gas near the front of the jet ($z \sim 35\text{cm}$) has yet to interact with the plasma and is still at a high density.

The neutral gas flow velocities are shown in Figure 3.20. It shows that the expansion of the jet is no longer symmetric about the injection point. Also, the plasma is turning the neutral flow. This is due to the plasma/neutral gas elastic collisions.

From the plasma density contour plot at three microseconds (Figure 3.21) one can see that the neutrals that were ionized downstream of the neutral gas jet at two microseconds have been convected both axially and radially with the bulk plasma flow. The net radial expansion has been slowed with the interaction with the neutral gas (the plasma has already hit the wall in the reference case). More importantly, one does not see a continuing increase in plasma density down stream of the neutral jet. This is an indication that the neutral jet cannot continue to support the reaction rates that occur in the jet/plasma interaction.

This is better seen in Figure 3.22, the reaction rate plot at three microseconds. Here it can be seen that the neutral density is falling off very rapidly when it starts to interact with the plasma (at $z \sim 5\text{cm}$). The neutral peak that was at $z = 32\text{cm}$ at two microseconds has convected downstream to $z = 35\text{cm}$. At two microseconds the neutral peak had not yet reacted significantly with the plasma flow, and therefore maintained its density at approximately the input jet density ($10.e + 14 \text{ part}/\text{cm}^3$). The neutral density now is significantly reduced ($\sim 2.e + 14 \text{ part}/\text{cm}^3$) because of these interactions. The plasma density trace peaks and gradually falls off as one would expect for the plasma expanding along the field lines. Then at $z = 35\text{cm}$ the plasma profile sharply peaks. This plasma peak is because the neutrals that were ionized downstream of the neutral jet have now been convected downstream (this can be seen in Figure 3.21). That the plasma peak corresponds to the neutral peak at this time step is just a coincidence.

The reaction rate plots show the dominance of the charge-exchange reaction. There

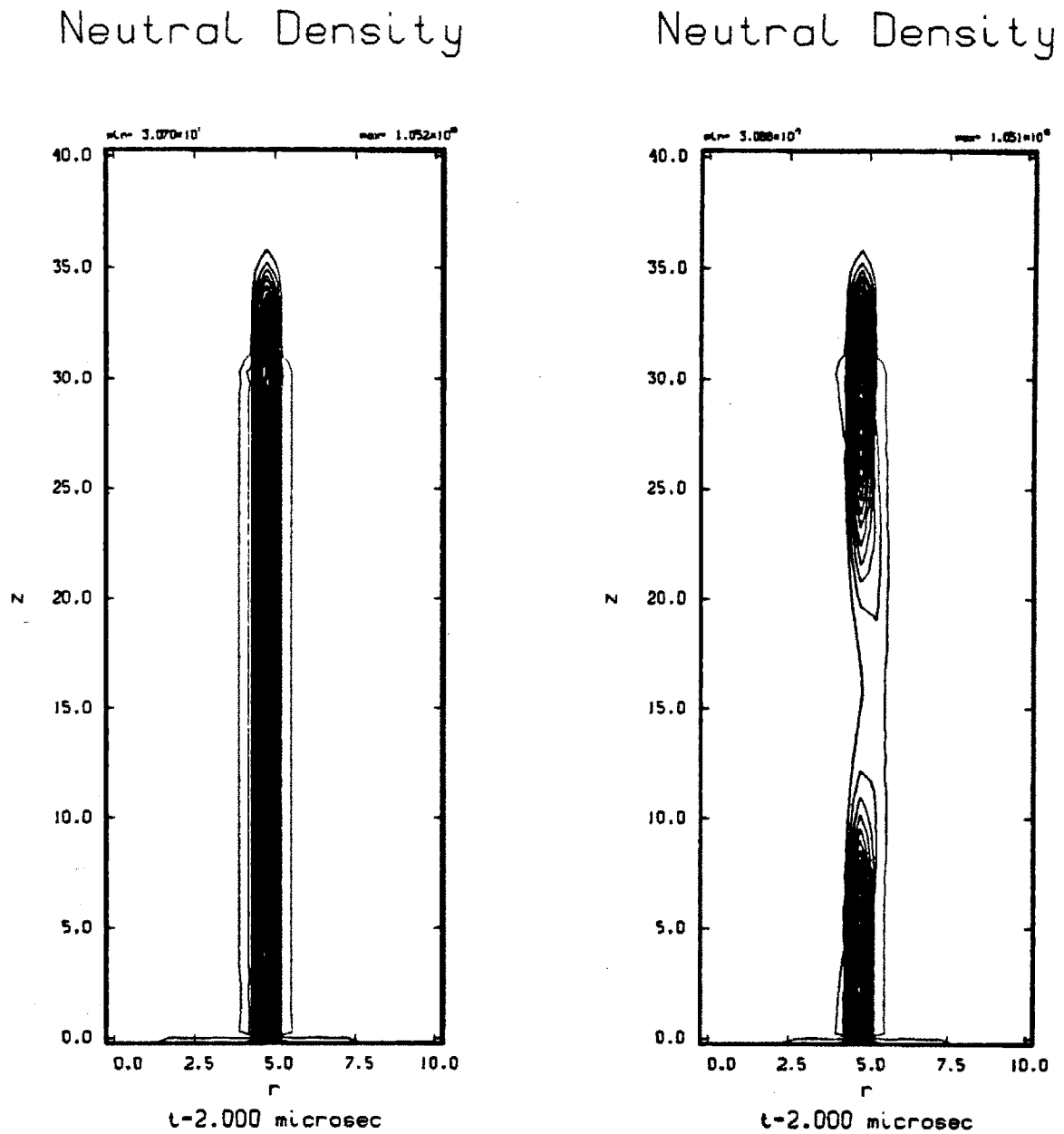


Figure 3.19: Comparison of neutral gas density at two microseconds for reference case and even injection case

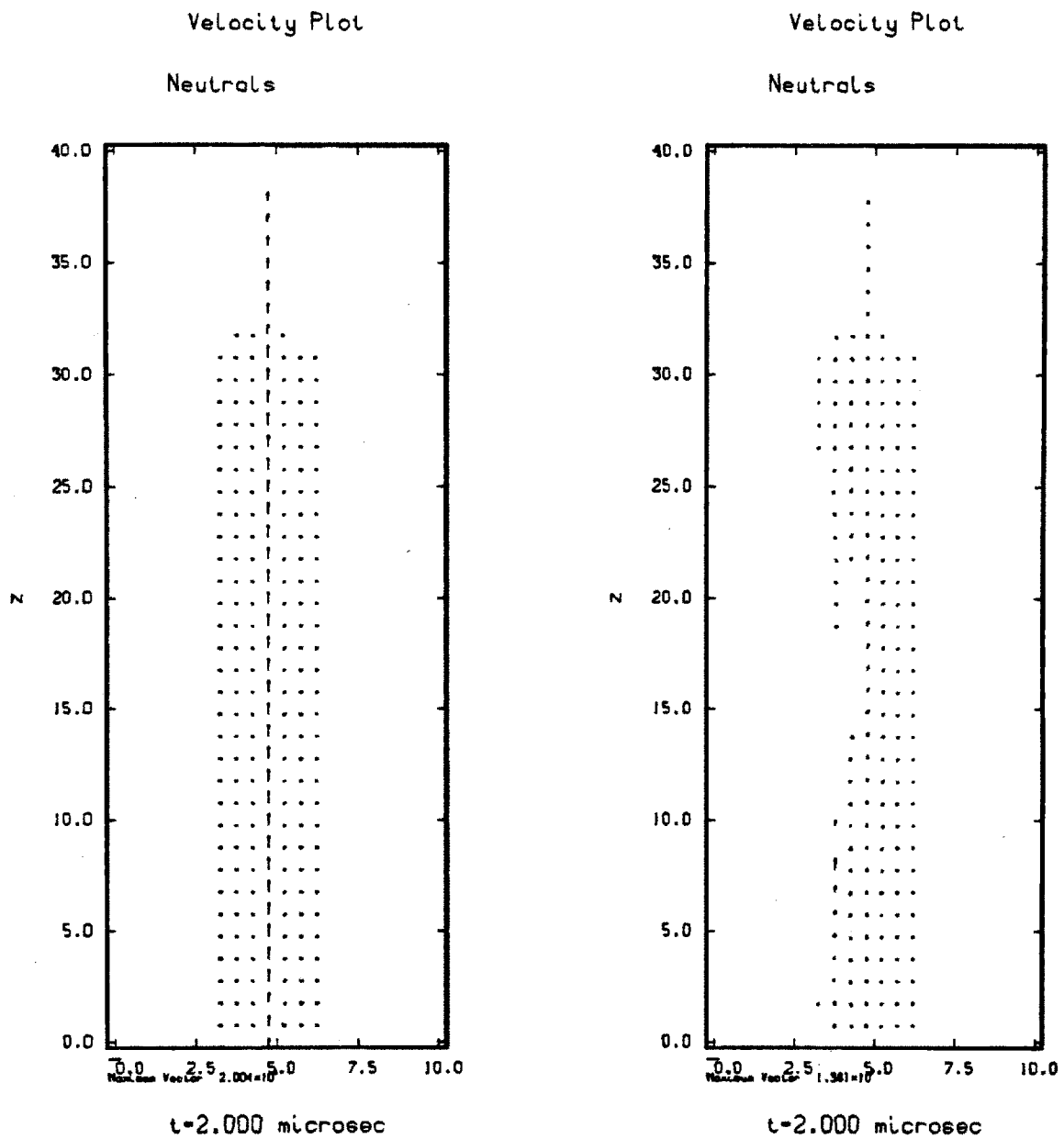
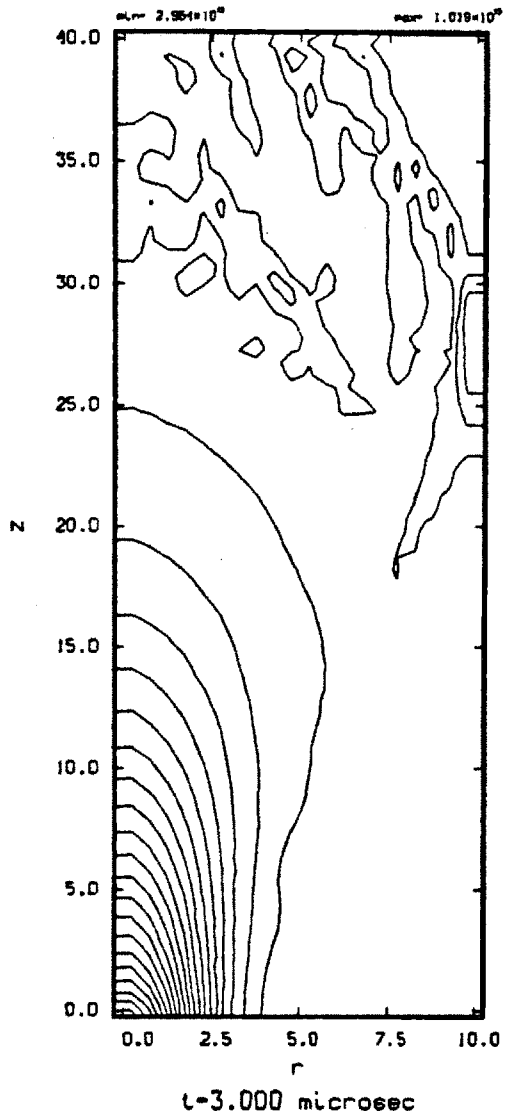


Figure 3.20: Comparison of neutral gas velocity plots at two microseconds for reference case and even injection case.

Ion Density



Ion Density

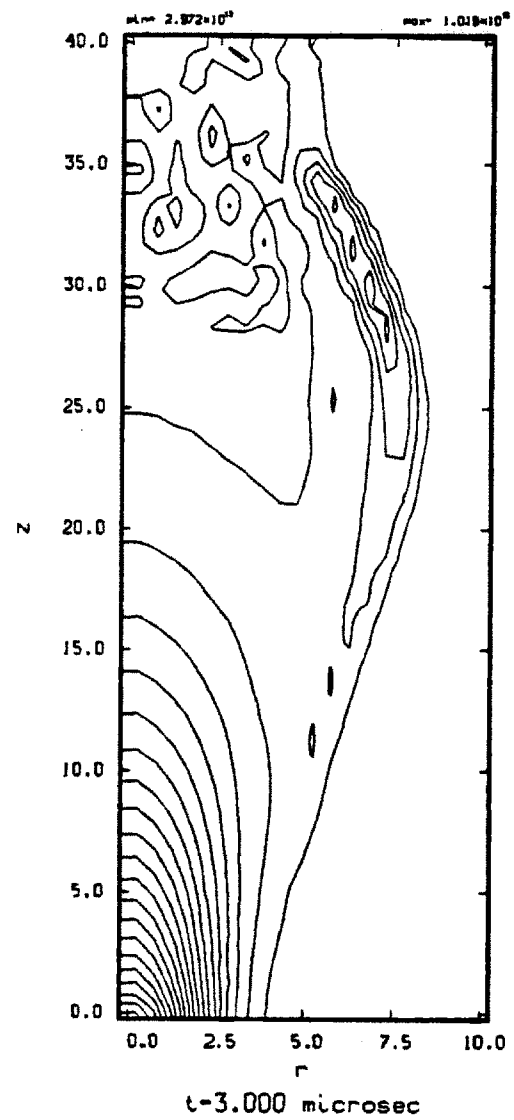


Figure 3.21: Comparison of plasma density plots at three-microseconds for reference case and even injection case.

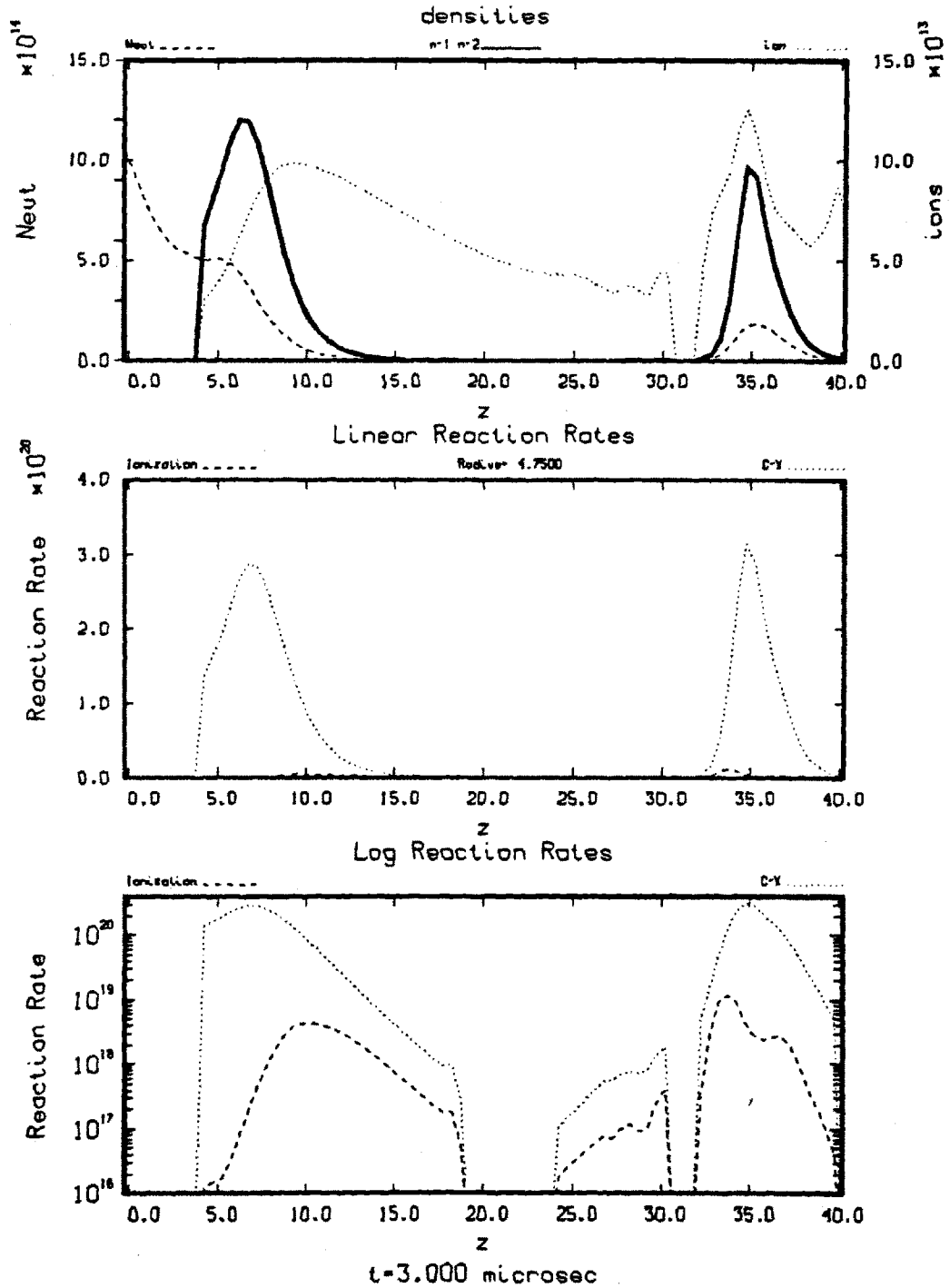


Figure 3.22: Reaction rate plots at three microseconds for even injection case.

is an initial reaction region near $z = 5\text{cm}$ and then nothing until the plasma reaches the final island of neutral gas that has yet to be engulfed by the plasma flow. The coupling coefficients in Figure 3.23 again tell the story. It is important to note that the scales on the plots are self scaling, and thus span the range from the minimum value encountered to the greatest. In this case, the maximum momentum increase that the plasma felt was less than one tenth of one percent. The plasma axial momentum was actually reduced in certain regions, again by a small factor. The coupling coefficients are also small. The magnetic interaction parameters are very large. Upon combining these factors clearly the jet is not having a significant effect on the plasma.

Figure 3.24 shows the velocity flow field at three microseconds. It gives a good qualitative summary of the effect of the neutral gas injection. Though the plasma has yet to hit the wall in this case, it shows that the velocity vectors are still field aligned. The neutral gas jet is not forcing the plasma from the field lines.

Figure 3.25 compares the neutral density at three microseconds. It shows that except for a small island at $z = 35\text{cm}$, the neutral gas has all been eroded away.

To close out the description of the even neutral gas injection case I will look at the results at four microseconds. The reference case never made it to four microseconds because of a numerical instability when it interacted with the wall. The results are nevertheless informative because they confirm the trend that was established up to three microseconds.

Figure 3.26 is the plasma density contour plot at four microseconds. It shows that indeed the plasma has continued to expand and follow the field lines. It has expanded up against the wall at r_{max} as the reference case did at a slightly earlier time step.

Figure 3.27 are the reaction rate plots at four microseconds. The top plot shows the density traces for the neutrals and plasma. It can be seen from this plot that the plasma has completed eroded the neutral gas away. The wild peaks in the plasma trace near z_{max} are due to the plasma flow interacting with the plasma that is building up against the wall at r_{max} . This is consequence of the boundary conditions used at r_{max} and not physically significant here.

The final figure, Figure 3.28, is the velocity flow field plot at four microseconds. It shows that the plasma flow has stayed field aligned and intersected with the wall at r_{max} .

This concludes the analysis of the even neutral gas density injection case. In sum-

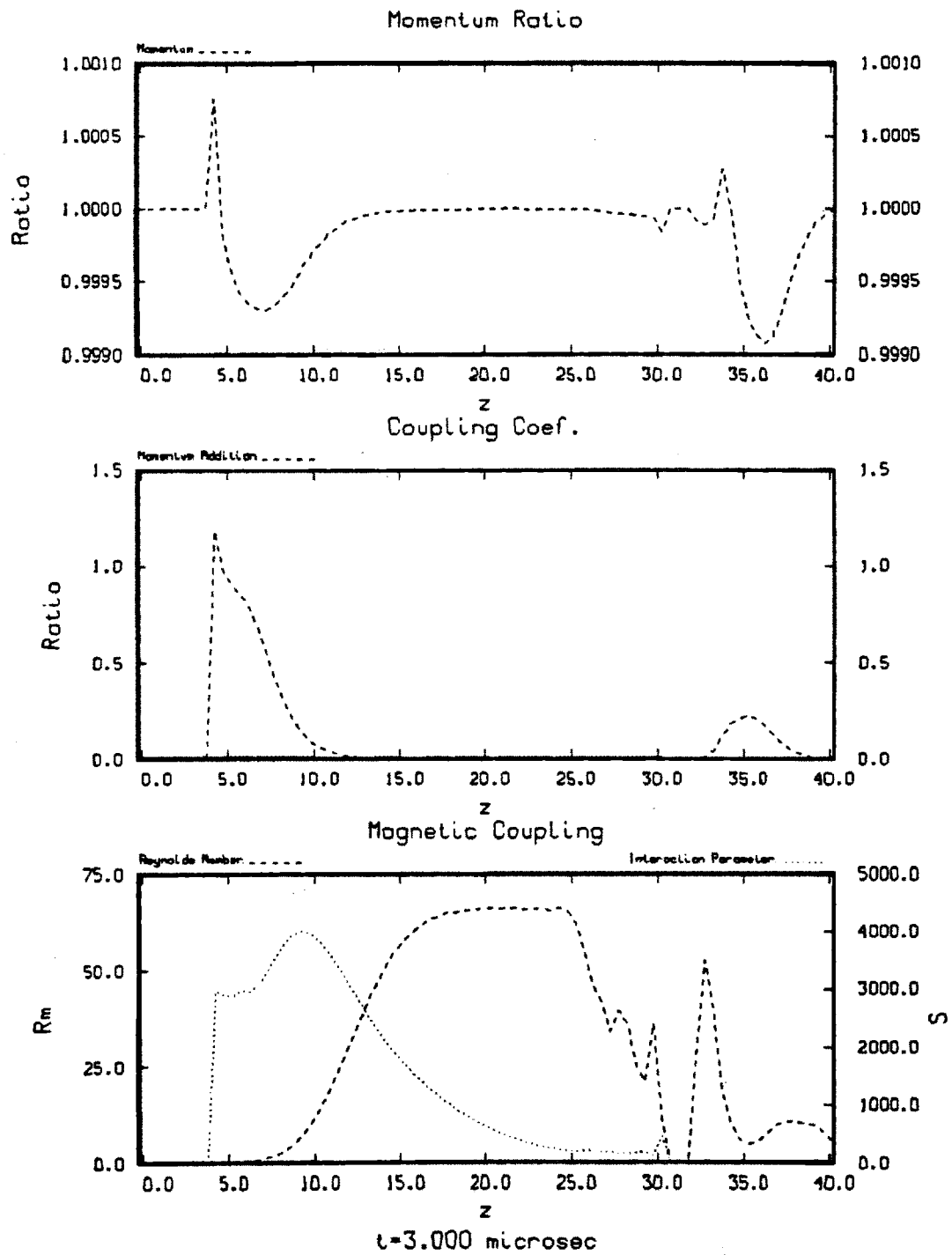


Figure 3.23: Coupling Coefficient at three microseconds for even injection case.

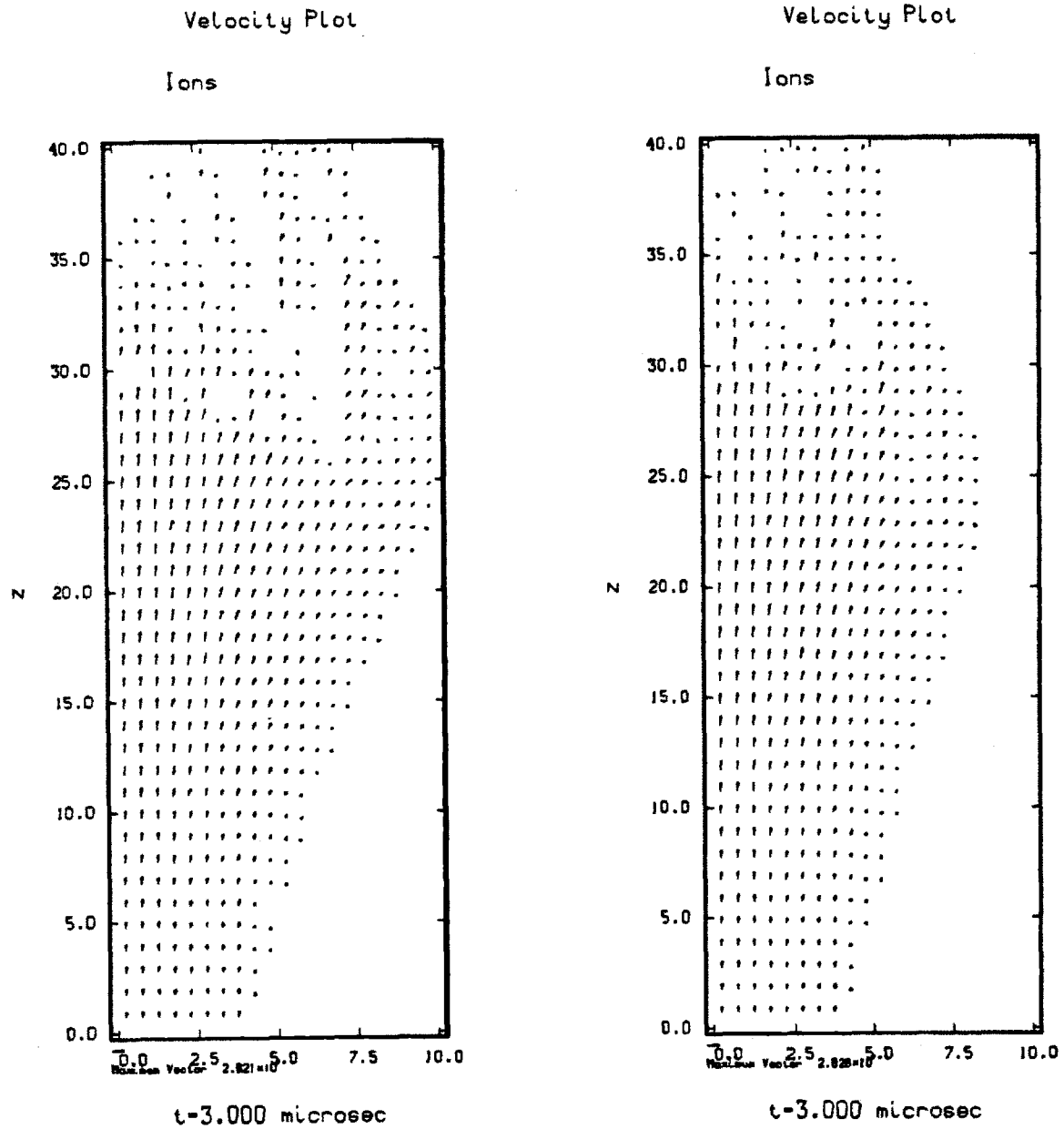


Figure 3.24: Comparison of plasma velocity plots at three microseconds for reference case and even injection case.

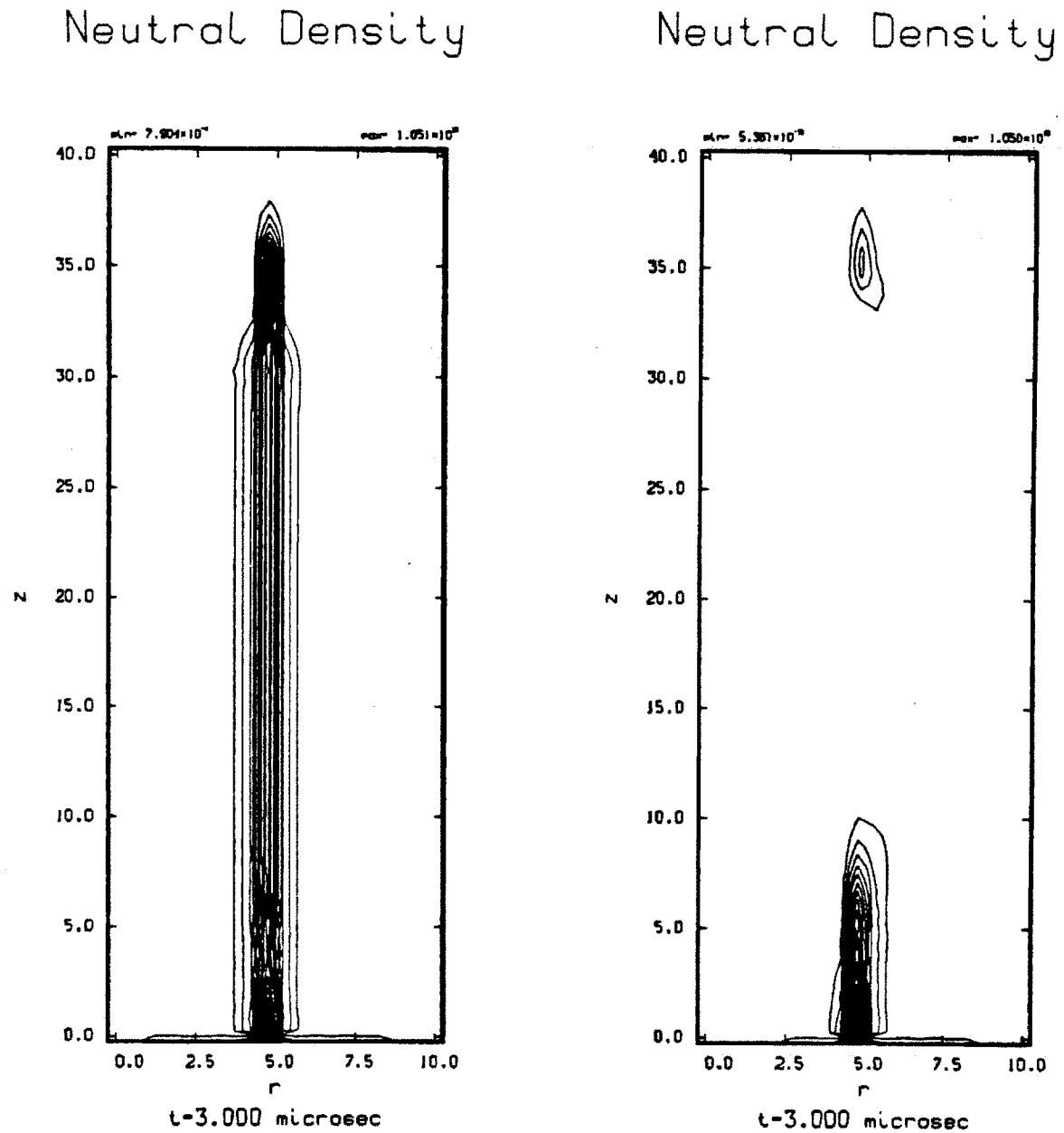


Figure 3.25: Comparison of neutral gas densities at three microseconds for reference case and even injection case.

Ion Density

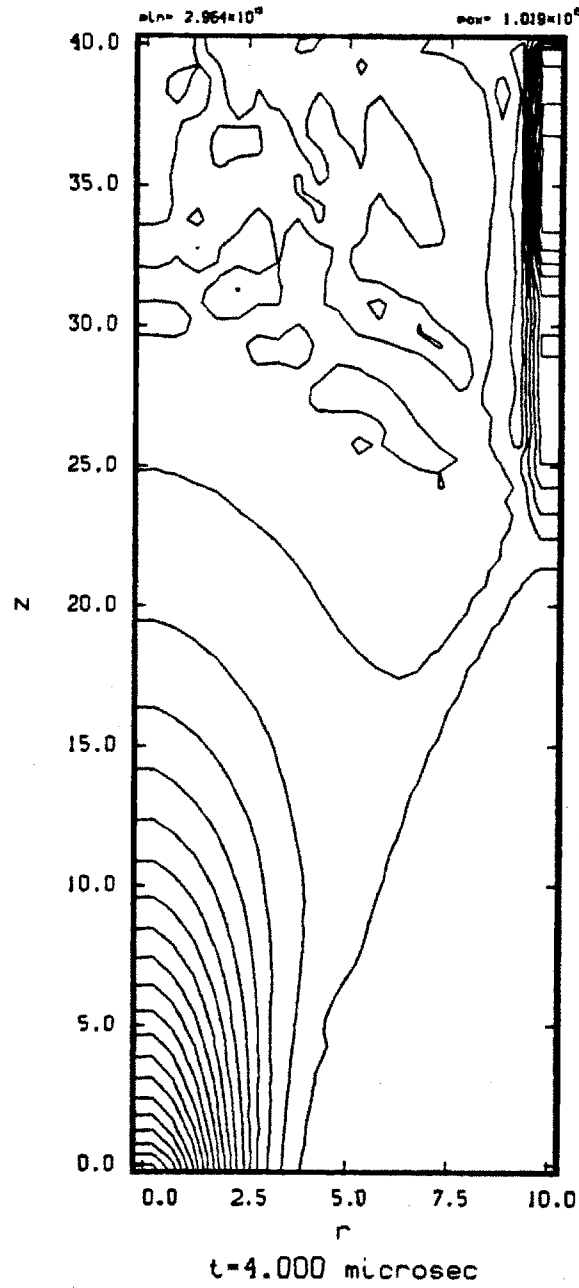


Figure 3.26: Plasma density plot at four microseconds for even injection case.

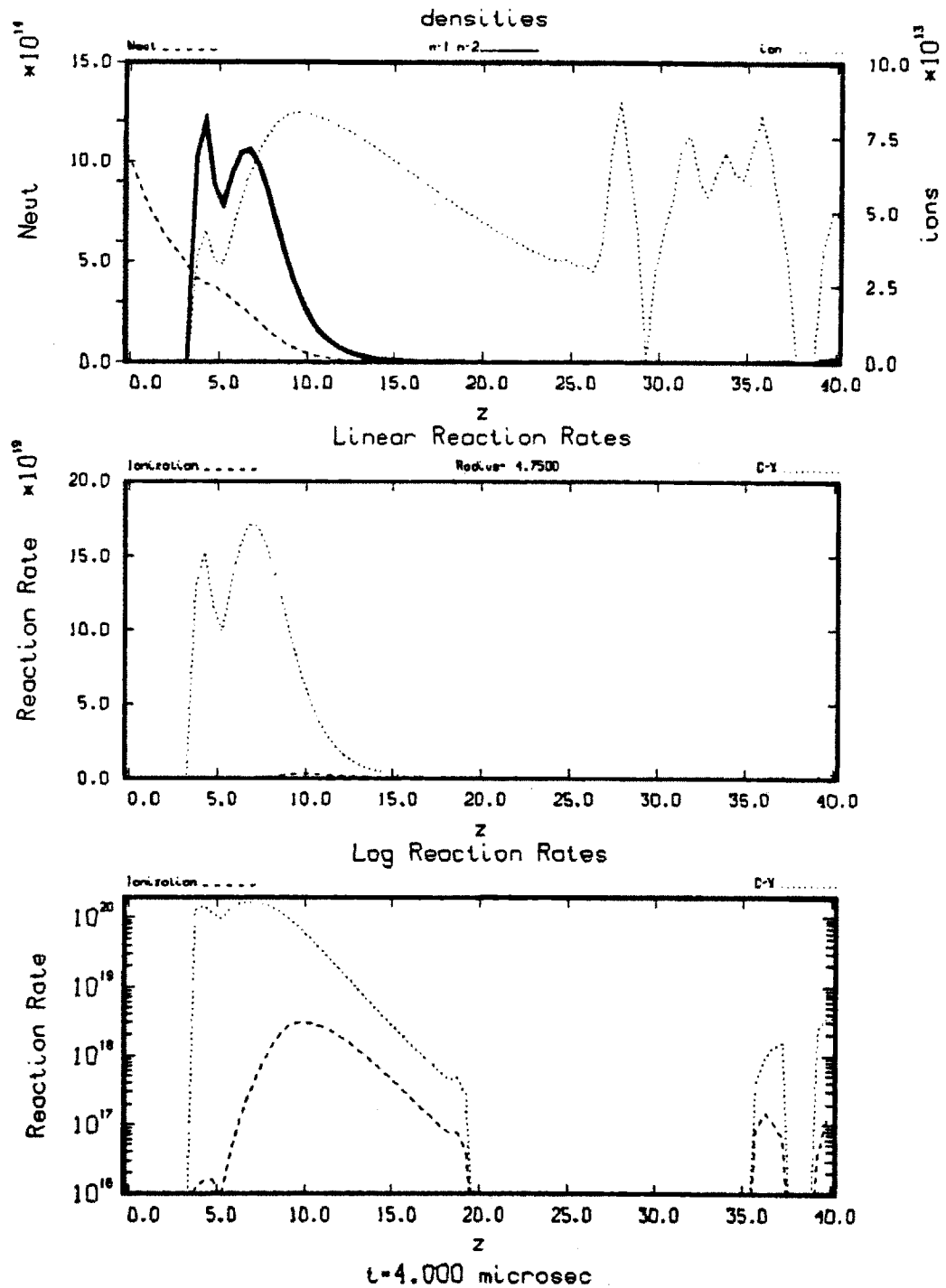


Figure 3.27: Reaction rates at four microseconds for even injection case.

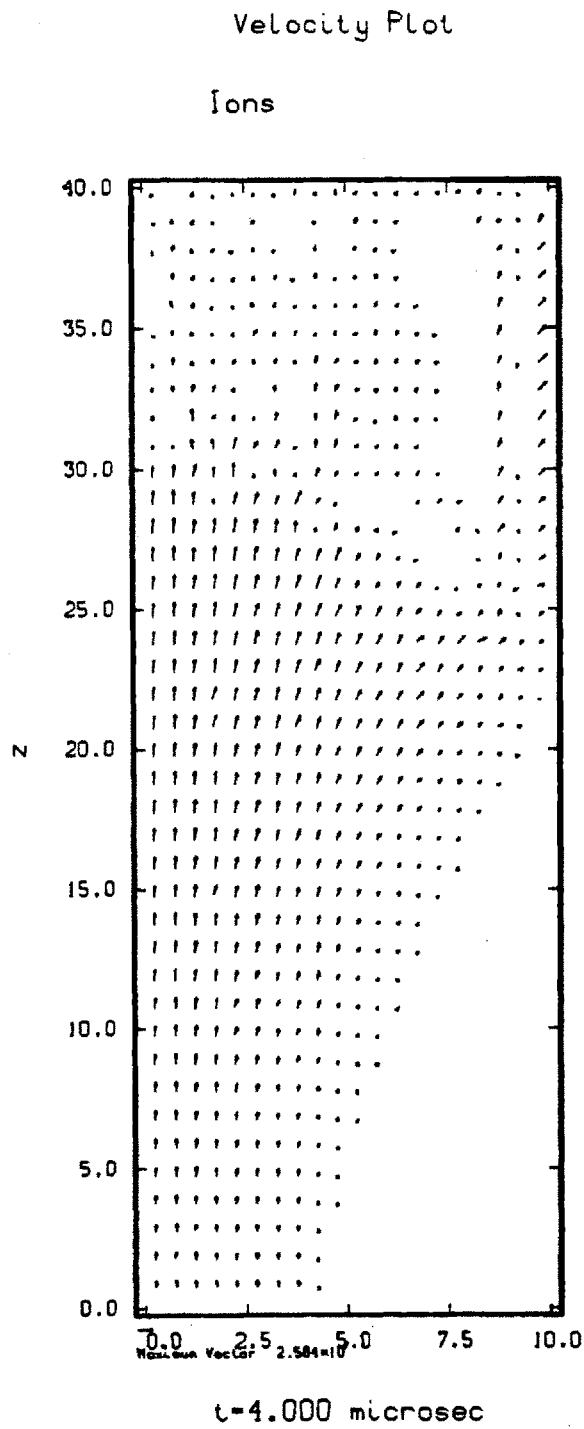


Figure 3.28: Plasma velocity plot at four microseconds for even injection case.

mary, it was seen that the plasma erodes the neutral gas away and the neutral gas can never recover. This is primarily because the neutral gas is having very little effect on the plasma due to the long time scales involved in momentum transfer events. With the plasma streaming time scales being much shorter than the momentum adding time scale, the plasma streams through the region of interaction with little effect. In addition, the magnetic interaction parameters always remain very much greater than one, indicating that the magnetic field is dominating the flow. The net result is that the plasma erodes the neutral gas away and then continues to expand along the stream line as if the neutral gas injection was not present. In this case, the axial injection of a neutral gas jet has no lasting effect on the plasma and will not sustain the formation of a hybrid plume.

3.3.3 High beta

The next case that will be presented is the high-beta case. The reference case and the even neutral gas density injection case were run with a beta of approximately one percent. In the high beta case the plasma beta is increased to approximately 50%. It is hoped that this increase in beta will increase the effect that the plasma has against the magnetic field. The specific parameter to watch is the magnetic interaction parameter (defined in Equation 3.13). As S becomes smaller, it means that the plasma inertia force is starting to play a more significant role in the plasma dynamics. The beta will be increased by reducing the magnetic field strength. This will keep the plasma parameters constant from the reference case and even injection case. The other property that must remain constant for the comparison to be meaningful is the magnetic field geometry. The magnetic field must expand at the same rate that it did in the previous case, even if the overall field strength is reduced. This is easily accomplished when working with the A_θ representation for the magnetic field ($B = \nabla \times A$). All one has to do is to scale A_θ by the amount that one desires to change the magnetic field. In this manner, the field geometry is *exactly* the same from the previous run; only the magnitude is changed. The input parameters are shown in Table 3.3.

The results will be compared against the case with low beta and the reactions turned on. The low beta case will be on the left and the high beta case will be on the right. It should be noted here that the terms *high beta* and *low beta* as used in this chapter do not imply that there is anything particularly *high* or *low* about the beta in the

Item	Ions	Neutrals
mass flow rate (\dot{m}), kg/sec	$2.87e - 04$	$3.86e - 05$
Thrust, Newtons	32.47	0.6
Power, MWatts	1.83	0.005
Temperature, eV	100.0	0.025
Density, part/cm ³	$1.0e+15$	$1.0e+15$
Velocity, cm/sec	$1.13e+07$	$1.5e+06$
I_{sp} , sec	11,500	1,600
I_{sp} net, sec	10,350	

Table 3.3: Input parameters for the high beta case.

respective case. The terms are used simply as a means to differentiate the two runs.

The first time step that will be presented is at two microseconds. No interactions have occurred at the one microsecond time step so those figures are skipped.

The first figure, Figure 3.29, is the plasma density at two microseconds. Qualitatively there is not a significant difference between the two plots. Both graphs show that the plasma is peaking downstream of the neutral gas injection.

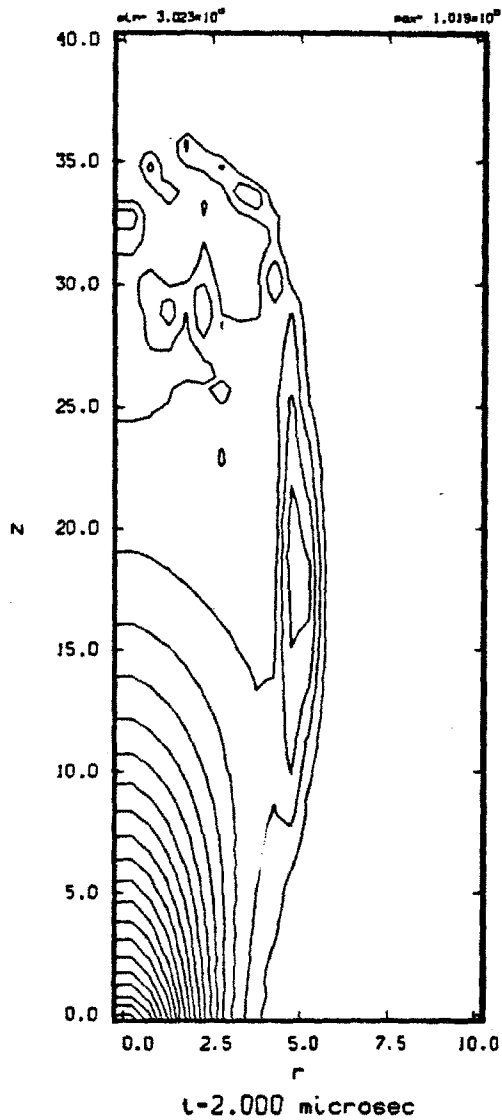
The next figure, Figure 3.30, shows the density profiles and reaction rates. Again there is not a significant difference between the two runs. The plasma density in the low beta case (on the left hand side) has a slightly higher peak ($2.e + 14 \text{ part/cm}^3$) than the high beta case ($1.5e + 14 \text{ part/cm}^3$). The high beta case has slightly flatter plasma profile than the low beta case. The reaction rate plots are also similar.

The next figure, Figure 3.31, shows the first significant change between the runs. The top plot, the momentum ratio, closely follows the low beta result. There is a large peak near the end of the interaction region that is not present in the low beta case, but is still of very small magnitude. The over all momentum coupling is still small.

The second plot shows the coupling coefficient. This is an indication of the relative time scales of convection to momentum adding events. One would like large coupling coefficients for the plasma rocket to work. The peak coupling coefficient at approximately $z = 5\text{cm}$ is greater than in the low beta case. In the high beta case it is slightly greater than 2. In the low beta case the peak is less than two. Though the absolute change is not that significant, it is at least in the right direction (toward greater coupling).

The final plot in this figure shows the magnetic coupling. The magnetic Reynolds

Ion Density



Ion Density

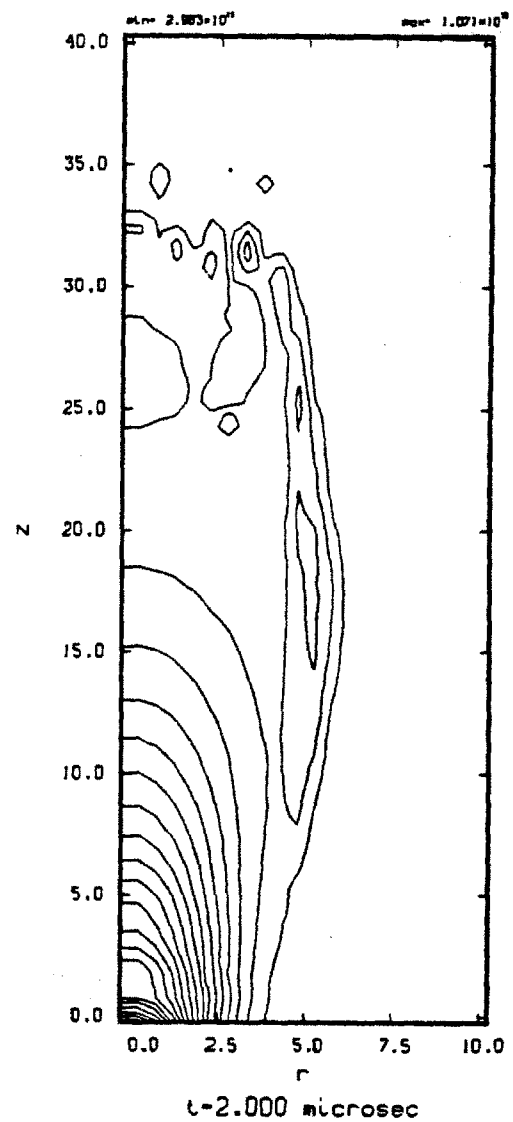


Figure 3.29: Comparison of plasma density at two microseconds. Low beta case on the left, high beta case on the right.

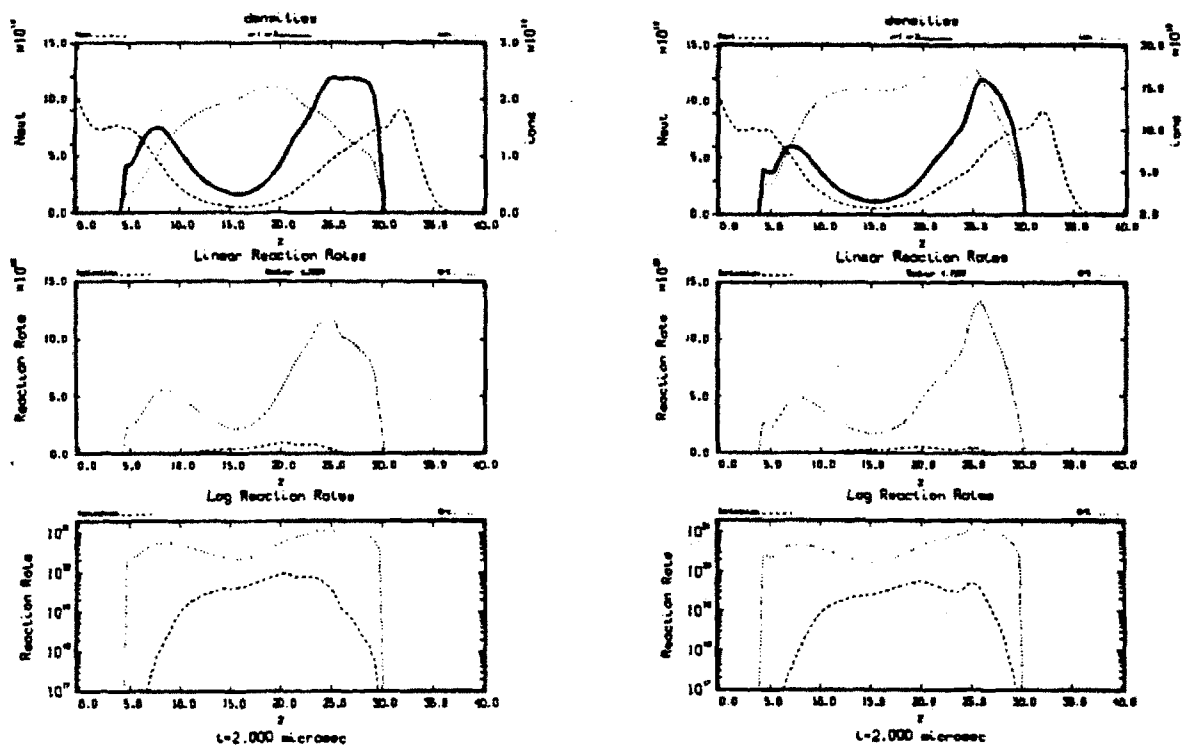


Figure 3.30: Comparison of reaction rate plots at two microseconds. Low beta case on the left, high beta case on the right.

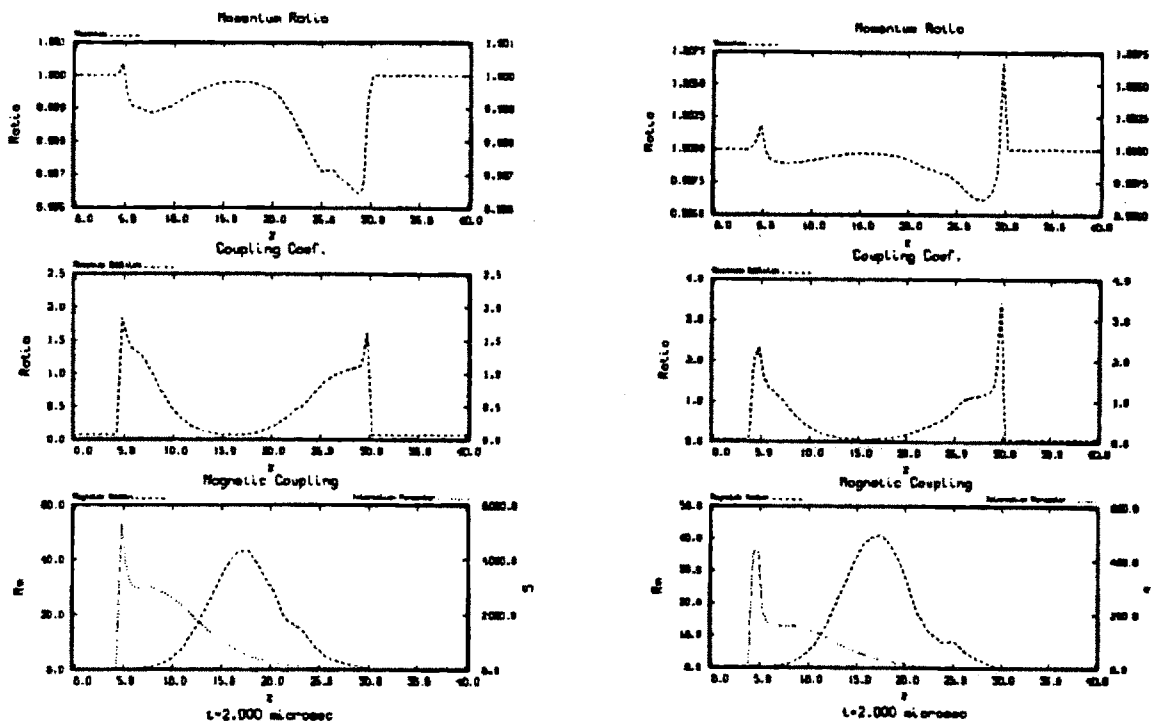


Figure 3.31: Comparison of coupling coefficients at two microseconds. Low beta case on the left, high beta case on the right.

number remains almost unchanged in both magnitude and form. The magnetic Reynolds number is a function of the plasma streaming velocity and the plasma conductivity. That the Reynolds number remains unchanged is an indication that these properties of the plasma have remained almost constant. The magnetic interaction parameter has changed significantly, as one would expect. It is directly proportional to the square of the magnetic field strength. The magnetic interaction parameter dropped by over a factor of ten. Unfortunately, in the low beta case $S \sim 5000$, so a factor of ten does not reduce S to the point where one would expect that the inertia of the plasma should start playing a significant role. It does show that the $J \times B$ force is reduced relative to the inertia force, just not to a sufficient enough degree. The plasma velocity plots at two microseconds are shown in Figure 3.32. The graphs show qualitatively the same flow pattern.

Advancing to three microseconds, the first figure to be shown will be for the plasma density, Figure 3.33. The details of the propagation of the neutrals that have been ionized are different, but qualitatively the results are the same. No significant difference is seen at the intersection of the neutral gas jet and expanding plasma. One would hope that the reduced field strength would be enough to allow the neutral gas to impart enough momentum to push the flow down stream.

The next figure, Figure 3.34, compares the reaction rates at three microseconds. The top plot shows that the neutral gas jet is being eroded away equally in both cases. The reaction rate plots are similar in both cases.

Figure 3.35 compares the coupling information at three microseconds. It can be seen from the top figure that the momentum ratio peak in the high beta case is significantly higher than the low beta case, but still too low to make any significant effect. In a narrow region it approaches 1%, which is far too small to have any real effect.

In the second plot the reason for the increase momentum ratio can be seen. The coupling coefficient peaks at over three in the area where the momentum ratio had its peak. This is consistent in that there is now sufficient time for a significant amount of ionization and charge exchange events to happen to influence the plasma in this region.

Unfortunately the third plot shows that the plasma must still be sufficiently warm to maintain a large magnetic interaction parameter in this region. This implies that whatever neutral gas is being sourced into the plasma will be strongly influenced by the magnetic field. Overall, the magnetic interaction parameter is greatly reduced

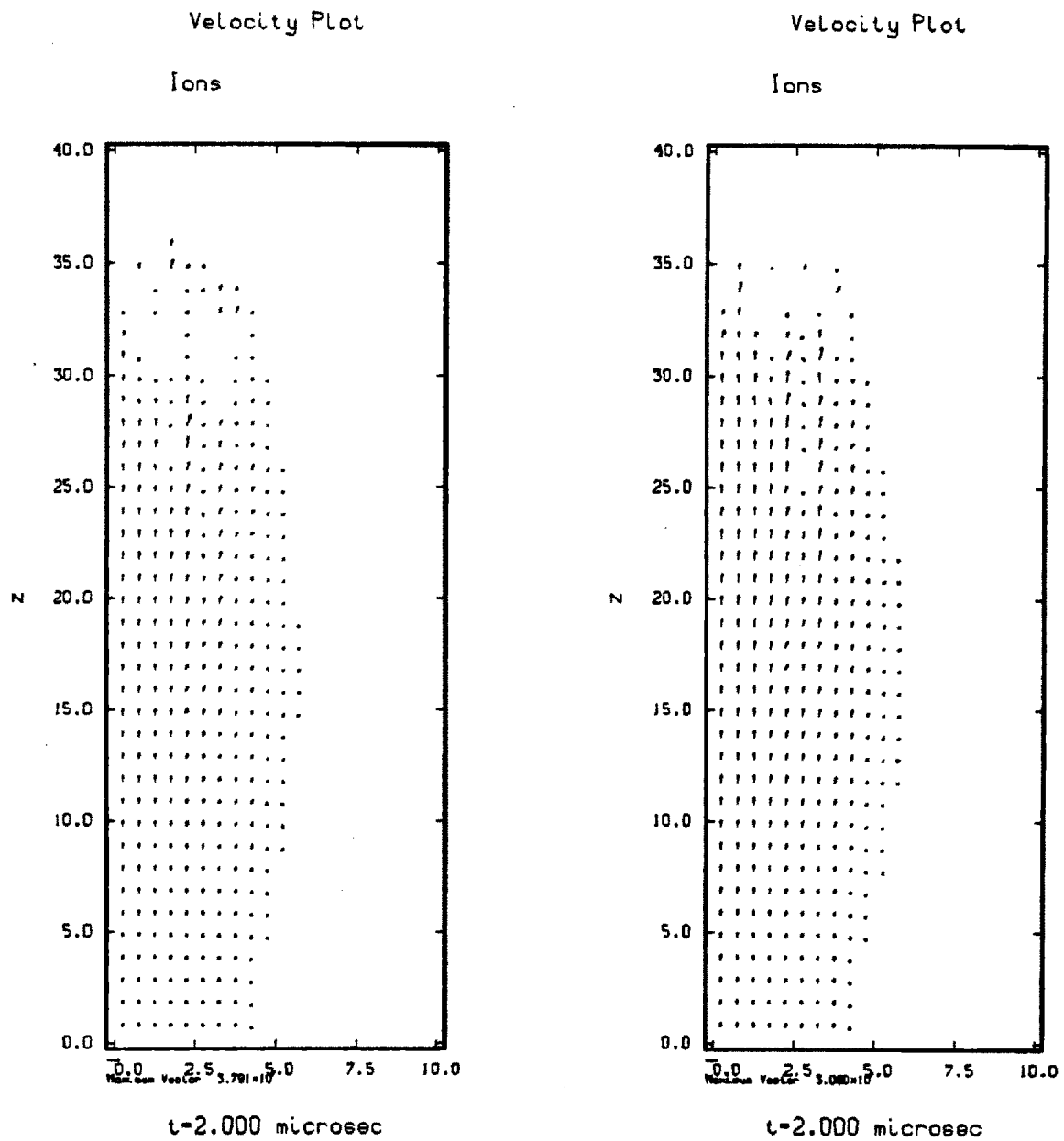


Figure 3.32: Comparison of plasma velocity plots at two microseconds. Low beta case on the left, high beta case on the right.

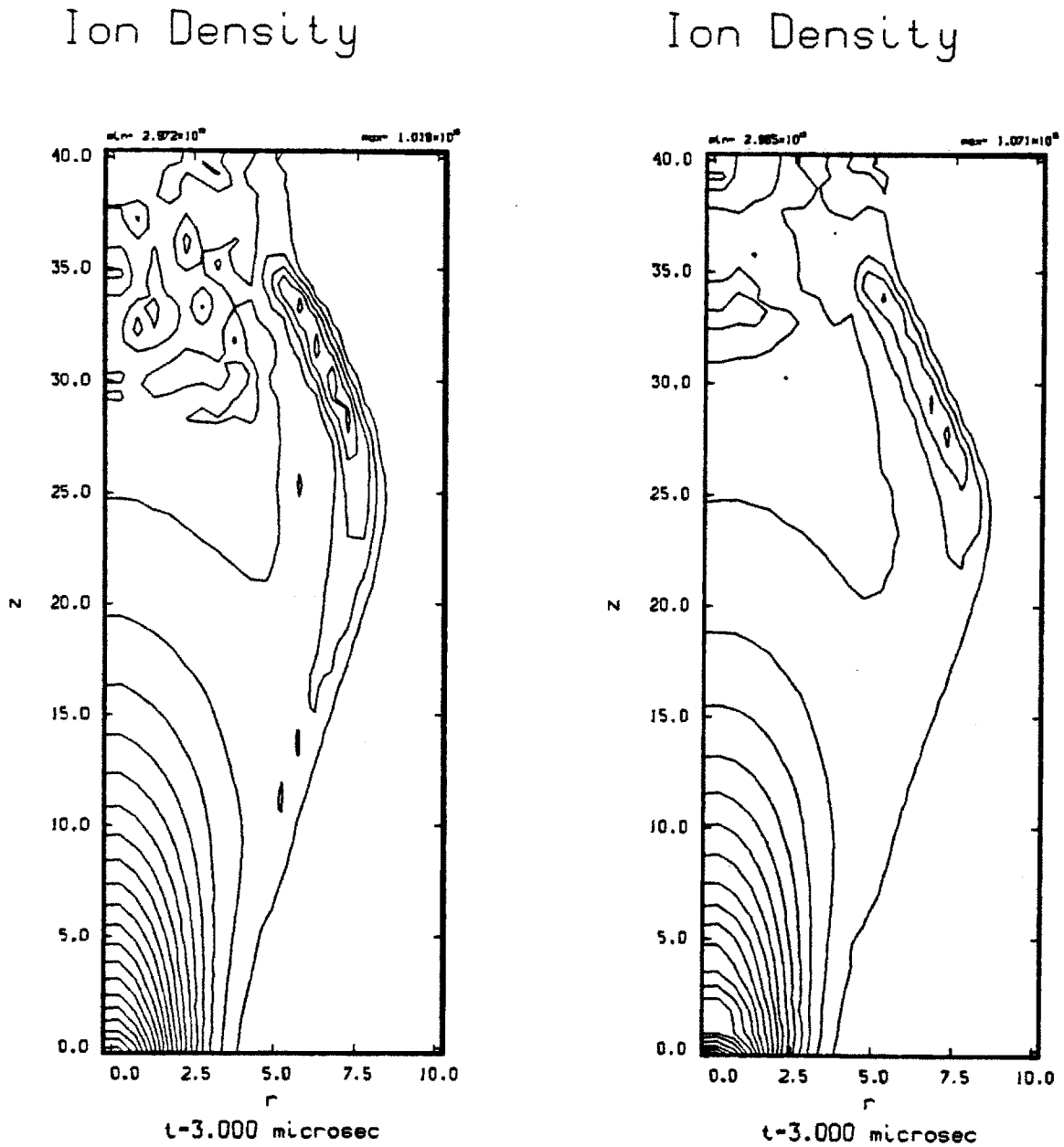


Figure 3.33: Comparison of plasma density plots at three microseconds. Low beta case on the left, high beta case on the right.

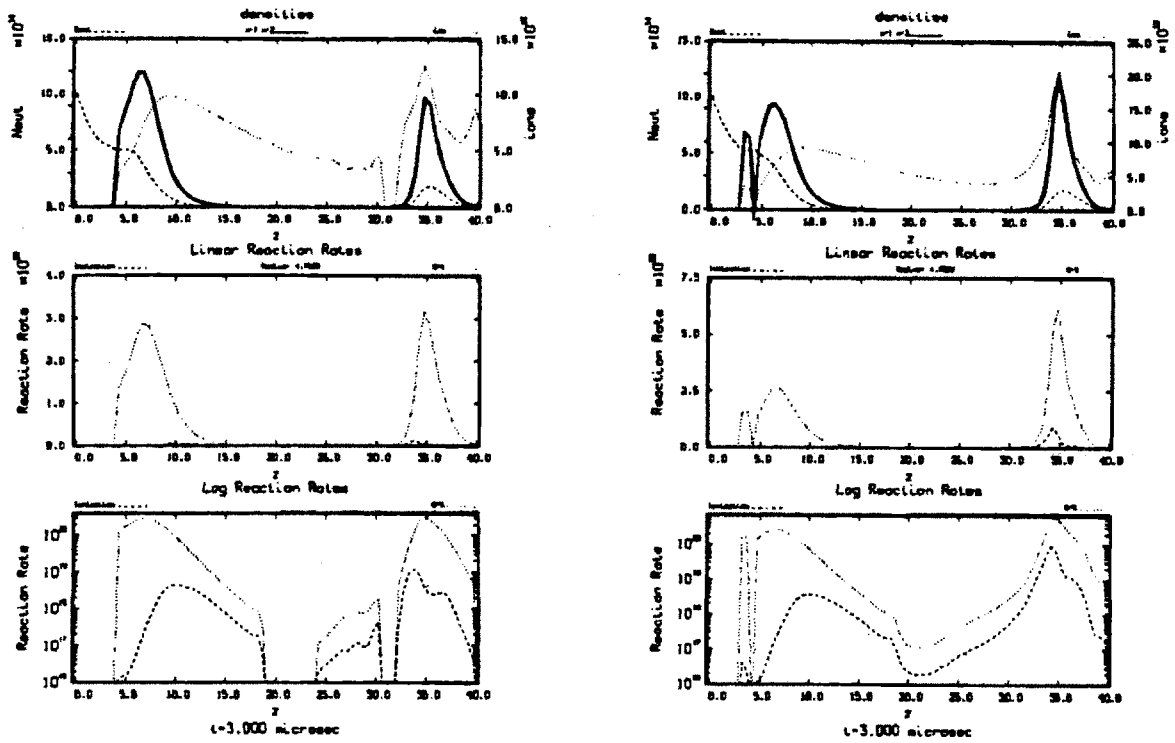


Figure 3.34: Comparison of reaction rate plots at three microseconds. Low beta case on the left, high beta case on the right.

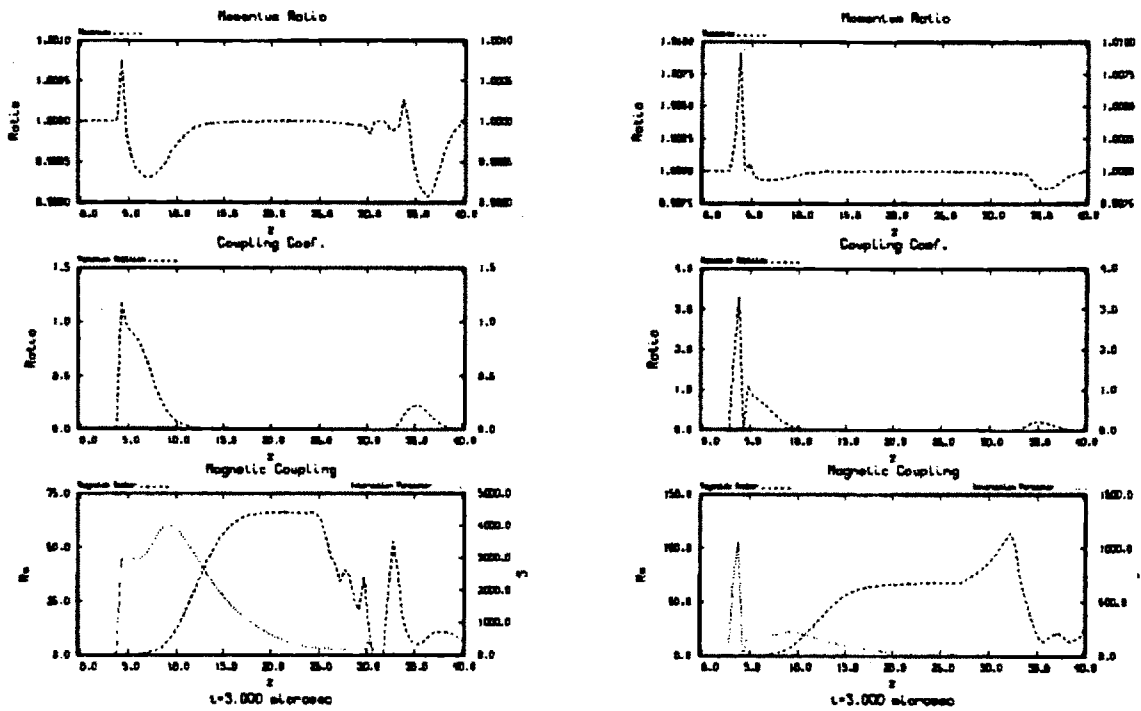


Figure 3.35: Comparison of coupling coefficients at three microseconds. Low beta case on the left, high beta case on the right.

compared to the high beta case. S is sufficiently large ($S \sim 250$) to indicate that the plasma still does not have a good chance at breaking off the field line. This is compared to $S \sim 4000$ for the low beta case, so one can see that the reduced field has a significant effect; it is just not significant enough.

The plasma velocity plots, Figure 3.36, are almost identical. This is a good qualitative guide that the two runs are very similar.

To round-out the presentation of three microsecond results the neutral gas density contour plots are shown in Figure 3.37. They too, are almost identical. The characteristic island downstream (at this time step located at $z \sim 35cm$) of the neutral jet injection is observed in both plots. Remember that the existence of this island is due to the neutral gas being prestreamed down the duct at $t = 0$. The plasma has yet to reach this area of the duct so the neutral gas in this region has not been eroded.

The results at four microseconds will complete the comparison of the high beta case to the low beta case. The first plot at four microseconds will be the plasma density, Figure 3.38. It shows that the plasma has expanded into the wall at r_{max} . This alone summarizes the effect of the low beta case.

The reaction rate plots, shown in Figure 3.39, are now very similar. In the top plot, both the plasma density trace and neutral density trace are almost identical. Correspondingly the reaction rate graphs in the second and third plots are also the nearly the same.

The coupling information in Figure 3.40 shows that the optimistic increase in both the momentum ratio and coupling coefficients seen at three microseconds is not maintained. The momentum ratio is worse than for the low beta case, and the momentum coupling coefficient is now less than one everywhere. The magnetic interaction parameter is still very large ($S \sim 200$).

The final figure, Figure 3.41, summarizes the results of the high beta plasma case. It is a graph of the plasma velocity at four microseconds. It shows that in both the low beta plasma case and the high beta injection case that the plasma flow has expand along the magnetic field. The field strength was reduced by a factor of 5 (from approximately 15,000Gauss to 3,000Gauss). This was not enough to allow the neutral gas to push the plasma across the field lines and allow the plasma to detach from the field.

The main reason can be seen in analyzing the momentum coupling plots and the magnetic coupling plots. The momentum coupling parameter was always near unity.

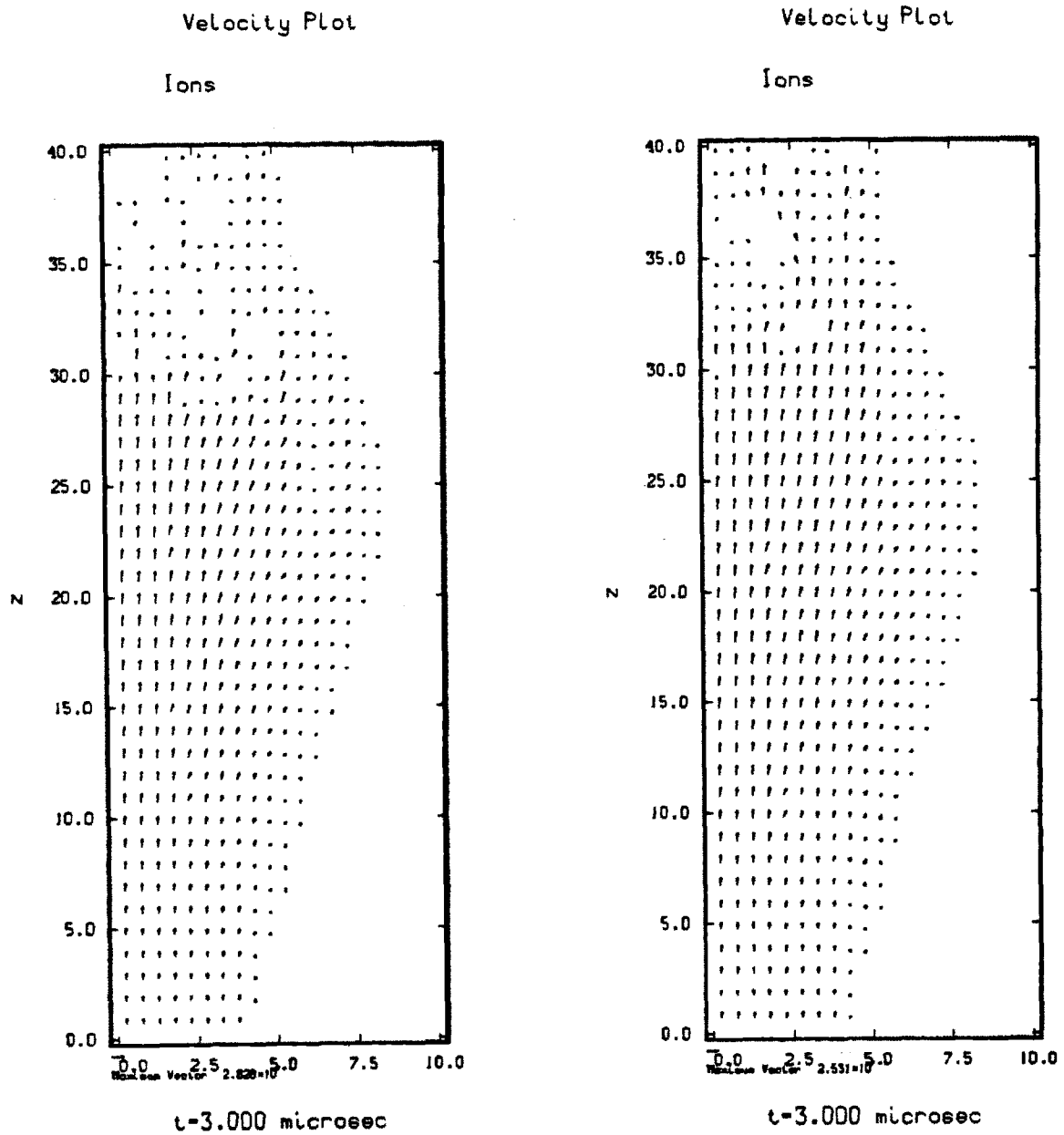
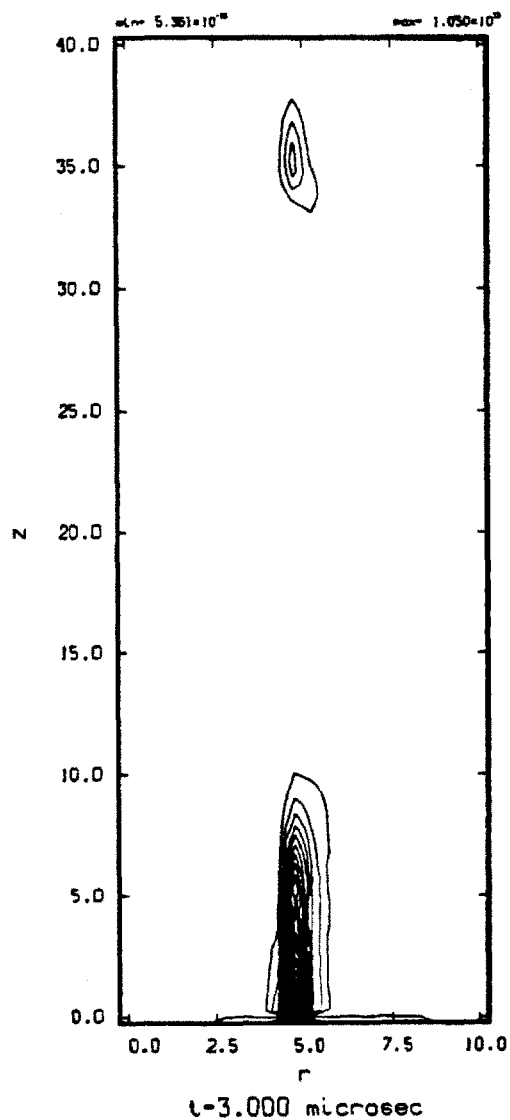


Figure 3.36: Comparison of plasma velocity plots at three microseconds. Low beta case on the left, high beta case on the right.

Neutral Density



Neutral Density

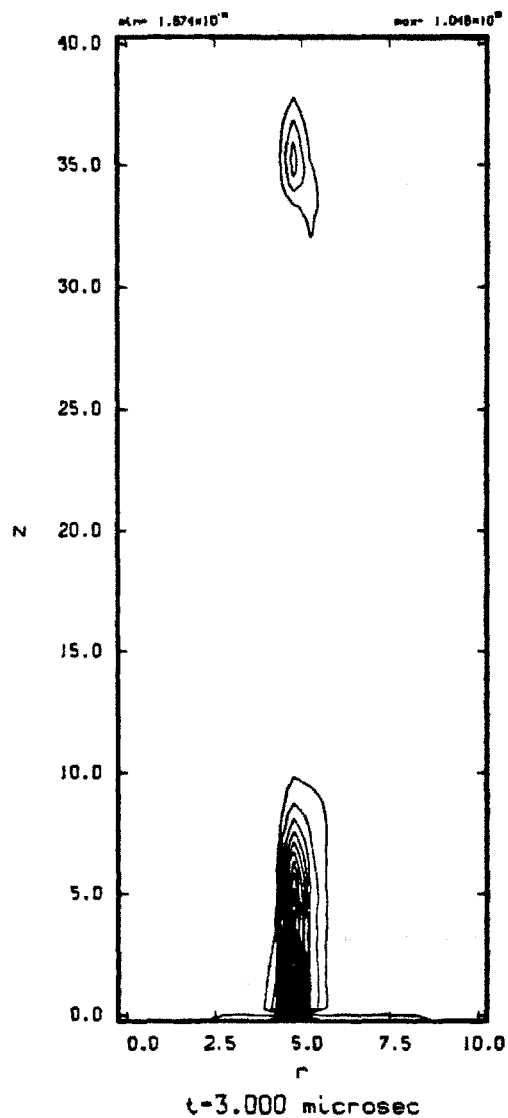


Figure 3.37: Comparison of neutral density plots at three microseconds. Low beta case on the left, high beta case on the right.

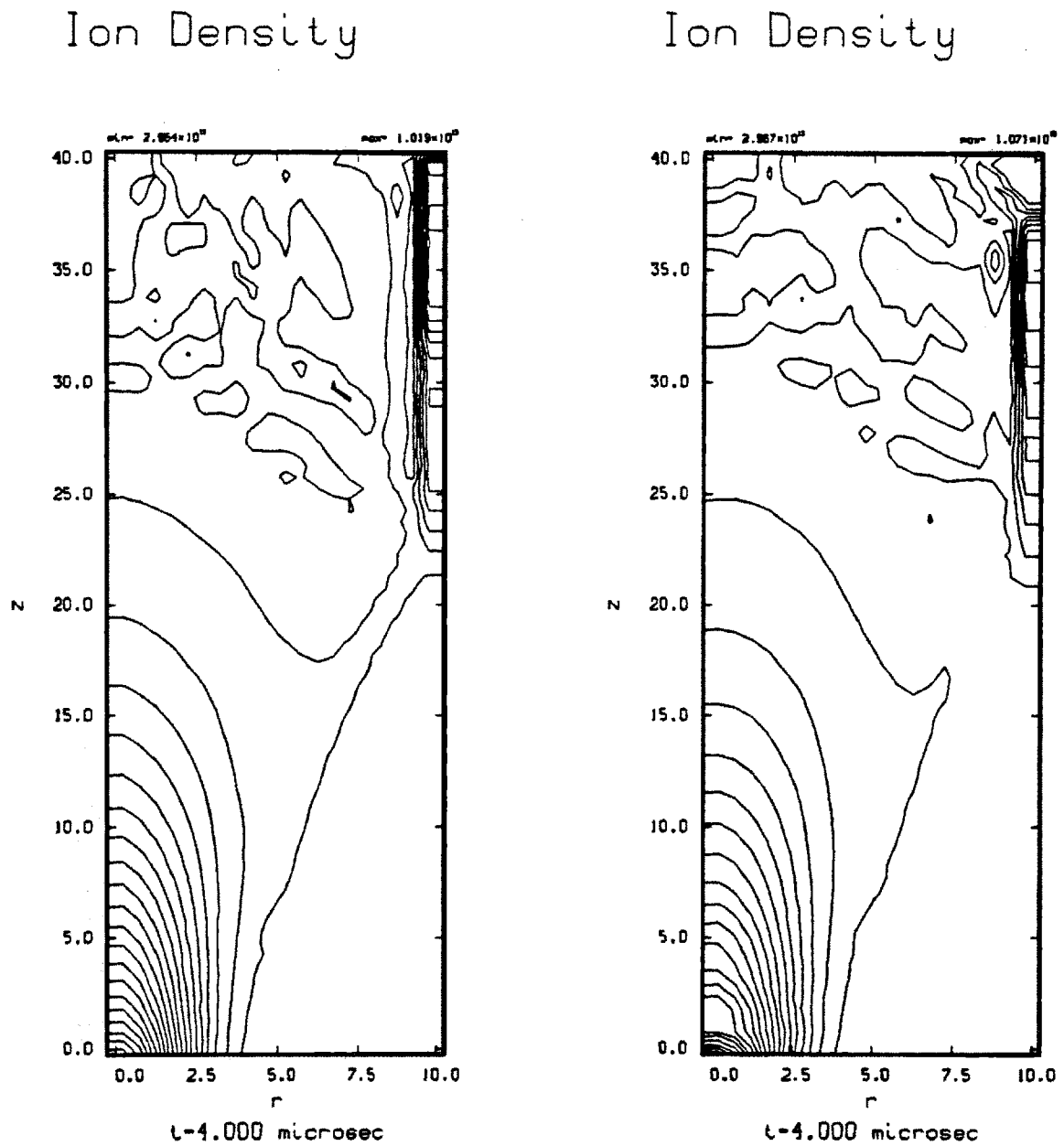


Figure 3.38: Comparison of plasma density plots at four microseconds. Low beta case on the left, high beta case on the right.

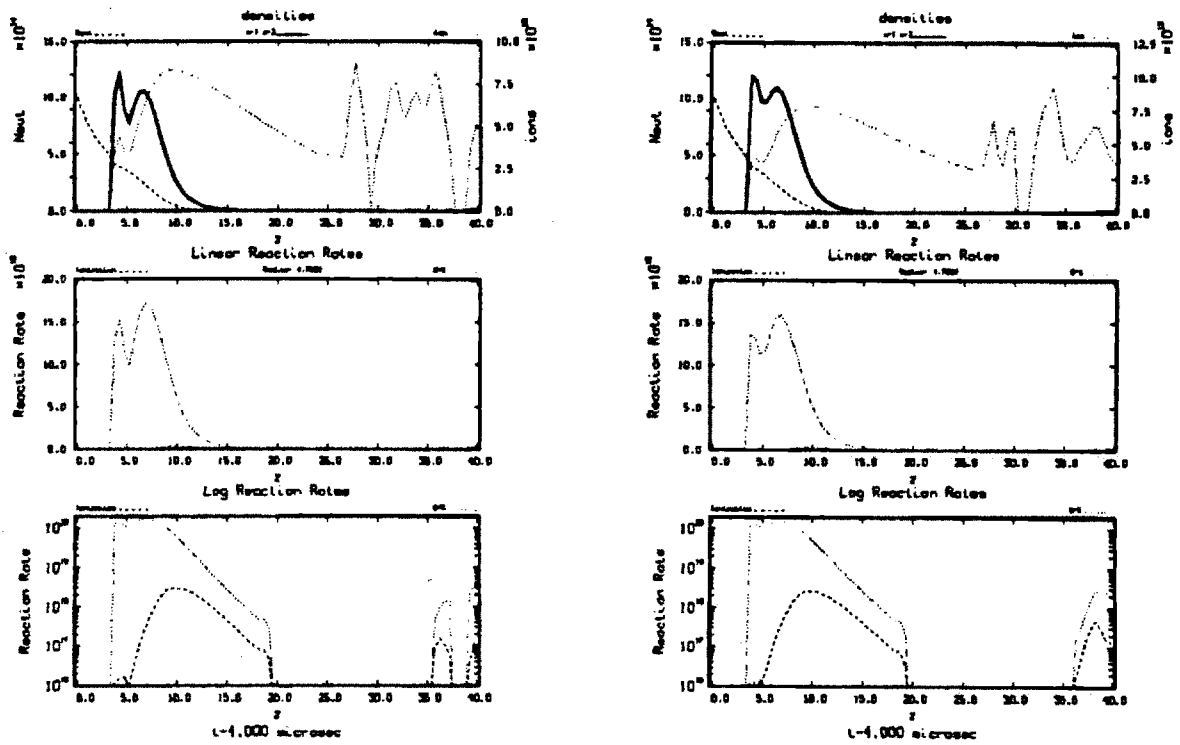


Figure 3.39: Comparison of reaction rate plots at four microseconds. Low beta case on the left, high beta case on the right.

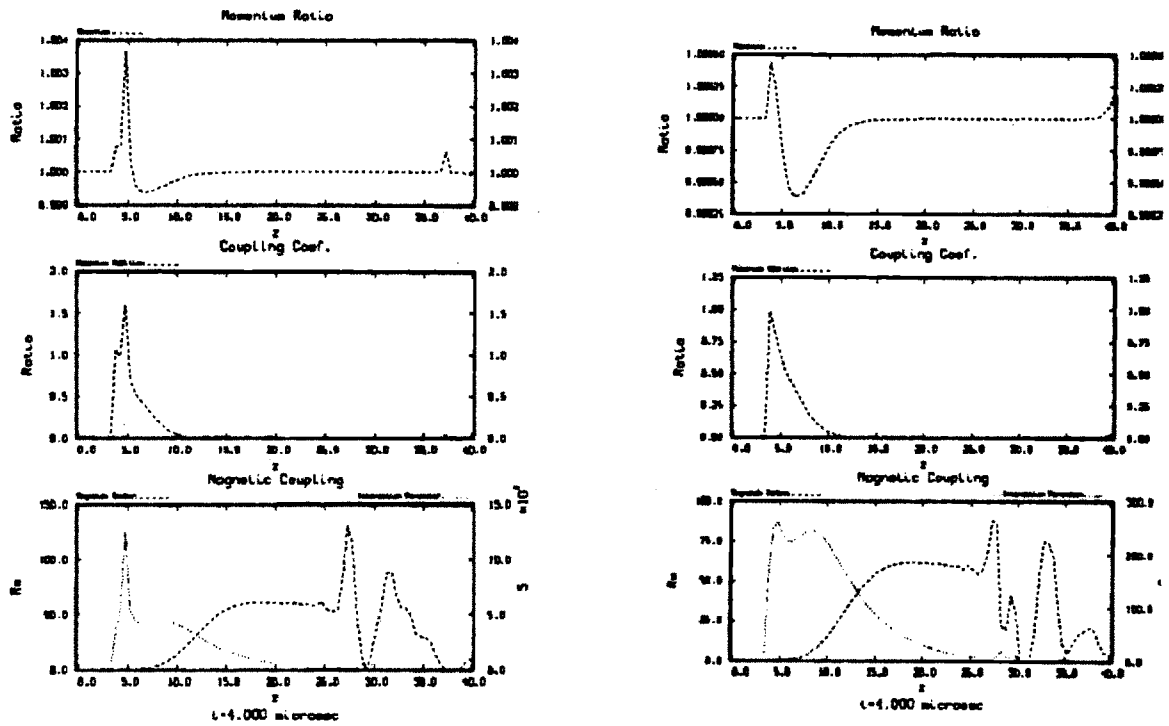


Figure 3.40: Comparison of coupling coefficients at four microseconds. Low beta case on the left, high beta case on the right.

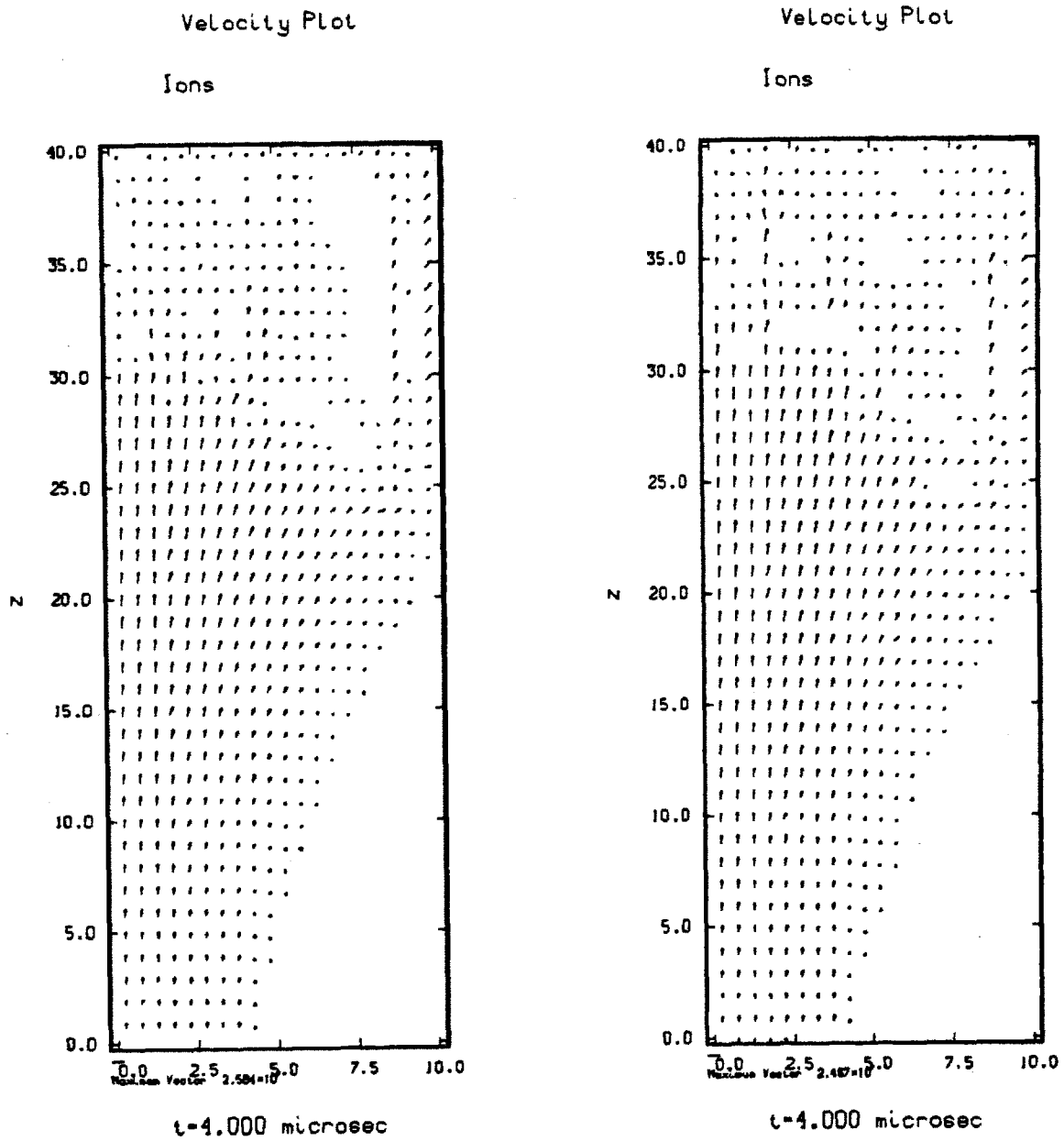


Figure 3.41: Comparison of plasma velocity at four microseconds. Low beta case on the left, high beta case on the right.

The momentum coupling parameter is the ratio of the streaming time scale to the interaction time scale. It is intuitive that if the streaming time scale is much faster than the interaction time scale, one would not expect much effect from the interaction, and this is what is observed. The situation is made even worse by the fact that the magnetic interaction parameter, which is a gauge of the effect of the magnetic field on the flow, was still very large. The interaction parameter was greatly reduced compared to the low beta case, but not to a significant enough degree. The final result is that the plasma still clings to the field line and expands and ultimately runs into the imaginary wall at r_{max} . This indicates that high beta injection of plasma will not be the mechanism that will enable the plasma thruster to work.

3.3.4 Gas density ten-times the plasma density.

The next case that will be presented is the injection of the neutral gas at ten times the peak plasma density. The equal injection case the neutral gas density was set equal to the peak plasma density. Since the neutral gas jet was in a narrow jet and interacting with the edge of the plasma, the neutral gas density in the region of interactions was usually higher than the local plasma density. Even with this higher density, the plasma still eroded through the neutral gas. The next test was to increase the neutral gas density. The concern with increasing the neutral gas density is twofold. The first concern is that one could gain more thrust from the neutral fluid than from the plasma fluid. When this condition is met, the benefit of having the plasma component is lost. One might as well just use the neutral gas jet for the propulsion device and have a less complex system. The second concern is the impact that the increased neutral gas density will have on the overall specific impulse of the device. Remember that the specific impulse of the device is the mass averaged velocity of the entire flow field, both the neutral fluid and plasma fluid. The neutral fluid specific impulse is low, so increasing the neutral gas density would increase its contribution to the specific impulse integral, lowering the overall specific impulse of the device. This case is presented to determine whether one can influence the plasma in the manner desired rather than to suggest an actual operating condition.

The input parameters are shown in Table 3.4. In the first three rows note the increase in neutral mass flow rate, thrust, and input power proportional to the increase in neutral gas density. The specific impulse of the neutral fluid has remained unchanged

Item	Ions	Neutrals
mass flow rate (\dot{m}), kg/sec	$2.87e - 04$	$3.86e - 04$
Thrust, Newtons	32.47	6.0
Power, MWatts	1.83	0.046
Temperature, eV	100.0	0.025
Density, part/cm ³	$1.0e+15$	$1.0e+16$
Velocity, cm/sec	$1.13e+07$	$1.5e+06$
I_{sp} , sec	11,500	1,600
I_{sp} net, sec	5,832	

Table 3.4: Input parameters for neutral gas density ten times that of the peak plasma density.

because only the neutral gas density was changed. The neutral gas velocity was held constant. The effect on the overall specific impulse is considerable, as seen in the last row. The overall specific impulse is reduced almost by a factor of two.

The results will be compared against the case with the even injection of neutral gas. The even injection case will be on the left and the high density case will be on the right.

The first time step that will be presented is at two microseconds. No interactions have occurred at the one microsecond time step so those figures are skipped.

The first figure, Figure 3.42, is the plasma density at two microseconds. A slight difference can be seen in the expansion of the plasma fluid through the neutral gas. The increased neutral gas density has slowed the plasma expansion.

The next figure, Figure 3.43, shows the density profiles and reaction rates at two microseconds. From these plots it can be seen that the neutral gas density has not been eroded away in this case as much as in the even injection case. The maintaining of neutral gas density at this radius has, as a consequence, the effect of holding back the plasma fluid. This can be seen by noting that the plasma fluid has not crossed this plain as much as compared to the even injection case (note the increased length of the plasma profile in the even injection case). The increased length at this radius indicates that more of the plasma fluid has expanded past this radius in the even injection case.

The next two plots are the reaction rate plots. They show that the charge-exchange reaction dominates over ionization events. Moreover, ionization events are almost non-existent.

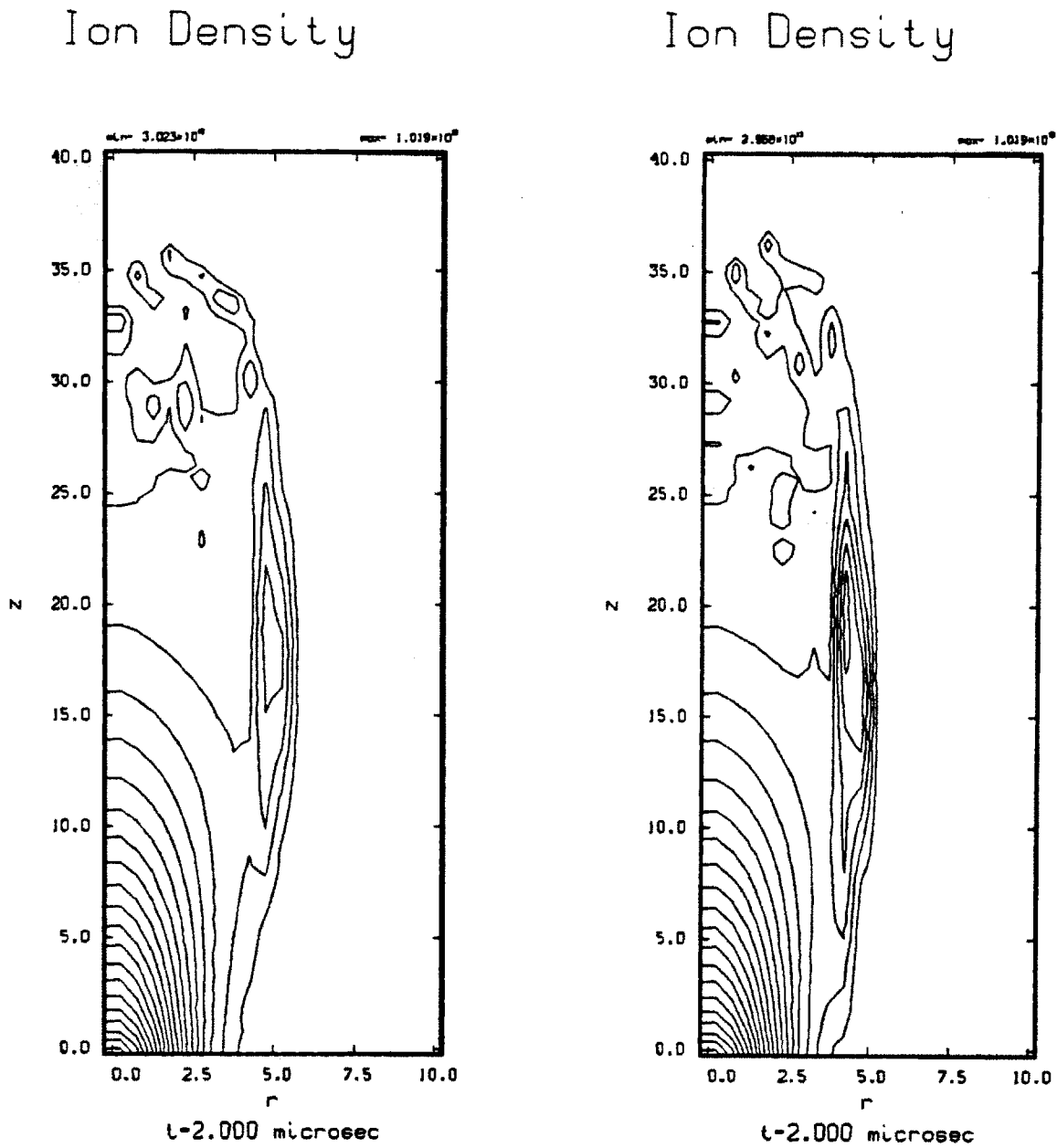


Figure 3.42: Comparison of plasma density at two microseconds. Even injection case on the left, ten times neutral injection on the right.

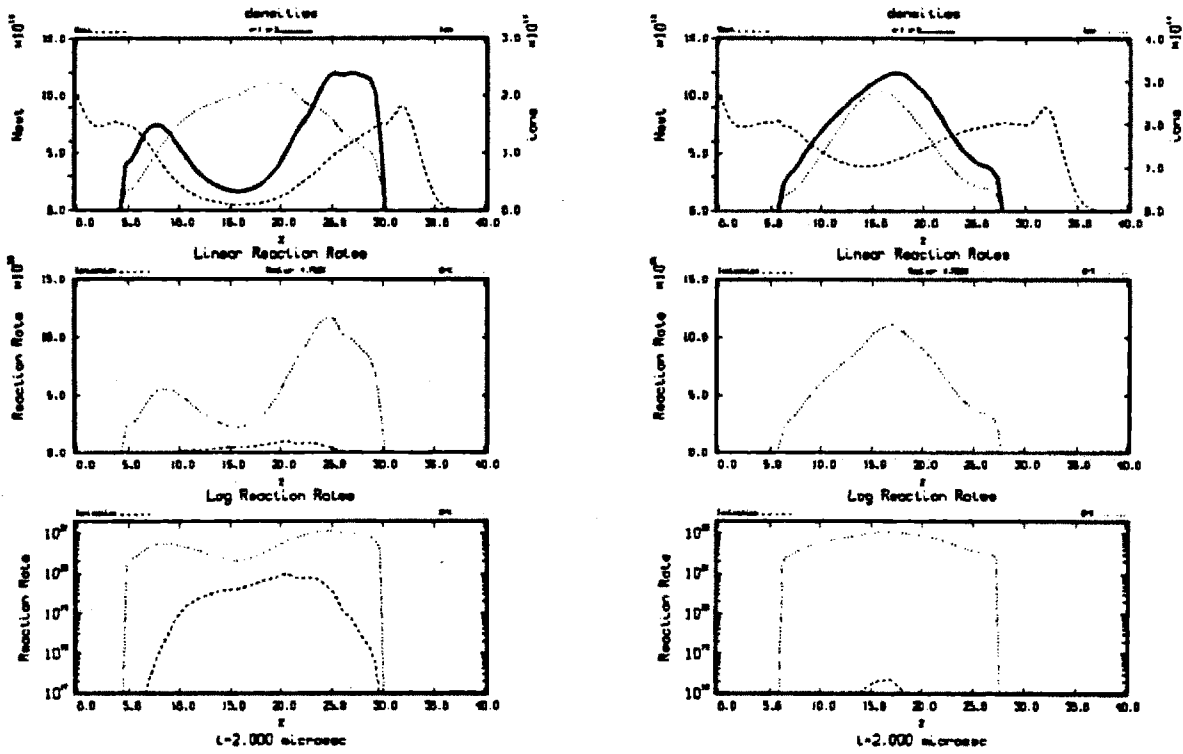


Figure 3.43: Comparison of reaction rate plots at two microseconds. Even injection case on the left, ten times neutral injection on the right.

The next figure, Figure 3.44, shows the coupling information at two microseconds. The momentum ratio, seen in the top plot, is increased as compared to the even injection case, but not enough to be significant.

The second plot shows the coupling coefficient for this time step. The coupling coefficient is greatly increased for the ten times neutral gas injection. One would like to have large coupling coefficients because they are an indication of the relative time scale of convection through the cell compared to momentum adding events. At this time step one sees that the coupling is indeed greater than one, indicating that there should be sufficient time for momentum adding events to take place. Unfortunately from the top plot one sees that the amount of momentum being coupled to the plasma by these events is small as compared to the overall plasma momentum. This long interaction time is an indication that the plasma fluid is moving slower in the ten times neutral gas injection case as compared to the even injection case. This means the neutral gas is slowing the radial expansion of the plasma fluid. It is also an indication that the neutral gas is slowing the plasma in general (in the axial direction as well). This is not necessarily advantageous because it is the axial momentum that gives us the thrust we desire.

The final plot shows the magnetic coupling. The magnetic Reynolds number is very small for the ten times neutral injection case. This is an indication that the local plasma temperature is very low. This explains why the ionization reaction on the previous plot was low. The magnetic interaction parameter is still much greater than one. This implies that the magnetic field dominates the interactions.

At this time step I will also present the plasma temperature, show in Figure 3.45. This confirms the prediction from the low ionization rate that the local plasma temperature was low. As can be seen from the figure, the plasma temperature drops sharply in radius near the neutral gas jet, and is very low down stream of the injection. The cooling of the plasma in the region of interaction with the neutral gas flow is characteristic of all the cases presented in this section. The dropping of the plasma temperature decreases the interaction potential between the two fluids, and limits the effect the neutral gas can have on the plasma. It is almost self-limiting, in the sense that an increase in the reaction rate between the two fluids leads to the decrease in the temperature of the plasma, which then decreases the interactions between the fluids. Since one would like large interactions with a hot plasma, this feed back is unfortunate.

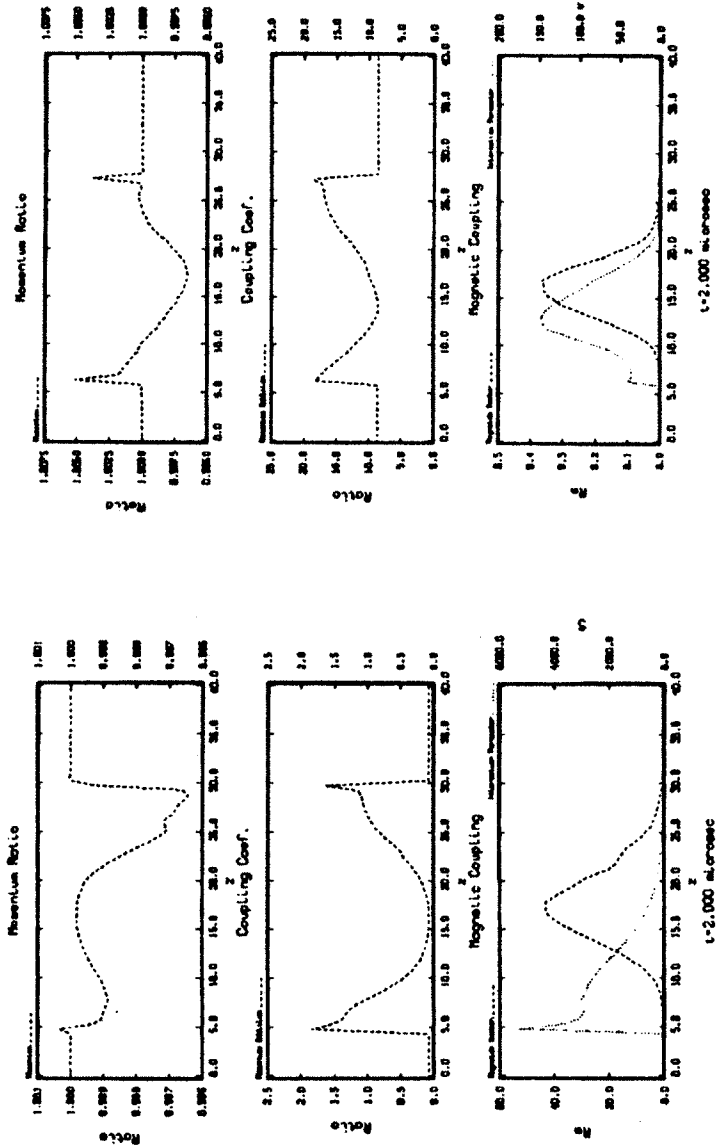


Figure 3.44: Comparison of coupling coefficients at two microseconds. Even injection

Ion Temperature

Ion Temperature

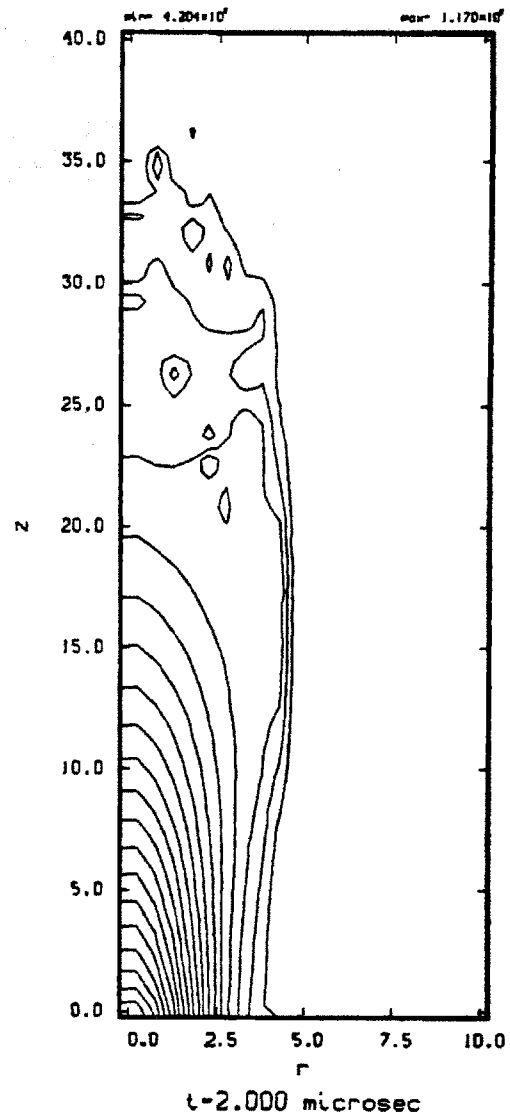
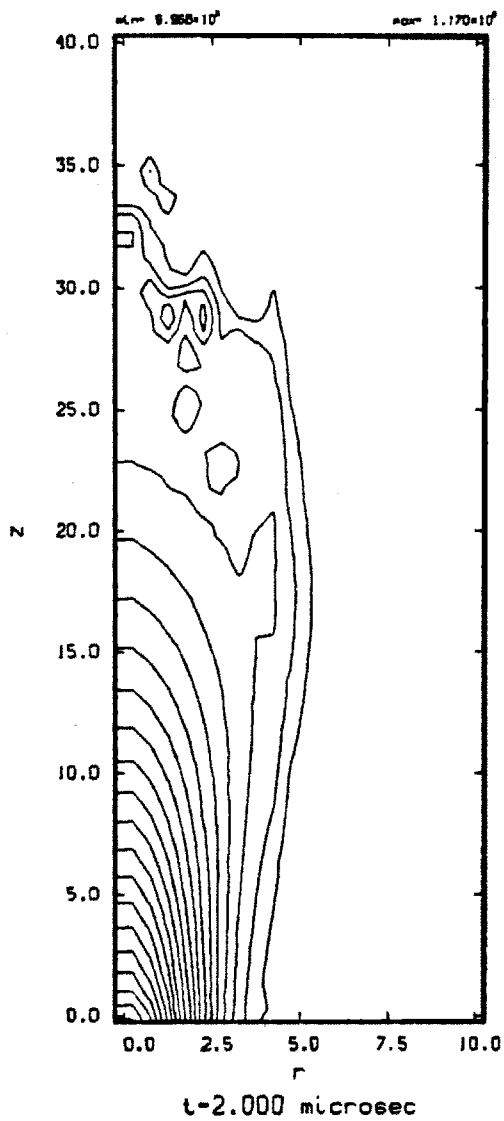


Figure 3.45: Comparison of plasma temperature at two microseconds. Even injection case on the left, ten times neutral injection on the right.

The next figure, Figure 3.46, compares the neutral gas densities at two microseconds. It can be seen that in the higher neutral gas injection case the neutral gas is much more robust.

Advancing to three microseconds a dramatic difference between the two cases appears. Figure 3.47 shows the plasma density. Here it can be seen that the neutral gas is still confining the plasma flow to a channel inside of the neutral gas injection. In the even injection case the plasma has expanded past the radius of neutral gas injection and is heading toward the wall. In the ten times neutral gas injection case the plasma is significantly peaked downstream of the gas injection indicating that there is still significant interactions between the plasma and the neutral gas jet in this region.

The next figure, Figure 3.48, shows the density profiles and reaction rate plots at three microseconds. The neutral density profile in the top plot for the ten times neutral gas injection case looks similar to the even gas injection case. Both profiles show the neutral gas being eroded away in the middle of the plot, and the characteristic neutral gas bump near z_{max} . It must be remembered that the scale for the ten times injection case is ten times that of the even injection case. So in regions where there is still neutral gas present there can be interactions on the same order as when the even gas injection case just started to interact. This is seen in the second plot for the reaction rates.

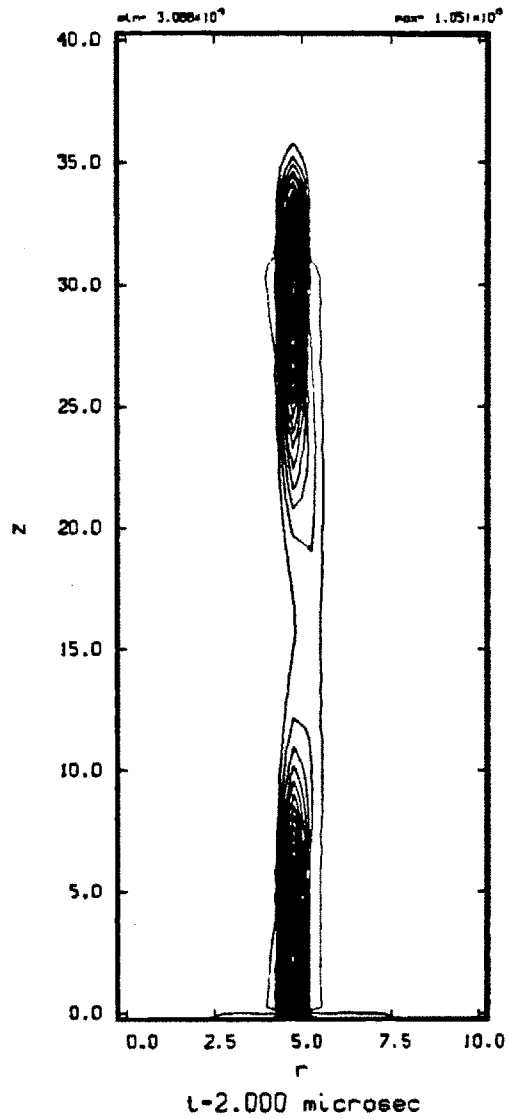
The reaction rate plot shows that the charge-exchange reaction still is the dominate interaction. It is an order of magnitude greater than for the even injection case and is indeed on the same order of magnitude as that of the even injection case at two microseconds.

The next figure, Figure 3.49, is the comparison of the coupling coefficients at three microseconds. The top plot shows that the momentum ratio for the ten times neutral gas injection case is higher than for the even injection case, but not significant enough to make a difference.

The coupling coefficient in the second plot is again much greater than one for the ten times neutral injection case. This plot peaks in the same axial location that the momentum ratio plot (the top plot) peaked. This is a good indication that there is a strong interaction region in this location. However, looking at the final plot, the overall picture is not as encouraging as the first two graphs might suggest.

The final plot shows that the magnetic Reynolds number in this interaction region is vanishingly small. Combine this with the magnetic interaction parameter being

Neutral Density



Neutral Density

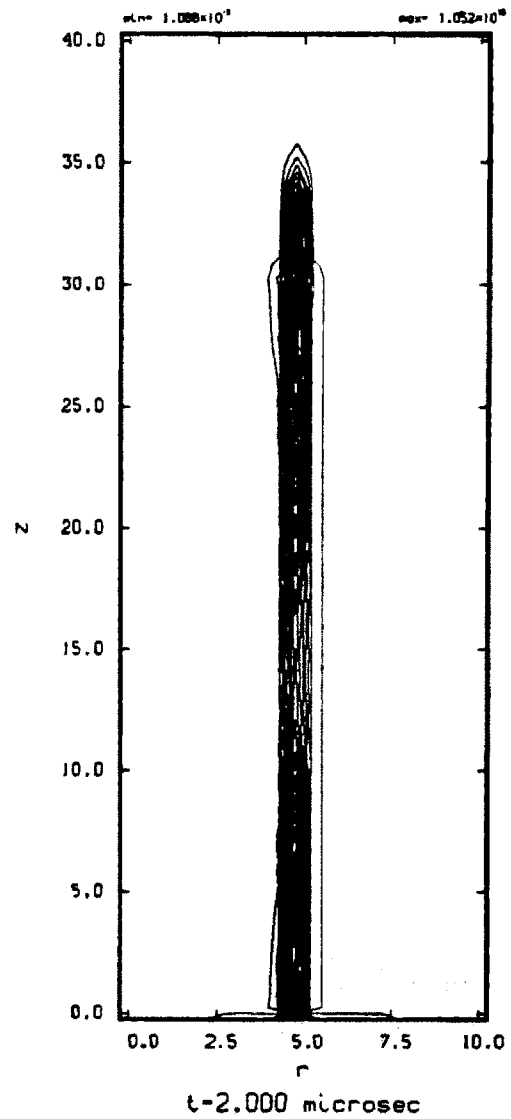
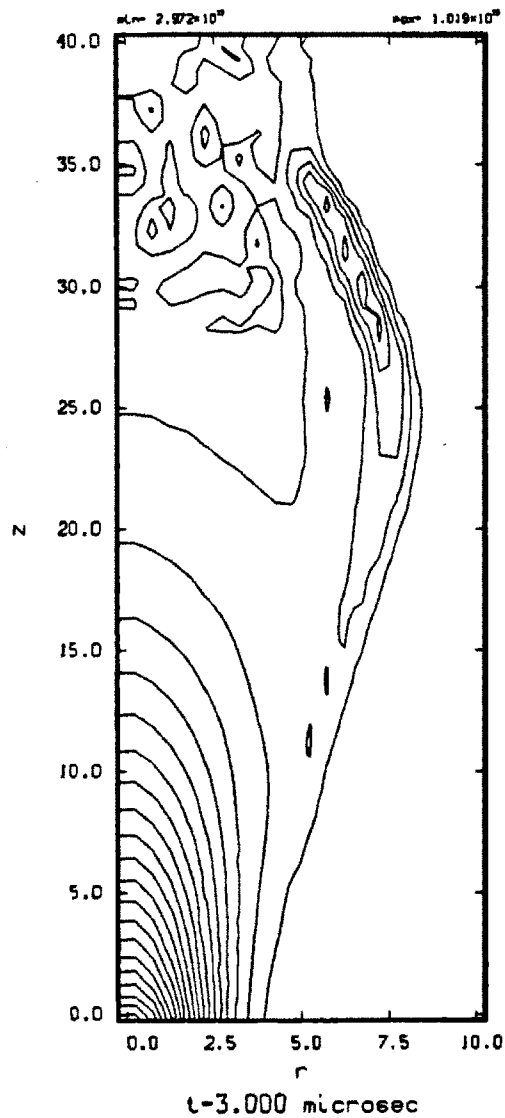


Figure 3.46: Comparison of neutral density at two microseconds. Even injection case on the left, ten times neutral injection on the right.

Ion Density



Ion Density

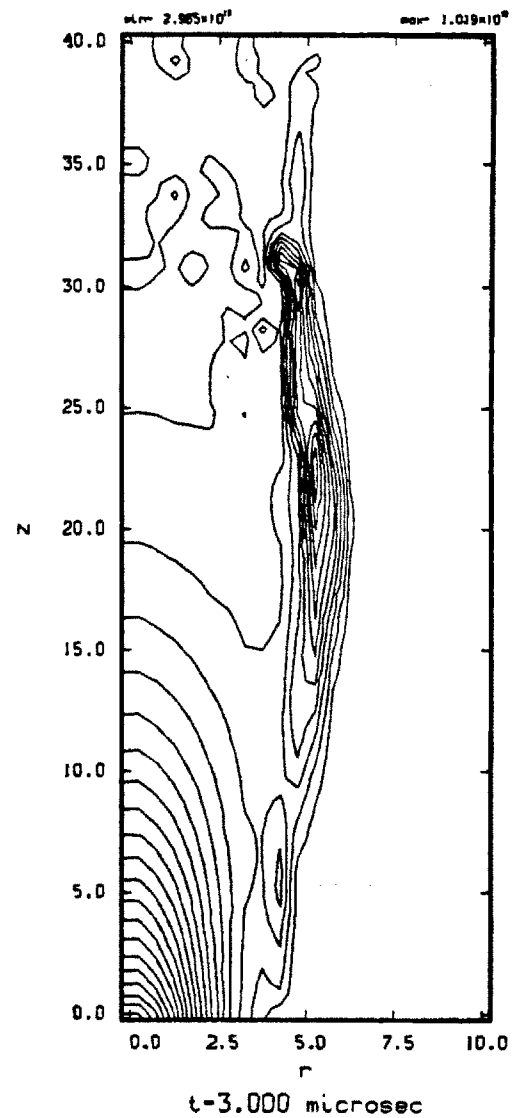


Figure 3.47: Comparison of plasma density at three microseconds. Even injection case on the left, ten times neutral injection on the right.

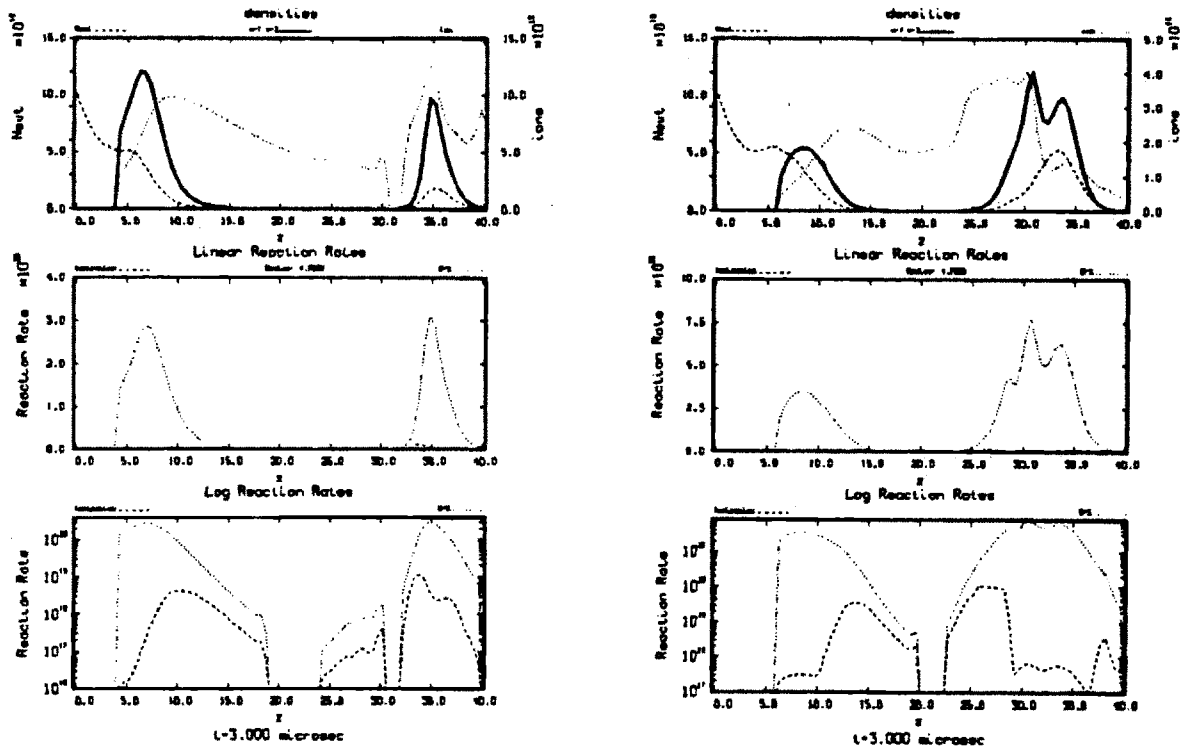


Figure 3.48: Comparison of reaction rate plots at three microseconds. Even injection case on the left, ten times neutral injection on the right.

large in this region and the story becomes clear. From the Reynolds number it can be determined that the plasma must be cold in this region. The cold plasma would be flowing slowly so the cell transient time would be large, thus accounting for the large coupling coefficients in this region. The large momentum ratio in this region can be understood by analyzing the density profiles of the previous figure. The plasma density in this region is very low. The neutral density is relatively large because it has not been eroded away by the plasma. Couple this to the fact that the plasma has a low flow velocity in this region and one comes to the conclusion that the plasma has a small momentum in this region. The neutral gas could then have a large momentum ratio, as seen in the top plot, but still not be very significant. This combined with a large magnetic interaction parameter in this region suggests that the overall effect on the plasma by the neutral gas in this region is unimportant. The coupling coefficients tend towards zero in the middle of the duct where the main plasma flow is found.

Moving on to four microseconds, Figure 3.50 shows the plasma density. For the ten times neutral gas injection case it can be seen that the neutral gas that has been added to the plasma flow downstream of the neutral gas injection has started to be convected radially outward along the field lines. This figure is the most compelling macroscopic argument that the neutral gas injection did not have a significant effect on the plasma flow. If this ionized and charge-exchanged increase in plasma density could have been able to continue to flow axially downstream, there could be optimism that this injection technique might bring about the results hoped for. Combine the plasma expansion with the fact that there is now no longer any neutral gas in the central region of the duct (as will be seen in the next figure), one can conclude that this injection method will not work.

The density profiles at four microseconds shown in Figure 3.51 show the erosion of the neutral gas in the central region of the duct. This is similar to the erosion in the even injection case. The interactions in this region are rapidly going towards zero as can be seen in the reaction rate plots.

The plasma velocity plots are shown in Figure 3.52 for four microseconds. The plots confirm that the plasma is flowing along the field lines in the ten times neutral gas injection case as was the result in the even injection case. The even injection case is seen to have expanded a bit further in radius than for the ten times injection case, but this can be considered simply as a transient phase. Because there is no longer any

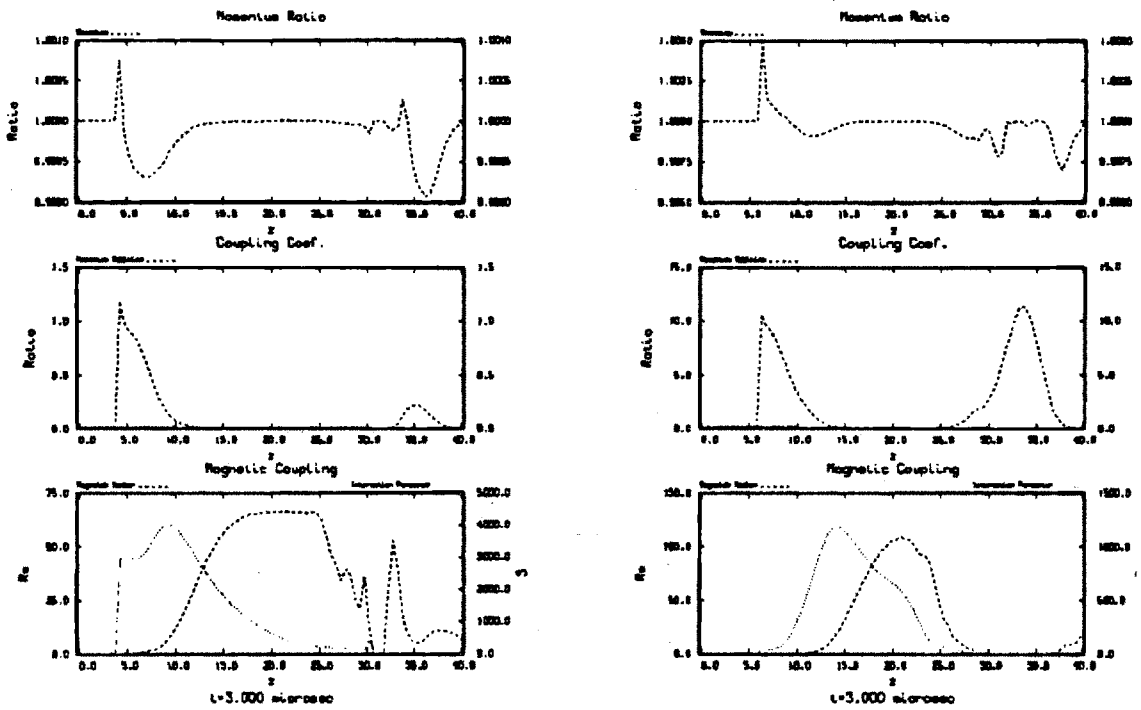


Figure 3.49: Comparison of coupling coefficients at three microseconds. Even injection case on the left, ten times neutral injection on the right.

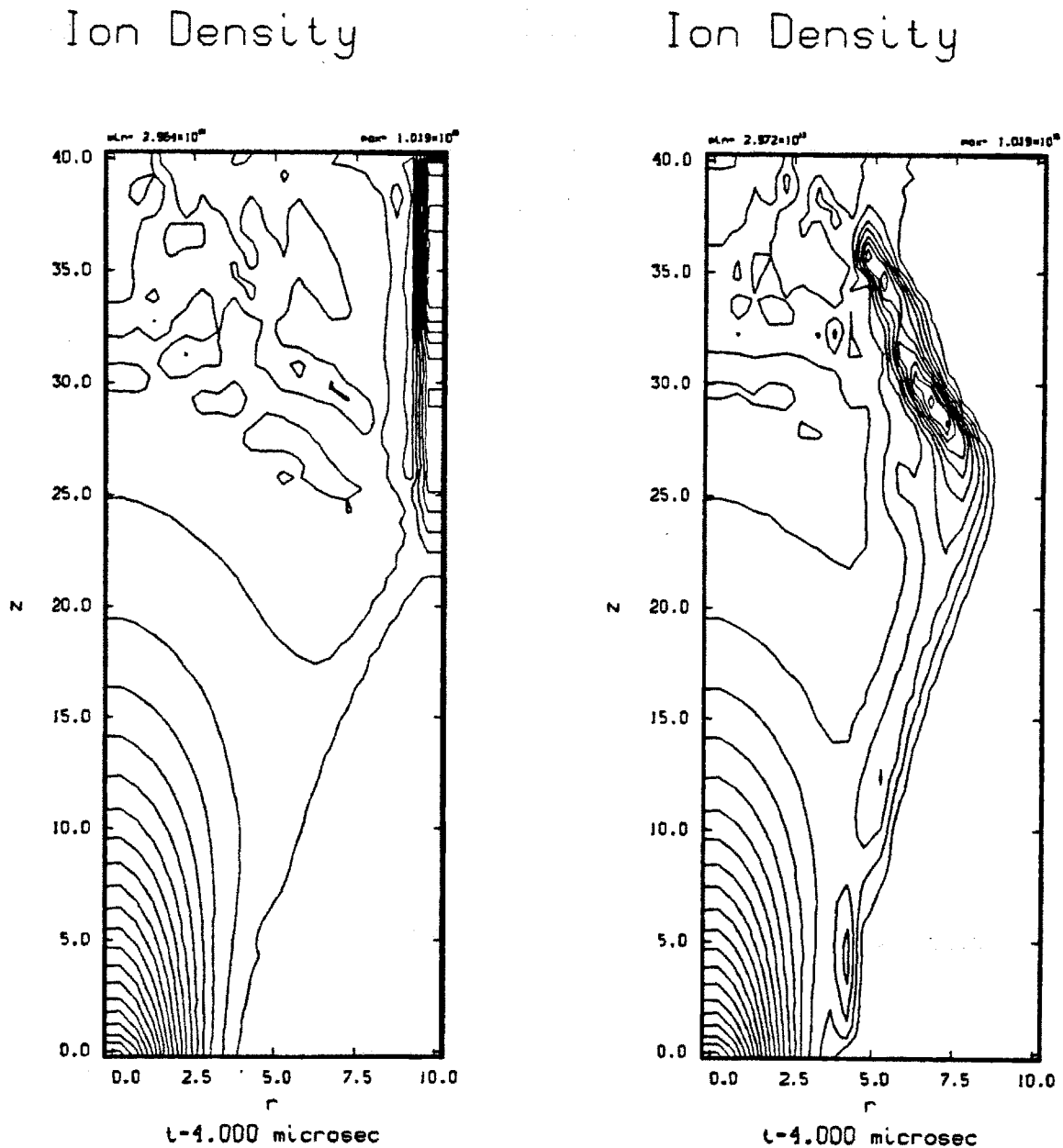


Figure 3.50: Comparison of plasma density at four microseconds. Even injection case on the left, ten times neutral injection on the right.

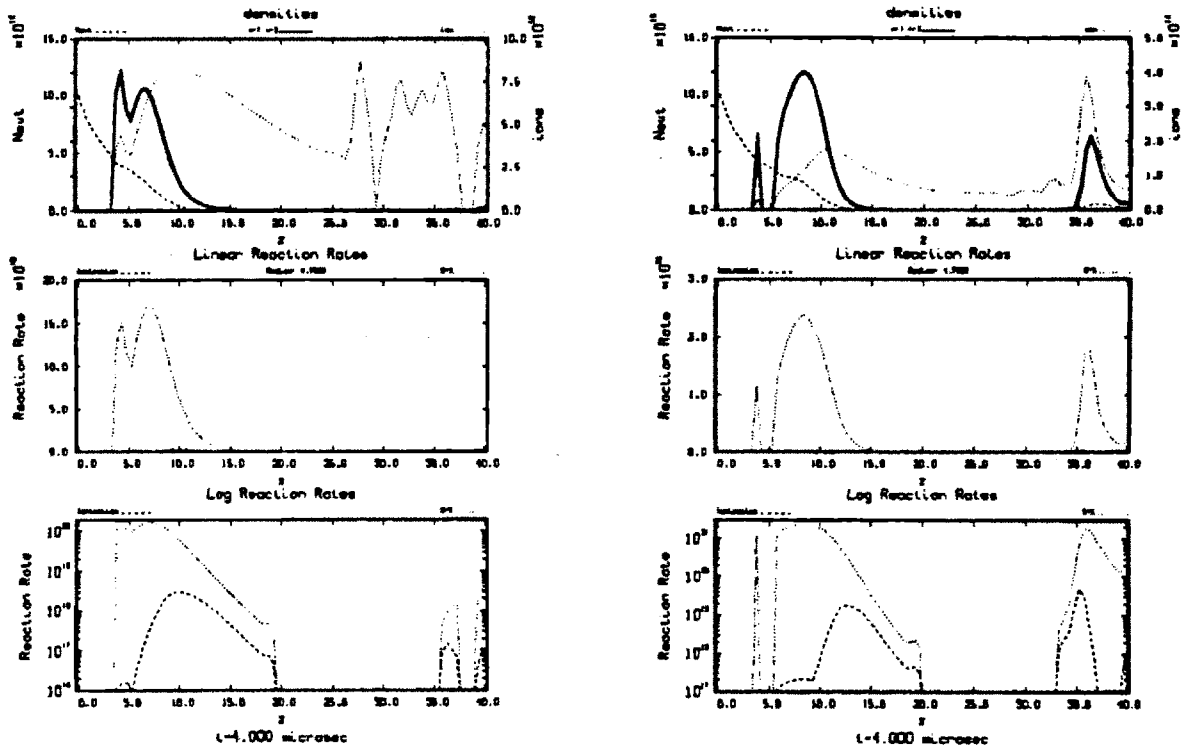


Figure 3.51: Comparison of reaction rate plots at four microseconds. Even injection case on the left, ten times neutral injection on the right.

neutral gas in the central duct to affect the plasma flow, the time independent state would be one in which the plasma is flowing unimpeded along the field lines for both injection methods.

This can be seen most obviously in the final figure for this case, Figure 3.53, comparing the neutral gas densities at four microseconds. Though the scales are different on the two plots, qualitatively they exhibit the same behavior. The neutral gas flow that remains after the plasma has eroded away the central region is almost identical in shape for both the injection methods.

It can be concluded that injecting the neutral gas at a density ten times that of the central plasma region does not have a significantly different effect on the plasma flow than for even injection of neutral gas in this parameter regime. The details of the transient stage before a steady state is obtained are different between the two cases, but not in a significant nature. In both cases the neutral gas in the central region of the duct is eroded away by the interactions with the plasma. After this start-up phase, the neutral gas density does not recover in this central region and the plasma flows unimpeded along the field lines, indicating that neither method would bring about the formation of the hybrid plume needed to make the plasma thruster operable.

3.3.5 Equal plasma and neutral gas momentum.

As observed in the ten times neutral gas injection case, even though the neutral gas density is significantly greater than the plasma density, it still does not have a significant effect on the plasma flow. The prestreamed neutral gas is eroded by the plasma and when this process is complete, the plasma then is free to expand radially along the magnetic field. This initial erosion of the neutral gas by the plasma is a start-up transient in the system. If one compares the average fluid velocities for the plasma and the neutral gas, it is found that the plasma velocity is about an order of magnitude greater than for the neutral gas. This is for a cold neutral gas ($.025eV$) injected at a Mach number of seven.

It is hypothesized that the transient nature of the plasma neutral gas interactions can be accounted for by this velocity difference. The neutral gas is prestreamed in the duct to allow interactions to take place. Once the gas is eroded, it seems logical that if the axial flow speed of the neutral gas is significantly less than that for the plasma, the neutral gas does not have a chance to replenish the gas in the interaction region.

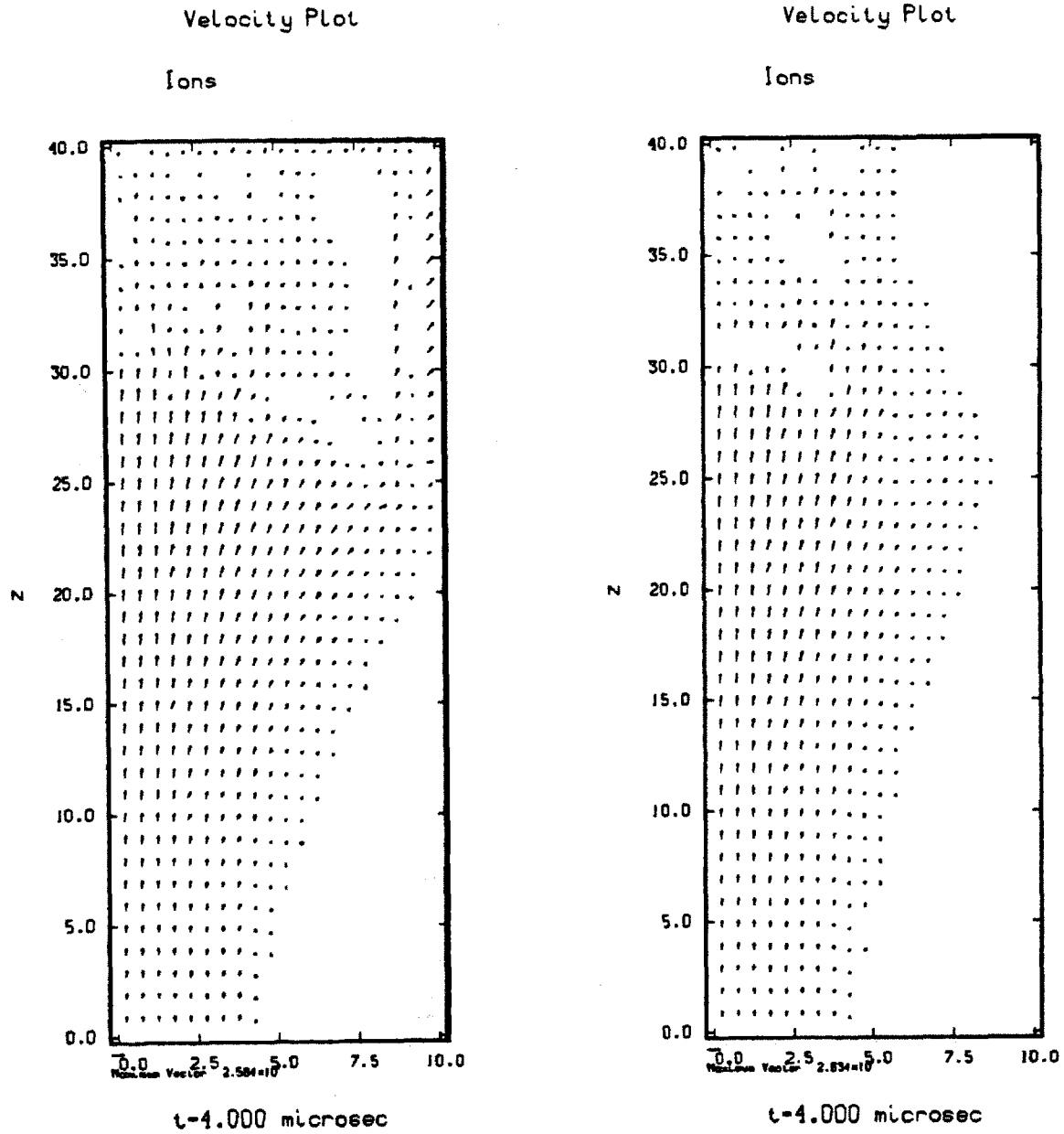
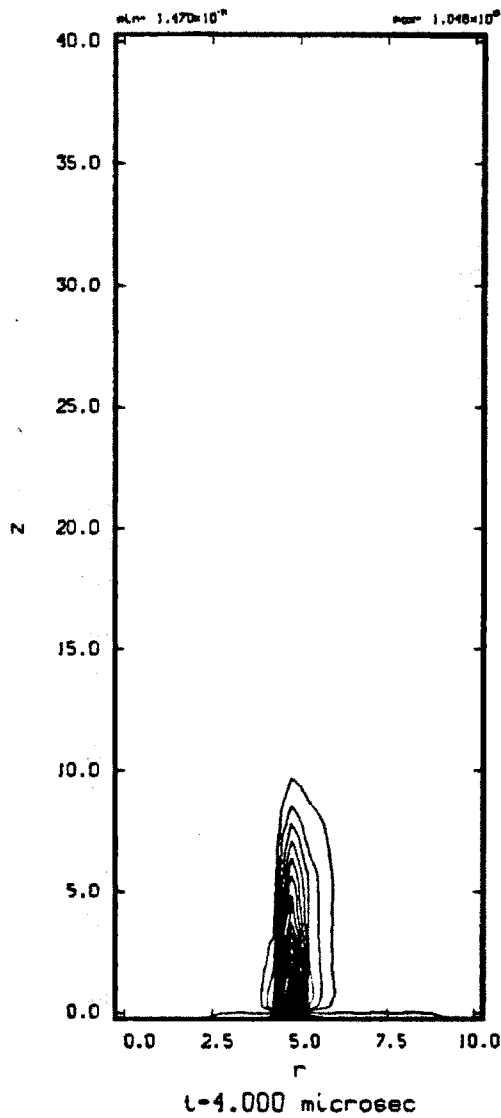


Figure 3.52: Comparison of plasma velocity plots at four microseconds. Even injection case on the left, ten times neutral injection on the right.

Neutral Density



Neutral Density

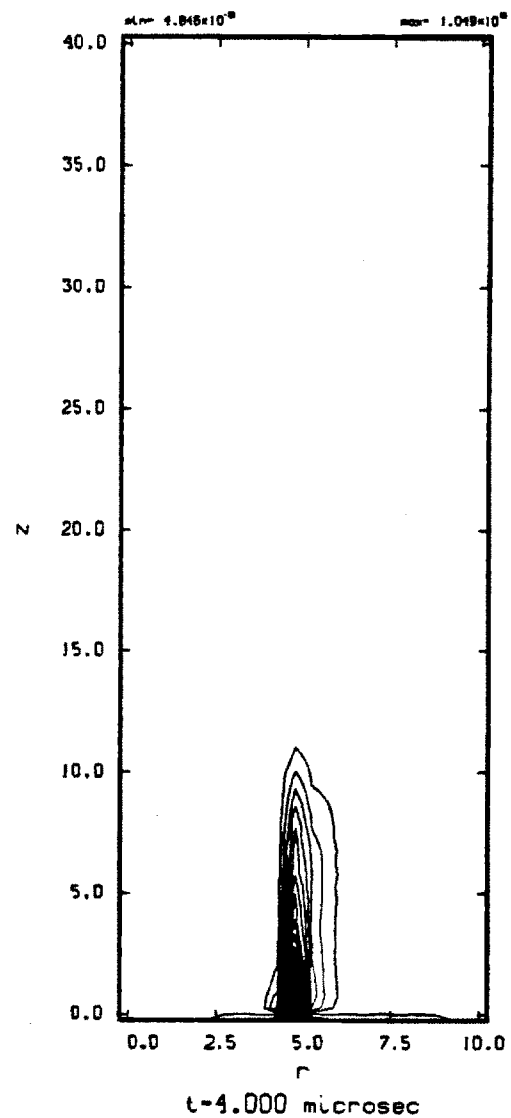


Figure 3.53: Comparison of neutral density at four microseconds. Even injection case on the left, ten times neutral injection on the right.

Item	Ions	Neutrals
mass flow rate (\dot{m}), kg/sec	2.87e - 04	2.81e - 04
Thrust, Newtons	32.47	31.93
Power, MWatts	1.83	1.83
Temperature, eV	100.0	0.025
Density, part/cm ³	1.0e+15	1.0e+15
Velocity, cm/sec	1.13e+07	1.14e+07
I_{sp} , sec	11,500	11,600
I_{sp} net, sec	11,558	

Table 3.5: Input parameters for neutral gas momentum equal to that of the plasma.

To test this hypothesis the neutral gas is injected with an axial velocity equal to that of the plasma axial velocity near $r = 0$, $z = 0$. This is accomplished by setting the neutral gas Mach number such that the velocities are equal at $z = 0$. For a peak plasma temperature of 100eV the corresponding neutral gas Mach number is approximately 51. No consideration is given to whether a neutral gas Mach number of 51 can be achieved. The Mach number is artificially set in the code; this is the wonder of numerics!

This case is titled *Equal Plasma and Neutral Gas Momentum*, but it should be noted that the axial neutral gas momentum in the interaction region can be very much greater than the axial momentum of the plasma in this location. This is because the equal momentum condition stems from the matching of momentum of the plasma at $r = 0$. At $r = 0$ the plasma has its peak density and greatest velocity. The interaction region forms with the radial expansion of the plasma into the location downstream of the neutral gas jet. The plasma density drops as it expands, and the velocity vector is redirected radially, so the local axial plasma momentum is reduced as compared to the peak plasma axial momentum.

The input parameters for this case are shown in Table 3.5. In the first three rows note the increase in neutral mass flow rate, thrust, and input power. All three parameters are nearly identical to the plasma parameters, as is expected. The specific impulse of the neutral fluid is now equal to that of the plasma fluid, so there is no overall degradation of the specific impulse of the device.

The results will be compared against the case with the even injection case. The even injection case will be on the left and the equal momentum case will be on the right.

The first time step that will be presented is at two microseconds. No interactions have occurred at the one microsecond time step so those figures are skipped.

The first figure, Figure 3.54, is the plasma density at two microseconds. The interaction region does not seem to be as peaked as compared to the even injection case. The plasma has also expanded a bit further in radius. It seems that the equal momentum case does not slow the radial expansion of the plasma as much as the even injection case does.

That the plasma has expanded further in the equal momentum case is peculiar because the radial component of the neutral gas as remained essentially constant in the two cases. Any radial flow in the neutral gas is from one of two sources: elastic collisions with the ions or radial pressure gradients in the neutral gas. The ion velocity is the same so this should not cause a difference. The neutral gas temperature is the same, as is the density, so the radial pressure gradients should also be approximately the same.

The answer lies in the detailed analysis of the start up phase of the interaction. The first results that are presented are at two microseconds. The interactions actually start at approximately 1.25 microseconds. Because of the matching axial velocities, the neutral gas does not impede the plasma flow in the z direction. The interactions do impede the flow in the radial direction, but the plasma does not build up as much due to the fact that the axial expansion is not slowed down. This increase in plasma density in the even injection case leads to a greater ∇p force acting in the negative r direction. This force opposes the radial expansion of the plasma. Because the flow behind this interaction region is not changed it continues to stream into this region at a constant rate. Meanwhile, the plasma in the interaction region is slowed radially, causing the plasma density to increase in this region. This is analogous to a flow impinging on a wall, where the wall in this case is the neutral gas.

This accumulation of plasma is a positive feedback mechanism which is mediated by other physical processes. For instance, the increased plasma density increases the ∇p force in the positive r direction on the outside of the plasma peak. This would tend to accelerate the plasma *away* from the interaction region and decrease the plasma density there. Another mechanism arises from the plasma neutral gas interaction. The plasma is eroding the neutral gas away which decreases the interaction rate. As the gas is removed, the source of the positive feedback is removed. Finally, as the interactions

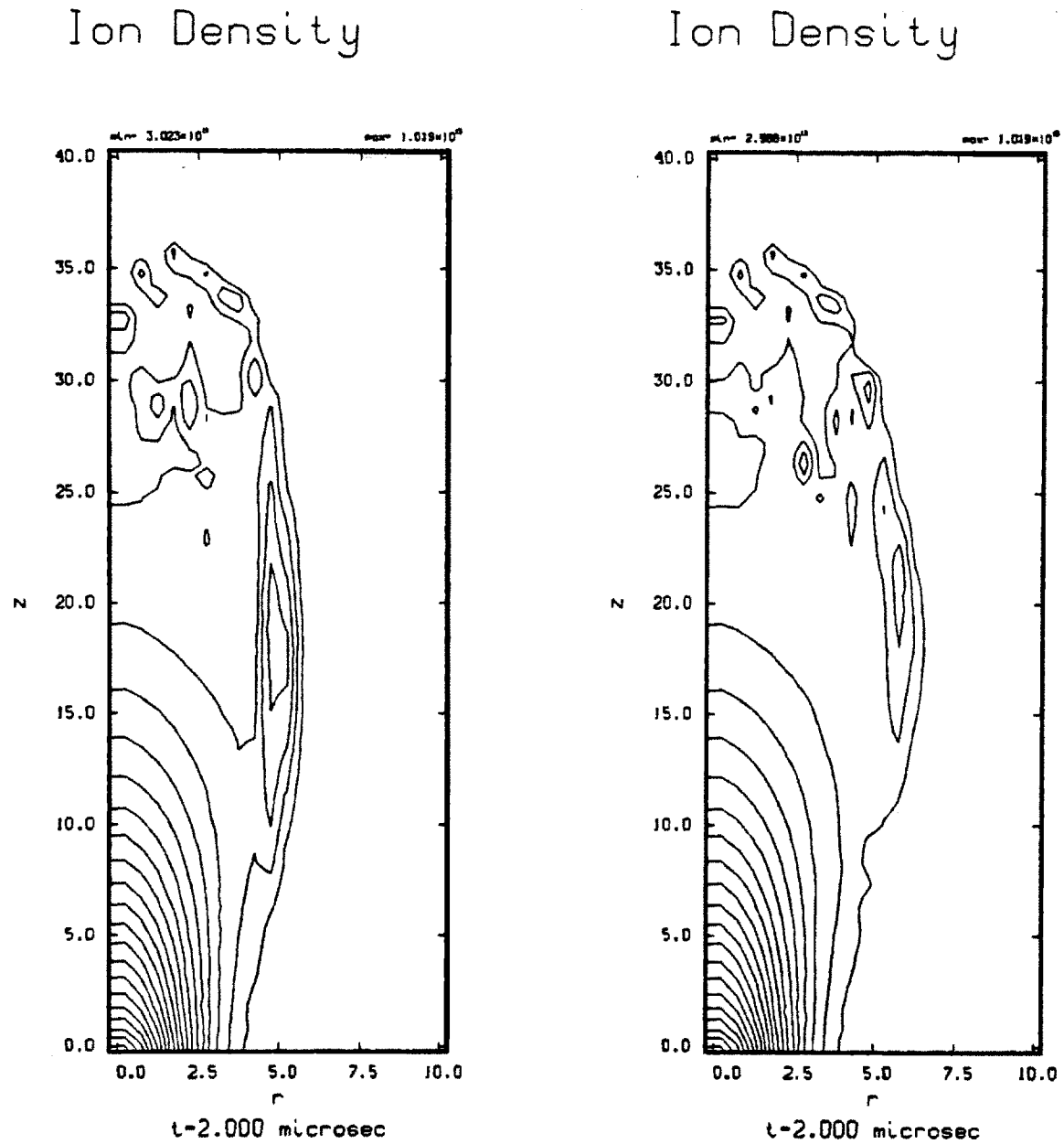


Figure 3.54: Comparison of plasma density at two microseconds. Even injection case on the left, even momentum case on the right.

take place, they locally cool the plasma which drops the interaction cross sections, reducing the interaction rate.

Through the detailed dynamics of the combination of the above processes, the plasma peak as seen in the even density injection case does not form in the even momentum injection case. The radial expansion of the plasma is still slowed down as compared to when the neutral gas is not present. This can be seen from the plasma density plot in Figure 3.3 on page 56.

The density profiles and reaction rate plots are shown in Figure 3.55. From the neutral gas density profile it can be seen that the increase in neutral gas jet velocity has indeed helped to resupply the area downstream of the injection with gas. As compared to the even density injection case (low velocity), the neutral gas density profile falls off smoothly. At approximately $z = 10\text{cm}$ the even momentum injection case neutral density has declined to $\sim 7.5e - 14$. The even density injection case (low velocity) has declined to $\sim 2.5e - 14$ at the same location. The significance of the numbers at $z = 10\text{cm}$ is not clear, since it seems that the neutral gas density profile has simply shifted downstream. The minimum neutral gas density in both cases approaches zero, indicating that the plasma is eroding away the neutral gas.

The neutral gas profile is flat near the exit, at $z = 40\text{cm}$. The neutral gas is now moving fast enough now to travel a significant distance on this time scale. With the low velocity neutral gas injection, the front of the neutral gas jet never really propagated downstream very far. This was due to the widely disparate time scales between the plasma and neutral gas fluids. Now the two time scales are nearly identical, and neutral gas propagation is seen. In fact, there was a numerical instability in the neutral flow that stopped the calculation before it reached the usual four microsecond stopping time. It usually has been the stability of the plasma outflow conditions that has lead to a cap on the simulation time.

The second and third plots of this figure show the reaction rates. Qualitatively they are similar indicating that there is the same order of reactions present in both cases.

The next figure, Figure 3.56, shows the coupling information at two microseconds. From the top plot, the momentum ratio plot, it can be seen that the momentum ratio is significantly greater in the even momentum injection case. It is greater than one nearly every where, indicating that the reactions with the neutral gas are not slowing the plasma down. The overall magnitude of the momentum coupling is still too small

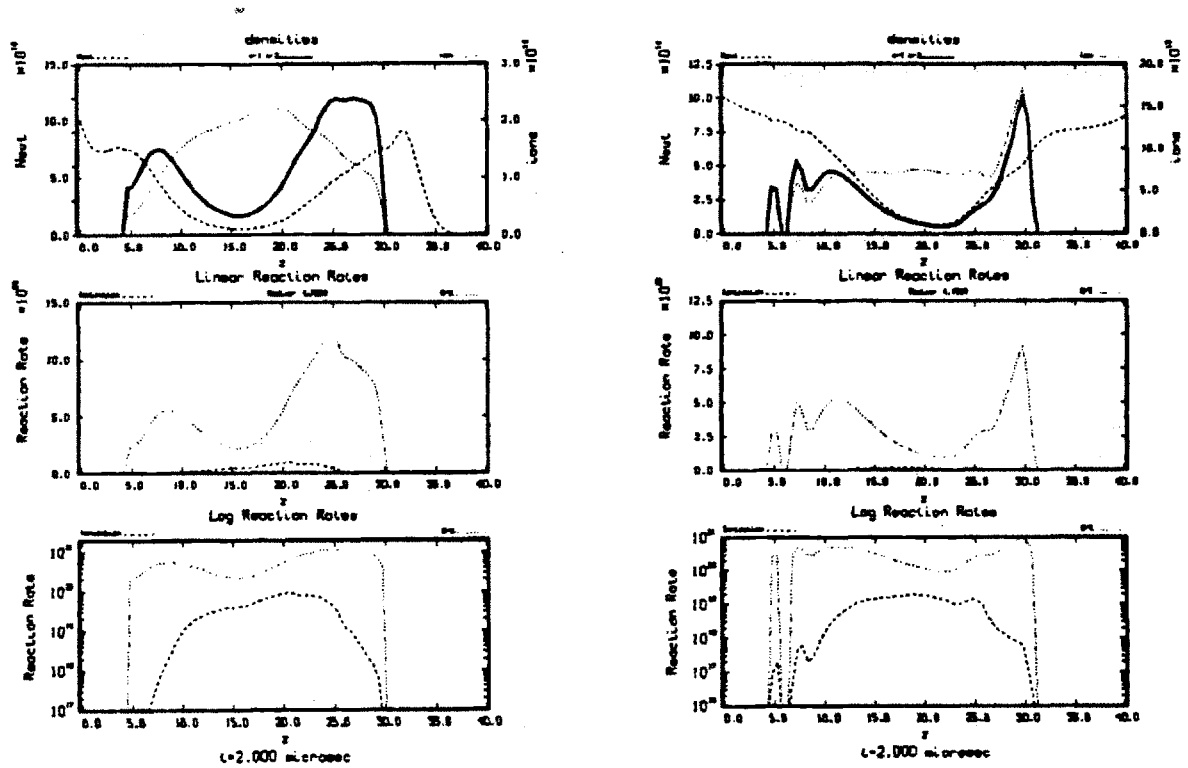


Figure 3.55: Comparison of reaction rate plots at two microseconds. Even injection case on the left, even momentum case on the right.

to be of any consequence.

The reason for the low momentum ratio even in the case with equal injection of momentum is obvious from the second plot, the coupling coefficients. The coupling coefficients are very much less than one nearly everywhere. So even though the neutral gas velocity is very large, the plasma transient time through the cell is still very much smaller than the characteristic time for momentum adding events.

The final plot in this figure shows that the magnetic interaction parameter is still very large, indicating that the magnetic field still dominates the flow. The neutral gas density at two microseconds is shown in Figure 3.57. It can be seen here that the front of the neutral gas jet has stream out of the computational domain. The erosion in the middle of the duct has moved downstream as compared to the even density injection case.

The final time step to be presented for the even momentum injection case will be three microseconds. This is because of the previously mentioned numerical instability. Only the contour plots for the plasma density and neutral density will be presented because they summarize the overall results.

Figure 3.58 shows the plasma density at three microseconds. The plasma density has expanded to the wall at r_{max} and is starting to build up. The plasma has actually expanded faster in the even momentum injection case than for the case with even density injection. The reasons for this were presented in the discussion of the plasma density at two microseconds (Figure 3.54).

The neutral gas density at three microseconds is presented in Figure 3.59. Here it can be seen that the neutral gas jet has managed to resupply itself a bit further down into the duct than compared to the even density (low velocity) injection case. The neutral gas still gets eroded away sufficiently downstream of the injection. The density contours at the outflow boundary at z_{max} are the beginning of the previously mentioned numerical instability. The plasma has barely reached this point so it is not clear whether the neutral gas at this location should actually be entirely eroded. Considering the direction the simulation has evolved to at this point, the reflection is of little consequence.

From these last two figures it is clear that the even injection of momentum in the neutral gas fluid will not bring about the creation of the hybrid plume. The interactions are such that the even with sufficient momentum to affect the plasma

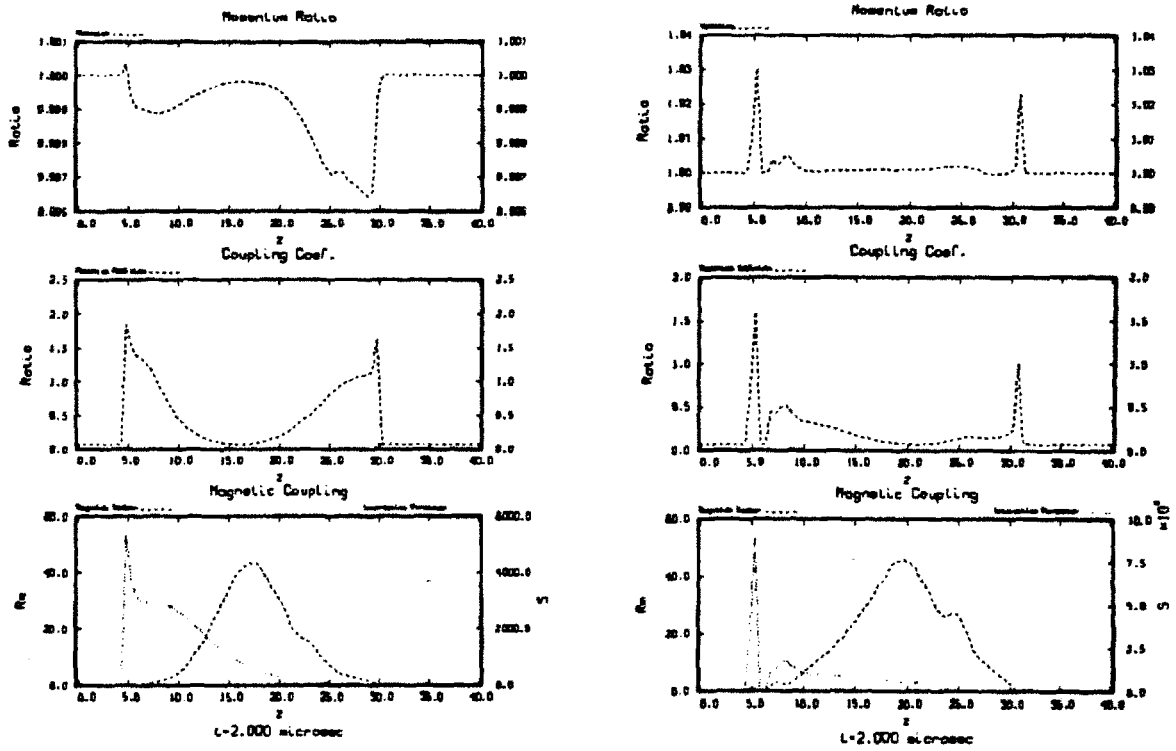


Figure 3.56: Comparison of coupling coefficients at two microseconds. Even injection case on the left, even momentum case on the right.

Neut Temperature

Neut Temperature

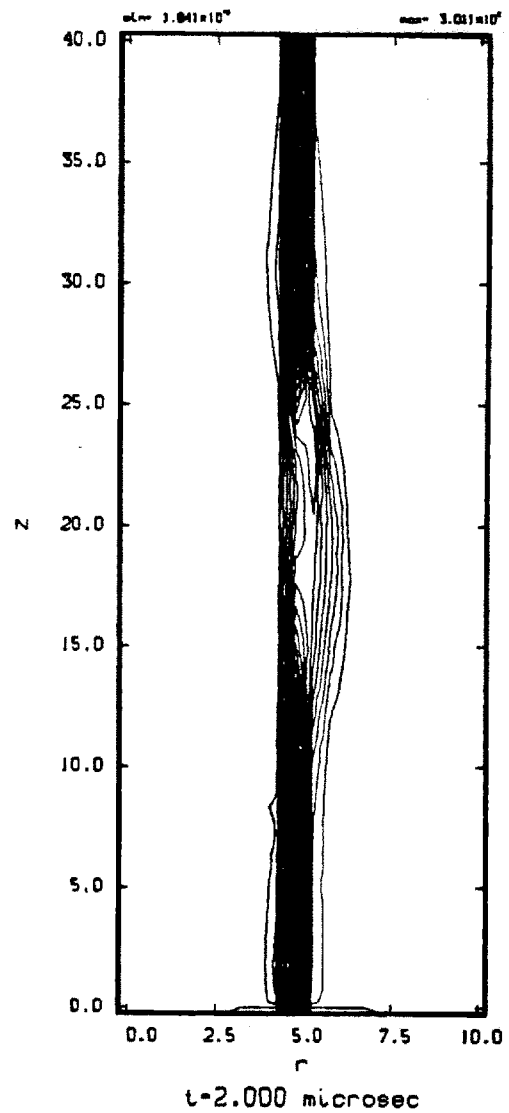
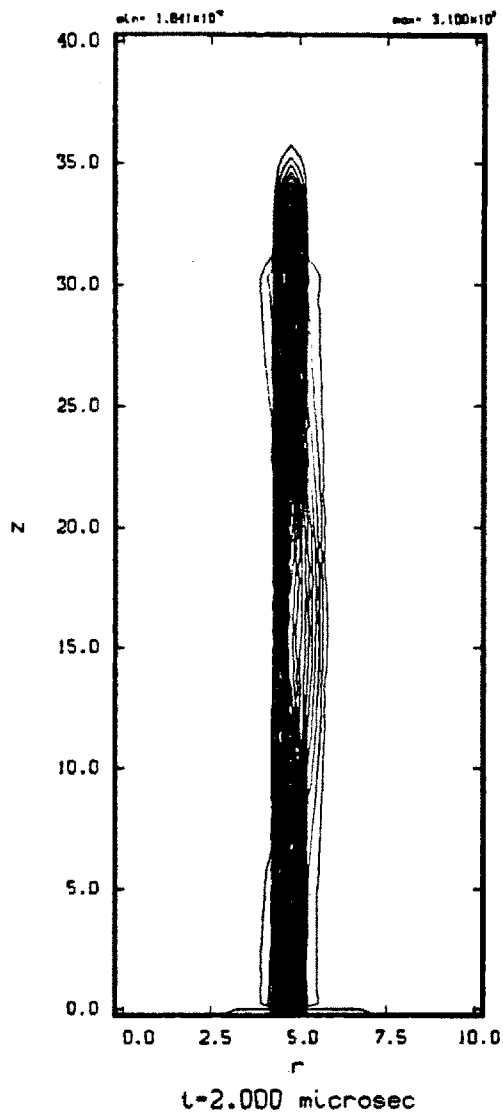


Figure 3.57: Comparison of neutral density at two microseconds. Even injection case on the left, even momentum case on the right.

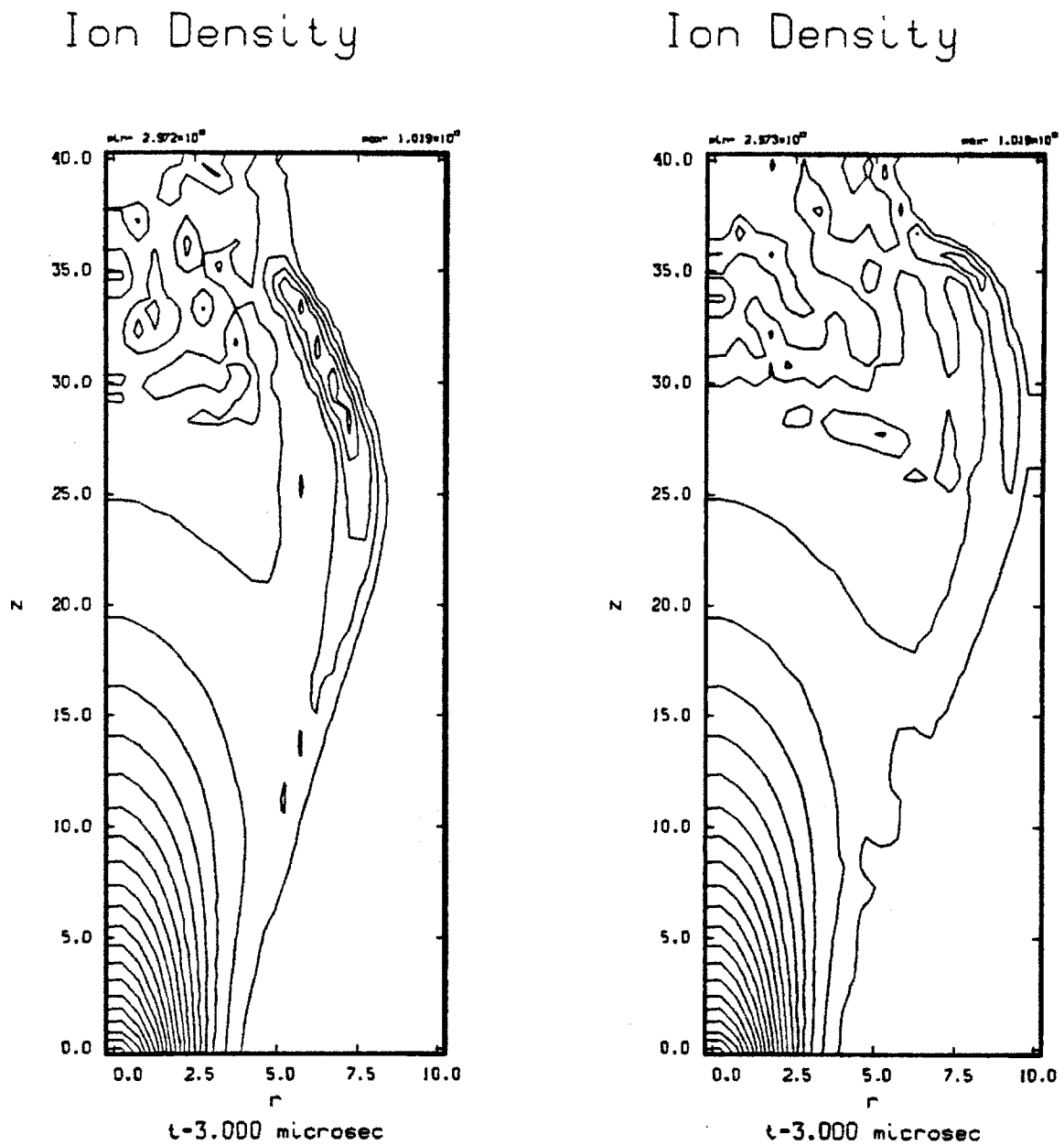
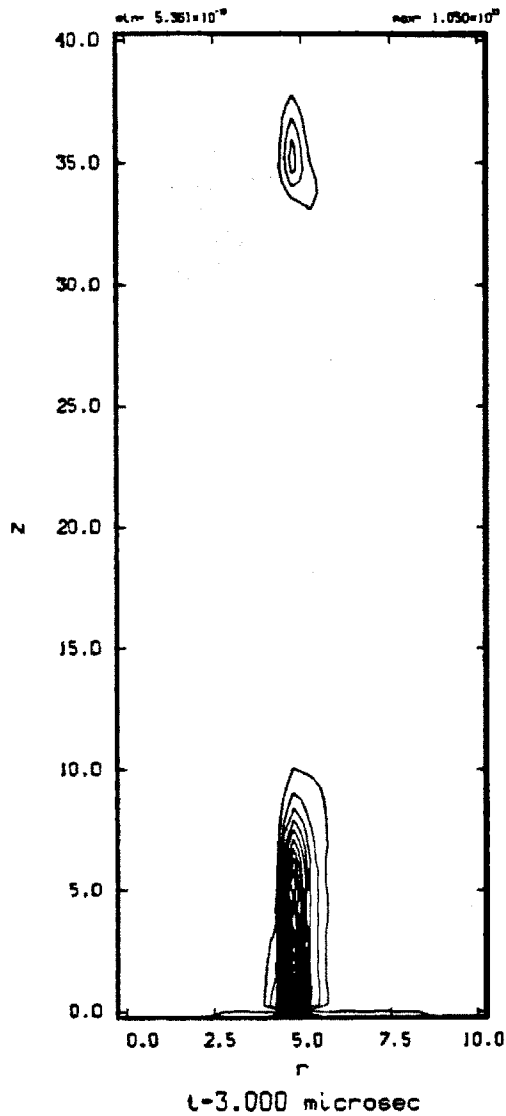


Figure 3.58: Comparison of plasma density at three microseconds. Even injection case on the left, even momentum case on the right.

Neutral Density



Neutral Density

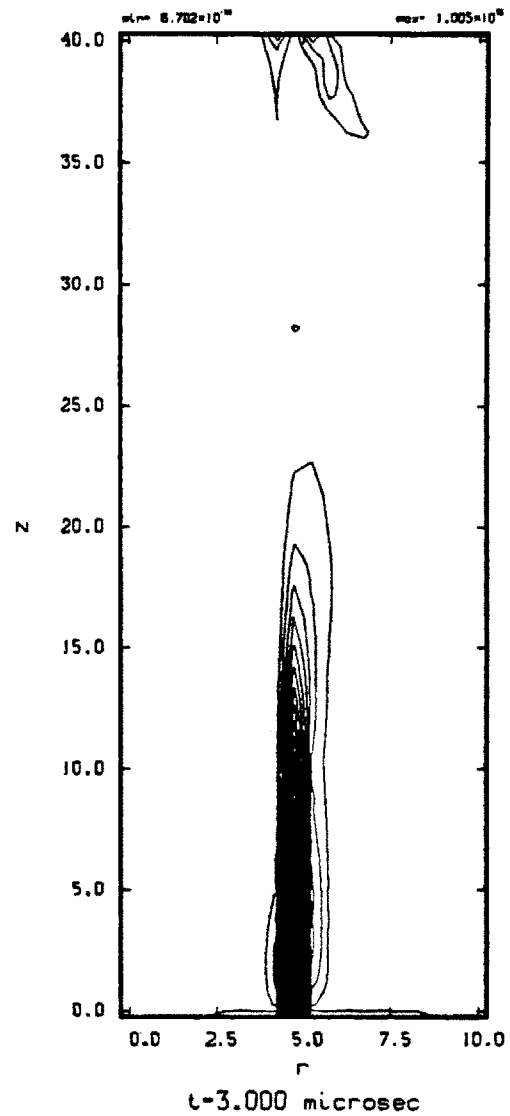


Figure 3.59: Comparison of neutral density at three microseconds. Even injection case on the left, even momentum case on the right.

flow and fast enough neutral flow to replenish the neutral gas in the duct, the actual coupling between the fluids remain small.

3.3.6 Gas density one hundred times the plasma density.

The next case that will be presented is the injection of neutral gas at one hundred times the peak plasma density. This is a continuation of the attempt to see if an increase in neutral gas density will be enough to cause the neutral gas jet to affect the plasma flow. The first attempt at this was the previous results at a neutral gas density of ten times the plasma peak density (see section 3.3.4). As one saw with those results, the increase in neutral gas density did little more than to cool the plasma, which caused the plasma to have even less of an effect on the magnetic field. This case will be the final attempt to determine if an increase in neutral gas density is expected to have a significant effect on the plasma dynamics.

The concerns that were discussed in the section for ten times neutral gas injection (see page 112), are even of more concern in this case. The concerns were that the thrust component from the neutral gas would negate the need to have the plasma. Also, the overall specific impulse of the device would decrease with the increased contribution from the slow neutral component. As mentioned in that section, these cases are presented to suggest actual operating conditions for the hybrid plume, but to gain insight in the the dynamics involved in the interactions between the plasma and neutral gas jet.

The input parameters are shown in Table 3.6 The thrust provided by the neutral gas is twice that of the plasma thrust. The input power is still reasonable because the plasma is cold and relatively low velocity. The low velocity of the neutral gas jet is reflected in the low specific impulse of the neutral component. The overall specific impulse for the device is not even a factor of two greater than the neutral specific impulse alone. This indicates that most of the mass flow is in the slow fluid. In fact, the mass flow rate for the neutral gas is an order of magnitude greater than that of the plasma. Clearly this would not be a configuration viable for the hybrid plume.

The results will be compared against the case with even injection of neutral gas. The even injection case will be on the left and the super high density case will be on the right.

The first time step that will be presented is at two microseconds. No interactions

Item	Ions	Neutrals
mass flow rate (\dot{m}), kg/sec	2.87e - 04	3.86e - 03
Thrust, Newtons	32.47	60.16
Power, MWatts	1.83	0.47
Temperature, eV	100.0	0.025
Density, part/cm ³	1.0e+15	1.0e+17
Velocity, cm/sec	1.13e+07	1.56e+06
I_{sp} , sec	11,500	1,590
I_{sp} net, sec	2,279	

Table 3.6: Input parameters for neutral gas density one hundred times that of the peak plasma density.

have occurred at the one microsecond time step so those figures are skipped.

The first figure, Figure 3.60, is the plasma density at two microseconds. There is a significant build up of plasma density as the plasma intersects the neutral gas jet. The build up is extremely rapid.

As seen in the reaction rate plots in Figure 3.61 for two microseconds, only a thin slice of plasma has actually expanded across the plain of the neutral jet. Very little, if any, erosion of the neutral gas jet has taken place. The reaction plots show that the charge-exchange reaction rate is two orders of magnitude greater in the one hundred times neutral gas injection case than for the even gas injection case. This is consistent with the reaction rate scaling as $n_1 n_2$ and the cross section for charge exchange being fairly constant with temperature. The ionization reaction rate is four orders of magnitude less than the charge exchange reaction rate indicating that the plasma temperature must be extremely cold. Even with a two order of magnitude increase in density the reaction rate for ionization has fallen by a least two orders of magnitude as compared to the even injection case. This indicates a strong temperature dependence of the ionization cross section on temperature.

The coupling coefficient information is presented in Figure 3.62. From the top plot one sees a strong coupling of neutral momentum to the plasma. The neutral gas is adding on the order of 15% of the plasma axial momentum to the plasma fluid. It is highly localized but it is hoped that this is just the beginning of the interaction and that this interaction may grow as the system evolves.

The coupling coefficient in the second plot shows a very large ratio of the cell

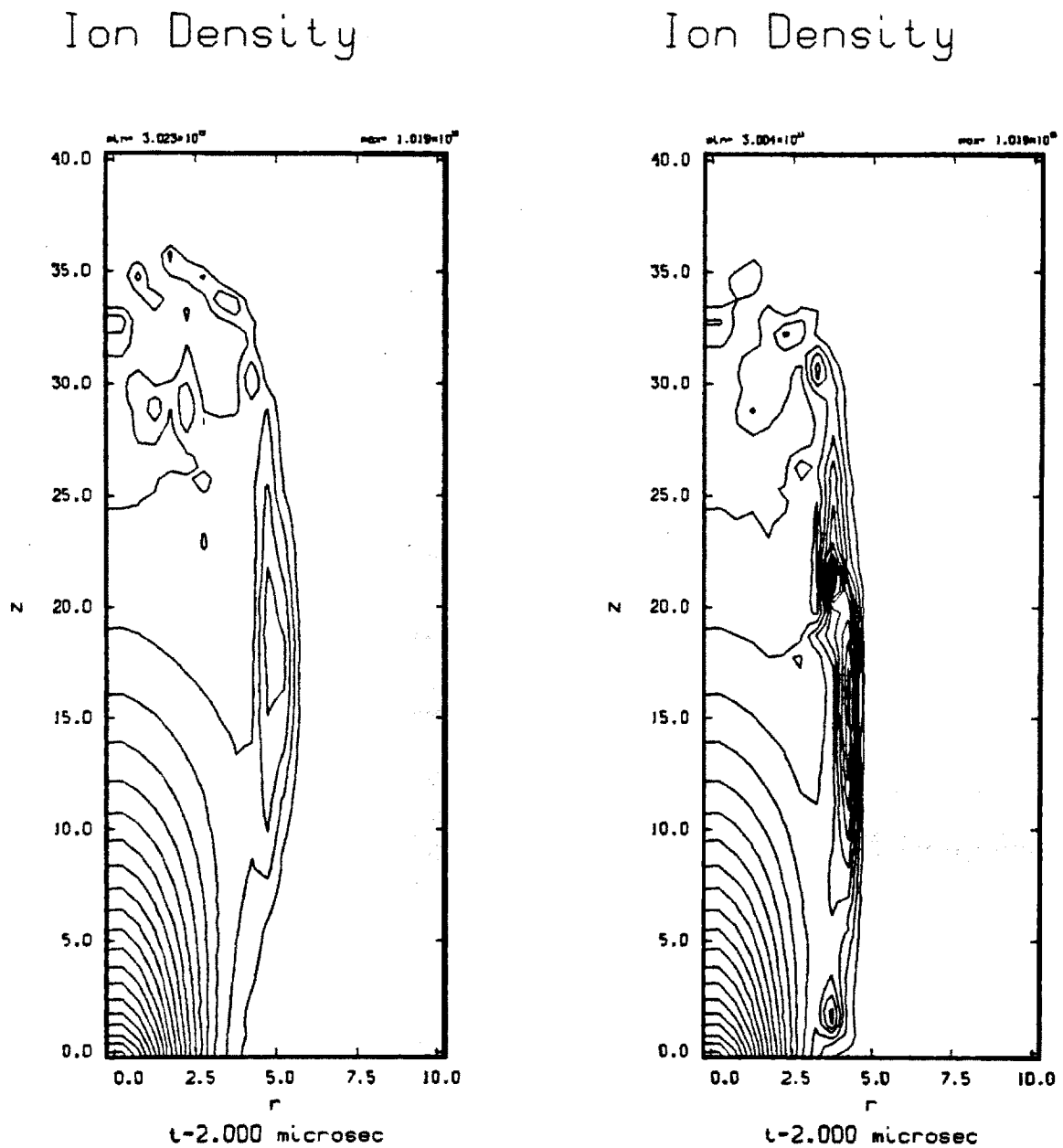


Figure 3.60: Comparison of plasma density at two microseconds. Even injection case on the left, one hundred times neutral injection on the right.

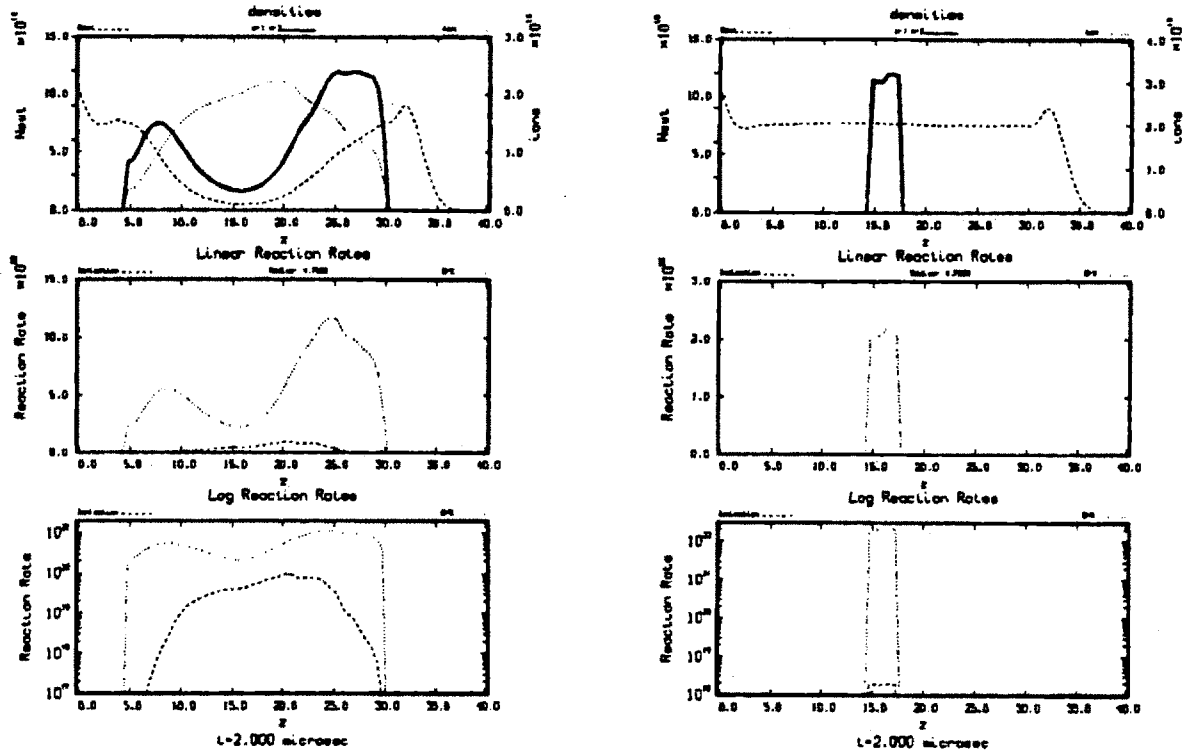


Figure 3.61: Comparison of reaction rate plots at two microseconds. Even injection case on the left, one hundred times neutral injection on the right.

streaming time compared to the characteristic time scale of momentum adding events. This explains why such a significant amount of momentum was shown to be coupled to the plasma fluid by the top plot.

However, when the Reynolds number on the bottom plot is studied, it is seen to be extremely low. This indicates that the plasma temperature is very low. With such a low Reynolds number it is not expected that the plasma could deform the magnetic field significantly. Taking into account the magnetic interaction parameter being significantly greater than the Reynolds number, it is expected that little field deformation would happen.

The reason for the shape of the of the plasma density profile observed in the top plot in Figure 3.61 is seen clearly in Figure 3.63. This is the plasma velocity plot at two microseconds. The velocity is very low near the interface with the neutral gas jet. At approximately $z = 15\text{cm}$ down the duct one sees three small velocity vectors that have expanded into the radius that is profiled in the density traces of Figure 3.61. This accounts for the very sharp, almost step like, rise and fall-off of the plasma density profile at this location.

The plasma temperature plot at two microseconds, presented in Figure 3.64, confirms the conclusions from the analysis of the previous graphs. The plasma temperature drops sharply near the interface with the neutral gas jet. It is seen that the plasma temperature has expanded less than in the even neutral gas injection case. This is a consequence of the plasma not expanding as much and the intense cooling that is taking place in the interaction region. The temperature in the center of the plasma column is nearly unaffected by the cooling taking place at the edge. The drop off in the central temperature (at $r = 0$) is nearly identical in both cases.

Figure 3.65 shows the neutral density contour plot at two microseconds. Very little erosion is seen in the one hundred times neutral gas injection case. For the even neutral gas injection case a significant amount of erosion has already taken place at this early time step. The neutral gas contour plot looks like a solid jet, but it has in fact started to expand slightly in radius due to the thermal pressures in the jet. This is seen more clearly in the neutral gas velocity plot.

Figure 3.65 shows the neutral velocity plot at two microseconds. From this figure it is clear that some expansion has occurred in the neutral gas. This figure helps to explain the shape of the axial plasma profile observed in the reaction rate plots (Figure 3.61).

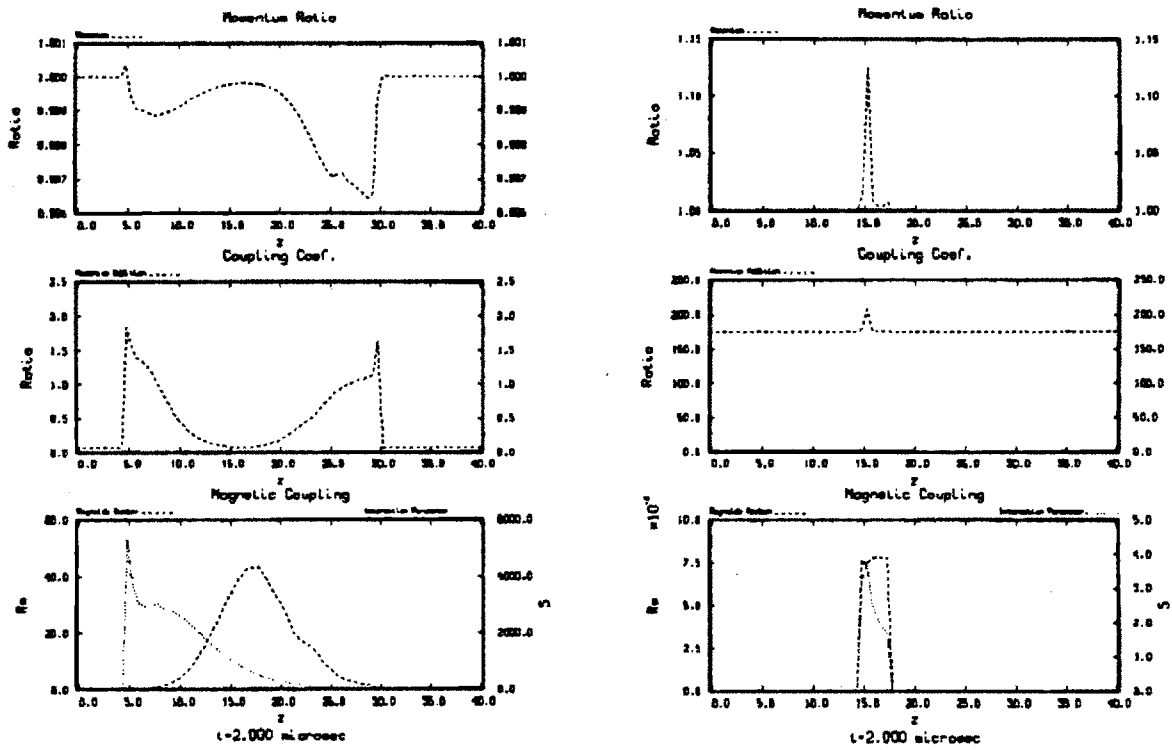


Figure 3.62: Comparison of coupling coefficients at two microseconds. Even injection case on the left, one hundred times neutral injection on the right.

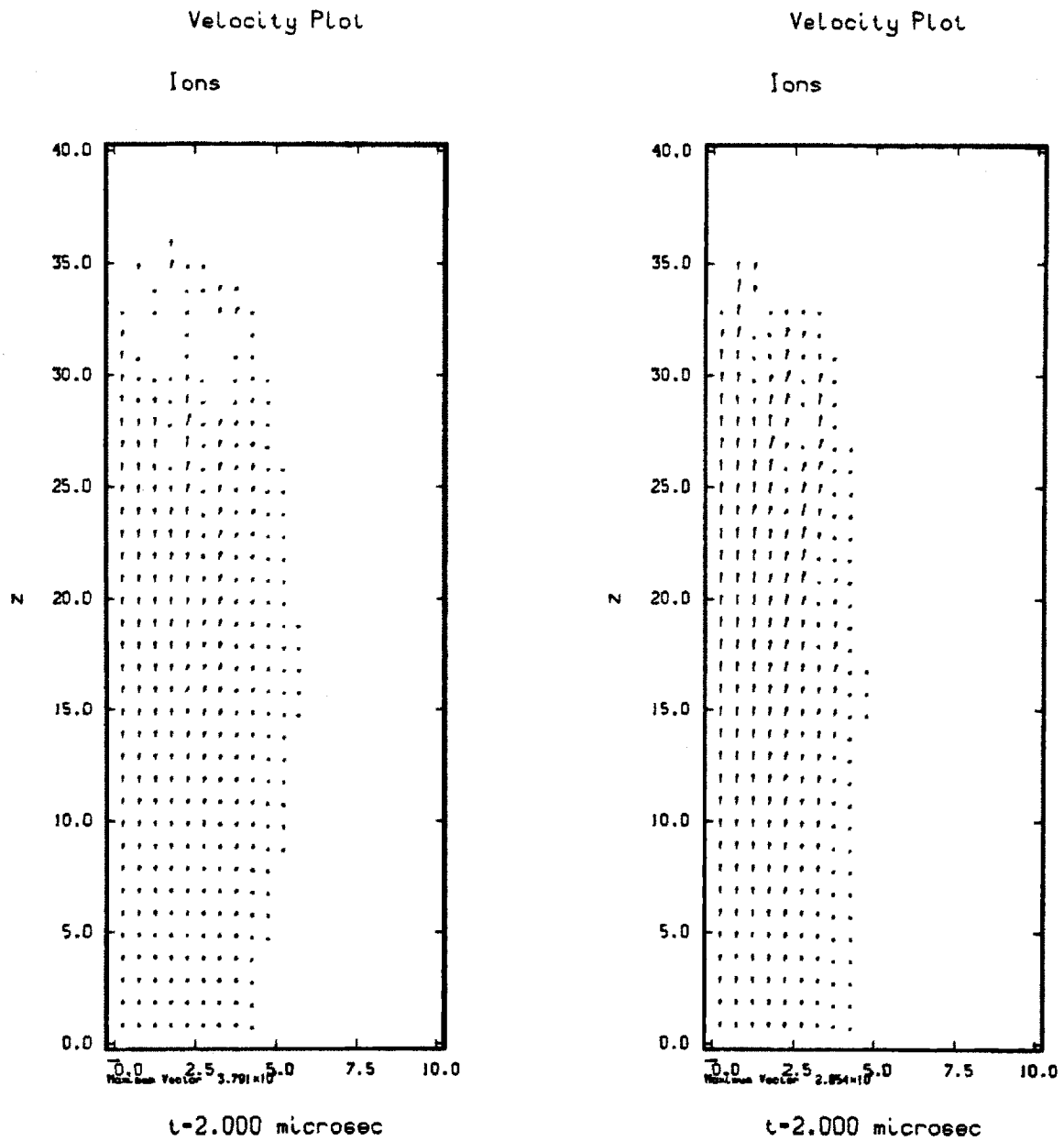


Figure 3.63: Comparison of plasma velocity plot at two microseconds. Even injection case on the left, one hundred times neutral injection on the right.

Ion Temperature

Ion Temperature

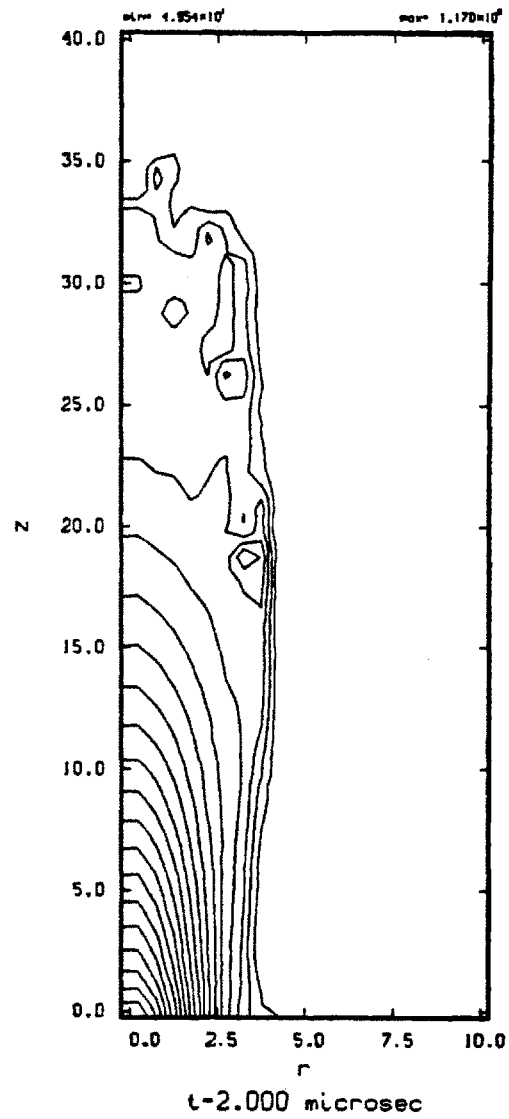
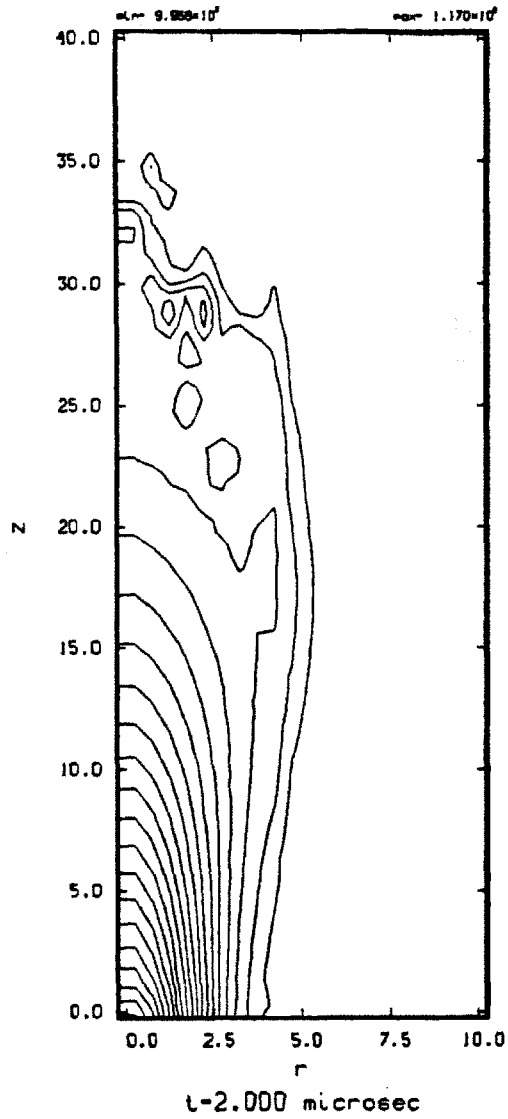
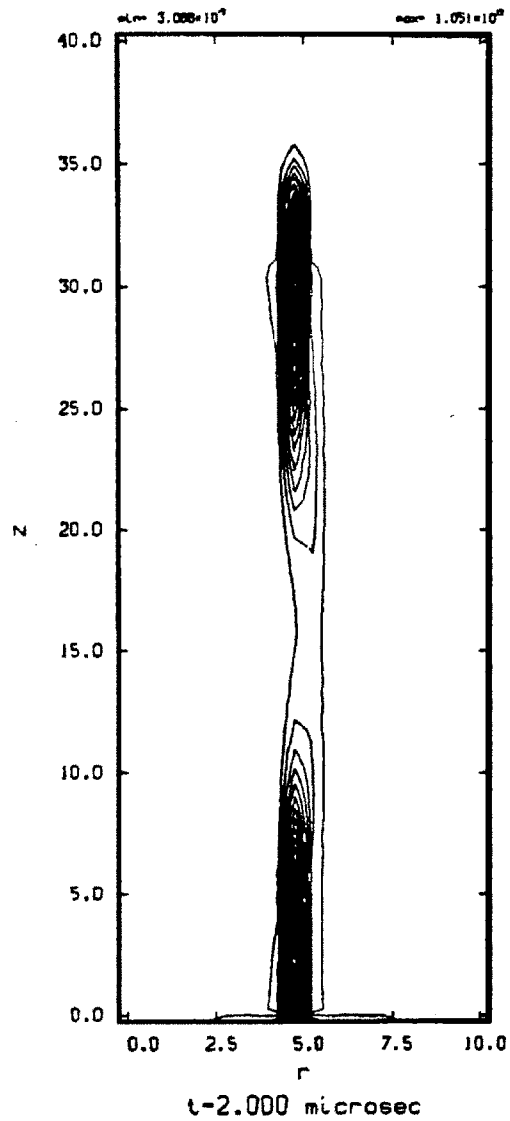


Figure 3.64: Comparison of plasma temperature at two microseconds. Even injection case on the left, one hundred times neutral injection on the right.

Neutral Density



Neutral Density

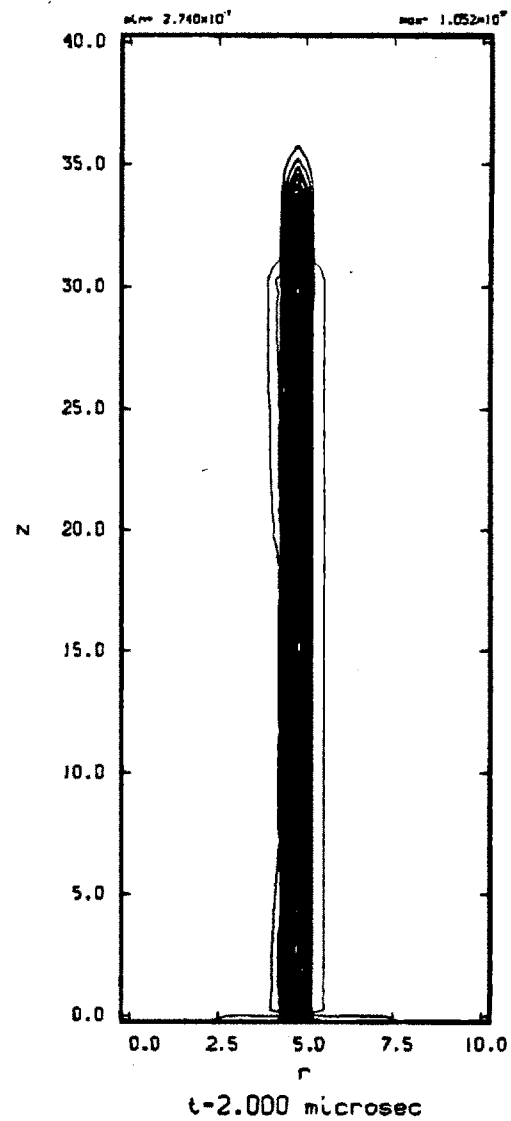


Figure 3.65: Comparison of neutral density at two microseconds. Even injection case on the left, one hundred times neutral injection on the right.

Because of the radial expansion of the neutral gas the interaction region begins before the radius depicted in the reaction rate plots. In the one hundred time neutral gas injection case this neutral gas expansion has sufficient density to cause a significant amount of reactions to take place with the plasma. The neutral gas density in this expansion region could be as high as the peak neutral gas density in the even injection case. These interactions in the expansion region tend to slow the plasma expansion down before the plasma expands into the region that is depicted in the reaction rate plots.

This helps to explain some of the structure observed in the plasma density contour plot at this time step (Figure 3.60 on page 142). There is a peak in plasma density inside the radius of the neutral jet at approximately $z = 20\text{cm}$. This peak does not appear on the plasma density profile trace in the reaction rate plots because it is off the axis of neutral injection. This holds for the plasma density increase between $z = 10\text{cm}$ and $z = 20\text{cm}$. Here there is a significant increase in plasma density, due to the interactions with the neutral gas that has expanded in radius from the neutral jet, that is slowing the expansion of the plasma. The neutral velocity plot helps in explaining the small plasma peak that is forming at approximately $z = 0$. The neutral velocity plot shows neutral gas velocity vectors in this location, indicating that there is a significant amount of neutral gas present in this location.

The next figure to be presented, Figure 3.67, is the plasma density at three microseconds. The plasma density build up that was observed at two microseconds continues. More plasma has expanded into the region directly downstream of the neutral gas jet. This will be seen better in the next figure. The small plasma peak near $z = 0$ that was observed at two microseconds also grows. One can see the plasma density contours deforming around this peak. This is an indication that the boundary conditions used at z_{min} are not appropriate for this case. That plasma peak near z_{min} would tend to flow out of the system at z_{min} . Currently, the boundary conditions for the plasma properties at z_{min} are held fixed in time at the initial conditions. This inconsistency does not affect the goal of the simulation, but the peak should not be considered real.

The interaction region has expanded from about $z = 10 - 25\text{cm}$ at two microseconds to about $z = 10 - 30\text{cm}$ at three microseconds. If not careful, it could be interpreted that the plasma in this interaction region has been convected downstream in the z direction. It is important to point out that the plasma density that was formed through

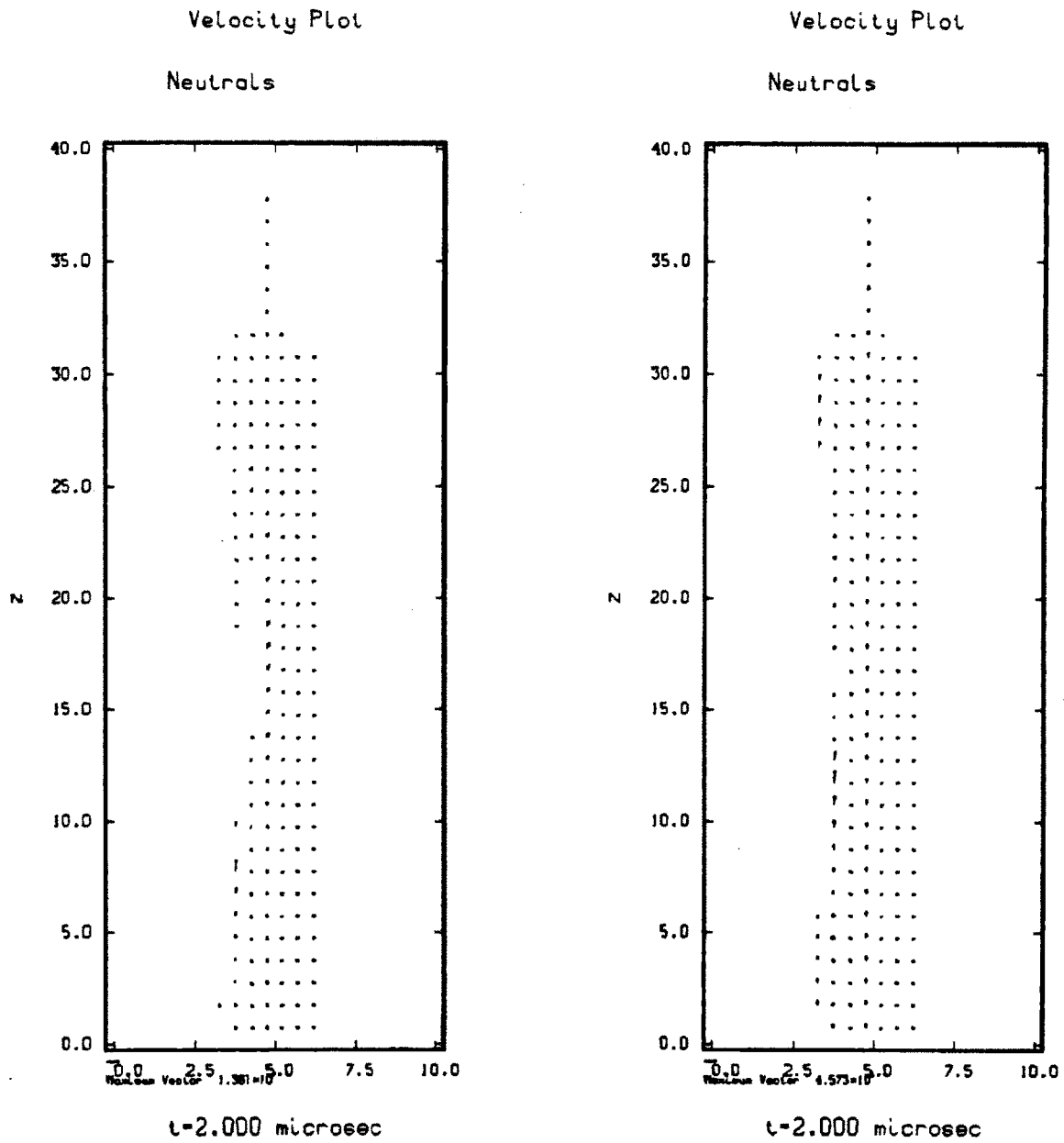
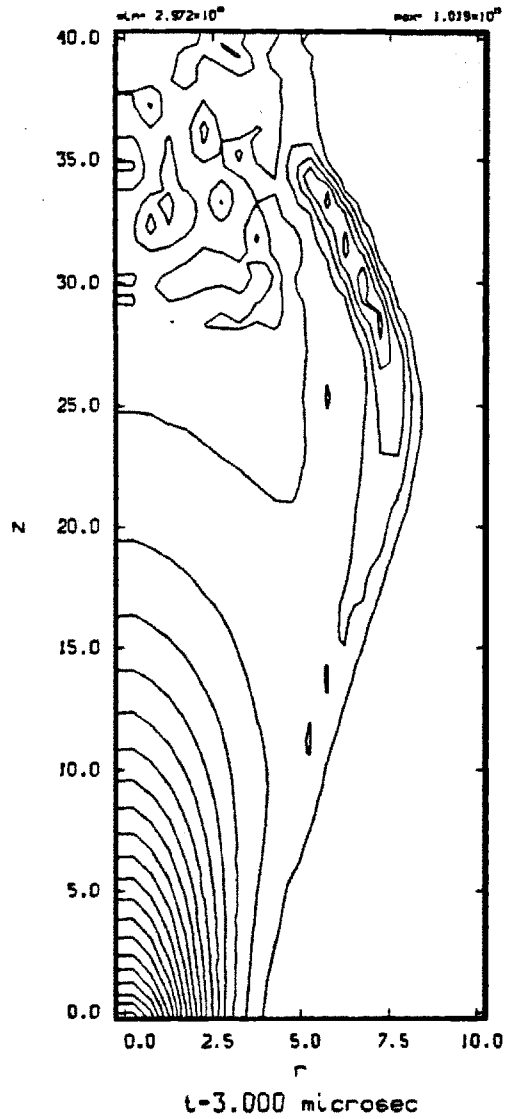


Figure 3.66: Comparison of neutral velocity plot at two microseconds. Even injection case on the left, one hundred times neutral injection on the right.

Ion Density



Ion Density

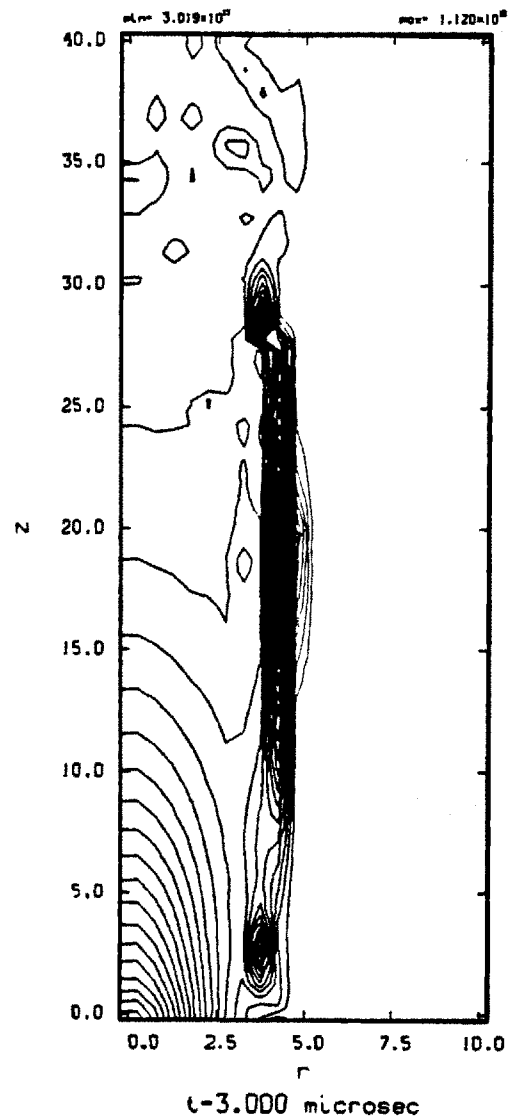


Figure 3.67: Comparison of plasma density at three microseconds. Even injection case on the left, one hundred times neutral injection on the right.

the interactions with the neutral gas jet at two microseconds has *not* been convected downstream. In looking only at the static plots of the plasma density at discrete time plots it is easy to infer that this density has been convected downstream, indicating that perhaps this would be a possible configuration for the plasma thruster (if the neutral gas density did not preclude it from being considered). What is actually happening is as follows. The magnetic field profile (Figure 3.2) governs how fast the plasma expands radially. Initially the flow is field aligned and to zero order remains so. The first plasma to expand to a point such that it can interact with the neutral gas jet will be the plasma furthest out in radius. This will intersect the neutral gas jet downstream at some location in z . This is where the plasma/gas interaction region will start. Further interaction with the jet will happen downstream from this initial location (unless the neutral gas expands and interacts with the plasma upstream of this point). The plasma has to travel a longer distance to intersect the jet at these locations, and hence will start interacting with the jet later in time.

In this figure, the plasma has now intersected with the neutral gas jet for a longer distance than it had at two microseconds. Once the neutral gas is ionized into the plasma fluid (or via charge-exchange) the mixture comes to some new state governed by the fluid equations, and the plasma fluid is then convected in time via these local parameters. In this case the local plasma velocity in this region has been reduced to nearly zero, so the plasma does not expand in radius. With the increase in the length of the interaction region, it looks like the plasma fluid in this region has actually convected downstream, when in reality it has remained practically stationary.

That the ionized neutral gas does get convected with the plasma fluid is clearly seen in the left hand plot. This is the plasma density plot for the even injection of neutral. The neutral gas that was added to the plasma downstream of the jet injection has been convected with the plasma fluid, which in this case is predominately following the magnetic field lines and expanding radially.

The next figure, Figure 3.68 is the reaction rate information at three microseconds. The top plot shows the density traces. It can be seen that the plasma is starting to erode the neutral gas jet. The reaction rate plots show that the ionization rate is very much lower than the charge exchange rate, indicating that the plasma must be very cold in this location.

The next figure, Figure 3.69, is the coupling information at three microseconds. The

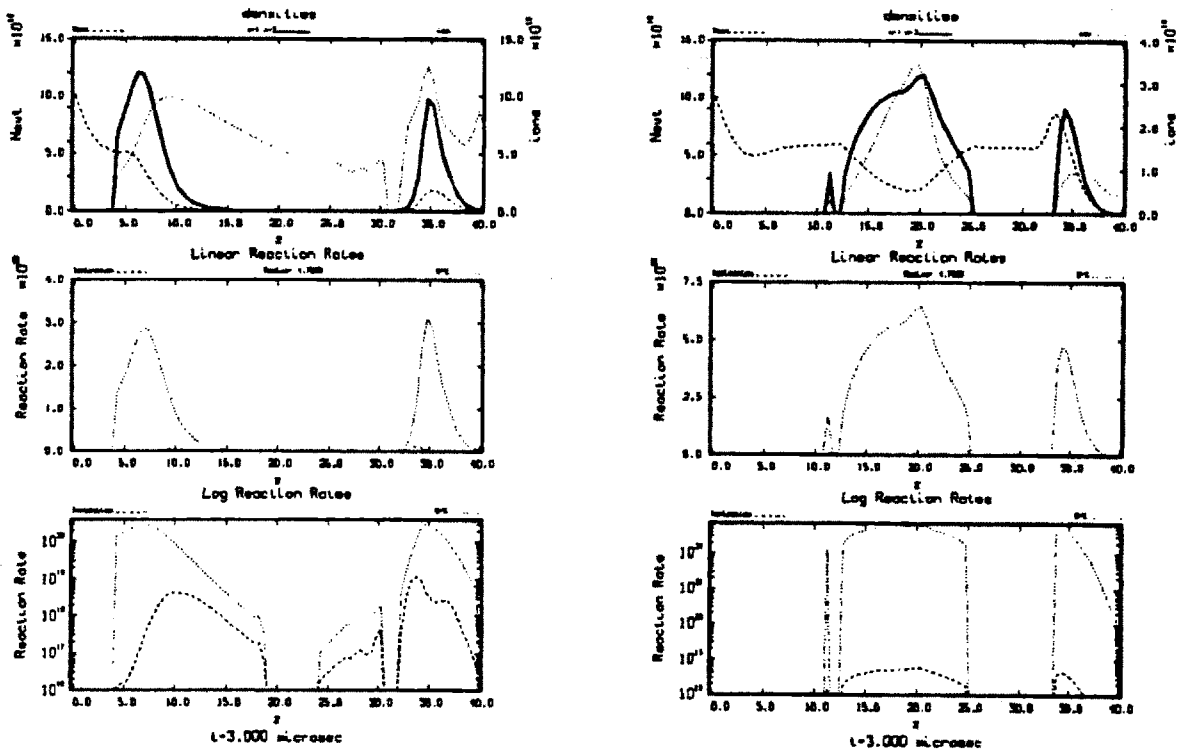


Figure 3.68: Comparison of reaction rate plots at three microseconds. Even injection case on the left, one hundred times neutral injection on the right.

top plot, the momentum ratio, is much lower now than it was at two microseconds. As described earlier, one way that the momentum ratio could be large is that the local plasma momentum is small. The plasma momentum could be small by having either a low density or a low velocity, or both. Then the momentum ratio between the plasma and the gas added to the plasma could look large, when in absolute momentum added is small. That the momentum ratio has dropped so significantly is an indication that more robust plasma must now be in this location, and that the absolute amount of momentum added to the plasma at this location is now small compared to the plasma momentum. The reaction rates have dropped slightly, about by a factor of two (compare Figure 3.61 and Figure 3.68, the second and third plots), but the momentum ratio has fallen by over a factor of thirty.

The large coupling coefficients in the second plot indicate that the plasma must be moving slowly in this region. Typically the coupling coefficients are small because of the difference in time scales between the plasma flow and momentum adding events. The two order of magnitude increase in neutral gas density would increase the reaction rate significantly, which would decrease the time scale for momentum adding events. Also, if the plasma is moving slowly in this region, that would tend to make the coupling coefficients larger.

The last plot in this figure shows the magnetic Reynolds number and magnetic interaction parameter. In the main interaction region the magnetic Reynolds number is very low, indicating that the plasma is very cold here. Combine this with a relatively large magnetic interaction parameter, one would expect that the plasma would follow the field lines.

The next figure, Figure 3.70, is the plasma density at four microseconds. It shows that the plasma density is starting to expand through the neutral gas jet. The contour lines near $z = 20\text{cm}$ are starting to spread out, indicating that it is not as sharp of peak as it was at three microseconds. The plasma before this location still does not have the velocity and/or temperature to erode the neutral gas jet away, so there remains a sharp build up of plasma density in this location. The even neutral gas injection case has already eroded away all the neutral gas and has expanded following the field lines into the wall at r_{max} .

Figure 3.71 shows the reaction rate information at four microseconds. The top plot shows that the plasma has eroded away a significant amount of the neutral gas near

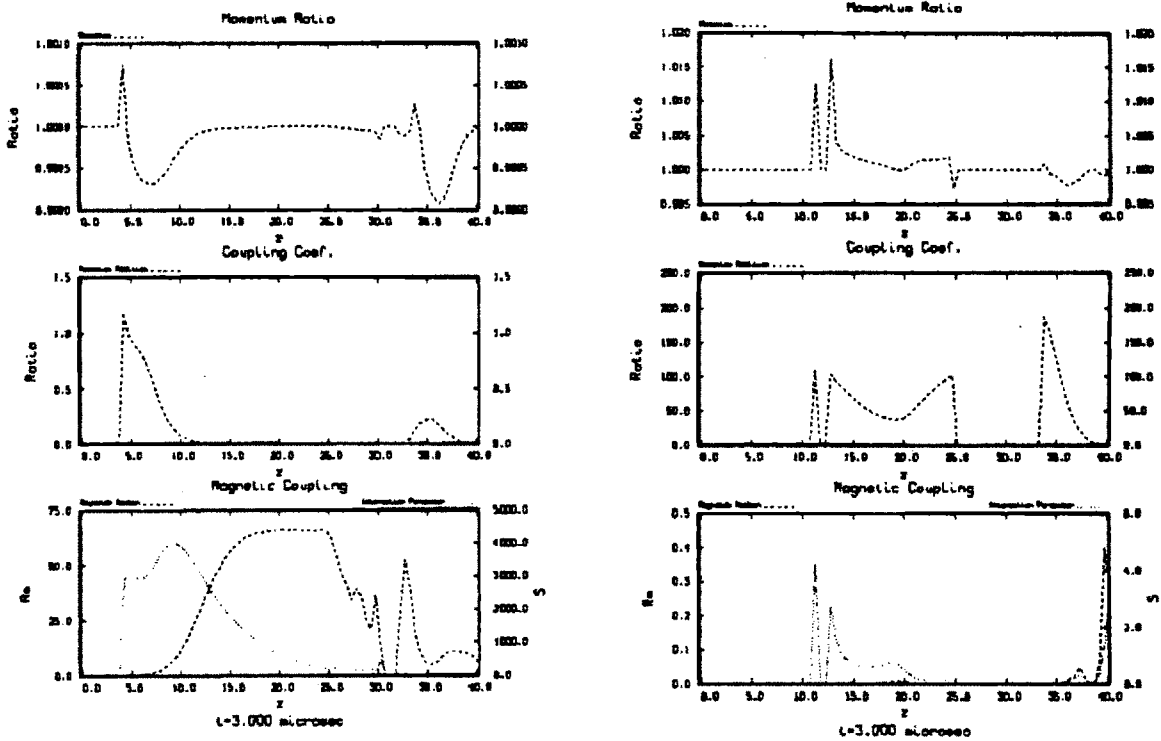


Figure 3.69: Comparison of coupling coefficients at three microseconds. Even injection case on the left, one hundred times neutral injection on the right.

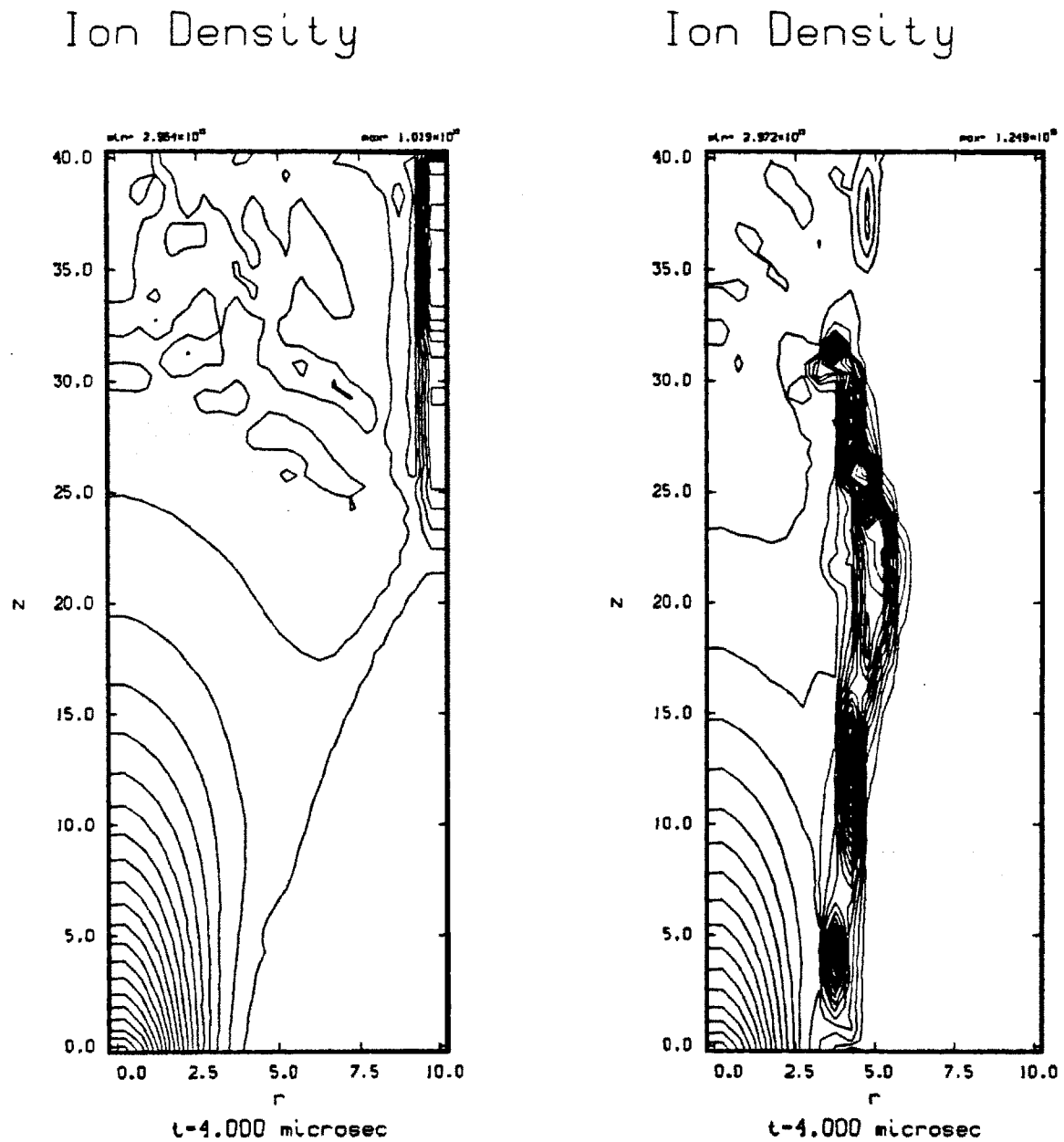


Figure 3.70: Comparison of plasma density at four microseconds. Even injection case on the left, one hundred times neutral injection on the right.

$z = 20\text{cm}$. This is reflected in the second and third plots as a drop in the reaction rates in this location. The third plot is interesting because it shows that the ionization reaction, that has been several orders of magnitude lower than the charge exchange rate, is starting to climb just before this region and just after this region. This is an indication that the plasma temperature in this region is starting to become significant. It is the loss of the neutral fluid that drops the reaction rates.

The next figure, Figure 3.72, shows the coupling information at four microseconds. The top plot shows that the momentum ratio is not significantly different than the results at two microseconds.

The second plot shows that there are still large coupling coefficients in certain regions of the interaction zone. The drop of the coupling coefficient in the region near $z = 20\text{cm}$ is consistent with the interpretation of the data up to this point. The neutral gas jet has been eroded in this location, allowing the plasma to free stream through this region. The absence of neutral gas limits the cooling of the plasma so the plasma remains hot. The hot plasma then free streams in this region at a velocity close to the velocity it would have without any reactions. This implies that the coupling coefficients in this region would drop because the plasma cell transient time has been reduced. Add this to the fact that the reaction rates in this region are dropping, indicates that the coupling coefficients should be very small in this region, as is observed.

Also consistent with this interpretation is the magnetic Reynolds number in the final plot. It is small everywhere and suddenly peaks in this region near $z = 20\text{cm}$. This is another indication that the plasma is hot in this location. Unfortunately, the magnetic interaction parameter is even large in this same location, indicating that the magnetic field is going to dominate the flow.

The neutral gas density plot in Figure 3.73 clearly shows the erosion of the neutral gas fluid in this region. The slowing of the plasma by the interactions with the neutral gas has enabled a neutral gas island to exist downstream of this location. Now that the plasma is free to expand into this region, this neutral gas island should be eroded by the plasma.

The plasma and neutral gas densities are presented in the next four figures, Figure 3.74–Figure 3.77, to confirm that the plasma does indeed continue to expand and follow the magnetic field.

Figure 3.74 shows the plasma density at five microseconds. It has expanded out

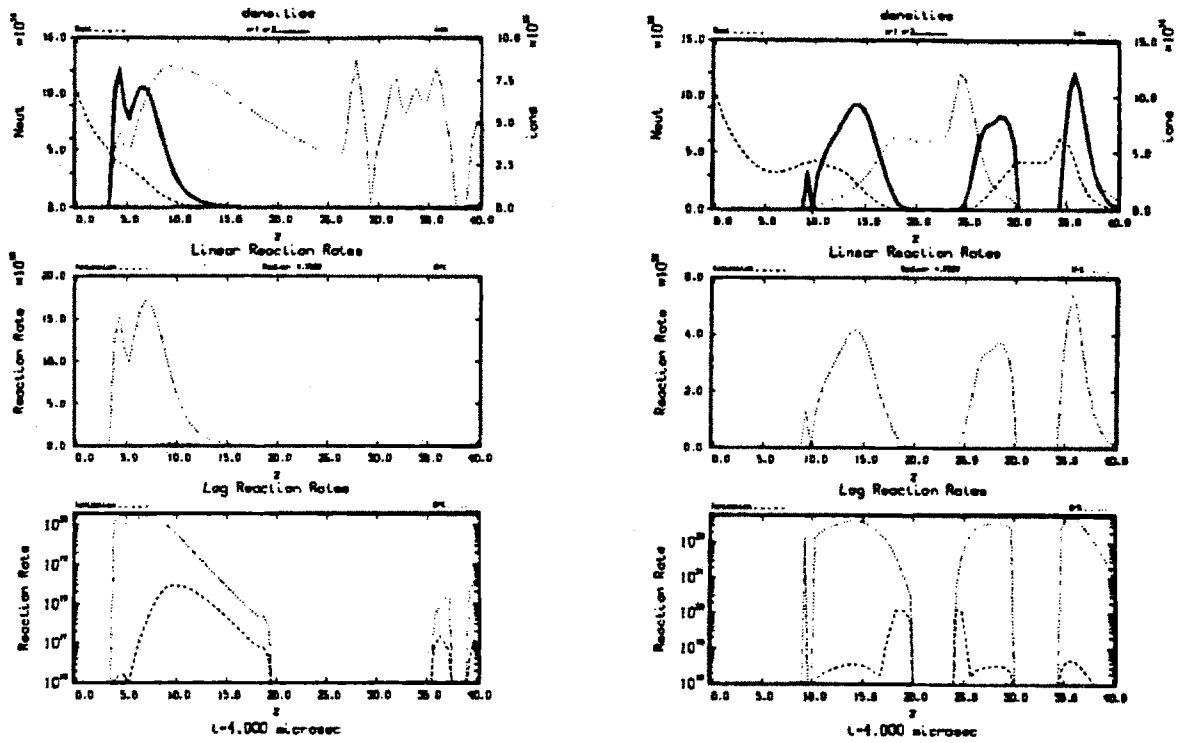


Figure 3.71: Comparison of reaction rate plot at four microseconds. Even injection case on the left, one hundred times neutral injection on the right.

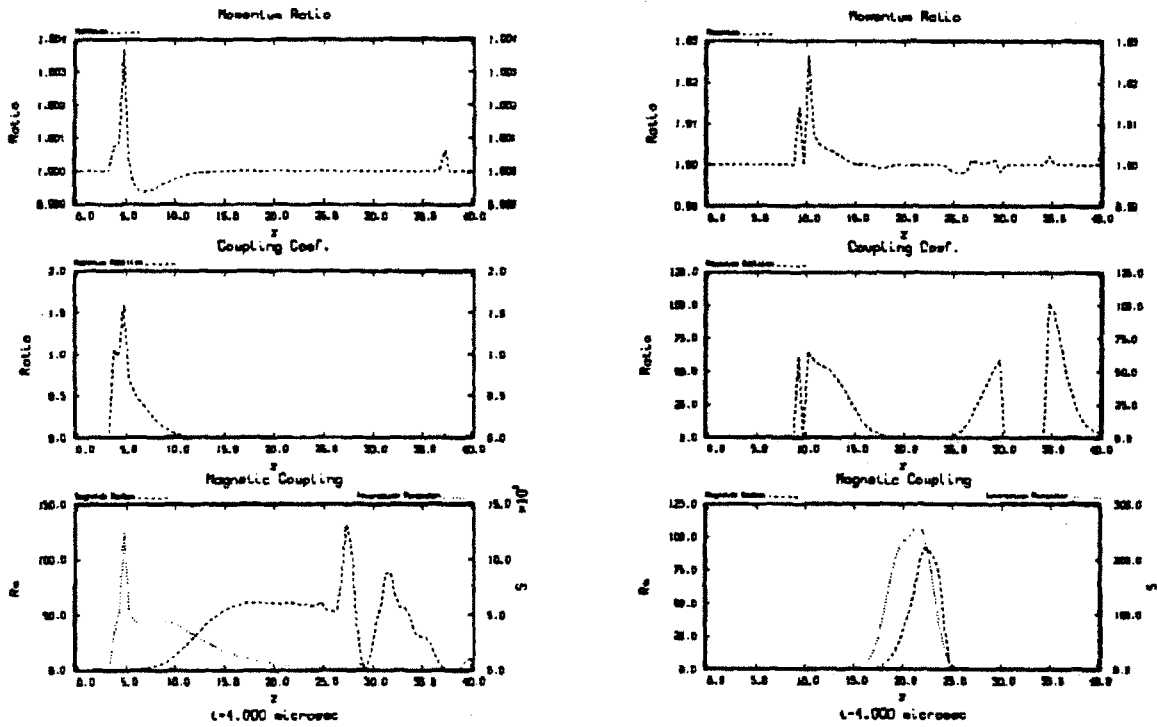
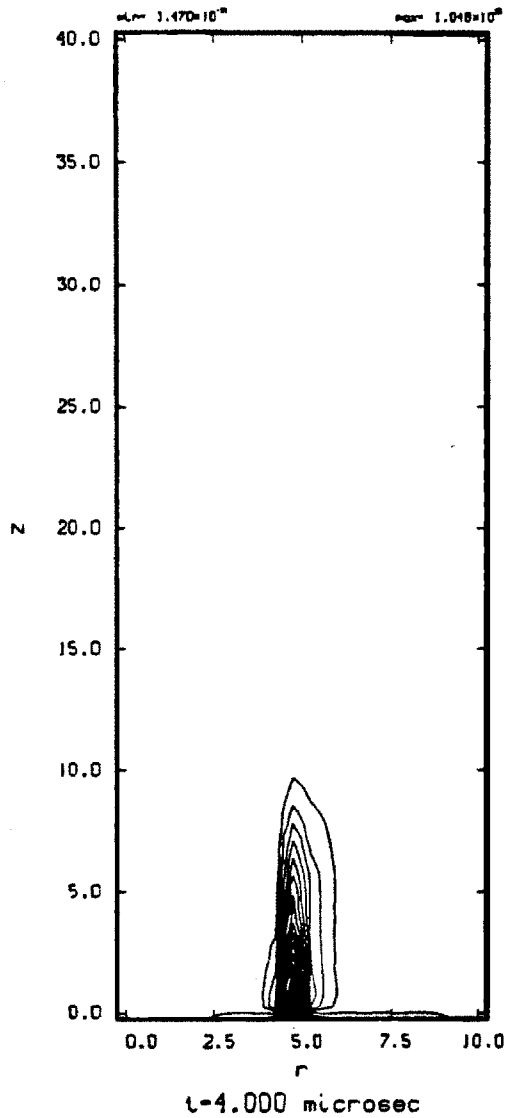


Figure 3.72: Comparison of coupling coefficients at four microseconds. Even injection case on the left, one hundred times neutral injection on the right.

Neutral Density



Neutral Density

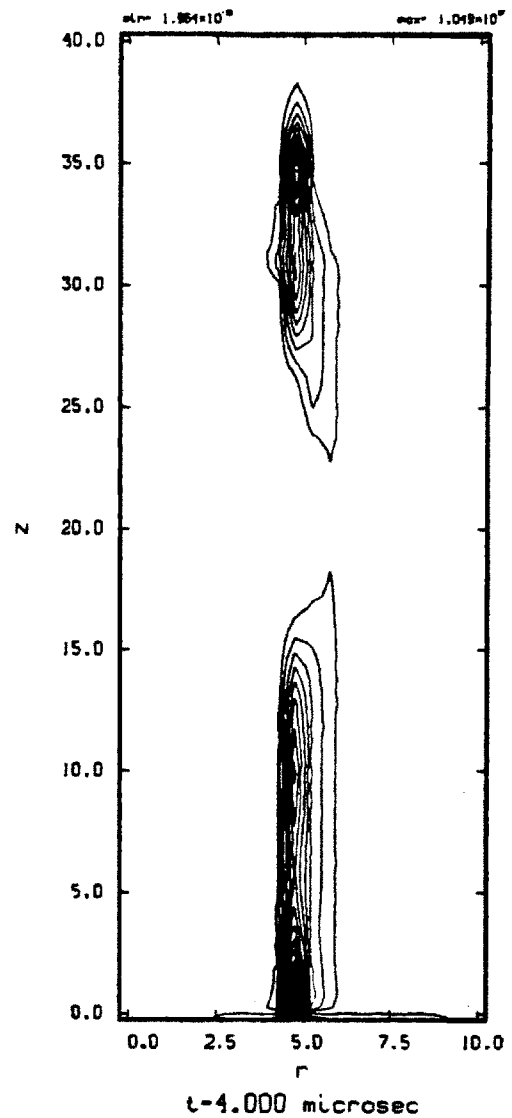


Figure 3.73: Comparison of neutral density at four microseconds. Even injection case on the left, one hundred times neutral injection on the right.

Ion Density

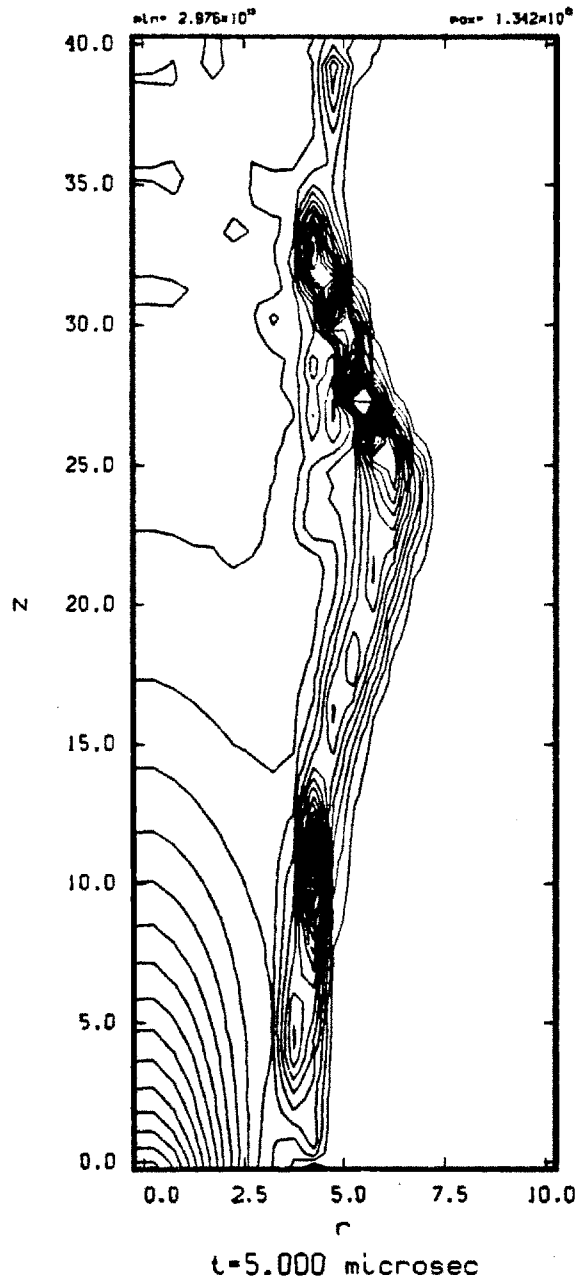


Figure 3.74: Plasma density at five microseconds. One hundred times neutral injection case.

more in radius than at four microseconds. The length of the whole that has been eroded through the neutrals has also increased.

Figure 3.75 shows the neutral gas density at five microseconds. The distance downstream that the neutrals flow before being eroded by the neutral gas as decrease slightly, indicating that the plasma in this location is finally getting hot enough to have significant reactions. The island downstream is starting to disappear.

Figure 3.76 shows the plasma density at six microseconds. This figure clearly shows that the plasma is freely expanding along the field lines

The final figure for the one hundred times neutral injection case is Figure 3.77, the neutral gas density at six microseconds. The island that survived near the end of the duct is now gone. Also, the neutral gas jet has been eroded back towards $z = 0$ to about the same length as in the lower neutral gas injection case. This indicates that the increase in the neutral gas density for the jet did little more than to change the details of the initial start-up phase of the device. It had no long lasting effect on the outcome of the interactions. It is clear that an increase in the neutral gas density is not the mechanism that will enable the hybrid plume plasma rocket to work.

3.3.7 Wide neutral jet injection.

The next case that will be considered in the injection of neutral gas through a wider jet. The width of the jet in all the previous cases was half a centimeter. In this case that width will be increased to two centimeters. This case is done to see how the interactions scale with the increase in jet width. The concerns mention in the high density gas injection are a concern here, too. In this case the gas density will not be increased, only the width of the jet will vary. This still increases the fraction of mass flow rate that is associated with the low velocity fluid, potentially dropping the specific impulse of the device.

The input parameters for this case are presented in Table 3.7. The mass flow rate is almost the same in the two fluids. The thrust component in the neutral is now one-eighth of that of the plasma component. The overall specific impulse of the device has been reduced to half of the specific impulse of the plasma fluid. In the even injection case the overall specific impulse was only slightly reduced.

The results will be compared against the case with even injection of neutral gas. The even injection case will be on the left and the wide injection case will be on the

Neutral Density

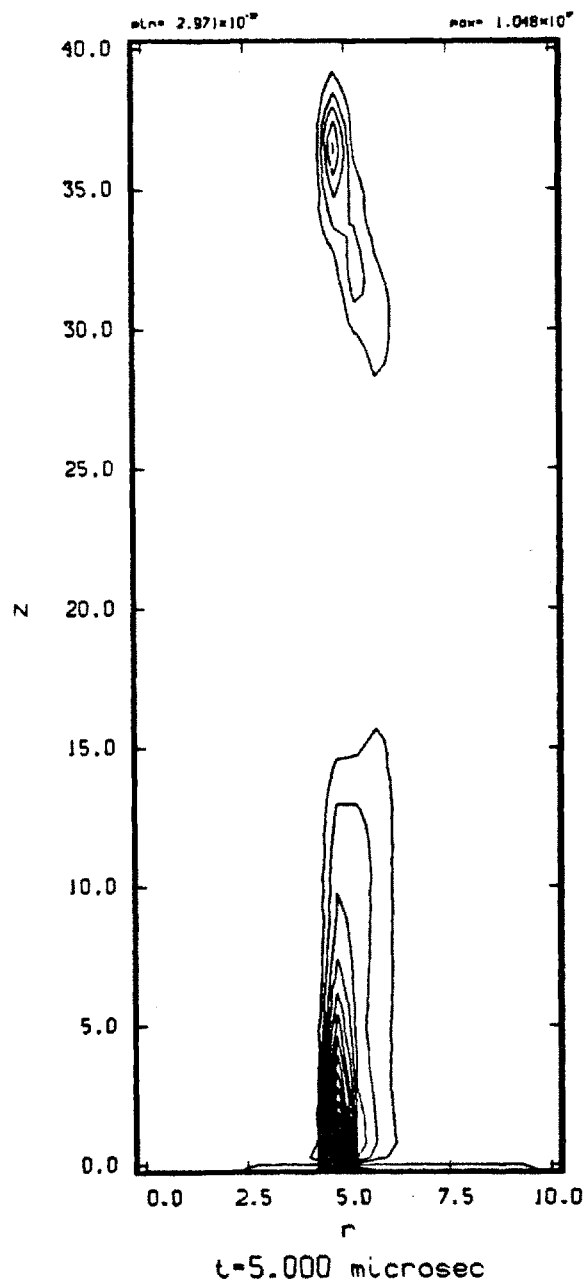


Figure 3.75: Neutral density at five microseconds. One hundred times neutral injection case.

Ion Density

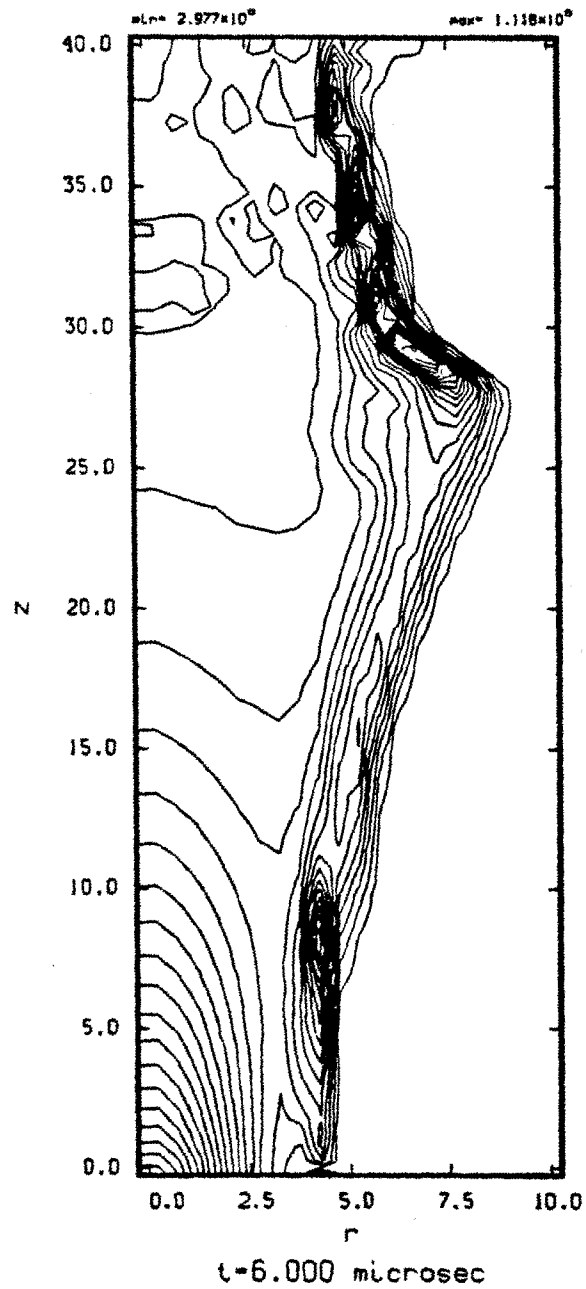


Figure 3.76: Plasma density at six microseconds. One hundred times neutral injection case.

Neutral Density

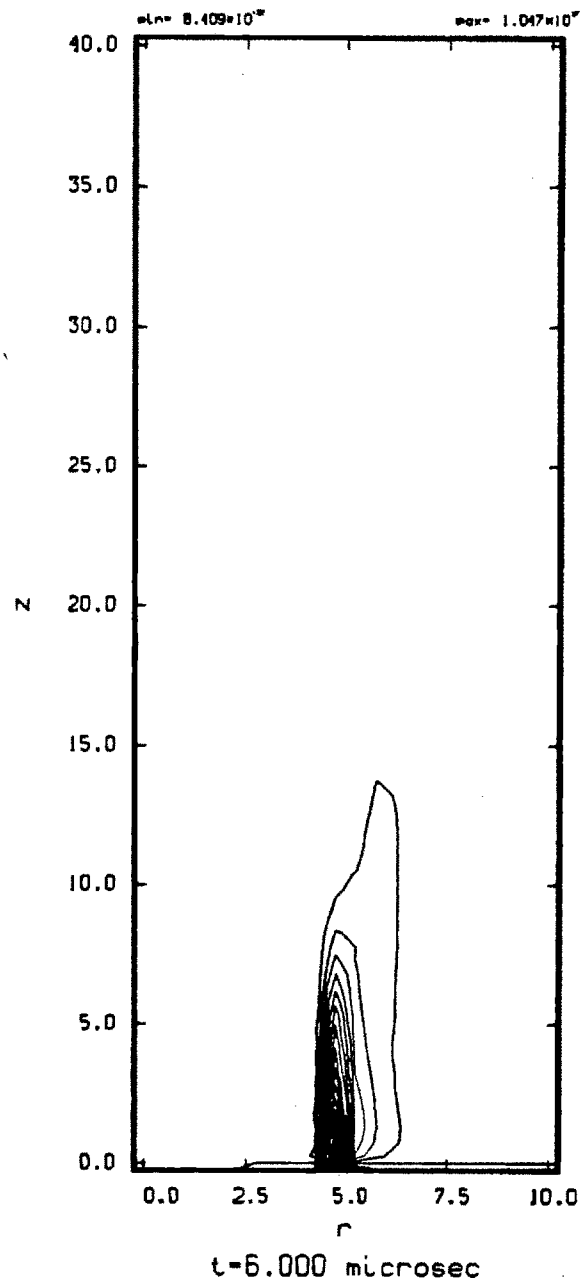


Figure 3.77: Neutral density at six microseconds. One hundred times neutral injection case.

Item	Ions	Neutrals
mass flow rate (\dot{m}), kg/sec	2.87e - 04	2.54e - 04
Thrust, Newtons	32.47	3.95
Power, MWatts	1.83	0.03
Temperature, eV	100.0	0.025
Density, part/cm ³	1.0e+15	1.0e+15
Velocity, cm/sec	1.13e+07	1.56e+06
I_{sp} , sec	11,500	1,590
I_{sp} net, sec	6,866	

Table 3.7: Input parameters for wide neutral gas injection.

right.

The first time step that will be presented is at three microseconds. Interactions with the neutral gas jet can be observed in the plasma density and neutral density contour plots starting at two microseconds. The reaction rate plots do not show the interactions until the three microsecond plots. This is because the radius at which the profiles are shown for is at the center of the jet. It takes a while for the interactions to make their way into the the center of the neutral gas jet. Because of this, the first time step that will be presented will be at three microseconds.

The first figure, Figure 3.78, is the plasma density at three microseconds. The figure shows an increase in plasma density on the same scale as for the even injection case. The even injection case has expanded a bit further in radius. This is due to the fact that the narrow neutral gas jet is eroded more quickly than the wide case.

The next figure, Figure 3.79, show the reaction rate information at three microseconds. It can be seen that the even injection case (narrow neutral gas jet) that the neutral jet is almost entirely eroded by this time. The neutral gas in the wide injection case shows significant erosion, but is not completely eroded away at this radius. Remember that the radius that this profile is for is in the middle of the jet, so there are reactions before this point that may have eroded the neutral gas further.

The bottom reaction rate plot shows that the ionization reaction rate peaks in the middle of the dip of the neutral gas. This is an indication that the plasma temperature is the hottest in this location, as we have seen before. The ionization reaction is still significantly smaller than the charge-exchange reaction.

Figure 3.80 shows the coupling coefficients at three microseconds. The results of

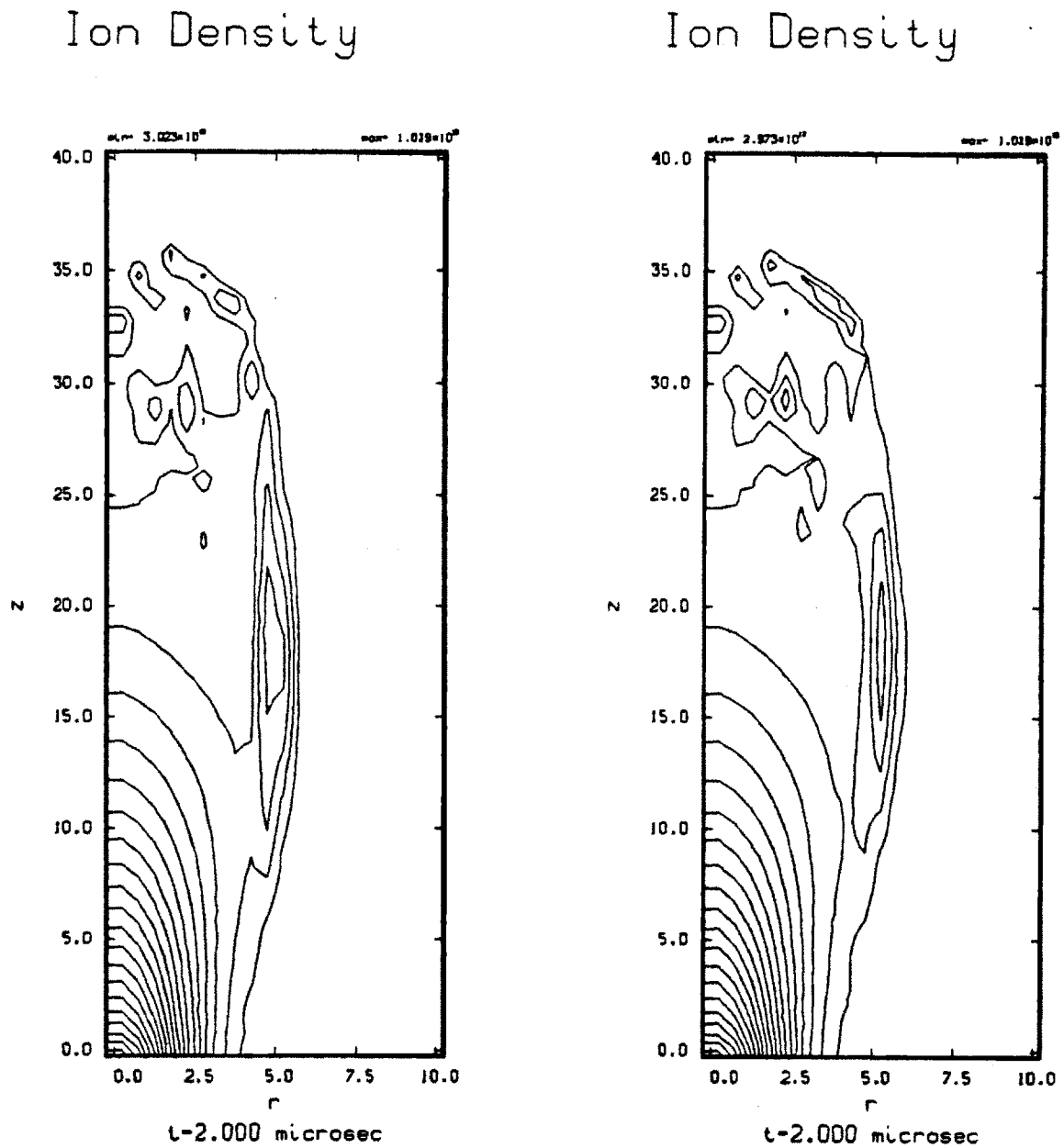


Figure 3.78: Comparison of plasma density at three microseconds. Even injection on the left, wide neutral gas jet on the right.

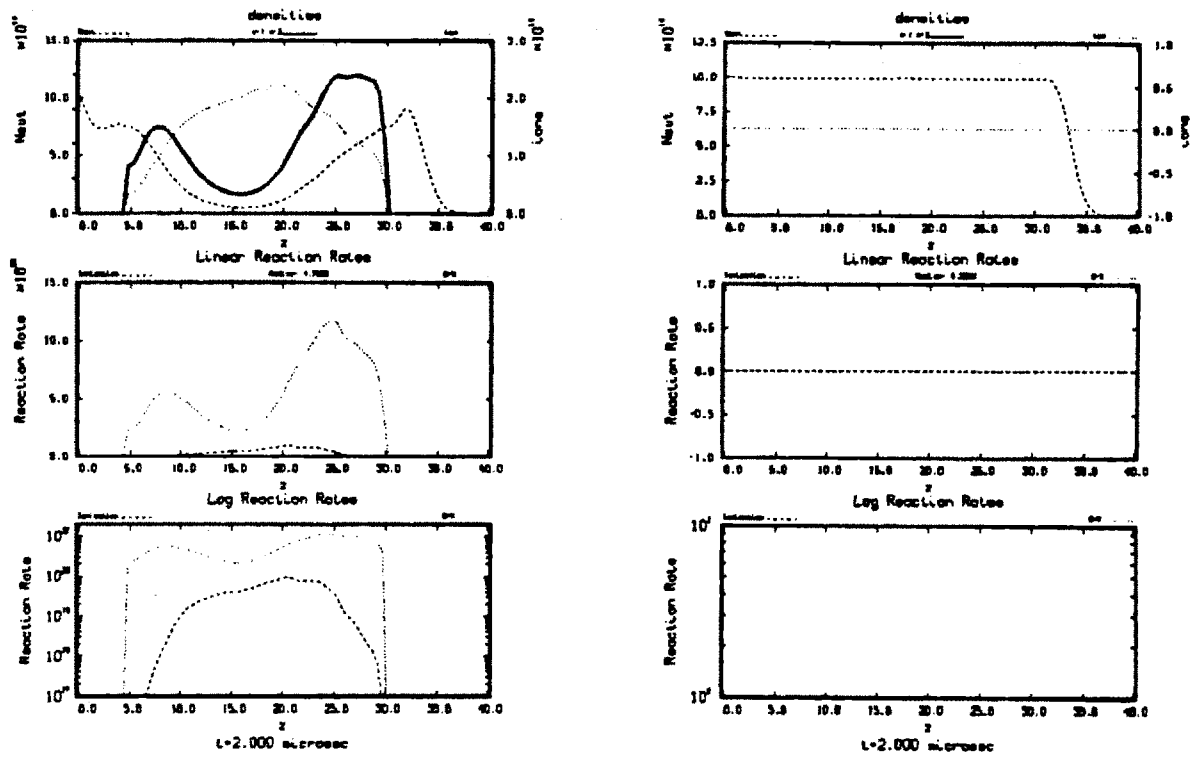


Figure 3.79: Comparison of reaction rate plots at three microseconds. Even injection on the left, wide neutral gas jet on the right.

these plots are becoming standard. The peak in the momentum ratio in the top plot is at the very beginning and end of the interaction region. This is an indication that the plasma is moving slowly in these locations so the ratio of momentum addition is high. The coupling coefficients in the second plot tend to confirm this.

The coupling coefficients are large at the beginning and end of the interaction region, indicating a low velocity plasma fluid. The low coupling coefficients in the center of the interaction region indicate a high plasma velocity in this region. The coupling coefficients in the center region can also be lowered by a small reaction rate, which, from the previous figure, dips in the center of the reaction region.

The bottom plot in this figure also supports these findings. The large magnetic Reynolds number in the center of the reaction region imply that the plasma is hot in this area. However, the magnetic interaction parameter is very much greater than the Reynolds numbers in this area, so it would be assumed that the plasma flow would be dominated by the magnetic field.

Figure 3.81 shows the neutral density at three microseconds. The increase in width of the neutral gas jet is apparent. From the curved shape of the edge of the density profile one can infer the front of the plasma expansion.

Figure 3.82 shows the plasma density at four microseconds. One can see that the neutral gas that was added to the plasma fluid at earlier time steps is being convected along the field lines toward the wall. The expansion has been slowed compared to the even injection (narrow jet) case, as can be seen in the plot on the left. This slowing of the expansion of the plasma fluid is a transient feature of the wide neutral gas jet case, and the expansion will be the same as the comparison case once the neutral gas has been eroded. The width of the jet just changes the time scale for this expansion, but not the underlying basic behavior of the system.

Figure 3.83 shows the reaction rate plots at four microseconds. The top plot shows that the neutral density extends further down the duct in the wide neutral jet injection case compared to the reference case. One must remember that the radius at which the comparisons have been made are different in each case. The radius is chosen to be the center of the neutral gas jet. To make the comparison between a narrow jet and wide jet, it was decided that the variable to keep constant between the two cases was the inner radius of the neutral jet. This was chosen to ensure that the reactions between the two fluids started at approximately the location in the duct so that the

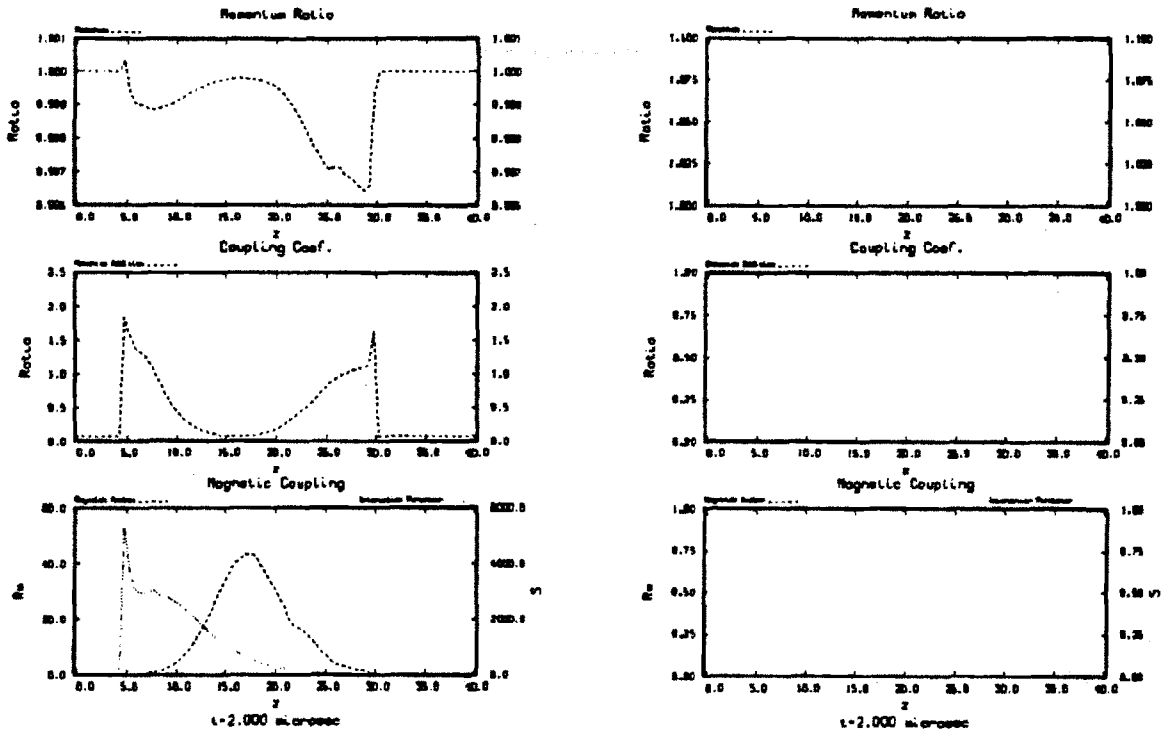


Figure 3.80: Comparison of coupling coefficients at three microseconds. Even injection on the left, wide neutral gas jet on the right.

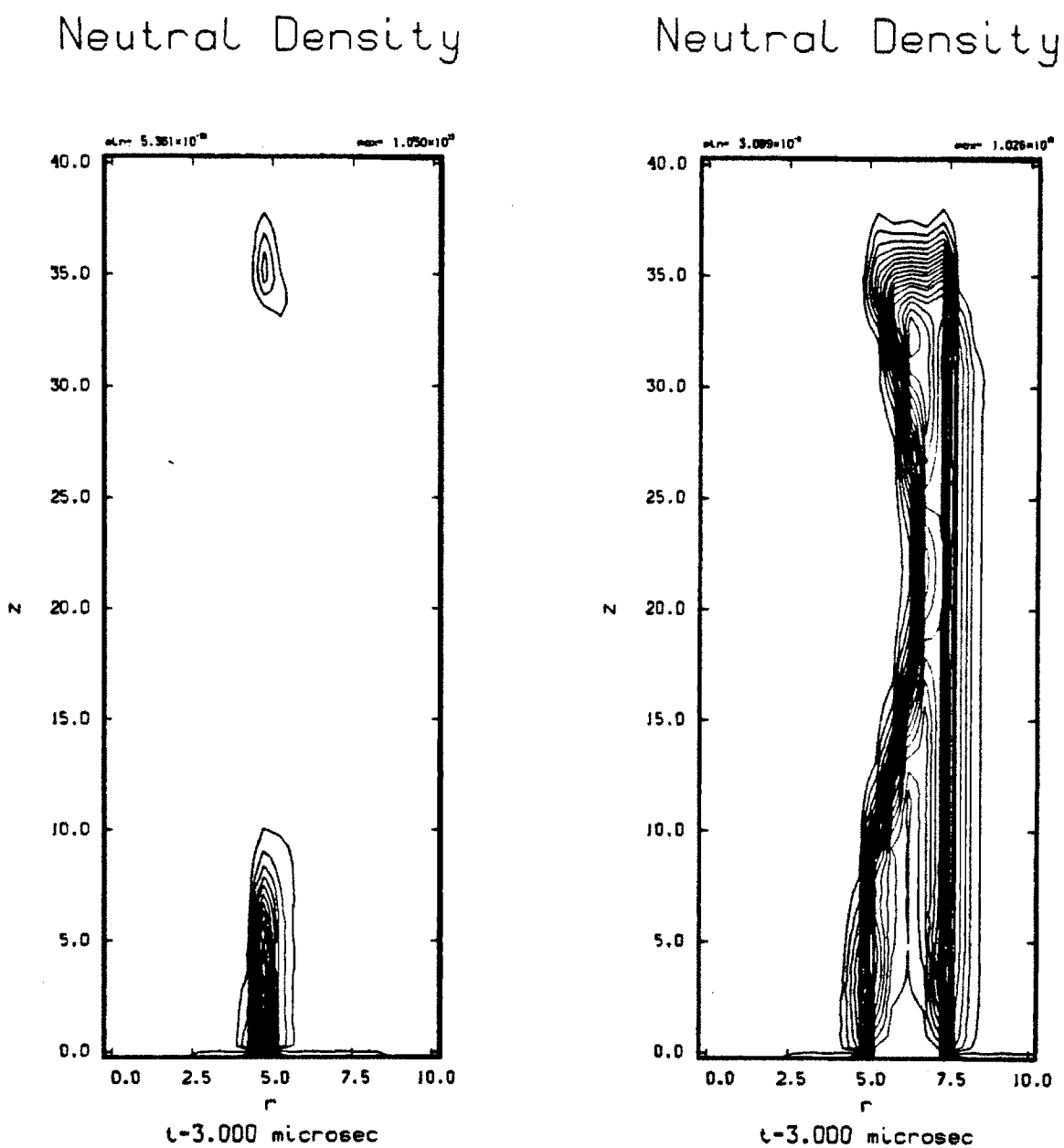
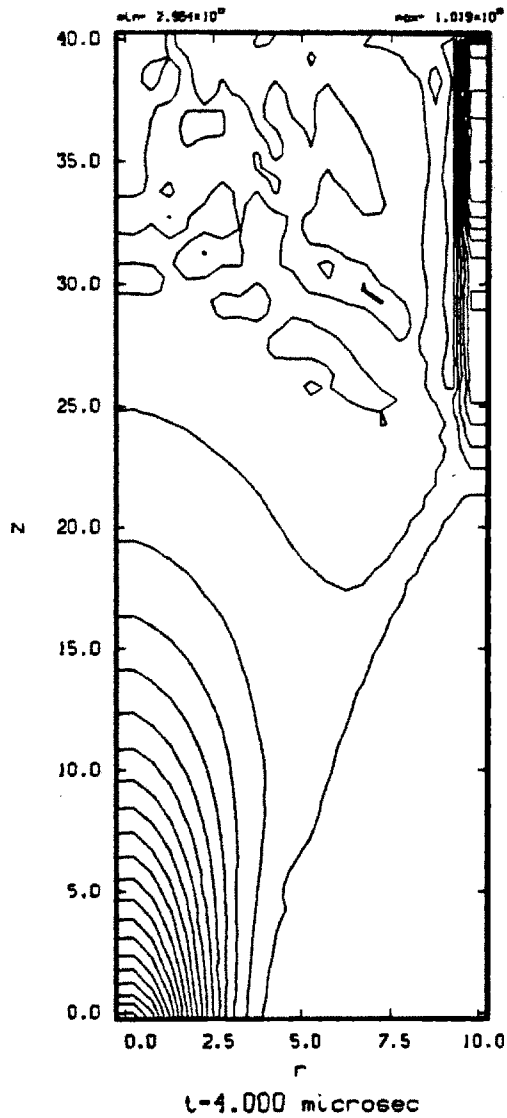


Figure 3.81: Comparison of neutral density at three microseconds. Even injection on the left, wide neutral gas jet on the right.

Ion Density



Ion Density

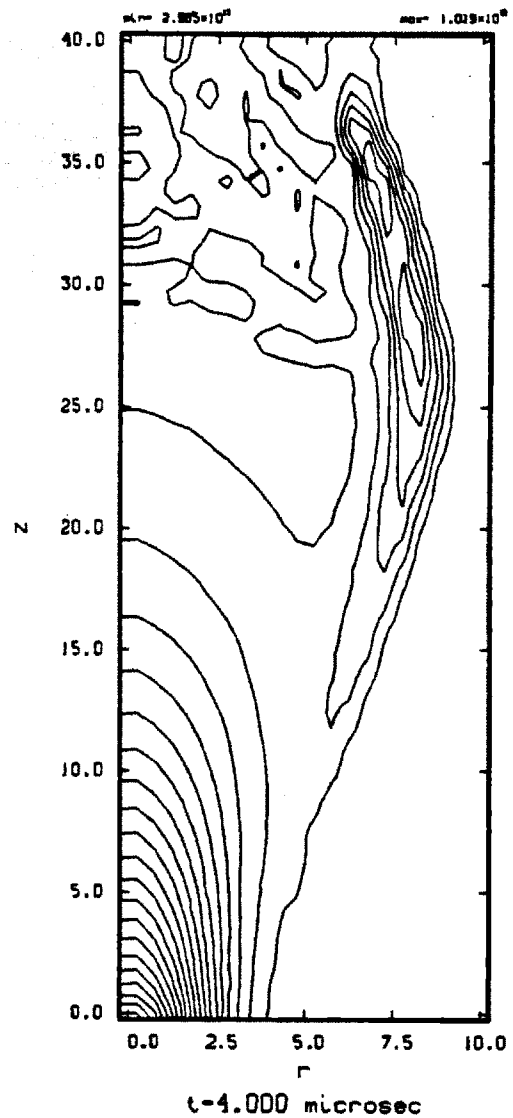


Figure 3.82: Comparison of plasma density at four microseconds. Even injection on the left, wide neutral gas jet on the right.

other parameters governing the result of the interaction (e.g., magnetic field strength) where approximately the same. The neutral density trace in the top plot in this figure is further out in radius ($r = 6.25\text{cm}$) than in the comparison case ($r = 4.75\text{cm}$). This explains the difference in length that the neutral gas has flowed into the duct before being eroded by the plasma. As has been observed in the previous cases, this distance is determined by the radius of plasma injection and magnetic field fall off. To zero order, the fluid at the very edge of the plasma column will expand and follow the field line that it was on at $z = 0$. The rate at which the magnetic field expands will govern when this field line will cross the radius of neutral gas injection. It is this distance downstream in the duct that the neutral gas flow will remain after the bulk of the neutral gas has been eroded by the plasma. In this case, that length is slightly longer at $r = 6.25\text{cm}$ than at $r = 4.75\text{cm}$, and this explains the increased length of the neutral gas column in the wide injection case as compared to the narrow injection case.

The next figure to be presented, Figure 3.84, is the neutral density at four microseconds. The variable length of the neutral gas flow discussed above is clearly seen in this figure. The plasma is expanding along the magnetic field line and that defines the front of the neutral gas that remains. The front of the plasma expansion has not quite reached the very end of the neutral gas column, but has otherwise eroded almost entirely through the neutral gas column.

The next two figures, Figure 3.85 and Figure 3.86, show the plasma and neutral gas density at five microseconds. These figures show conclusively that the plasma does indeed erode through the wide neutral gas jet and runs into the wall at r_{max} .

It is obvious from this run that increasing the width of the neutral gas jet does little more than to change the time scale of the initial transient phase of the device. No significant change in the reaction mechanics were observed that would lead one to believe that the wide jet injection would make any difference in a full self consistent simulation (with a dynamic magnetic field). The plasma still clung to the magnetic field and the plasma parameters suggested that the plasma would not significantly distort the field.

The most promising cases that may induce some type of field line distortion were they high density neutral gas injection. Though these cases may not pose acceptable operating conditions for a hybrid plume rocket, they need to be examined further to see if they do in fact modify the field structure. If the full simulation shows that the

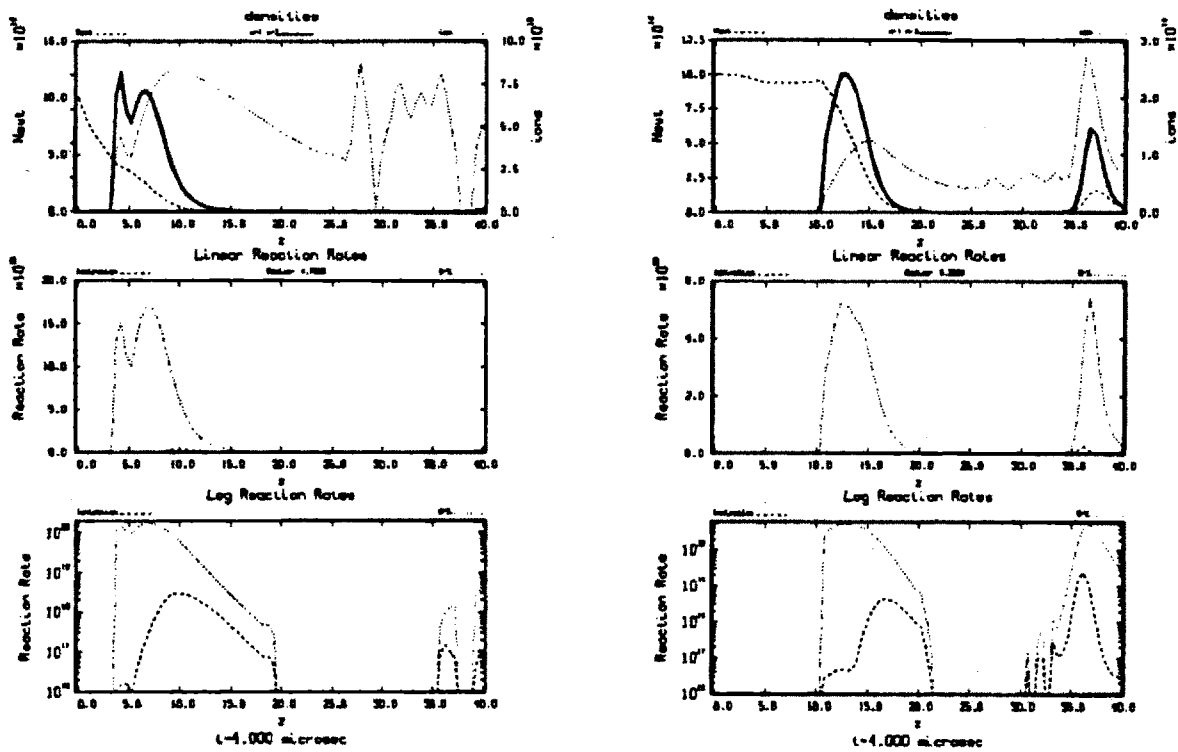


Figure 3.83: Comparison of reaction rate plots at four microseconds. Even injection on the left, wide neutral gas jet on the right.

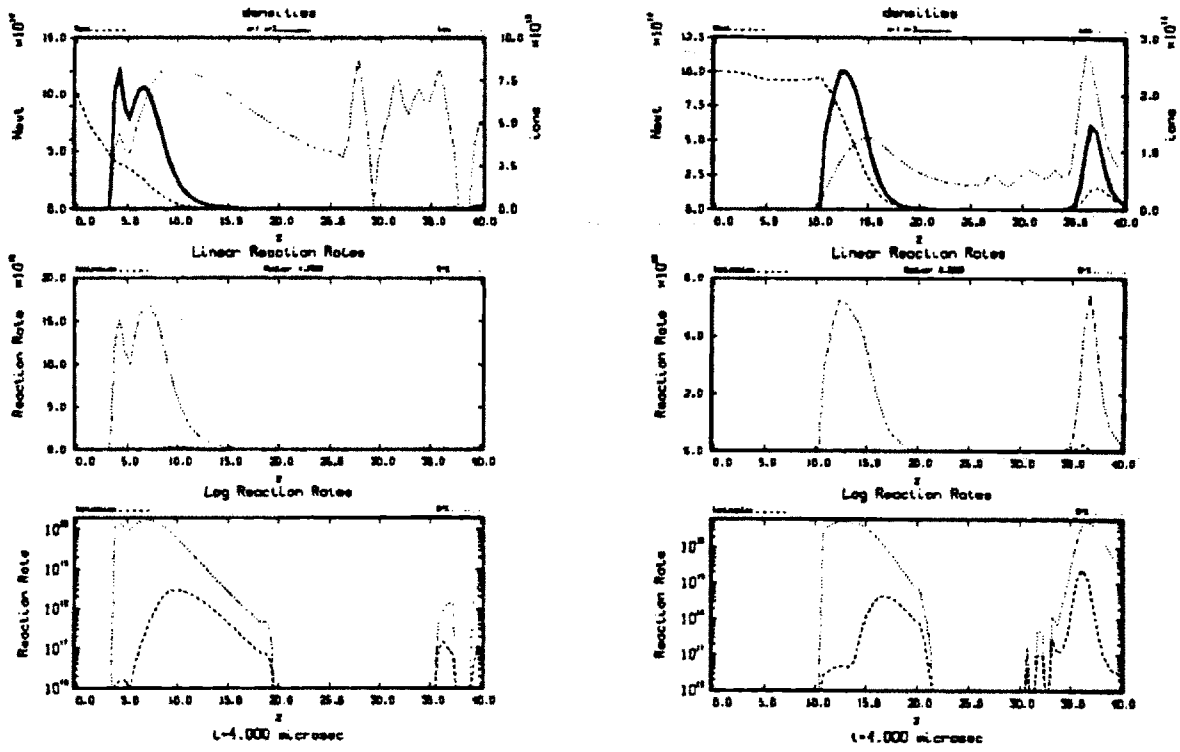


Figure 3.84: Comparison of neutral density at four microseconds. Even injection on the left, wide neutral gas jet on the right.

Ion Density

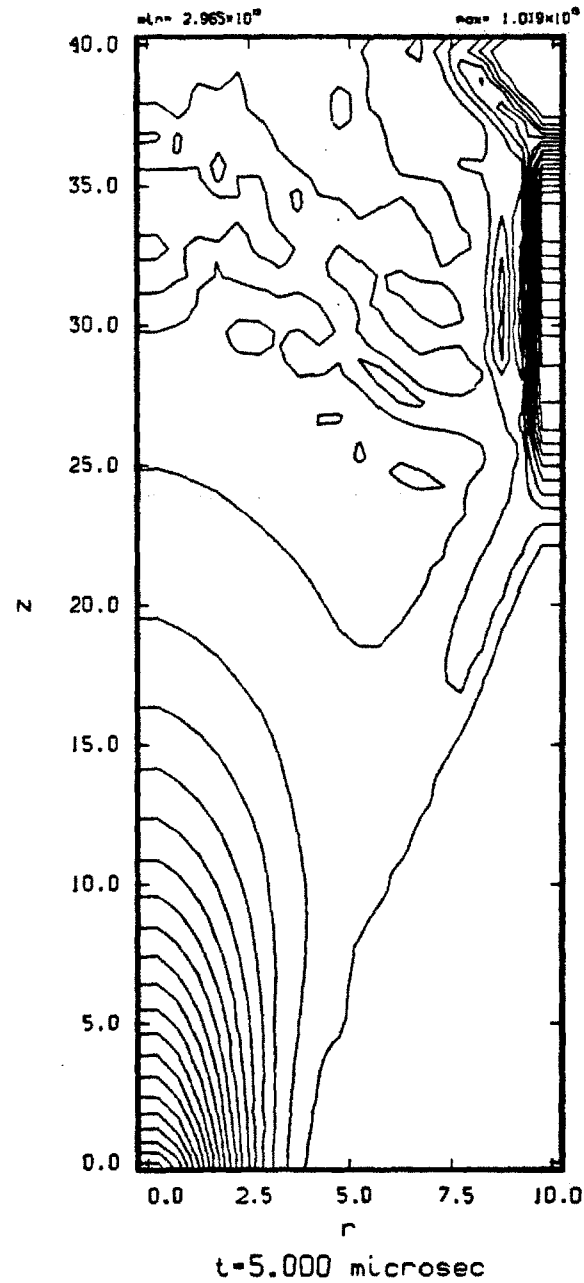


Figure 3.85: Plasma density at five microseconds for wide injection of the neutral gas jet.

Neutral Density

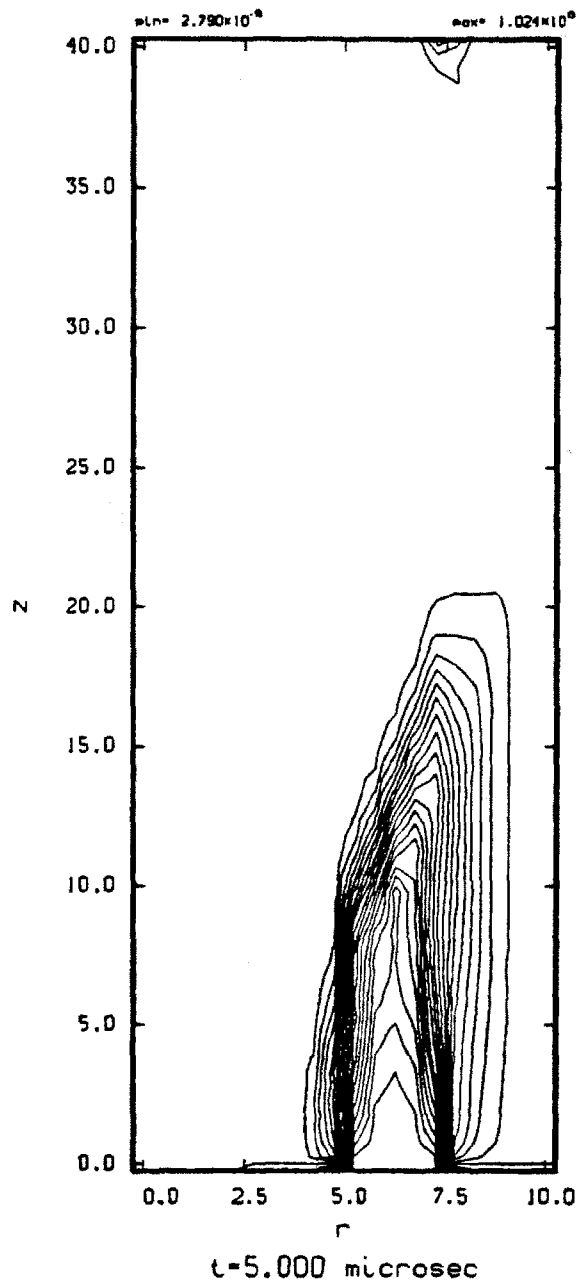


Figure 3.86: Neutral density at five microseconds for wide injection of the neutral gas jet.

field is modified in the manner that is promising to the operation of the hybrid plume plasma rocket, further research could be pursued to find alternative ways of obtaining similar results in a parameter regime that is optimistic for hybrid plume rocket. The results of the full simulation with a self consistent magnetic field will now be presented.

3.4 Code Results, Dynamic Magnetic Field

The previous sections results were obtained with a static magnetic field. The magnetic field was held constant in time at its original vacuum configuration. This was done to allow the code to be run out to longer times, as described in the previous section. This was done so that the reader could get a complete picture of the dynamics of the interaction between a plasma and a neutral gas jet. If the simulation ended at 2.25 microseconds, as some of the simulations in this section will, the complete picture of the interaction is not clear. The interactions would have just started to become significant and it would not be clear what the outcome might be if the simulation would run just a few more microseconds.

The results from the previous section leaves one with the opposite feeling. What would be the result of the interactions right at the start of the mixing, when the plasma/gas interactions are the strongest, if the magnetic field were allowed to change in time. It is the purpose of this section to answer this question. In doing so the analysis will focus on the dynamics of the magnetic field. The simulations will stop at about 2.5 microseconds (one simulation made it to a little past 2.25 microseconds). The figures presented in the previous section started at two microseconds, so one might assume that a very short time span of the interactions are being modeled. The previous sections results were shown at time increments of one microsecond for brevity because the simulations continued out for several microseconds. In the proposed simulations the time increments between the plots will be one quarter of a microsecond. This is to ensure that an important transient of the simulation is not missed.

The following cases will be analyzed.

1. Thirty percent beta case, equal neutral gas injection. In the previous section the low beta cases were the least promising, so the concentration in this chapter will be on higher beta cases.

2. One hundred percent beta, equal neutral gas injection. The actual beta for the simulation was set in the high nineties.
3. One hundred percent beta, hundred times neutral gas injection. This case showed the most promise in the previous section.

The only plots that will be presented in the following cases will be for the magnetic field configuration. The details of the dynamics are very similar to the results from the previous sections. From the previous section the basic flow behavior is known, the question is what is the time dependent field response.

3.4.1 Thirty percent beta

The results for plasma injection at thirty percent beta will now be presented. The first figure will consist of a time series of plots depicting the magnetic field at several time intervals. All of the magnetic field plots in this section will have this basic form. The individual subplots on the graph will have no markings such as axes labels, axes length, etc. The subplots should look similar to the plots presented in the previous section. The vertical axis is the z axis, and ranges from $z = 0cm$ at the bottom of the plot, to $z = 40cm$ at the top of each plot. The horizontal axis is the r axis, and ranges from $r = 0cm$ at the left hand side, to $r = 10cm$ at the right hand side of each plot. The tick intervals are $5cm$ in the z dimension and $2.5cm$ in the r dimension. The only label each subplot will have is a time label near the top of the plot. This is to ensure that the time sequence is interpreted in the correct order. The time label will be in units of microseconds, and will range from $t = 0.00$ microseconds in the upper left hand corner of the figure, to $t = 2.25$ microseconds in the lower right hand corner of the figure. The sequence proceeds from left to right in each of three rows.

Figure 3.87 is the time evolution of the magnetic field for the thirty percent beta case with no reactions between the plasma and neutral gas jet. This figure will be used as a reference case for comparison to the case with reactions turned on. The vacuum field at $t = 0$. is shown in the upper left hand corner. At z_{min} a radial force balance is imposed between the plasma and the magnetic field.

To help visualize the flow, remember that the plasma radius is $4cm$ (the center tick mark on the r axis is $5cm$). At the current injection velocity the plasma travels approximately $5cm$ in each $.25$ microsecond interval. As the plasma expands radially, this

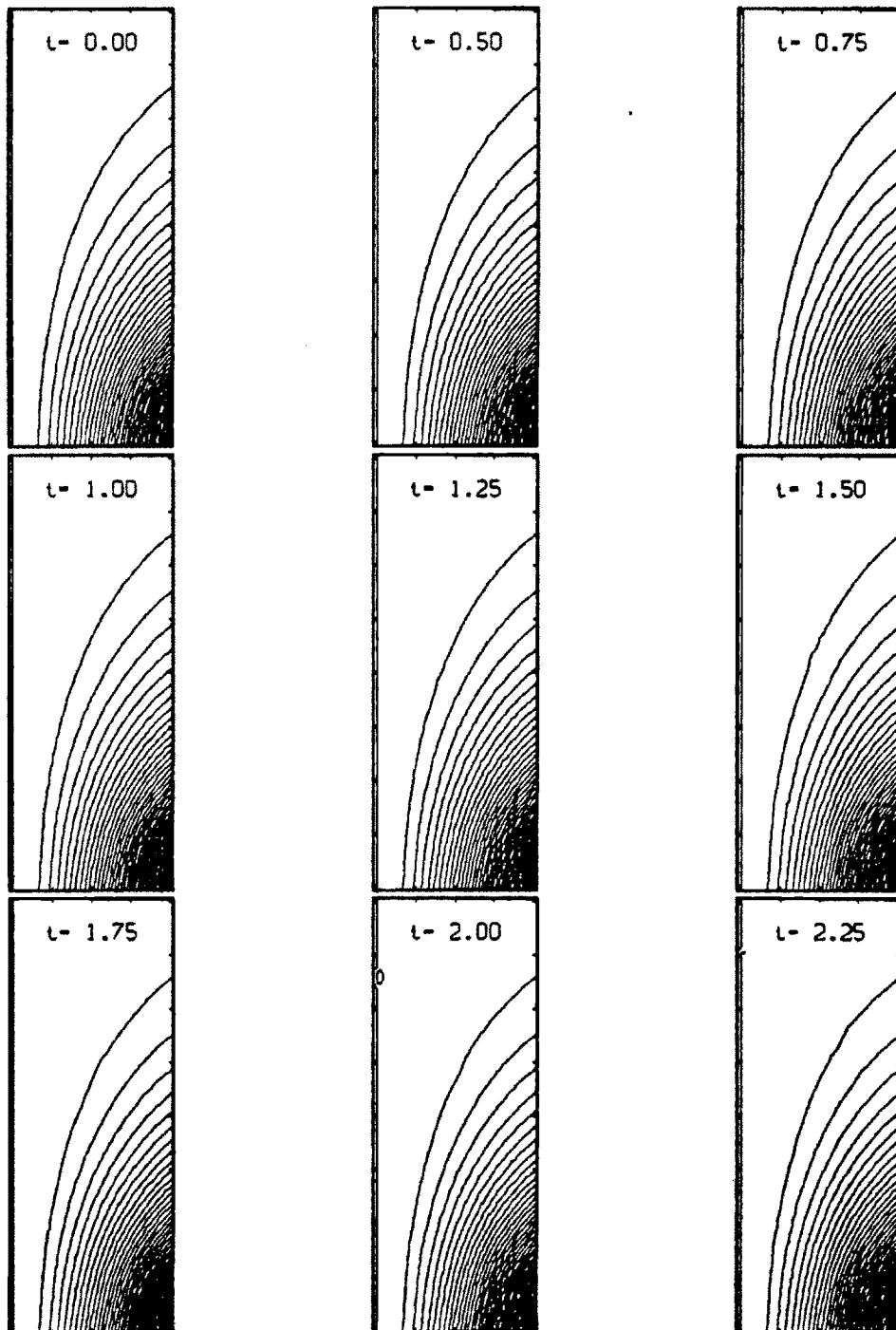


Figure 3.87: Magnetic field time evolution for thirty percent beta case. No interactions between the plasma and neutral gas jet. Time is in microseconds

distance is reduced, beginning at approximately 1.5 microseconds. At 1.5 microseconds, the plasma has streamed to just short of 30cm. At 2.25 microseconds, the plasma has stream to just past 35cm.

There is a very slight disturbance in the field visible at the $t = 2.25$ plot. This is where the front of the plasma has propagated to, and the vacuum field is adjusting to the presence of the plasma. It is very slight and for all practical purposes the field can be assumed to be static.

The next figure, Figure 3.88, is the same time series but with the reactions between the plasma and the neutral gas jet turned on. As one can see, the two figures are nearly identical. When an individual subplot is enlarged and super-imposed on the correspond reference plot, a very slight difference in field can be seen. The difference is absolutely non-consequential to the flow and the field can be assumed static in time.

3.4.2 One-hundred percent beta case

The next case to consider is the case with the plasma injected at a beta of one-hundred percent. The first figure to be presented, Figure 3.89, is the reference case for the plasma flow with no interactions. In this case it is more obvious that something is actually happening in the plots.

The first time dependent behavior is seen on the first subplot after $t = 0$. It can be seen that the magnetic field has been pushed out radially by the plasma pressure. At such a high beta, one would expect to see that the plasma should have some effect on the magnetic field.

The first significant field distortion happens at $t = 1.5$ microseconds. This distortion can now be followed through the plots. It develops sharp kinks and $t = 2$. and $t = 2.25$ microseconds. These kinks are a consequence of the relatively course grid used in this simulation. The actual magnetic field would allow be smooth. It can be seen in this series of plots that the plasma is expanding radially and pushing on the magnetic field. At these time scales the magnetic field does not have a chance to diffuse through the plasma and hence the plasma expansion changes the magnetic field configuration slightly.

The next figure, Figure 3.90, shows the field response with the reactions between the plasma and neutral gas jet turned on.

The strong influence that was seen at the $t = 2.2$ microsecond time step has been

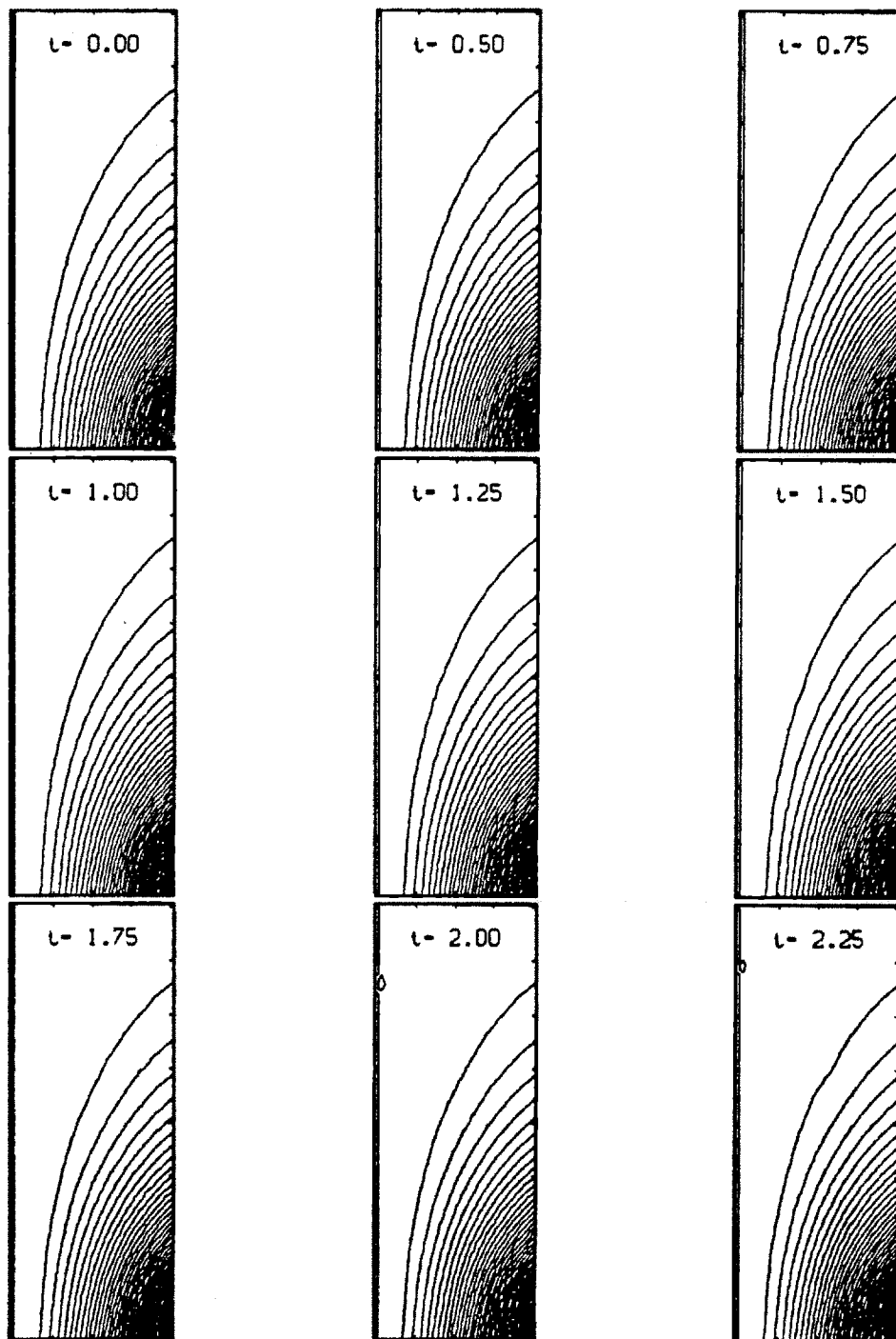


Figure 3.88: Magnetic field time evolution for thirty percent beta case. Reactions between the plasma and neutral gas jet turned on. Time is in microseconds

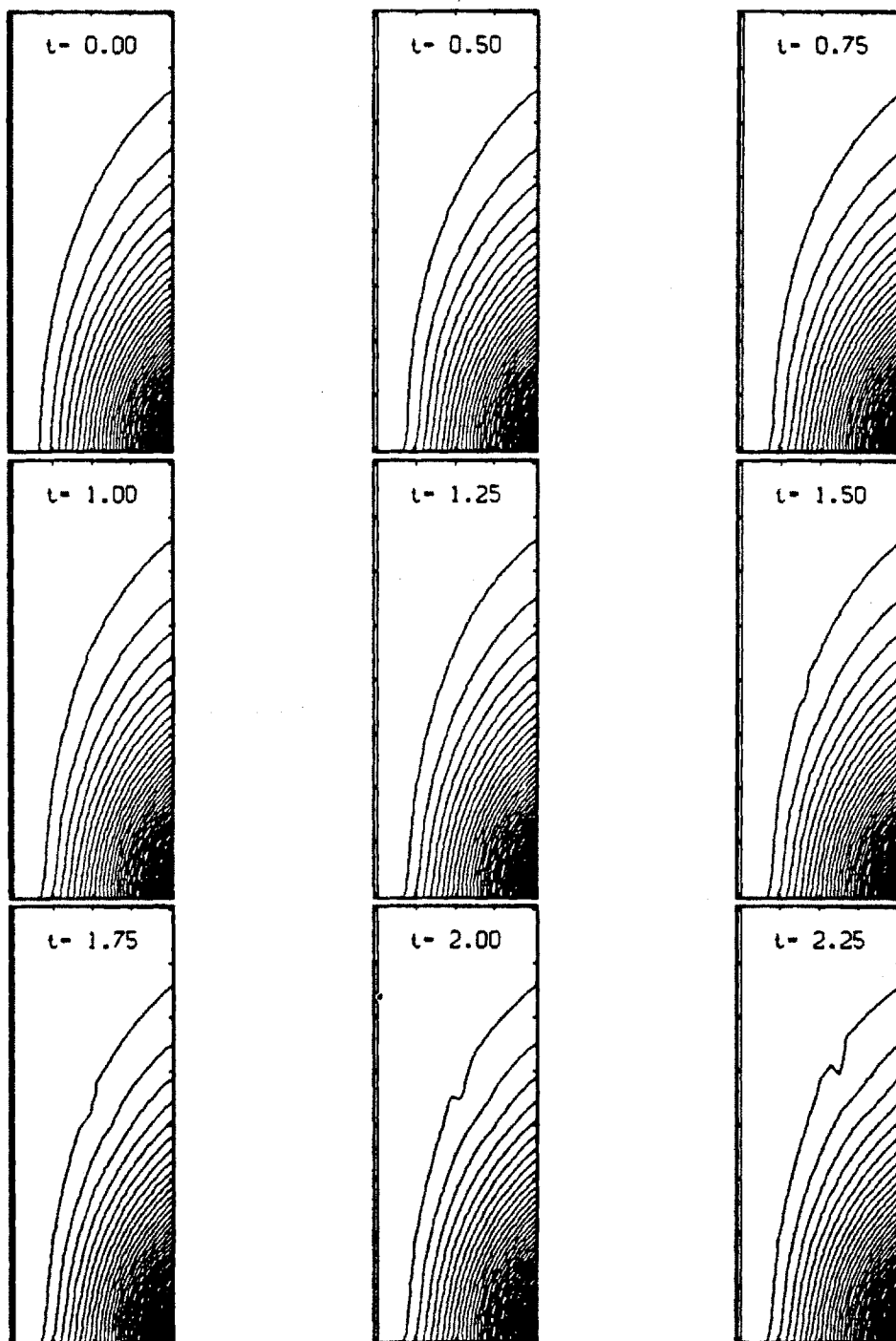


Figure 3.89: Magnetic field time evolution for one-hundred percent beta case. No reactions between the plasma and neutral gas jet. Time is in microseconds

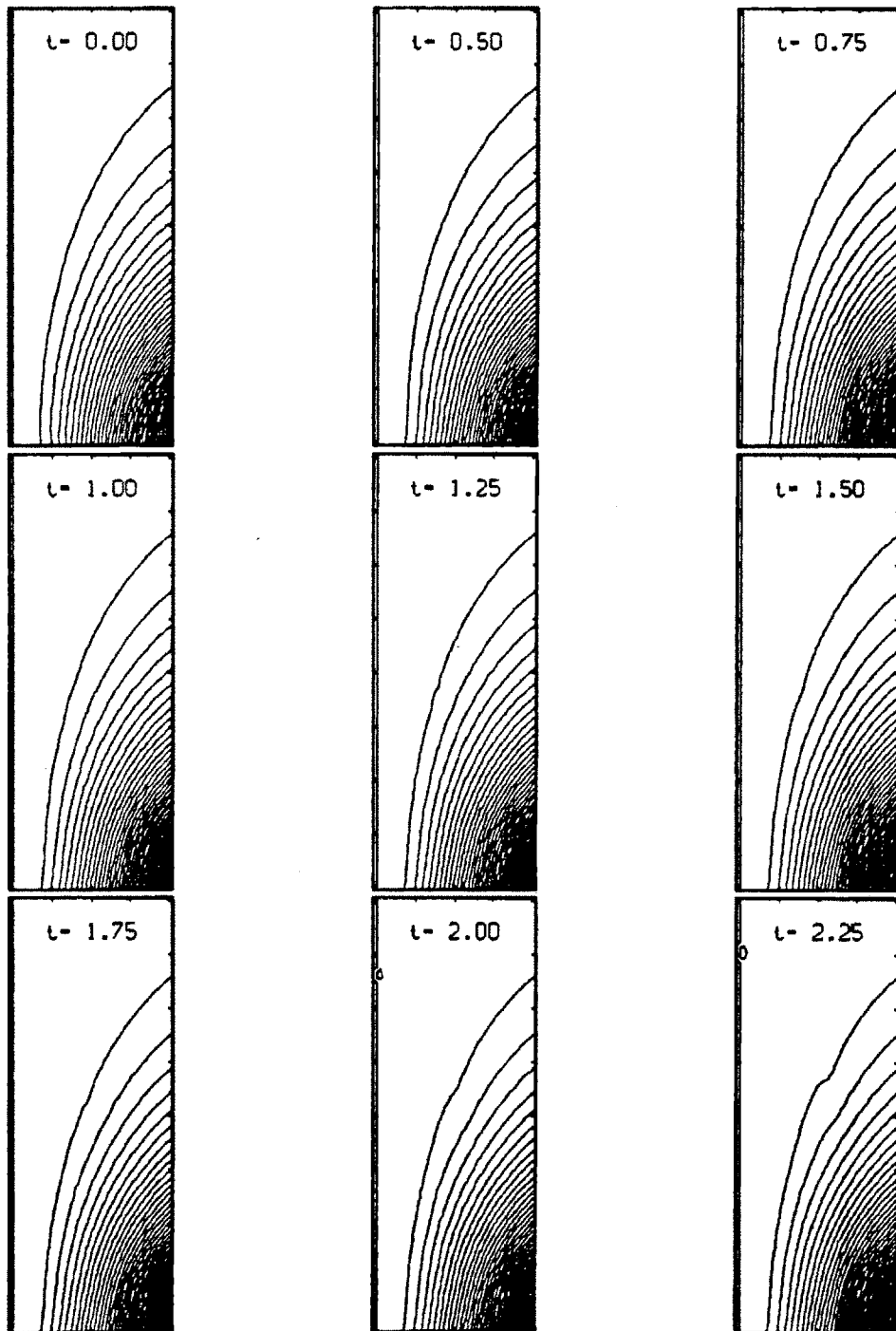


Figure 3.90: Magnetic field time evolution for one-hundred percent beta case. Reactions between the plasma and neutral gas jet turned on. Time is in microseconds

greatly reduced. A slight disturbance is still seen propagating along the magnetic field but it is has been greatly reduced. The reason for this is that the interactions between the plasma and neutral gas jet have slowed the plasma's radial expansion. In fact the local temperature and flow velocities have been reduced in the region near the neutral jet, and the plasma no longer can have a significant effect on the magnetic field configuration. This will be discussed in more detail in the next section.

3.5 Discussion

The two previous sections' results show that the axial injection of neutral gas does not have a significant effect on the plasma flow. This is very surprising because in some simulations the momentum of the neutral gas is larger than the momentum of the plasma. When the two flows interact the numerical results predict that the neutral gas will have very little effect on the plasma fluid. The explanation of this result lies in understanding the coupling between the two fluids and the relative strength of the magnetic field to the plasma inertia. This explanation was described in several sections in the above analysis, and will be summarized here.

The two quantities that were used extensively to characterize the interactions were the magnetic Reynolds number, R_m , and the magnetic interaction parameter, S . The magnetic Reynolds number was defined in Equation 3.12 on page 63. It is the ratio of convection of plasma fluid to the diffusion of the magnetic lines of force through the plasma. The magnetic interaction parameter was defined in Equation 3.13 on page 64. It is the ratio of plasmas' $\mathbf{J} \times \mathbf{B}$ force to the plasmas' inertia force.

If the magnetic Reynolds number is very much less than one the behavior of the fluid is dominated by diffusive effects. This means the magnetic lines of force are free to diffuse (slip) through the plasma fluid (or the plasma can diffuse through the magnetic field). In the opposite limit, $R_m \gg 1$, the reverse behavior is expected, and the magnetic lines of force are said to be frozen into the plasma fluid. However, the magnetic Reynolds number being very large or very small does not absolutely predict the behavior of the flow. If the magnetic Reynolds number is very small, it means that the magnetic lines of force *can* diffuse through the plasma (or that the plasma *can* diffuse across the magnetic field). It does not *mandate* that the magnetic field (or plasma fluid) will behave in a certain manner. A high magnetic Reynolds number

	$S \ll 1$	$S \gg 1$
$R_m \ll 1$	case 1	case 2
$R_m \gg 1$	case 3	case 4

Table 3.8: Simple table depicting relationships between magnetic Reynolds number and Magnetic interaction parameter.

implies that the plasma and field move together, but it does not answer whether the plasma distorts the field lines or just flows along the background magnetic field.

The other dimensionless parameter characterizing the plasma fluid is the magnetic interaction parameter. It, too, has limiting cases, but again the behavior at these limits cannot be predicted from this parameter alone. For example, the magnetic interaction parameter being very much greater than one does not guarantee that the magnetic field is not distorted in any way. Clearly, other physical parameters must be considered.

With two dimensionless parameters characterizing the flow, there exist four possible combinations of these parameters. The characteristic behavior of each combination of parameters would be expected to be different. These combinations are depicted in Table 3.8.

The off diagonal entries in this table are the most straightforward to understand. They represent the cases where the two parameters are at opposite extremes. In the following analysis it helps to think of the magnetic Reynolds number not only as implying frozen flow, but also as the importance of the induced magnetic field of the plasma.

In terms of the nomenclature of Table 3.8, consider *case 3* first. Here we have a low magnetic interaction parameter indicating that the relative strength of the $\mathbf{J} \times \mathbf{B}$ compared to the plasma inertia force is small. The magnetic Reynolds number is very much greater than one, indicating that the magnetic field is frozen in the plasma fluid. Does the field deform? In this case, it does. $R_m \gg 1$ suggests that the induced magnetic field is significant. This induced field can modify the background field ($S \ll 1$). The plasma flow will still be field aligned. The plasma produces its own field that deforms the background field and the plasma then follows this *new* field.

Now consider *case 2*. In this scenario $R_m \ll 1$ is assumed. This implies that the plasma is not frozen to the magnetic field. Perhaps a more appropriate interpretation is that the significance of the magnetic field induced by the plasma fluid is reduced. Now

consider that $S \gg 1$. This implies that the magnetic force is significantly greater than the plasma inertia. This suggests that the plasma flow will be strongly influenced by the magnetic field, implying that the flow will tend to follow the magnetic field lines.

The diagonal cases in Table 3.8 are more difficult to analyze. In *case 4* both the magnetic Reynolds number and the magnetic interaction parameter are assumed to be very much greater than one, making it difficult to decide if one parameter dominates the interaction. The same uncertainty applies to *case 1*, when both parameters are small. One needs a new tool to help decide the characteristics of the interaction when both parameters are in the same extreme.

An obvious comparison is the ratio of the two dimensionless parameters involved. One would expect *case 1* and *case 4* to have two subcases, when the ratio $R_m/S \gg 1$ and when $R_m/S \ll 1$. The ratio of R_m/S is

$$\frac{R_m}{S} = \frac{\frac{1}{2}\rho u^2}{B^2/2\mu_0}. \quad (3.16)$$

The physical interpretation of this ratio is as follows. The numerator is the plasma ram pressure[†] that was discussed at the beginning of this chapter (Equation 3.2). The denominator is the magnetic field energy density. This ratio is an indication of whether the plasma has enough directed energy to deform the magnetic field. It will be referred to as the ram pressure ratio.

Considering the ram pressure ratio, the diagonal cases in Table 3.8 become easier to analyze. Start with *case 4* and assume the ram pressure ratio is large. As discussed earlier, $R_m \gg 1$ suggests that the induced field is significant. Because the ram pressure ratio is also large suggests that the induced field will deform the background field. The frozen flow principle implies that the flow and field lines will move together.

The other extreme in *case 4* is when the ram pressure ratio is small. From this, one would not expect the plasma to deform the field very much. The Reynolds number associated with this case implies that the flow is frozen, so the field and plasma move as one. Here, the plasma simply follows the background field without distorting it.

Case 1 is a bit more challenging to consider. The important point to remember is that the magnetic Reynolds number is very much less than one. In either limit of the ram pressure ratio, the induced magnetic field is very small, and the field will not be

[†]Ram pressure as used here has units of energy density, so the units come out correctly.

	$S \ll 1$	$S \gg 1$
$R_m \ll 1$	$R_m/S \ll 1$ No effect on B . No ram pressure, field aligned flow. <hr/> $R_m/S \gg 1$ High ram pressure, flow crosses field without deforming.	No effect on magnetic field. Field aligned flow.
$R_m \gg 1$	Deform field. Frozen flow.	$R_m/S \ll 1$ No effect on field. Field aligned flow. <hr/> $R_m/S \gg 1$ Deform field, frozen flow.

Table 3.9: Full table depicting relationships between magnetic Reynolds number, Magnetic interaction parameter, and ram pressure ratio.

significantly distorted. In the limiting case that the ram pressure ratio is very much less than one, the fluid will predominately follow the background field. There is not enough ram pressure in the fluid for the plasma to flow across the field lines (assuming a slowly expanding field).

In the limit when the ram pressure ratio is much greater than one, the induced magnetic field is very small, and the ram pressure of the flow is significantly greater than the energy density in the magnetic field. One would expect that the fluid could flow across the field without distorting it.

Notice that the interpretation using the ram pressure ratio also holds for the off diagonal cases already considered. In *case 2*, with the ram pressure ratio much less than one, it was concluded that the flow would not distort the magnetic field. In *case 3*, the ram pressure ratio is very much greater than one and it was concluded that the field would be deformed. Both of these cases are consistent with the ram pressure ratio interpretation of the interaction. In fact, in the cases with mixed extremes, the ram pressure ratio alone is sufficient to predict the behavior of the flow. In the cases involving similar extremes, additional information from other the parameters involved had to be evaluated.

These results are summarized in Table 3.9. With these results now let us consider what was observed in the simulations.

In all the cases the interactions between the plasma and the neutral gas jet had

the same qualitative behavior. There was an initial state of intense interaction that lead to an increase in plasma density. Because of the shape of the magnetic field and the manner in which the plasma was injected into the system, the plasma intersected with the neutral gas at some location downstream of the injection site. It started to interact at this location first, with the area of interaction expanding downstream along the neutral gas jet as the plasma at inner radii expanded and intersected with the neutral gas. This could give one the false impression that the plasma fluid that had first interacted with the neutral jet had been convected downstream. A time series of the two fluid flows clearly shows the actual result. Looking only at separate density plots it is easy to be fooled.

The interactions with the neutral gas slowed the plasma expansion in several ways. First, the interactions with the neutral gas jet cooled the plasma. This is because both the ionization reaction and the charge-exchange reaction cool the plasma fluid if the neutral temperature is lower than the plasma temperature, which it was. This cooling will decrease the plasma velocity. The second manner in which the interactions slowed the plasma velocity is through the momentum coupling. If the plasma velocity was lower than the neutral velocity, which it was in most of the simulations, the plasma fluid would equilibrate with the newly formed plasma at some lower velocity. The third manner in which the interactions slowed the plasma is the pressure gradient increase experienced when the plasma density increased in the interaction region.

Through these mechanisms the plasma velocity in the interaction region slowed. This increased the time it took for the plasma to transit the interaction region. This in turn increased the ratio of the plasma cell transient time compared to the characteristic reaction time, called the coupling coefficient in the analysis. The increase in the coupling coefficient could indicate that more of the neutral gas was being coupled into the plasma, when it really showed that the reactions are slowing and cooling the plasma. The slowing of the plasma can be tolerated if the neutral gas could redirect it axially without too much loss in the net momentum of the plasma.

The cooling of the plasma was more serious. The cooling dropped the reaction cross sections, essentially shutting off the interactions between the two fluids. This acted as a built in limiting effect, never allowing a significant amount of the neutral gas to become coupled to the plasma flow.

The reactions slowly eroded the neutral gas, the exact time scale depending on

the neutral gas density and the width of the neutral jet. After the initial erosion, the neutral gas could never recover and resupport itself downstream of the injection. Even with a neutral gas velocity equal to the plasma velocity, the neutral gas could not effectively couple to the plasma flow. The answer is again in the characteristic time scales for plasma fluid convection through the interaction region versus the time scale for neutral gas addition. Even with a high neutral gas axial velocity the ratio of these characteristic times was still very large because of the built in limiting effect of the interactions. This allowed the plasma to transit the interaction region acquiring only a small fraction of its total momentum. This small addition of momentum did little to deflect the plasma flow, and the effect on the field was negligible. All the neutral gas was eventually eroded away (coupled to the plasma flow) but on too long of a time scale to affect the field. The coupling was spread out over too many plasma fluid cells to affect any single plasma cell significantly.

3.6 Conclusion

The results of these simulations were unable to reproduce, through axial injection, the approximate smoke ring structure of Figure 3.1. Therefore, this potential disconnection mechanism does not appear to be a viable candidate to induce plasma/field detachment. Other possible mechanisms need to be investigated to alleviate this potentially serious problem. These include: radial injection, magnetic field shaping and pulsed operation of the neutral gas jets. Some of these mechanisms are discussed in Chapter 4.

Chapter 4

Recommendations

This chapter suggests ideas that can be pursued to create the conditions necessary for the formation of the hybrid plume rocket. It also suggests improvements to the numerical code developed to study the hybrid plume system.

4.1 Hybrid Plume Possibilities

Section 3.5 and Section 3.6 of Chapter 3 summarized the results of the axial injection of neutral gas for the formation of the hybrid plume plasma concept. The simulations of the hybrid plume as presented in this thesis have shown that the simple axial injection of a neutral gas jet will not bring about the formation of the hybrid plume. As shown in Chapter 3, the primary reason for this is the cooling effect of the interactions on the plasma, creating a self limiting effect. This effect prevents the neutral gas from sufficiently coupling to the plasma flow to allow the detachment process to take place. The results indicate that the reduction in plasma temperature in the interaction region is the main cause for the self limiting effect. This suggests the first idea to generate the hybrid plume.

4.1.1 Auxiliary Heating

Since the cooling of the plasma by the neutral gas in the interaction region is the prime cause of the poor coupling between the plasma fluid and the neutral gas, it has been suggested [13] that auxiliary heating in the interaction region could prevent this effect. ECH heating could be highly localized to the narrow interaction region to minimize the amount of power required. This heating could maintain the plasma temperature

sufficiently high to prevent the cross sections for plasma/neutral gas interactions from dropping significantly. This effect would sustain a high degree of momentum coupling to the plasma flow, possibly allowing the neutral gas to drive the disconnection of the plasma from the magnetic field.

4.1.2 Radial Injection of Neutral Gas

Another potential problem with the axial injection of neutral gas that was discovered was that the velocity of the neutral gas compared to the plasma velocity was low. The plasma velocity can easily be an order of magnitude higher than the neutral gas velocity. With axial injection, the plasma erodes the neutral gas on a time scale much faster than the neutral gas can resupply the region. This leads to the initial transient phase seen in the simulations. It should be restated here that even in the simulations where the neutral gas velocity equaled the plasma velocity, the same effect was observed. This can be attributed in part to the self limiting effect of the interactions discussed above.

To overcome this problem, the radial injection of the gas could be attempted. In this way one is matching the slow time scale of the plasma evolution (radial expansion) to the fast time scale of the neutral gas jet. The field could be configured to allow a very slow expansion of the magnetic field, and therefore a low radial plasma velocity. One can match the streaming velocity of the neutral gas jet more closely to the radial velocity of the plasma. This would prevent the plasma from expanding radially and guide the plasma downstream in the axial direction to a region where the field strength is low enough for detachment.

If the plasma temperature could be maintained in this region, this flow could develop a shear layer between the plasma and the neutral gas jet. If the plasma velocity could be maintained, it would tend to force the field lines to be convected downstream with the plasma, eventually detaching themselves from the ship.

Preliminary work has shown that radial injection of the neutral gas does have a significant effect on the plasma flow. Whether it can guide the plasma downstream in the manner described above has yet to be examined. A significant amount of work needs to be done to study this possibility. In particular, viscous effects should really be added to the code to better model the large radial variations in the axial velocities expected to be formed in such a simulation.

4.2 Possible Code Improvements

In this section, improvements to the numerical code will be suggested.

4.2.1 Outflow Boundary Condition

Any improvements to the outflow boundary conditions would greatly improve the robustness of the code. Currently the outflow boundary condition is very sensitive to the exact physics that is happening in the computational domain. For instance, it is sensitive to the angle that the magnetic field makes with the outflow boundary. Also, it is very unstable if a large reaction zone crosses the outflow boundary. Many attempts have been made over the years to improve these boundary conditions. At best what is now implemented is a network of fixes that are dependent on the exact nature of the problem being studied. Any improvement to these boundary conditions would greatly enhance the functionality of the code.

4.2.2 Particle-In-Cell Simulation

Switching to a Particle-In-Cell (PIC) simulation technique would greatly increase the parameter space where one would expect the code to give accurate results. For instance, because of the range of the magnetic field properties encountered in the hybrid plume, the plasma fluid travels through regions where the Larmor orbits of the particles change by orders of magnitude. The PIC simulation technique would better model these situations than a simple fluid code. Converting the code to use PIC techniques would be a major undertaking. Not only would the PIC algorithm itself need to be developed, but it would have to include the source terms that are an essential part of the hybrid plume simulation.

Appendix A

General Equations

The equations to be solved are Braginskii's[4] fluid continuity equation and energy equation for each species.

$$\frac{\partial n}{\partial t} + \nabla \cdot (\Gamma) = 0 \quad (\text{A.1})$$

$$\frac{3}{2} \frac{dT}{dt} + p \nabla \cdot \mathbf{v} = -\nabla \cdot \mathbf{q} - \pi \cdot \nabla \mathbf{v} + Q \quad (\text{A.2})$$

where n is density and T temperature. Γ is the flux vector and \mathbf{v} the fluid velocity. p is the isotropic part of the pressure, $p = nkT$. \mathbf{q} is heat flux vector and π is the pressure tensor. S_n and Q are source/sinks to density and energy, respectively. More will be said of these equations later, but for now it is enough to realize that they are coupled, non-linear, partial differential equations. Without parallel heat conduction in the energy equation, both equations are parabolic, and can be easily finite differenced and solved with a tri-diagonal solve routine. Iterations between the energy and density equations are needed to converge to a steady state answer. The equations are very sensitive to S_n and Q , and thus to the rate-coefficient $\langle \sigma v \rangle$ of the various reactions. To allow the code to iterate to convergence, one must under-relaxate the code by starting with an artificially low value of $\langle \sigma v \rangle$ for all the reactions. Once the code converges for a given value of $\langle \sigma v \rangle$, $\langle \sigma v \rangle$ is slowly increased until the true value of $\langle \sigma v \rangle$ is obtained.

An exact description of the equations and physical model used in the solution technique will be presented in the next section.

A.1 Derivation of Transport Equations

Braginskii derived Eqs. (1.1) and (1.2) by taking appropriate moments of the Fokker-Planck equation

$$\frac{\partial f}{\partial t} + \nabla \cdot (\mathbf{v}f) + \frac{\partial}{\partial \mathbf{v}} \cdot \left(\frac{\mathbf{F}}{m} f \right) = C. \quad (\text{A.3})$$

Here f is the distribution function for each species, \mathbf{v} is the velocity, m is the particle mass, and \mathbf{F} is the force exerted on a particle. On the right hand side of Eq. A.3, C , called the collision term, takes into account the complex behavior of rapid close "collisions" through particle microfields. Particles can collide with different species, including themselves, so one must write

$$C_a = \sum_b C_{ab}(f_a, f_b) \quad (\text{A.4})$$

where C_a is the total collision term for species a , and C_{ab} is the collision term for species a with species b . The actual form of C for this treatment is not needed; one only needs to know that C obeys various conservation conditions:

$$\int d\mathbf{v} C_{ab} = 0 \quad (\text{A.5})$$

$$\int d\mathbf{v} m_a \mathbf{v} C_{aa} = 0 \quad (\text{A.6})$$

$$\int d\mathbf{v} \frac{m_a v^2}{2} C_{aa} = 0 \quad (\text{A.7})$$

Equation A.5 implies that collisions with species b conserves particles. If collisions change species the actual conservation equation would be

$$\int d\mathbf{v} C_{ab} + \int d\mathbf{v} C_{ba} = 0 \quad (\text{2.3a})$$

Braginskii did his derivation assuming form [Eq. A.5] was valid, i.e., there were no sinks or sources of particles due to collisions. As will be seen, assuming form Eq. (2.3a) will only introduce a source term S_n on the right hand side of Eq. (1.1).

Assuming collisions between species are elastic, two more conservation relations are obvious:

$$\int d\mathbf{v} m_a \mathbf{v} C_{ab} + \int d\mathbf{v} m_b \mathbf{v} C_{ba} = 0 \quad (\text{A.8})$$

$$\int d\mathbf{v} \frac{m_a v^2}{2} C_{ab} + \int d\mathbf{v} \frac{m_b v^2}{2} C_{ba} = 0 \quad (\text{A.9})$$

A.1.1 Density

Taking the particle moment ($\int d\mathbf{v}$) of Eq. A.3 gives

$$\frac{\partial}{\partial t} \int d\mathbf{v} f_a + \int d\mathbf{v} \nabla \cdot (\mathbf{v} f_a) + \int d\mathbf{v} \nabla_{\mathbf{v}} \cdot \left(\frac{\mathbf{F} f_a}{m_a} \right) = \int d\mathbf{v} C_{ab}. \quad (\text{A.10})$$

The integral in the first term of Eq. A.10 is by definition n , so the first term becomes $\partial n / \partial t$. For the second term, define the mean velocity of species a as

$$\mathbf{V}_a = \frac{1}{n} \int d\mathbf{v} \mathbf{v} f_a \equiv \langle \mathbf{v} \rangle. \quad (\text{A.11})$$

The second term in Eq. A.10 is then $\nabla \cdot (n \mathbf{V})$. The third term of Eq. A.10 can be converted into a surface integral, and since f_a goes to zero as v goes to infinity for any physical distributions, the surface integral vanishes. The right hand side of Eq. A.3 would equal zero if Eq. A.5 was used, and thus Eq. A.10 becomes

$$\frac{\partial n}{\partial t} + \nabla \cdot (n \mathbf{V}) = 0 \quad (\text{A.12})$$

which is Braginskii's equation (1.11). For our model, Eq. (2.3a) must be used. Defining

$$S_n = - \int d\mathbf{v} C_{ba} \quad (\text{A.13})$$

the right hand side becomes the source term of particles, and thus Eq. A.10 becomes

$$\frac{\partial n}{\partial t} + \nabla \cdot (n \mathbf{V}) = S_n \quad (\text{A.14})$$

A.1.2 Momentum

Taking the momentum moment ($\int d\mathbf{v} m\mathbf{v}$) of Eq. A.3 gives

$$m \frac{\partial}{\partial t} \int d\mathbf{v} \mathbf{v} f + m \int d\mathbf{v} \mathbf{v} \nabla \cdot (\mathbf{v} f) + \int d\mathbf{v} \mathbf{v} \nabla \cdot (\mathbf{F} f) = \int d\mathbf{v} m\mathbf{v} C. \quad (\text{A.15})$$

The first term by Eq. refvbar is $\frac{\partial}{\partial t} (mn\mathbf{V})$. In the second term, ∇ , which is $\nabla_{\mathbf{x}}$, can be taken outside of the velocity integral, and we have $\nabla \cdot (mn\langle \mathbf{v}\mathbf{v} \rangle)$. Integrating the third term by parts once, assuming $f \rightarrow 0$ as $\mathbf{v} \rightarrow \infty$, gives $-\int d\mathbf{v} \mathbf{F} f$. Here $\mathbf{F} = (q\mathbf{E} + \frac{q}{c}\mathbf{v} \times \mathbf{B})$, so the third term becomes $-\int d\mathbf{v} (q\mathbf{E} + \frac{q}{c}\mathbf{v} \times \mathbf{B}) f$, which can be rewritten as $-q\mathbf{E} \int d\mathbf{v} f + \frac{q}{c}\mathbf{B} \times \int d\mathbf{v} \mathbf{v} f$, or, $-q\mathbf{E}n + \frac{q}{c}\mathbf{B} \times \mathbf{V}n$, which is $-qn(\mathbf{E} + \frac{1}{c}\mathbf{V} \times \mathbf{B})$. Adding terms gives Braginskii's Eq. (1.12)

$$\frac{\partial}{\partial t} (mn\mathbf{v}) + \nabla \cdot (mn\langle \mathbf{v}\mathbf{v} \rangle) - qn \left(\mathbf{E} + \frac{1}{c}\mathbf{V} \times \mathbf{B} \right) = \int d\mathbf{v} m\mathbf{v} C. \quad (\text{A.16})$$

A.1.3 Energy

Taking the energy moment ($\int d\mathbf{v} \frac{mv^2}{2}$) of Eq. A.3 gives

$$\int d\mathbf{v} \frac{\partial f}{\partial t} \frac{mv^2}{2} + \int d\mathbf{v} \frac{mv^2}{2} \nabla \cdot (\mathbf{v} f) + \int d\mathbf{v} \frac{mv^2}{2} \frac{\partial}{\partial \mathbf{v}} \cdot \left(\frac{\mathbf{F}}{m} f \right) = \int d\mathbf{v} \frac{mv^2}{2} C. \quad (\text{A.17})$$

By pulling the time derivative out of the first term, and defining the average of any quantity Q as $\langle Q \rangle = \frac{1}{n} \int d\mathbf{v} Q f$, the integral becomes $\frac{\partial}{\partial t} \left(\frac{mn}{2} \langle v^2 \rangle \right)$. Cancelling m 's in the third term and integrating by parts once with respect to \mathbf{v} , we reduce the term to $-\int d\mathbf{v} \mathbf{v} \cdot \mathbf{F} f$, remembering that the constant term obtained by integration of parts does not contribute for physical distributions ($f \rightarrow 0$ as $\mathbf{v} \rightarrow \infty$). With \mathbf{F} the Lorentz force on the particle,

$$\mathbf{v} \cdot \mathbf{F} = \left(q\mathbf{E} \cdot \mathbf{v} + \frac{q}{c} \mathbf{v} \cdot \mathbf{v} \times \mathbf{B} \right). \quad (\text{A.18})$$

The second term simplifies because \mathbf{v} and $\mathbf{v} \times \mathbf{B}$ are orthogonal. With the definition of the fluid velocity, Eq. A.11, the remaining term becomes $-qn\mathbf{E} \cdot \mathbf{V}$. Adding the terms on the left hand side we find

$$\frac{\partial}{\partial t} \left(\frac{mn}{2} \langle v^2 \rangle \right) + \nabla \cdot \left(\frac{mn}{2} \langle v^2 \mathbf{v} \rangle \right) - qn\mathbf{E} \cdot \mathbf{V} = \int d\mathbf{v} \frac{mv^2}{2} C \quad (\text{A.19})$$

which is Braginskii's energy Eq. (1.13).

With Eqs. A.12, A.16, and A.19 we have a complete set of transport equations. Braginskii then rewrote Eq. A.16, the momentum equation, and Eq. A.19, the energy equation, obtaining the equation of motion and the equation of transport of internal energy, respectively. The details of this transformation will be presented in the next section.

A.2 Velocity Decomposition Transformation

To transform the momentum equation (Eq. A.16) and the energy equation (Eq. A.19) to a more convenient form, we decompose the velocity \mathbf{v} into a mean velocity \mathbf{V} , and a random part $\mathbf{v}' \equiv \mathbf{v} - \mathbf{V}$. By definition, $\langle \mathbf{v}' \rangle = 0$, thus $\mathbf{v} = \mathbf{V} + \mathbf{v}'$, where $\langle \mathbf{v} \rangle \equiv \mathbf{V}$.

A.2.1 Momentum Transport Equation

For the momentum equation, (Eq. A.16) we need to average the dyad $\mathbf{v}\mathbf{v}$. In the new notation, this becomes

$$\begin{aligned} \langle \mathbf{v}\mathbf{v} \rangle &= \langle (\mathbf{V} + \mathbf{v}')(\mathbf{V} + \mathbf{v}') \rangle \\ &= \langle \mathbf{V}\mathbf{V} + 2\mathbf{V}\mathbf{v}' + \mathbf{v}'\mathbf{v}' \rangle \\ &= \langle \mathbf{V}\mathbf{V} \rangle + 2\mathbf{V}\langle \mathbf{v}' \rangle + \langle \mathbf{v}'\mathbf{v}' \rangle \\ &= \mathbf{V}\mathbf{V} + \langle \mathbf{v}'\mathbf{v}' \rangle \end{aligned} \quad (\text{A.20})$$

where $\langle \mathbf{v}' \rangle = 0$. The first two terms of Eq. A.16 become

$$\frac{\partial}{\partial t} (mn\mathbf{v}) + \nabla \cdot (mn\langle \mathbf{v}\mathbf{v} \rangle) = mn \frac{\partial \mathbf{V}}{\partial t} + m\mathbf{V} \frac{\partial n}{\partial t} + \nabla \cdot (mn\mathbf{V}\mathbf{V}) + \nabla \cdot (mn\langle \mathbf{v}'\mathbf{v}' \rangle). \quad (\text{A.21})$$

The third term on the right hand side of Eq. A.21 can be written as

$$\begin{aligned} \nabla \cdot (mn\mathbf{V}\mathbf{V}) &= \frac{\partial}{\partial x_i} \left[m(nV_i)V_j \right] \\ &= mV_j \frac{\partial}{\partial x_i} nV_i + mnV_i \frac{\partial}{\partial x_i} V_j \\ &= m\mathbf{V}\nabla \cdot (n\mathbf{V}) + mn\mathbf{V} \cdot \nabla \mathbf{V}. \end{aligned} \quad (\text{A.22})$$

Equation A.21 then becomes

$$\begin{aligned} \frac{\partial}{\partial t} (mn\mathbf{v}) + \nabla \cdot (mn\langle \mathbf{v}\mathbf{v} \rangle) &= mn \frac{\partial \mathbf{v}}{\partial t} + m\mathbf{V} \frac{\partial n}{\partial t} + m\mathbf{V}\nabla \cdot (n\mathbf{V}) + mn\mathbf{V} \cdot \nabla \mathbf{V} \\ &\quad + \nabla \cdot (mn\langle \mathbf{v}'\mathbf{v}' \rangle) \\ &= mn \left(\frac{\partial}{\partial t} + \mathbf{V} \cdot \nabla \right) \mathbf{V} + m\mathbf{V} \left(\frac{\partial n}{\partial t} + \nabla \cdot n\mathbf{V} \right) \\ &\quad + \nabla \cdot (mn\langle \mathbf{v}'\mathbf{v}' \rangle) \\ &= mn \frac{d\mathbf{V}}{dt} + \nabla \cdot mn\langle \mathbf{v}'\mathbf{v}' \rangle. \end{aligned} \quad (\text{A.23})$$

The definition of the total derivative was used in the first term of Eq. A.23 and the continuity equation, Eq. A.12 was used to eliminate the second term. It should be noted here that if the general form of the continuity equation was used with a source term on the right hand side, there would be an extra term $m\mathbf{V}S_n$, S_n defined in Eq. A.13. Continuing with the assumption that the collision operator conserves particles, we need to express $\langle \mathbf{v}'\mathbf{v}' \rangle$. Note that

$$\begin{aligned}
\langle \mathbf{v}'\mathbf{v}' \rangle &= \langle v_i'v_j' - \frac{v'^2}{3}\delta_{ij} + \frac{v'^2}{3}\delta_{ij} \rangle \\
&= \langle v_i'v_j' - \frac{v'^2}{3}\delta_{ij} \rangle + \frac{\langle v'^2 \rangle}{3}\delta_{ij}.
\end{aligned} \tag{A.24}$$

If we define the stress tensor as

$$\underline{\pi} = mn \langle v_i'v_j' - \frac{v'^2}{3}\delta_{ij} \rangle \tag{A.25}$$

and the isotropic pressure p as

$$p = mn \frac{\langle v'^2 \rangle}{3} \tag{A.26}$$

then $\nabla \cdot mn \langle \mathbf{v}'\mathbf{v}' \rangle$ becomes, with Eq. A.24

$$\nabla \cdot mn \langle \mathbf{v}'\mathbf{v}' \rangle = \nabla \cdot \underline{\pi} + \nabla p. \tag{A.27}$$

Substituting for the new form of the first two terms of Eq. A.16, we find the equation of motion

$$mn \frac{d\mathbf{V}}{dt} = -\nabla p - \nabla \cdot \underline{\pi} + qn \left(\mathbf{E} + \frac{1}{c} \mathbf{V} \times \mathbf{B} \right) + \mathbf{R} \tag{A.28}$$

where we define \mathbf{R} as

$$\begin{aligned}
\mathbf{R} &= \int d\mathbf{v} m\mathbf{v} C \\
&= \int d\mathbf{v} m(\mathbf{V} + \mathbf{v}') C \\
&= m\mathbf{V} \int d\mathbf{v} C + \int d\mathbf{v} m\mathbf{v}' C \\
&= \int d\mathbf{v} m\mathbf{v}' C
\end{aligned} \tag{A.29}$$

if the collision operator conserves particles. It should be noted that if the general form of the continuity equation was used, the first term of Eq. A.29 would be mvS_n . This would appear on the left hand side of Eq. A.28 and would cancel with the added term on the right hand side of Eq. A.28 discussed after Eq. A.23. The final form for the equation of motion is independent of S_n .

A.2.2 Energy Transport Equation

Applying the same concept of velocity decomposition to the energy equation, Eq. A.19 on page 199

$$\frac{\partial}{\partial t} \left(\frac{mn}{2} \langle v^2 \rangle \right) + \nabla \cdot \left(\frac{mn}{2} \langle v^2 \mathbf{v} \rangle \right) - qn\mathbf{E} \cdot \mathbf{V} = \int d\mathbf{v} \frac{mv^2}{2} C$$

and expanding the first two terms

$$\begin{aligned} \frac{\partial}{\partial t} \left(\frac{mn}{2} \langle v^2 \rangle \right) + \nabla \cdot \left(\frac{mn}{2} \langle v^2 \mathbf{v} \rangle \right) &= \frac{\partial}{\partial t} \left(\frac{mn}{2} \langle V^2 + 2\mathbf{V} \cdot \mathbf{v}' + v'^2 \rangle \right) \\ &+ \nabla \cdot \left[\frac{mn}{2} \langle (\mathbf{V} + \mathbf{v}') (V^2 + 2\mathbf{V} \cdot \mathbf{v}' + v'^2) \rangle \right] \\ &= \frac{\partial}{\partial t} \left[\frac{mn}{2} (V^2 + 2\mathbf{V} \cdot \langle \mathbf{v}' \rangle + \langle v'^2 \rangle) \right] \\ &+ \nabla \cdot \left[\frac{mn}{2} (V^2 \mathbf{V} + 2\mathbf{V} (\mathbf{V} \cdot \langle \mathbf{v}' \rangle) + \mathbf{V} \langle v'^2 \rangle \right. \\ &\quad \left. + V^2 \langle \mathbf{v}' \rangle + 2\mathbf{V} \cdot \langle \mathbf{v}' \mathbf{v}' \rangle + \langle v'^2 \mathbf{v}' \rangle) \right], \end{aligned}$$

with $\langle \mathbf{v}' \rangle = 0$ this reduces to

$$\begin{aligned} \frac{\partial}{\partial t} \left(\frac{mn}{2} \langle v^2 \rangle \right) + \nabla \cdot \left(\frac{mn}{2} \langle v^2 \mathbf{v} \rangle \right) &= \frac{\partial}{\partial t} \left(\frac{mn}{2} V^2 + \frac{mn \langle v'^2 \rangle}{3} \right) \\ &+ \nabla \cdot \left[\frac{mn}{2} (V^2 \mathbf{V} + \mathbf{V} \langle v'^2 \rangle + 2\mathbf{V} \cdot \langle \mathbf{v}' \mathbf{v}' \rangle + \langle v'^2 \mathbf{v}' \rangle) \right]. \end{aligned}$$

Substituting for the isotropic pressure (Eq. A.26) in the second and fourth terms above, this becomes

$$\begin{aligned} \frac{\partial}{\partial t} \left(\frac{mn}{2} \langle v^2 \rangle \right) + \nabla \cdot \left(\frac{mn}{2} \langle v^2 \mathbf{v} \rangle \right) &= \frac{\partial}{\partial t} \left(\frac{mnV^2}{2} + \frac{3}{2}p \right) \\ &+ \nabla \cdot \left(\frac{mnV^2}{2} \mathbf{V} + \frac{3}{2}p\mathbf{V} + mn \langle \mathbf{v}' \mathbf{v}' \rangle \cdot \mathbf{V} + \frac{mn}{2} \langle v'^2 \mathbf{v}' \rangle \right). \end{aligned}$$

Using $\nabla \cdot mn \langle \mathbf{v}' \mathbf{v}' \rangle = \nabla \cdot \underline{\pi} + \nabla p$ in the fifth term above, the first two terms of energy equation then reduces to

$$\begin{aligned} \frac{\partial}{\partial t} \left(\frac{mn}{2} \langle v^2 \rangle \right) + \nabla \cdot \left(\frac{mn}{2} \langle v^2 \mathbf{v} \rangle \right) &= \frac{\partial}{\partial t} \left(\frac{mnV^2}{2} + \frac{3}{2}p \right) + \nabla \cdot \left(\frac{mnV^2}{2} \mathbf{V} + \frac{3}{2}p\mathbf{V} \right) \\ &+ \nabla \cdot (\underline{\pi} \cdot \mathbf{V} + p\mathbf{V}) + \nabla \cdot \left(\frac{mn}{2} \langle v'^2 \mathbf{v}' \rangle \right). \quad (\text{A.30}) \end{aligned}$$

If we define \mathbf{q} as

$$\mathbf{q} = \int d\mathbf{v} \frac{mv'^2}{2} \mathbf{v} f, \quad (\text{A.31})$$

then Eq. A.30, with $p = nT$, becomes

$$\begin{aligned} \frac{\partial}{\partial t} \left(\frac{mn}{2} \langle v^2 \rangle \right) + \nabla \cdot \left(\frac{mn}{2} \langle \mathbf{v} v^2 \rangle \right) &= \frac{\partial}{\partial t} \left(\frac{mnV^2}{2} + \frac{3}{2}nT \right) \\ &+ \nabla \cdot \left(\frac{mnV^2}{2} \mathbf{V} + \frac{3}{2}nT\mathbf{V} \right) + \nabla \cdot \left[(\underline{\pi} \cdot \mathbf{V} + nT\mathbf{V}) + \mathbf{q} \right]. \quad (\text{A.32}) \end{aligned}$$

This is the final form of the first two terms of the energy equation, Eq. A.19. Looking at the right hand side of Eq. A.19 we need to express $\int d\mathbf{v} \frac{mv^2}{2} C$.

$$\begin{aligned}
\int dv \frac{mv^2}{2} C &= \int dv \frac{m}{2} (V^2 + 2\mathbf{V} \cdot \mathbf{v}' + v'^2) C \\
&= \frac{m}{2} V^2 \int dv C + \mathbf{V} \cdot \int dv m \mathbf{v}' C + \int dv \frac{mv'^2}{2} C. \quad (\text{A.33})
\end{aligned}$$

The first term on the right hand side vanishes if there are no particle sources; the second term is defined by Eq. A.29 as \mathbf{R} , and if we define Q as

$$Q = \int dv \frac{mv'^2}{2} C, \quad (\text{A.34})$$

this reduces to

$$\int dv \frac{mv'^2}{2} C = \mathbf{V} \cdot \mathbf{R} + Q. \quad (\text{A.35})$$

(If $\int dv C \neq 0$, then we would have an extra term of $\frac{mV^2}{2} S_n$ on the right hand side). Substituting Eq. A.32 for the first two terms of the left hand side of Eq. A.19, and Eq. A.35 for the right hand side, the energy equation becomes

$$\frac{\partial}{\partial t} \left(\frac{mnV^2}{2} + \frac{3}{2}nT \right) + \nabla \cdot \left[\left(\frac{mn}{2}V^2 + \frac{5}{2}nT \right) \mathbf{V} + (\underline{\pi} \cdot \mathbf{V}) + \mathbf{q} \right] = qn\mathbf{E} \cdot \mathbf{V} + \mathbf{R} \cdot \mathbf{V} + Q. \quad (\text{A.36})$$

Equation A.36 is Braginskii's energy transport equation (1.20).

A.3 The Heat-Balance Equation

If we eliminate the kinetic energy from Eq. A.36 we obtain an equation for the transport of internal energy, or the heat-balance equation. Starting with the left hand side of Eq. A.36 and combining the first and third terms

$$\frac{\partial}{\partial t} \left(\frac{mn}{2}V^2 \right) + \nabla \cdot \left(\frac{mn}{2}V^2 \mathbf{V} \right)$$

$$\begin{aligned}
&= nm \frac{\partial}{\partial t} \left(\frac{V^2}{2} \right) + \left(\frac{V^2}{2} \right) \frac{\partial}{\partial t} nm + nm \mathbf{V} \cdot \nabla \left(\frac{V^2}{2} \right) + \left(\frac{V^2}{2} \right) \nabla \cdot nm \mathbf{V} \\
&= nm \mathbf{V} \cdot \frac{\partial \mathbf{V}}{\partial t} + \frac{mV^2}{2} \left[\frac{\partial n}{\partial t} + \nabla \cdot (n\mathbf{V}) \right] + nm \mathbf{V} \cdot (\mathbf{V} \cdot \nabla) \mathbf{V}. \quad (\text{A.37})
\end{aligned}$$

If we assume $S_n = 0$, the second term in Eq. A.37 vanishes. If $S_n \neq 0$, then the second term in Eq. A.37, on the left hand side, cancels with the term on the right hand side discussed after Eq. A.35, so the form is independent of S_n . Reducing Eq. A.37 and assuming $S_n = 0$, we find

$$\frac{\partial}{\partial t} \left(\frac{mn}{2} V^2 \right) + \nabla \cdot \left(\frac{mn}{2} V^2 \mathbf{V} \right) = \mathbf{V} \cdot \left(nm \frac{\partial \mathbf{V}}{\partial t} + mn \mathbf{V} \cdot \nabla \mathbf{V} \right) \equiv \mathbf{V} \cdot mn \frac{d\mathbf{V}}{dt}. \quad (\text{A.38})$$

Substituting this back into the remaining terms on the left hand side of Eq. A.36, the energy equation becomes

$$\mathbf{V} \cdot nm \frac{d\mathbf{V}}{dt} + \frac{\partial}{\partial t} \left(\frac{3}{2} nT \right) + \nabla \cdot \left(\frac{3}{2} nT \mathbf{V} + nT \mathbf{V} \right) + \nabla \cdot (\underline{\pi} \cdot \mathbf{V}) + \nabla \cdot \mathbf{q} = \mathbf{V} \cdot (qn\mathbf{E} + \mathbf{R}) + Q.$$

Rewriting the left hand side we have

$$\begin{aligned}
&\frac{\partial}{\partial t} \left(\frac{3}{2} nT \right) + \nabla \cdot \left(\frac{3}{2} nT \mathbf{V} \right) + nT \nabla \cdot \mathbf{V} + \mathbf{V} \cdot (\nabla nT) + \underline{\pi} : \nabla \mathbf{V} \\
&+ \mathbf{V} \cdot (\nabla \cdot \underline{\pi}) + \nabla \cdot \mathbf{q} + \mathbf{V} \cdot \left(mn \frac{d\mathbf{V}}{dt} \right) = \mathbf{V} \cdot (qn\mathbf{E} + \mathbf{R}) + Q. \quad (\text{A.39})
\end{aligned}$$

Combining terms with a like factor of $\mathbf{V} \cdot$ we obtain

$$\begin{aligned}
&\frac{\partial}{\partial t} \left(\frac{3}{2} nT \right) + \nabla \cdot \left(\frac{3}{2} nT \mathbf{V} \right) + nT \nabla \cdot \mathbf{V} + \underline{\pi} : \nabla \mathbf{V} + \nabla \cdot \mathbf{q} \\
&+ \mathbf{V} \cdot \left(nm \frac{d\mathbf{V}}{dt} + \nabla nT + \nabla \cdot \underline{\pi} \right) = \mathbf{V} \cdot (qn\mathbf{E} + \mathbf{R}) + Q. \quad (\text{A.40})
\end{aligned}$$

By noting that $\mathbf{V} \cdot \mathbf{V} \times \mathbf{B} = 0$, the right hand side can be rewritten

$$\begin{aligned} \frac{\partial}{\partial t} \left(\frac{3}{2} nT \right) + \nabla \cdot \left(\frac{3}{2} nT\mathbf{V} \right) + nT\nabla \cdot \mathbf{V} + \underline{\underline{\pi}} : \nabla\mathbf{V} + \nabla \cdot \mathbf{q} \\ + \mathbf{V} \cdot \left(nm \frac{d\mathbf{V}}{dt} + \nabla nT + \nabla \cdot \underline{\underline{\pi}} \right) = \mathbf{V} \cdot \left(qn\mathbf{E} + q\frac{1}{c}\mathbf{V} \times \mathbf{B} + \mathbf{R} \right) \quad (\text{A.41}) \end{aligned}$$

Subtracting [\mathbf{V} · equation of motion], (equation of motion is Eq. A.28 on page 201), from this we see that the last group of terms on the left hand side of Eq. A.41 cancel as do the first group of terms on the right hand side of Eq. A.41, and we are left with

$$\frac{3}{2} \frac{\partial nT}{\partial t} + \nabla \cdot \left(\frac{3}{2} nT\mathbf{V} \right) + nT\nabla \cdot \mathbf{V} + \underline{\underline{\pi}} : \nabla\mathbf{V} + \nabla \cdot \mathbf{q} = Q \quad (\text{A.42})$$

which is Braginskii's Eq. (1.23). Since the equation of motion [Eq. A.28] contained a multiple of the energy equation, Eq. A.36, the difference contains the essential information of the energy balance. Note that Eq. A.42 is independent of the form of S_n to this point.

Appendix B

Code Listing

A selection of the critical subroutines of PGaS follow. The subroutines are described in more detail in Chapter 2. All of the support routines are not presented. In particular, subroutine BDYP is not included. Subroutine BDYP is the subroutine that sets the boundary conditions of a particular array. It is called with the inner cells set at some particular time level, and it returns the same array with the ghost cell values set at the appropriate values such that the desired boundary conditions at the boundary are satisfied.

B.1 Fluidi

```
c      subroutine fluidi
c(
      USE PARAMCM
      USE PARCOM
      USE CELLCOM
      USE BECOM
      USE NCOM
      dimension bc(4)
c
      vmi=1./pmass
      ci=1./c
      qfac=qele*vmi
c
c      given: den(n),ti(n),e(n),b(n),fji(n-1/2),
c             and fji(n)...(stored in aden(n)*ui(n) )
c      advance to: den(n+1),ti(n+1),fji(n+1/2), and ui(n+1)
c
c      use ti components for temporary storage
c             also vs,sti,ste,s
c      if (nerdsta.eq.1) call teeqti
c
c      =====
c      Set up temp. storage arrays.
c      =====
c
```



```

do 100 k=1,nr2nz2
    ste(k)=den(k)
    tir(k)=fjir(k)
    tiq(k)=fjiq(k)
    tiz(k)=fjiz(k)
    vs(k)=ti(k)
    sar(k)=denn(k)
    sr(k)=fjnr(k)
    sq(k)=fjng(k)
    sz(k)=fjnz(k)
    saz(k)=tn(k)
100 continue
c
    dt1=.5*dt
    dt2=dt
    nerdti=0.
    tdt=dt1*float(1-nerdti)
    i2cyl=0
120 i2cyl=i2cyl+1
c
c
c               =====
c               Set up (nu) arrays for momentum equation.
c               =====
c
do 130 k=1,nr2nz2
    s(k)=den(k)
    sti(k)=ti(k)*skey(k)
    fjir(k)=aden(k)*uir(k)*skey(k)
    fjiq(k)=aden(k)*uiq(k)*skey(k)
    fjiz(k)=aden(k)*uiz(k)*skey(k)
    saq(k)=denn(k)
    stn(k)=tn(k)*skeyn(k)
130 continue
do 131 i=2,nr1
    kstar=i+nr2
    do 131 k=kstar,nr2nz1,nr2
        adenn=amax1(dnmin,
    *   .125*(denn(k+1)+denn(k-1)+denn(k+nr2)
    *   +denn(k-nr2)+4.*denn(k)))
        adenn=amax1(adenn,denn(k))
        adenn=amax1(adenn,1.)
        fjnr(k)=adenn*unr(k)*skeyn(k)
        fjng(k)=adenn*unq(k)*skeyn(k)
        fjnz(k)=adenn*unz(k)*skeyn(k)
131 continue
cdir\$ ivdep
do 132 i=2,nr1
    ki=i+nr2
    ko=i+nr2nz
    adenni=amax1(dnmin, .125*(denn(ki+1)+denn(ki-1)+
    *   denn(ki+nr2)+denn(ki-nr2)+4.*denn(ki)))
    adenni=amax1(adenni,denn(ki))
    adenni=amax1(adenni,1.)
    fjnr(i)=adenni*unr(i)*skeyn(i)
    fjng(i)=adenni*unq(i)*skeyn(i)
    fjnz(i)=adenni*unz(i)*skeyn(i)

```

```

      adenno=amax1(dnmin, .125*(denn(ko+1)+denn(ko-1)+
*       denn(ko+nr2)+denn(ko-nr2)+4.*denn(ko)))
      adenno=amax1(adenno,denn(ko))
      adenno=amax1(adenno,1.)
      fjnr(i+nr2nz1)=adenno*unr(i+nr2nz1)*skeyn(i+nr2nz1)
      fjnq(i+nr2nz1)=adenno*unq(i+nr2nz1)*skeyn(i+nr2nz1)
      fjnz(i+nr2nz1)=adenno*unz(i+nr2nz1)*skeyn(i+nr2nz1)
132 continue
      jo=nr2
cdir\$ ivdep
      do 133 j=2,nz1
          jo=jo+nr2
          ji=jo-nr1
          ki=ji+1
          ko=jo-1
          adenni=amax1(dnmin, .125*(denn(ki+1)+denn(ki-1)+
*       denn(ki+nr2)+denn(ki-nr2)+4.*denn(ki)))
          adenni=amax1(adenni,denn(ki))
          adenni=amax1(adenni,1.)
          fjnr(ji)=adenni*unr(ji)*skeyn(ji)
          fjnq(ji)=adenni*unq(ji)*skeyn(ji)
          fjnz(ji)=adenni*unz(ji)*skeyn(ji)
          adenno=amax1(dnmin, .125*(denn(ko+1)+denn(ko-1)+
*       denn(ko+nr2)+denn(ko-nr2)+4.*denn(ko)))
          adenno=amax1(adenno,denn(ko))
          adenno=amax1(adenno,1.)
          fjnr(jo)=adenno*unr(jo)*skeyn(jo)
          fjnq(jo)=adenno*unq(jo)*skeyn(jo)
          fjnz(jo)=adenno*unz(jo)*skeyn(jo)
133 continue
c
c
c       =====
c       Set up rate coefficients in arrays so main loop
c       will vectorize
c       =====
c
      call rateset(6,ti,tn,tp,skey,skeyn)
      call rateset(8,ti,tn,t0,skey,skeyn)
      call rateset(9,te,tn,tm,skey,skeyn)
c
c      CSIN is Cross section (CS) for Ion/Neutral (IN) collisions.
      csin=5.e-15*float(ielastic)
c
c
c       =====
c       MAIN LOOP
c       =====
c
      do 151 i=2,nr1
          ri=1./rg(i)
          rp=rg(i)+drh
          rm=rg(i)-drh
          k=i
cdir\$ ivdep
          do 150 j=2,nz1
              k=k+nr2

```

```

kp=k+1
km=k-1
kpn=k+nr2
kmn=k-nr2
c      advective terms  evaluation of div.(ui fji,s,sti )
c      a0=0. , b0=1.  interpolated donor cell
c      a0=0. , b0=0.  pure center differencing
c      a0=0.5, b0=0.  pure donor cell
c      commonly use b0=0., 0.<a0<.5
tkeyi=.20001*(skey(k)+skey(kp)+skey(km)+skey(kpn)+skey(kmn))
keyi=ifix(tkeyi)
tkeyn=.20001*(skeyn(k)+skeyn(kp)+skeyn(km)+skeyn(kpn)+skeyn(kmn))
keyn=ifix(tkeyn)
c
a0i=.1*(1-keyi)+.4
b0i=0.
a0n=.1*(1-keyn)+.4
b0n=0.
uirp=.5*(uir(kp)+uir(k))
uirm=.5*(uir(k)+uir(km))
uizp=.5*(uiz(kpn)+uiz(k))
uizm=.5*(uiz(k)+uiz(kmn))
unrp=.5*(unr(kp)+unr(k))
unrm=.5*(unr(k)+unr(km))
unzp=.5*(unz(kpn)+unz(k))
unzm=.5*(unz(k)+unz(kmn))
crp=dt*dri*uirp
crm=dt*dri*uirm
czp=dt*dzi*uizp
czm=dt*dzi*uizm
crp=amax1(crp,-.5)
crp=b0i*amin1(crp,.5)+sign(a0i,uirp)
crm=amax1(crm,-.5)
crm=b0i*amin1(crm,.5)+sign(a0i,uirm)
czp=amax1(czp,-.5)
czp=b0i*amin1(czp,.5)+sign(a0i,uizp)
czm=amax1(czm,-.5)
czm=b0i*amin1(czm,.5)+sign(a0i,uizm)
cnrp=dt*dri*unrp
cnrm=dt*dri*unrm
cnzp=dt*dzi*unzp
cnzm=dt*dzi*unzm
cnrp=amax1(cnrp,-.5)
cnrp=b0n*amin1(cnrp,.5)+sign(a0n,unrp)
cnrm=amax1(cnrm,-.5)
cnrm=b0n*amin1(cnrm,.5)+sign(a0n,unrm)
cnzp=amax1(cnzp,-.5)
cnzp=b0n*amin1(cnzp,.5)+sign(a0n,unzp)
cnzm=amax1(cnzm,-.5)
cnzm=b0n*amin1(cnzm,.5)+sign(a0n,unzm)

```

```

c
c
c
c

```

```

=====
Conservation Equations all have same form
=====

```

```

dendoti=-ri*dri*(uirp*rp*((.5-crp)*s(kp)+(.5+crp)*s(k))
*   -uirm*rm*((.5-crm)*s(k)+(.5+crm)*s(km))
*   -dzi*(uizp*((.5-czp)*s(kpn)+(.5+czp)*s(k))
*   -uizm*((.5-czm)*s(k)+(.5+czm)*s(kmn))
dendotn=-ri*dri*(unrp*rp*((.5-cnrp)*saq(kp)+(.5+cnrp)*saq(k))
*   -unrm*rm*((.5-cnrm)*saq(k)+(.5+cnrm)*saq(km))
*   -dzi*(unzp*((.5-cnzp)*saq(kpn)+(.5+cnzp)*saq(k))
*   -unzm*((.5-cnzm)*saq(k)+(.5+cnzm)*saq(kmn))
frdoti=-ri*dri*(uirp*rp*((.5-crp)*fjir(kp)+(.5+crp)*fjir(k))
*   -uirm*rm*((.5-crm)*fjir(k)+(.5+crm)*fjir(km))
*   -.25*dzi*((uir(kpn)+uir(k))*(fjiz(kpn)+fjiz(k))
*   -(uir(k)+uir(kmn))*(fjiz(k)+fjiz(kmn)))
*   +uiq(k)*fjiq(k)*ri
frdotn=-ri*dri*(unrp*rp*((.5-cnrp)*fjnr(kp)+(.5+cnrp)*fjnr(k))
*   -unrm*rm*((.5-cnrm)*fjnr(k)+(.5+cnrm)*fjnr(km))
*   -.25*dzi*((unr(kpn)+unr(k))*(fjnz(kpn)+fjnz(k))
*   -(unr(k)+unr(kmn))*(fjnz(k)+fjnz(kmn)))
*   +unq(k)*fjinq(k)*ri
fqdoti=-.5*ri*dri2*(rp*(fjir(kp)+fjir(k))*(uiq(kp)+uiq(k))
x   -rm*(fjir(k)+fjir(km))*(uiq(k)+uiq(km))
*   -.25*dzi*((uiq(kpn)+uiq(k))*(fjiz(kpn)+fjiz(k))
*   -(uiq(k)+uiq(kmn))*(fjiz(k)+fjiz(kmn)))
*   -uir(k)*fjiq(k)*ri
fqdotn=-.5*ri*dri2*(rp*(fjnr(kp)+fjnr(k))*(unq(kp)+unq(k))
x   -rm*(fjnr(k)+fjnr(km))*(unq(k)+unq(km))
*   -.25*dzi*((unq(kpn)+unq(k))*(fjnz(kpn)+fjnz(k))
*   -(unq(k)+unq(kmn))*(fjnz(k)+fjnz(kmn)))
*   -unr(k)*fjinq(k)*ri
fzdoti=-.25*ri*dri*(rp*(uiz(kp)+uiz(k))*(fjir(kp)+fjir(k))
*   -rm*(uiz(k)+uiz(km))*(fjir(k)+fjir(km))
*   -dzi*(uizp*((.5-czp)*fjiz(kpn)+(.5+czp)*fjiz(k))
*   -uizm*((.5-czm)*fjiz(k)+(.5+czm)*fjiz(kmn)))
fzdotn=-.25*ri*dri*(rp*(unz(kp)+unz(k))*(fjnr(kp)+fjnr(k))
*   -rm*(unz(k)+unz(km))*(fjnr(k)+fjnr(km))
*   -dzi*(unzp*((.5-cnzp)*fjnz(kpn)+(.5+cnzp)*fjnz(k))
*   -unzm*((.5-cnzm)*fjnz(k)+(.5+cnzm)*fjnz(kmn)))
tdoti=-ri*dri*(uirp*rp*((.5-crp)*sti(kp)+(.5+crp)*sti(k))
*   -uirm*rm*((.5-crm)*sti(k)+(.5+crm)*sti(km))
*   -dzi*(uizp*((.5-czp)*sti(kpn)+(.5+czp)*sti(k))
*   -uizm*((.5-czm)*sti(k)+(.5+czm)*sti(kmn)))
tdotn=-ri*dri*(unrp*rp*((.5-cnrp)*stn(kp)+(.5+cnrp)*stn(k))
*   -unrm*rm*((.5-cnrm)*stn(k)+(.5+cnrm)*stn(km))
*   -dzi*(unzp*((.5-cnzp)*stn(kpn)+(.5+cnzp)*stn(k))
*   -unzm*((.5-cnzm)*stn(k)+(.5+cnzm)*stn(kmn)))
c   divergence ui term
tdoti=tdoti+.333333333333*sti(k)*(dzi2*(uiz(kpn)-uiz(kmn))
*   +ri*dri2*(rp*uir(kp)+dr*uir(k)-rm*uir(km)))
tdotn=tdotn+.333333333333*stn(k)*(dzi2*(unz(kpn)-unz(kmn))
*   +ri*dri2*(rp*unr(kp)+dr*unr(k)-rm*unr(km)))
c   ion electron equipartition

```

```

vtaue=36.2637*s(k)/amax1(1.e6,te(k)*sqrt(te(k)))
tdoti=tdoti+1.822e-27*vmi*vtaue*(te(k)-sti(k))
c      now add grad pi
frdoti=frdoti-boltzk*vmi*dri2*(s(kp)*sti(kp)-s(km)*sti(km))
fzdoti=fzdoti
* -boltzk*vmi*dzi2*(s(kpn)*sti(kpn)-s(kmn)*sti(kmn))
frdotn=frdotn-boltzk*vmi*dri2*(saq(kp)*stn(kp)-saq(km)*stn(km))
fzdotn=fzdotn
* -boltzk*vmi*dzi2*(saq(kpn)*stn(kpn)-saq(kmn)*stn(kmn))
c      now electromagnetic force
frdoti=frdoti+qfac*(s(k)*er(k)+ci*(fjiz(k)*bz(k)-fjiz(k)*bq(k)))
fqdoti=fqdoti+qfac*(s(k)*eq(k)+ci*(fjiz(k)*br(k)-fjir(k)*bz(k)))
fzdoti=fzdoti+qfac*(s(k)*ez(k)+ci*(fjir(k)*bq(k)-fjiz(k)*br(k)))
dnik=s(k)*saq(k)
spip=amin1(saq(k),dt1*dnik*tp(k))
spi0=amin1(s(k),dt1*dnik*t0(k))
spi0=amin1(spi0,saq(k))
spim=amin1(s(k),dt1*dnik*tm(k))
c
c
c
c
=====
Particle Source Terms
=====

spi=spip-spim
spn=-spi-spi0
znmaxio=amin1(saq(k),dt2*dnik*tp(k))
znmaxcx=amin1(saq(k),dt2*dnik*t0(k))
znmaxcx=amin1(znmaxcx,s(k))
znmax=amin1(saq(k),znmaxio+znmaxcx)

bottom=t0(k)
if (bottom.eq.0) bottom=1.
rrratio=tp(k)/bottom
zncx=znmax/(1.+rrratio)
if (bottom.eq.1.) zncx=0.
znio=znmax-zncx
rcn=amin1(s(k),dt2*dnik*tm(k))
vthi=sqrt(8.25481e+07*sti(k))
znuin=dt2*saq(k)*csin*vthi*skey(k)*skeyn(k)
if (znuin.gt.znuinmax) znuinmax=znuin
emir=s(k)*znuin*(unr(k)-uir(k))
emiq=s(k)*znuin*(unq(k)-uiq(k))
emiz=s(k)*znuin*(unz(k)-uiz(k))
c
c
c
c
c
=====
Momentum Source Terms
=====

smir= znio*unr(k)+zncx*(unr(k)-uir(k))-rcn*uir(k)+emir
smiq= znio*unq(k)+zncx*(unq(k)-uiq(k))-rcn*uiq(k)+emiq
smiz= znio*unz(k)+zncx*(unz(k)-uiz(k))-rcn*uiz(k)+emiz
smnr=-znio*unr(k)-zncx*unr(k)          +rcn*uir(k)-emir
smnq=-znio*unq(k)-zncx*unq(k)          +rcn*uiq(k)-emiq
smnz=-znio*unz(k)-zncx*unz(k)          +rcn*uiz(k)-emiz
c

```

```

      sei=saq(k)*(tp(k)+t0(k))*(stn(k)-sti(k))
c hot CX neutral assumed lost, for neutrals.
      sen=s(k)*tm(k)*(sti(k)-stn(k))

c
c
c
c
c
c
      den(k)=amax1(ste(k)+spi+dt1*dendoti,0.)
      tir(k)=tir(k)+smir+dt2*frdoti
      tiq(k)=tiq(k)+smiq+dt2*fqdoti
      tiz(k)=tiz(k)+smiz+dt2*fzdoti
      ti(k)=amax1(vs(k)+tdt*(tdoti+sei),0.)
      denn(k)=amax1(sar(k)+spn+dt1*dendotn,0.)
      sr(k)=sr(k)+smnr+dt2*frdotn
      sq(k)=sq(k)+smnq+dt2*fqdotn
      sz(k)=sz(k)+smnz+dt2*fzdotn
      tn(k)=amax1(saz(k)+tdt*(tdotn+sen),0.)
150 continue
151 continue

c
c
c
c
c
c
      call bdyp(den,aq,rmin,zmin,dri,dzi,nr2,nz2,t,1)
      call bdyp(ti,aq,rmin,zmin,dri,dzi,nr2,nz2,t,15)
      call bdyp(denn,s,rmin,zmin,dri,dzi,nr2,nz2,t,19)
      call bdyp(tn,s,rmin,zmin,dri,dzi,nr2,nz2,t,23)
      do 160 i=2,nr1
      kstar=i+nr2
      do 160 k=kstar,nr2nz1,nr2
      aden(k)=amax1(dmin,
* .125*(den(k+1)+den(k-1)+den(k+nr2)+den(k-nr2)+4.*den(k)))
      aden(k)=amax1(aden(k),den(k))
      aden(k)=amax1(aden(k),1.)
      skey(k)=cvmgm(0.,1.,den(k)-dmin)
160 continue

c
c
c
c
c
c
      call bdyp(den,aq,rmin,zmin,dri,dzi,nr2,nz2,t,1)
      call bdyp(ti,aq,rmin,zmin,dri,dzi,nr2,nz2,t,15)
      call bdyp(denn,s,rmin,zmin,dri,dzi,nr2,nz2,t,19)
      call bdyp(tn,s,rmin,zmin,dri,dzi,nr2,nz2,t,23)
      do 170 i=2,nr1
      kstar=i+nr2
      do 170 k=kstar,nr2nz1,nr2
      uir(k)=tir(k)/aden(k)
      uiq(k)=tiq(k)/aden(k)
      uiz(k)=tiz(k)/aden(k)
      skeyn(k)=cvmgm(0.,1.,denn(k)-dnmin)
170 continue

c
c
c
c
c
c
      do 171 i=2,nr1
      kstar=i+nr2
      do 171 k=kstar,nr2nz1,nr2
      adenn=amax1(dnmin,
* .125*(denn(k+1)+denn(k-1)+denn(k+nr2)+denn(k-nr2)+4.*denn(k)))
      adenn=amax1(adenn,denn(k))

```

```

      adenn=amax1(adenn,1.)
      unr(k)=sr(k)/adenn
      unq(k)=sq(k)/adenn
      unz(k)=sz(k)/adenn
171 continue
      call bdyp(aden,s,rmin,zmin,dri,dzi,nr2,nz2,t,17)
      call bdyp(skey,s,rmin,zmin,dri,dzi,nr2,nz2,t,17)
      call bdyp(uir,s,rmin,zmin,dri,dzi,nr2,nz2,t,9)
      call bdyp(uiq,aq,rmin,zmin,dri,dzi,nr2,nz2,t,10)
      if (idivzero.eq.1) call bdyp(uiz,uir,rmin,zmin,dri,dzi,
*   nr2,nz2,t,11)
      if (idivzero.eq.0) call bdyp(uiz,aq,rmin,zmin,dri,dzi,
*   nr2,nz2,t,11)
      call bdyp(skeyn,s,rmin,zmin,dri,dzi,nr2,nz2,t,17)
      call bdyp(unr,s,rmin,zmin,dri,dzi,nr2,nz2,t,20)
      call bdyp(unq,s,rmin,zmin,dri,dzi,nr2,nz2,t,21)
      call bdyp(unz,s,rmin,zmin,dri,dzi,nr2,nz2,t,22)
c
c               =====
c               Go back for second loop
c               =====
c
      if (i2cyl.eq.2) go to 200
      dt2=dt1
      dt1=dt
      tdt=dt*float(1-nerdti)
      go to 120
200 continue
      den(nr2nz1+1)=den(nr2nz1+2)
c
c
      call movlev(ti,tir,nr2nz2)
      call movlev(ti,tiq,nr2nz2)
      call movlev(ti,tiz,nr2nz2)
c
c               =====
c               Keep Track of what went where
c               =====
c
      if (iref.eq.0) return
      call rateset(6,ti,tn,tp,skey,skeyn)
      call rateset(8,ti,tn,t0,skey,skeyn)
      call rateset(9,te,tn,tm,skey,skeyn)
      call bdyp(tp,s,rmin,zmin,dri,dzi,nr2,nz2,t,17)
      call bdyp(t0,s,rmin,zmin,dri,dzi,nr2,nz2,t,17)
      call bdyp(tm,s,rmin,zmin,dri,dzi,nr2,nz2,t,17)
      if (isplot.gt.0) call srcplt
c calculate reaction-rate:
      do 801 i=2,nr1
      kstar=i+nr2
      do 801 k=kstar,nr2nz1,nr2
      dnik=den(k)*denn(k)
      tp(k)=dnik*tp(k)
      t0(k)=dnik*t0(k)
      tm(k)=dnik*tm(k)
801 continue
      do 802 i=2,nr1

```

```

      kstar=i+nr2
      do 802 k=kstar,nr2nzi,nr2
        volk=rg(i)*volelmt*dt
        tp(k)=tp(k)*volk
        t0(k)=t0(k)*volk
        tm(k)=tm(k)*volk
802  continue
      do 803 i=2,nr1
        kstar=i+nr2
        do 803 k=kstar,nr2nzi,nr2
          partion=partion+tp(k)
          partcxc=partcxc+t0(k)
          partrec=partrec+tm(k)
803  continue
      return
      end

```

B.2 Field

```

subroutine field
  USE PARAMCM
  USE PARCOM
  USE CELLCOM
  USE BECOM
  USE NCOM
c
  common / bcons / ierbcr(nt4),ieqbcr(nt4),iezbcr(nt4),
*               iabcr(nt4), ibbcr(nt4),itebcr(nt4),
*               ierbcz,ieqbcz,iezbcz,iabcz,ibbcz,itebcz
  data toomch / 0. /
  data fpvcc, cve / 1.398220225e-20, 6.241464024e19 /
c
  iwhen=1
  vqele=1./qele
  ci=1./c
  dmax=0.
  aqmax=0.
  bqmax=0.
  etamax=0.
  ueqmax=0.
  brmax=0.
  bzmax=0.
  ivc=0
  do 249 i=2,nr1
    k=i
    do 249 j=2,nz1
      k=k+nr2
      dmax=amax1(dmax,den(k))
      aqmax=amax1(aqmax,abs(aq(k)))
      bqmax=amax1(bqmax,abs(bq(k)))
      etamax=amax1(etamax,eta(k))
      ueqmax=amax1(ueqmax,abs(ueq(k)))
      bzmax=amax1(bzmax,bz(k))
      ivc=ivc+ifix(1.-skey(k))
      vs(k)=vqele*skey(k)/aden(k)
249  continue
  accept=amax1(amax1(dris,dzis)*etamax*(aqmax+bqmax)/fpvcc,

```



```

. ueqmax*amax1(dri*brmax,dzi*bzmax))
accept=.01*accept*dt
if (accept.eq.0.) accept=100.*amax1(dris,dzis)
subdt=dt/float(isub)
call bdyp(vs,s,rmin,zmin,dri,dzi,nr2,nz2,t,17)
call bdyp(den,aq,rmin,zmin,dri,dzi,nr2,nz2,t,1)
call bdyp(uir,s,rmin,zmin,dri,dzi,nr2,nz2,t,9)
call bdyp(uiq,aq,rmin,zmin,dri,dzi,nr2,nz2,t,10)
c
c *****
c   between these two coment cards the arrays contain
c       dmin-----qele*dmin
c       s-----qele*den
c       te,ste-----boltzk*te
c
c   dmin=qele*dmin
c   do 250 k=1,nr2nz2
c       s(k)=qele*den(k)
c       te(k)=boltzk*te(k)
c       ste(k)=te(k)
250 continue
c
c   iwhen=2
c
c           update of b
c
c   call bdyp(aq,s,rmin,zmin,dri,dzi,nr2,nz2,t,16)
c   call bdyp(bq,s,rmin,zmin,dri,dzi,nr2,nz2,t,4)
c   if(ifluid.eq.1) go to 251
c   call smooth(ti,tmp,nr2,nz1)
c   call bdyp(ti,s,rmin,zmin,dri,dzi,nr2,nz2,t,15)
c   call smooth(ti,tmp,nr2,nz1)
c   call bdyp(ste,s,rmin,zmin,dri,dzi,nr2,nz2,t,18)
c   iter=0
c   call movlev(bq,sq,nr2nz2)
c   call movlev(aq,saq,nr2nz2)
c   call movlev(te,ste,nr2nz2)
400 iter=iter+1
c
c           =====
c           Call to CPARA to advance A_theta and B_theta
c           =====
c
c   call cpara(iabcr,iabcz,ibbcr,ibbcz,itebcr,itebcz,subdt,
1   erra,errb,erza,erzb,iera,ierb,ieza,iezb,iter)
c
c           =====
c           Check Convergence
c           =====
c
c   toomch=abs(erra)+abs(errb)+abs(erza)+abs(erzb)
c   if (toomch.gt.accept)
*   print 451, it,iter,erra,errb,erza,erzb,iera,ierb,ieza,iezb
451 format (I5,21H iter,erra(b),erza(b),I4,4E11.4,5X,4I7)
c   if (iter.eq.1) toomch=toomch-abs(erra)-abs(errb)
c   if (toomch.lt.accept) go to 490
c
c           =====
c           If it is not converging, stop.

```

```

C          =====
C          post mortem and stop 333
470 continue
      ncplot=it
      call dpart
      call dfield
      call endplt
      call exit(1)
490 continue

      call movlev(sq,bq,nr2nz2)
      call movlev(saq,aq,nr2nz2)
      call movlev(ste,te,nr2nz2)
      if (iter.lt.isub) go to 400

C          =====
C          Fields are not at time (n+1)
C          =====
C          end of b calculation
C          iwhen=3

C          =====
C          Now Solve for E using electron momentum Equation
C          =====
C          now create er(q,z)

diverb=0.
do 700 i=2,nr1
  rp=rg(i)+drh
  rm=rg(i)-drh
  ri=1./rg(i)
  j=2
  kstar=i+nr2
  do 660 k=kstar,nr2nz1,nr2
    tmp(j)=ri*dri2*(rp*br(k+1)+dr*br(k)-rm*br(k-1))
*    +dзи2*(bz(k+nr2)-bz(k-nr2))
*    j=j+1
660  continue
      tmp(nz2)=diverb
      do 661 j=2,nz1
        tmp(nz2)=amax1(tmp(nz2),abs(tmp(j)))
661  continue
      diverb=tmp(nz2)
      k=i
      do 700 j=2,nz1
        k=k+nr2
        kp=k+1
        km=k-1
        kpn=k+nr2
        kmn=k-nr2
        clbr=-dzi2*(bq(kpn)-bq(kmn))
        clbq=dзи2*(br(kpn)-br(kmn))-dri2*(bz(kp)-bz(km))
        clbz=ri*dri2*(rp*bq(kp)+dr*bq(k)-rm*bq(km))
        fuer=uir(k)-vs(k)*cofp*clbr
        fuez=uiz(k)-vs(k)*cofp*clbz

```

```

      dker=-.5*dri2*((den(kp)+den(k))*(ste(kp)+ste(k))
x      -(den(k)+den(km))*(ste(k)+ste(km)))
      dkez=-.5*dzi2*((den(kpn)+den(k))*(ste(kpn)+ste(k))
x      -(den(k)+den(kmn))*(ste(k)+ste(kmn)))
      er(k)=(1.-skey(k))*er(k)+skey(k)*(vs(k)*dker
x      -ci*(ueq(k)*bz(k)-fuez*bq(k))+eta(k)*cofp*clbr)
      eq(k)=(1.-skey(k))*eq(k)+skey(k)*(
x      -ci*(fuez*br(k)-fuer*bz(k))+eta(k)*cofp*clbq)
      ez(k)=(1.-skey(k))*ez(k)+skey(k)*(vs(k)*dkez*ezkey
x      -ci*(fuer*bq(k)-ueq(k)*br(k))+eta(k)*cofp*clbz)
700 continue
      call bdyp(er,s,rmin,zmin,dri,dzi,nr2,nz2,t,6)
      call bdyp(eq,s,rmin,zmin,dri,dzi,nr2,nz2,t,7)
      call bdyp(ez,er,rmin,zmin,dri,dzi,nr2,nz2,t,8)
c
c      =====
c      Sovled for E in plasma, now couple to Vacuum E
c      Solves Laplace's Equation in Vacuum region
c      This is done with Dynamic ADI
c      =====
c
c      get vacuum e field
      if (ivc.eq.0) go to 795
      iwhen=4
      call ghtset(iap,ierbcr,ierbcz,s,er,rmin,rmax,dri,dzi)
      relax=1.35
      itt=900
      etest=1.e-05
c E_r
      call vdadirc(ierbcr,ierbcz,er,s,tp,tc,tm,t0,
* fsing,dr,nr2,
* dz,nz2,rg,skey,sq,rmin,rmax,itt,sar,saz,err,ier,etest)
      if (abs(err).gt.10.) go to 470
      iwhen=5
c E_q
      call bdyp(eq,s,rmin,zmin,dri,dzi,nr2,nz2,t,7)
      call ghtset(iap,ieqbcr,ieqbcz,s,eq,rmin,rmax,dri,dzi)
      relax=1.35
      itt=900
      etest=1.e-05
      call vdadirc(ieqbcr,ieqbcz,eq,s,tp,tc,tm,t0,
* fsing,dr,nr2,
* dz,nz2,rg,skey,sq,rmin,rmax,itt,sar,saz,err,ier,etest)
      if (abs(err).gt.10.) go to 470
      iwhen=6
c E_z
      call bdyp(ez,er,rmin,zmin,dri,dzi,nr2,nz2,t,8)
      call ghtset(iap,iezbcz,iezbcz,s,ez,rmin,rmax,dri,dzi)
      relax=1.35
      itt=900
      etest=1.e-05
      call vdadirc(iezbcz,iezbcz,ez,s,tp,tc,tm,t0,
* fsing,dr,nr2,
* dz,nz2,rg,skey,sq,rmin,rmax,itt,sar,saz,err,ier,etest)
      if (abs(err).gt.10.) go to 470

```



```

c                                     =====
c
c      set r boundary condition string for aq, bq, and te
ia=iabs(iar(2))
do 5 j=1,nz2
  ia=iabs(iar(j))
  bca(j,1)=bc(ia)
  if(iar(j).lt.0.and.rmin.gt.0.) bca(j,1)=bca(j,1)+bc(ia+1)/rmin
  bca(j,2)=bc(ia+1)
  bca(j,3)=bc(ia+2)
  if (iar(j).lt.0) bca(j,3)=bca(j,3)+bc(ia+3)/rmax
  bca(j,4)=bc(ia+3)
  ib=iabs(ibr(j))
  bcb(j,1)=bc(ib)
  if(ibr(j).lt.0.and.rmin.gt.0.) bcb(j,1)=bcb(j,1)+bc(ib+1)/rmin
  bcb(j,2)=bc(ib+1)
  bcb(j,3)=bc(ib+2)
  if (ibr(j).lt.0) bcb(j,3)=bcb(j,3)+bc(ib+3)/rmax
  bcb(j,4)=bc(ib+3)
5 continue
c      now set ghost cells of aq, bq, and te for cpara
call movlev(aq,saq,nr2nz2)
call movlev(bq,sq,nr2nz2)
call movlev(te,ste,nr2nz2)
do 7 j=1,nz2
  ra1=.5*bca(j,1)
  ra2=dri*bca(j,2)
  arf1(j)=ra1+ra2
  arf2(j)=ra1-ra2
  arf2i(j)=1./arf2(j)
  ra3=.5*bca(j,3)
  ra4=dri*bca(j,4)
  arf3(j)=ra3-ra4
  arf4(j)=ra3+ra4
  arf4i(j)=1./arf4(j)
  rb1=.5*bcb(j,1)
  rb2=dri*bcb(j,2)
  rb3=.5*bcb(j,3)
  rb4=dri*bcb(j,4)
  brf1(j)=rb1+rb2
  brf2(j)=rb1-rb2
  brf2i(j)=1./brf2(j)
  brf3(j)=rb3-rb4
  brf4(j)=rb3+rb4
  brf4i(j)=1./brf4(j)
  rt1=.5*bc(itr(j))
  rt2=dri*bc(itr(j)+1)
  rt3=.5*bc(itr(j)+2)
  rt4=dri*bc(itr(j)+3)

```

```

        trf1(j)=rt1+rt2
        trf2(j)=rt1-rt2
        trf2i(j)=1./trf2(j)
        trf3(j)=rt3-rt4
        trf4(j)=rt3+rt4
        trf4i(j)=1./trf4(j)
c 7 continue
  fix 13/03/82
  if (iap.ne.1) go to 20
  r1=.5*bc(iaz)
  r2=dzi*bc(iaz+1)
  r3=.5*bc(iaz+2)
  r4=dzi*bc(iaz+3)
  azf1=r1+r2
  azf2=r1-r2
  azf2i=1./azf2
  azf3=r3-r4
  azf4=r3+r4
  azf4i=1./azf4
  r1=.5*bc(ibz)
  r2=dzi*bc(ibz+1)
  r3=.5*bc(ibz+2)
  r4=dzi*bc(ibz+3)
  bzf1=r1+r2
  bzf2=r1-r2
  bzf2i=1./bzf2
  bzf3=r3-r4
  bzf4=r3+r4
  bzf4i=1./bzf4
  r1=.5*bc(itz)
  r2=dzi*bc(itz+1)
  r3=.5*bc(itz+2)
  r4=dzi*bc(itz+3)
  tzf1=r1+r2
  tzf2=r1-r2
  tzf2i=1./tzf2
  tzf3=r3-r4
  tzf4=r3+r4
  tzf4i=1./tzf4
cdir\$ ivdep
  20 j=1
    do 25 k=1,nr2nz2,nr2
      te(k)=trf2(j)*ste(k)+trf1(j)*ste(k+1)
      bq(k)=brf2(j)*sq(k)+brf1(j)*sq(k+1)
      aq(k)=arf2(j)*saq(k)+arf1(j)*saq(k+1)
      te(k+nr1)=trf4(j)*ste(k+nr1)+trf3(j)*ste(k+nr)
      bq(k+nr1)=brf4(j)*sq(k+nr1)+brf3(j)*sq(k+nr)
      aq(k+nr1)=arf4(j)*saq(k+nr1)+arf3(j)*saq(k+nr)
      j=j+1
    25 continue
  if (iaz.eq.2) go to 40
cdir\$ ivdep
  do 30 i=1,nr2
    te(i)=tzf2*ste(i)+tzf1*ste(i+nr2)
    bq(i)=bzf2*sq(i)+bzf1*sq(i+nr2)
    aq(i)=azf2*saq(i)+azf1*saq(i+nr2)
    te(i+nr2nz1)=tzf4*ste(i+nr2nz1)+tzf3*ste(i+nr2nz)

```

```

      bq(i+nr2nz1)=bzf4*sq(i+nr2nz1)+bzf3*sq(i+nr2nz)
      aq(i+nr2nz1)=azf4*saq(i+nr2nz1)+azf3*saq(i+nr2nz)
30 continue
40 continue
   call restvy
      iera=0
      ieza=0
      ierb=0
      iezb=0
      erra=0.
      erza=0.
      erreb=0.
      erzb=0.
      iwhen=2

```

c
c
c
c
c
c

```

=====
      Get electron Velocities
=====

```

first define uer

```

do 105 i=2,nr1
  ks=i+nr2
do 105 k=ks,nr2nz1,nr2
  uer(k)=uir(k)
*      +skey(k)*cofp*dzi2*(sq(k+nr2)-sq(k-nr2))/
*      (s(k)+1.-skey(k))
105 continue
   call bdyp(uer,s,rmin,zmin,dri,dzi,nr2,nz2,t,12)
   if (subdt.eq.0.) go to 262
   sbdt=.5*subdt
   vdt=1./sbdt

```

if(nerdbly.eq.1) go to 567

c
c
c
c
c
c
c
c
c

```

=====
      Set up for r direction implicit pass on A_theta
      Loop 150 sets up coefficient matrices
      for the ADI call. TP, TC, TM are the
      (i+1), (i), (i-1) coefficients.
      T0 is the explicit rhs
=====

```

set up r direction pass on aq.

```

   if (rmin.gt.0.) go to 120
      rmi1=4.*dri
      rmi2=-4.*dri
      go to 130
120 rmi1=1./rmin
      rmi2=rmi1
130 do 150 i=2,nr1
      rm1=rg(i-1)
      rp1=rg(i+1)
      rp=rg(i)+drh
      rpi=1./rp
      rm=rg(i)-drh
      ri=1./rg(i)
      rr=rg(i)
      ks=i+nr2
      j=1

```

```

do 140 k=ks,nr2nz1,nr2
  j=j+1
  tp(k)=-rp1*rpi*dris*eta(k)
  tm(k)=-rm1*rmi2*dris*eta(k)
  cp=-dzis*eta(k)
  cm=-dzis*eta(k)
  cc=2.*(dzis*eta(k))
  fak=fpvcc*vdt*skey(k)
  tc(k)=(dris*rr*(rpi+rmi1)*eta(k)+fak)*
  *      (1-skeyd(k)) +skeyd(k)
  t0(k)=fak*saq(k)
  fak=fpvcc*uer(k)*ri*dri2*skey(k)
  tp(k)=(tp(k)+fak*rp1)*(1-skeyd(k))
  tm(k)=(tm(k)-fak*rm1)*(1-skeyd(k))
  fak=fpvcc*uez(k)*dzi2*skey(k)
  cp=cp+fak
  cm=cm-fak
  t0(k)=(t0(k)-cp*saq(k+nr2)-cc*saq(k)-
  *      cm*saq(k-nr2))*(1-skeyd(k))+skeyd(k)*dval(j)
140  continue
  k=i
c check convergence
  do 145 j=2,nz1
    k=k+nr2
    tep=t0(k)-tp(k)*saq(k+1)-tc(k)*saq(k)-tm(k)*saq(k-1)
    iera=cvmgm(j+i*1000,iera,abs(erra)-abs(tep))
    erra=cvmgm(tep,erra,abs(erra)-abs(tep))
145  continue
    rmi1=rpi
    rmi2=rpi
150 continue
c
c
c
c
c
do 160 j=2,nz1
  fsing(j)=0.
  ks=(j-1)*nr2
  if (iar(j).ne.6) go to 156
  do 155 i=2,nr1
    fsing(j)=fsing(j)+skey(i+ks)
155  continue
    if (fsing(j).gt.0.) fsing(j)=1.
    fsing(j)=1.-fsing(j)
156  t0(ks+1)=aq(ks+1)
    t0(ks+nr2)=aq(ks+nr2)
160 continue
c
c
c
c
c
call vtrir(fsing,nr2,nz2,2,1,dr,bca,tp,tc,tm,t0)
call movlev(t0,saq,nr2nz2)
c

```



```

c          =====
c          Set BC, only need z boundary
c          =====
c          set z boundaries of saq
c          if (iaz.eq.2) go to 175
cdir\$ ivdep
c          do 170 i=1,nr2
c            saq(i)=azf2i*(aq(i)-azf1*saq(i+nr2))
c          170 saq(i+nr2nz1)=azf4i*(aq(i+nr2nz1)-azf3*saq(i+nr2nz))
c            go to 185
cdir\$ ivdep
c switch aq and saq
c 175 do 180 k=1,nr2
c         saq(k)=saq(k+nr2nz)
c         aq(k+nr2nz1)=saq(k+nr2nz)
c         saq(k+nr2nz1)=saq(k+nr2)
c         aq(k)=saq(k+nr2)
c 180 continue
c 185 continue

c          =====
c          Clean up vacuum B field at aq(n+1/2)
c          =====

c          if (ivc.gt.0)
c            * call cleanaq(saq,skey,sr,aq,tp,tc,tm,t0,dr,dz,nr2,nz2,
c            * fsing,sar,saz,rg,iar,iaz,rmin,zmin,rmax,3hsaq,skeyd,dval)
c            if(nerdaly.eq.1) go to 287
c            iwhen=3

c          =====
c          Get a temporary value for the z ADI path for Aq
c          This will be used as a estimate only
c          to calculate B_r,B_z, and u_eq
c          Same set-up as for r ADI pass
c          =====

c          set up z direction pass on temporary aq.
c          if (rmin.gt.0.) go to 320
c          rmi1=4.*dri
c          rmi2=-4.*dri
c          go to 330
c 320 rmi1=1./rmin
c          rmi2=rmi1
c 330 do 350 i=2,nr1
c         rmi=rg(i-1)
c         rpi=rg(i+1)
c         rp=rg(i)+drh
c         rpi=1./rp
c         rm=rg(i)-drh
c         ri=1./rg(i)
c         rr=rg(i)
c         fsing(i)=0.

```

```

ks=i+nr2
j=1
do 340 k=ks,nr2nz1,nr2
  j=j+1
  cp=-rpi*rpi*dris*eta(k)
  cm=-rmi*rmi2*dris*eta(k)
  cc=dris*rr*(rpi+rmi1)*eta(k)
  tp(k)=-dzis*eta(k)
  tm(k)=-dzis*eta(k)
c      parabolic terms-z pass aq
  fak=fpvcc*vdt*skey(k)
  tc(k)=(2.*dzis*eta(k)+fak)*(1-skeyd(k))+skeyd(k)
  t0(k)=fak*saq(k)
  fak=fpvcc*uer(k)*ri*dri2*skey(k)
  cp=cp+fak*rpi
  cm=cm-fak*rmi1
  fak=fpvcc*uez(k)*dzi2*skey(k)
  tp(k)=(tp(k)+fak)*(1-skeyd(k))
  tm(k)=(tm(k)-fak)*(1-skeyd(k))
  t0(k)=(t0(k)-cp*saq(k+1)-cc*saq(k)-cm*saq(k-1))*
  *      (1-skeyd(k))+skeyd(k)*dval(j)
  fsing(i)=fsing(i)+skey(k)
340  continue
  if (fsing(i).gt.0.) fsing(i)=1.
  fsing(i)=1.-fsing(i)
  if (iaz.ne.2.and.iaz.ne.6) fsing(i)=0.
  t0(i)=aq(i)
  t0(i+nr2nz1)=aq(i+nr2nz1)
  rmi1=rpi
  rmi2=rpi
350  continue
  call vtriz(fsing,nr2,nz2,2,1,dz,bc(iaz),tp,tc,tm,t0)
  call movlev(t0,sq,nr2nz2)
c      set r boundaries of sq (aq(n+1) temporary)
  j=2
cdir\$ ivdep
  do 370 k=nr3,nr2nz1,nr2
    sq(k)=arf2i(j)*(aq(k)-arf1(j)*sq(k+1))
    sq(k+nr1)=arf4i(j)*(aq(k+nr1)-arf3(j)*sq(k+nr))
    j=j+1
370  continue
c
c      clean up vacuum of sq (aq temporary)
  if (ivc.gt.0)
  * call cleanaq(sq,skey,sr,aq,tp,tc,tm,t0,dr,dz,nr2,nz2,
  * fsing,sar,saz,rg,iar,iaz,rmin,zmin,rmax,3hta,skeyd,dval)
c
  iwhen=4
c
c      =====
c      Get Estimates of B_r, B_z, and e_eq from estimate
c      for use in getting B_theta. This
c      is the nonlinear coupling
c      =====

```

```

c
c                                     define br, bz, and ueq
  if (rmin.gt.0.) go to 380
  rmi1=4.*dri
  rmi2=-4.*dri
  go to 385
380 rmi1=1./rmin
  rmi2=rmi1
385 do 395 i=2,nr1
      rmi=rg(i-1)
      rpi=rg(i+1)
      rp=rg(i)+drh
      rpi=1./rp
      rm=rg(i)-drh
      ri=1./rg(i)
      rr=rg(i)
      ks=i+nr2
      do 390 k=ks,nr2nz1,nr2
          br(k)=-dzi2*(sq(k+nr2)-sq(k-nr2))
          bz(k)=ri*dri2*(rp*sq(k+1)+dr*sq(k)-rm*sq(k-1))
          ueq(k)=uiq(k)+vs(k)*cofp*
*               (dris*(rpi*rpi*sq(k+1)-rr*(rpi+rmi1)*sq(k)+
*                   rmi1*rmi2*sq(k-1))
*               +dzis*(sq(k+nr2)-2.*sq(k)+sq(k-nr2)))
      continue
      rmi1=rpi
395   rmi2=rpi
395 continue
  call bdyp(ueq,s,rmin,zmin,dri,dzi,nr2,nz2,t,13)
  call bdyp(br,sq,rmin,zmin,dri,dzi,nr2,nz2,t,3)
  call bdyp(bz,sq,rmin,zmin,dri,dzi,nr2,nz2,t,5)

c
c                                     =====
c                                     Done with temporary Aq, restore B_q and set BC's
c                                     =====
c
c                                     restore bq into sq
  call movlev(bq,sq,nr2nz2)
567 continue
c                                     set r boundaries of sq
  j=1
cdir\$ ivdep
  do 570 k=1,nr2nz2,nr2
      sq(k)=brf2i(j)*(bq(k)-brf1(j)*sq(k+1))
      sq(k+nr1)=brf4i(j)*(bq(k+nr1)-brf3(j)*sq(k+nr))
      j=j+1
  570 continue
c                                     set z boundaries of sq
  if (ibz.eq.2) go to 575
cdir\$ ivdep
  do 670 i=1,nr2
      sq(i)=bzf2i*(bq(i)-bzf1*sq(i+nr2))
      sq(i+nr2nz1)=bzf4i*(bq(i+nr2nz1)-bzf3*sq(i+nr2nz))
  670 continue
  go to 585

```

```

cdir\$ ivdep
  575 do 680 k=1,nr2
        sq(k)=sq(k+nr2nz)
        sq(k+nr2nz1)=sq(k+nr2)
        bq(k)=sq(k)
        bq(k+nr2nz1)=sq(k+nr2nz1)
  680 continue
  585 continue
c
c
c
c
c
cc
=====
      Set r ADI pass for B_theta
=====
      set up r direction pass on bq.

  iwhen=5
  if (rmin.gt.0.) go to 220
  rmi1=4.*dri
  rmi2=-4.*dri
  go to 230
220 rmi1=1./rmin
  rmi2=rmi1
230 do 250 i=2,nr1
      rm1=rg(i-1)
      rp1=rg(i+1)
      rp=rg(i)+drh
      rpi=1./rp
      rm=rg(i)-drh
      ri=1./rg(i)
      ks=i+nr2
      do 235 k=ks,nr2nz1,nr2
          kp=k+1
          km=k-1
          kpn=k+nr2
          kmn=k-nr2
          ezzpr=.5*(eta(kp)+eta(k))
          ezzmr=.5*(eta(k)+eta(km))
          errpz=.5*(eta(kpn)+eta(k))
          errmz=.5*(eta(k)+eta(kmn))
          tp(k)=-rp1*rpi*dri*ezzpr
          tm(k)=-rm1*rmi2*dri*ezzmr
          cp=-dzis*errpz
          cm=-dzis*errmz
          cc=dzis*(errpz+errmz)
          fkey=cc*ifix(2.
*          -.200001*(skey(k)+skey(kp)+skey(km)+
*                      skey(kpn)+skey(kmn)))
          tc(k)=dri*rg(i)*(rpi*ezzpr+rmi1*ezzmr)+fkey
          cc=cc-fkey
c          parabolic terms-r pass bq
          fak=fpvcc+vdt*skey(k)
          tc(k)=tc(k)+fak
          facr=fak*sq(k)
c          nonlinear terms.....
          uerp=dri2*(uer(kp)+uer(k))
          uerm=dri2*(uer(k)+uer(km))

```

```

      uezp=dzi2*(uez(kpn)+uez(k))
      uezm=dzi2*(uez(k)+uez(kmn))
      crp=sign(.5,uerp)
      crm=sign(.5,uerm)
      czp=sign(.5,uezp)
      czm=sign(.5,uezm)
c
      tp(k)=tp(k)+skey(k)*fpvcc*uerp*(.5-crp)
      tc(k)=tc(k)+skey(k)*fpvcc*(uerp*(.5+crp)-uerm*(.5-crm))
      tm(k)=tm(k)-skey(k)*fpvcc*uerm*(.5+crm)
      cp=cp+skey(k)*fpvcc*uezp*(.5-czp)
      cc=cc+skey(k)*fpvcc*(uezp*(.5+czp)-uezm*(.5-czm))
      cm=cm-skey(k)*fpvcc*uezm*(.5+czm)
      facr=facr+skey(k)*fpvcc*
      *           (dri2*(ueq(kp)*br(kp)-ueq(km)*br(km))
      *           +dzi2*(ueq(kpn)*bz(kpn)-ueq(kmn)*bz(kmn)))
c  end nonlinear terms.....
      t0(k)=facr-cp*sq(kpn)-cc*sq(k)-cm*sq(kmn)
235  continue
      if (nerdbte.eq.1) go to 241
      do 240 k=ks,nr2nzi,nr2
          kp=k+1
          km=k-1
          kpn=k+nr2
          kmn=k-nr2
          grden=dri2*(s(kp)-s(km))
          gzden=dzi2*(s(kpn)-s(kmn))
          grte=dri2*(ste(kp)-ste(km))
          gzte=dzi2*(ste(kpn)-ste(kmn))
          facr=-skey(k)*fpvcc+cve*vs(k)*(gzden*grte-grden*gzte)
          t0(k)=t0(k)+facr
240  continue
241  continue
      k=i
      do 245 j=2,nzi
          k=k+nr2
          tep=t0(k)-tp(k)*sq(k+1)-tc(k)*sq(k)-tm(k)*sq(k-1)
          ierb=cvmgm(j+i*1000,ierb,abs(ierb)-abs(tep))
          errb=cvmgm(tep,errb,abs(errb)-abs(tep))
245  continue
          rmi1=rpi
          rmi2=rpi
250  continue
      do 260 j=2,nzi
          fsing(j)=0.
          ks=(j-1)*nr2
          if (ibr(j).ne.6) go to 256
          do 255 i=2,nr1
              fsing(j)=fsing(j)+skey(i+ks)
255  continue
          if (fsing(j).gt.0.) fsing(j)=1.
          fsing(j)=1.-fsing(j)
256  t0(ks+1)=bq(ks+1)
          t0(ks+nr2)=bq(ks+nr2)

```

```

260 continue
   call vtrir(fsing,nr2,nz2,2,1,dr,bcb,tp,tc,tm,t0)
   call movlev(t0,sq,nr2nz2)
c       set z boundaries of sq
262 continue
   if (ibz.eq.2) go to 275
cdir\$ ivdep
   do 270 i=1,nr2
       sq(i)=bzf2i*(bq(i)-bzf1*sq(i+nr2))
       sq(i+nr2nz1)=bzf4i*(bq(i+nr2nz1)-bzf3*sq(i+nr2nz))
270
   go to 285
cdir\$ ivdep
c
275 do 280 k=1,nr2
       sq(k)=sq(k+nr2nz)
       bq(k+nr2nz1)=sq(k+nr2nz)
       sq(k+nr2nz1)=sq(k+nr2)
       bq(k)=sq(k+nr2)
280 continue
285 continue
c
c       clean up vacuum region of sq(n+1/2)
   if (ivc.gt.1)
*   call cleanv(sq,skey,sr,bq,tp,tc,tm,t0,dr,dz,nr2,nz2,
*   fsing,sar,saz,rg,ibr,ibz,rmin,zmin,rmax,3h bq)
287 iwhen=6
c
c       =====
c       Now can solve for u_ez
c       =====
c
c       define uez
do 265 i=2,nr1
   ks=i+nr2
   ri=1./rg(i)
   rp=rg(i)+drh
   rm=rg(i)-drh
   do 265 k=ks,nr2nz1,nr2
       uez(k)=uiz(k)-skey(k)*cofp*ri*dri2*
*       (rp*sq(k+1)+dr*sq(k)-rm*sq(k-1))/(s(k)+1.-skey(k))
265 continue
   call bdyp(uez,s,rmin,zmin,dri,dzi,nr2,nz2,t,14)
   if (subdt.eq.0.) go to 800
   if (nerdaly.eq.1) go to 701
c
iwhen=7
c
c       =====
c       z ADI pass for B_theta
c       =====
c
c       set up z direction pass on bq.
   if (rmin.gt.0.) go to 420
   rmi1=4.*dri
   rmi2=-4.*dri
   go to 430

```

```

420 rmi1=1./rmin
    rmi2=rmi1
430 do 450 i=2,nr1
    rml=rg(i-1)
    rpl=rg(i+1)
    rp=rg(i)+drh
    rpi=1./rp
    rm=rg(i)-drh
    ri=1./rg(i)
    fsing(i)=0.
    ks=i+nr2
    do 435 k=ks,nr2nz1,nr2
        kp=k+1
        km=k-1
        kpn=k+nr2
        kmn=k-nr2
        ezzpr=.5*(eta(kp)+eta(k))
        ezzmr=.5*(eta(k)+eta(km))
        errpz=.5*(eta(kpn)+eta(k))
        errmz=.5*(eta(k)+eta(kmn))
        cp=-rpl*rpi*dri2*ezzpr
        cm=-rml*rmi2*dri2*ezzmr
        cc=dri2*rg(i)*(rpi*ezzpr+rmi1*ezzmr)
        tp(k)=-dzis*errpz
        tm(k)=-dzis*errmz
        fkey=cc*ifix(2.
*           -.200001*(skey(k)+skey(kp)+skey(km)+
*                   skey(kpn)+skey(kmn)))
        tc(k)=dzis*(errpz+errmz)+fkey
        cc=cc-fkey
c           parabolic terms-z pass bq
        fak=fpvcc*vdt*skey(k)
        tc(k)=tc(k)+fak
        facr=fak*sq(k)
c       nonlinear terms.....
        uerp=dri2*(uer(kp)+uer(k))
        uerm=dri2*(uer(k)+uer(km))
        uezp=dzi2*(uez(kpn)+uez(k))
        uezm=dzi2*(uez(k)+uez(kmn))
        crp=sign(.5,uerp)
        crm=sign(.5,uerm)
        czp=sign(.5,uezp)
        czm=sign(.5,uezm)
        cp=cp+skey(k)*fpvcc*uerp*(.5-crp)
        cc=cc+skey(k)*fpvcc*(uerp*(.5+crp)-uerm*(.5-crm))
        cm=cm-skey(k)*fpvcc*uerm*(.5+crm)
        tp(k)=tp(k)+skey(k)*fpvcc*uezp*(.5-czp)
        tc(k)=tc(k)+skey(k)*fpvcc*(uezp*(.5+czp)-
*                   uezm*(.5-czm))
        tm(k)=tm(k)-skey(k)*fpvcc*uezm*(.5+czm)
        facr=facr+skey(k)*fpvcc*
*           (dri2*(ueq(kp)*br(kp)-ueq(km)*br(km))
*           +dzi2*(ueq(kpn)*bz(kpn)-ueq(kmn)*bz(kmn)))

```

```

c end nonlinear terms.....
      t0(k)=facr-cp*sq(kp)-cc*sq(k)-cm*sq(km)
      fsing(i)=fsing(i)+skey(k)
435  continue
      if (fsing(i).gt.0.) fsing(i)=1.
      fsing(i)=1.-fsing(i)
      if (ibz.ne.2.and.ibz.ne.6) fsing(i)=0.
      if (nerdbte.eq.1) go to 441
      do 440 k=ks,nr2nz1,nr2
          kp=k+1
          km=k-1
          kpn=k+nr2
          kmn=k-nr2
          grden=dri2*(s(kp)-s(km))
          gzden=dzi2*(s(kpn)-s(kmn))
          grte=dri2*(ste(kp)-ste(km))
          gzte=dzi2*(ste(kpn)-ste(kmn))
          facr=-skey(k)*fpvcc*cve*vs(k)*(gzden*grte-grden*gzte)
          t0(k)=t0(k)+facr
440  continue
441  continue
      k=i
      do 445 j=2,nz1
          k=k+nr2
          tep=t0(k)-tp(k)*sq(kpn)-tc(k)*sq(k)-tm(k)*sq(kmn)
          iezb=cvmgm(j+i*1000,iezb,abs(erzb)-abs(tep))
          erzb=cvmgm(tep,erzb,abs(erzb)-abs(tep))
445  continue
          t0(i)=bq(i)
          t0(i+nr2nz1)=bq(i+nr2nz1)
          rmi1=rpi
          rmi2=rpi
450  continue
      call vtriz(fsing,nr2,nz2,2,1,dz,bc(ibz),tp,tc,tm,t0)
      call movlev(t0,sq,nr2nz2)
c          set r boundaries of sq
      j=1
cdir\$ ivdep
      do 470 k=1,nr2nz2,nr2
          sq(k)=brf2i(j)*(bq(k)-brf1(j)*sq(k+1))
          sq(k+nr1)=brf4i(j)*(bq(k+nr1)-brf3(j)*sq(k+nr))
470  j=j+1
470  continue
      if(nerdbly.eq.1) go to 780
c
c      iwhen=8
c
c      =====
c      Now we do the final z ADI pass on Aq, have B_q(n+1)
c      =====
c
c          set up final z direction pass on aq.
701  continue
      if (rmin.gt.0.) go to 720
      rmi1=4.*dri
      rmi2=-4.*dri
      go to 730

```



```

720 rmi1=1./rmin
    rmi2=rmi1
730 do 750 i=2,nr1
    rml=rg(i-1)
    rpl=rg(i+1)
    rp=rg(i)+drh
    rpi=1./rp
    rm=rg(i)-drh
    rr=rg(i)
    ri=1./rg(i)
    fsing(i)=0.
    ks=i+nr2
    j=1
    do 740 k=ks,nr2nz1,nr2
        j=j+1
        cp=-rpl*rpi*dris*eta(k)
        cm=-rml*rmi2*dris*eta(k)
        cc=dris*rr*(rpi+rmi1)*eta(k)
        tp(k)=-dzis*eta(k)
        tm(k)=-dzis*eta(k)
c
        parabolic terms-z pass aq
        fak=fpvcc*vdt*skey(k)
        tc(k)=(2.*(dzis*eta(k))+fak)*(1-skeyd(k))+skeyd(k)
        t0(k)=fak*saq(k)
        fak=fpvcc*uer(k)*ri*dri2*skey(k)
        cp=cp+fak*rpl
        cm=cm-fak*rml
        fak=fpvcc*uez(k)*dzi2*skey(k)
        tp(k)=(tp(k)+fak)*(1-skeyd(k))
        tm(k)=(tm(k)-fak)*(1-skeyd(k))
        t0(k)=(t0(k)-cp*saq(k+1)-cc*saq(k)-cm*saq(k-1))*
*
        (1-skeyd(k))+skeyd(k)*dval(j)
        fsing(i)=fsing(i)+skey(k)
740 continue
    if (fsing(i).gt.0.) fsing(i)=1.
    fsing(i)=1.-fsing(i)
    if (iaz.ne.2.and.iaz.ne.6) fsing(i)=0.
    k=ks
    do 745 j=2,nz1
        tep=t0(k)-tp(k)*saq(k+nr2)-tc(k)*saq(k)-
*
        tm(k)*saq(k-nr2)
        ieza=cvmgm(j+i*1000,ieza,abs(erza)-abs(tep))
        erza=cvmgm(tep,erza,abs(erza)-abs(tep))
        k=k+nr2
745 continue
    t0(i)=aq(i)
    t0(i+nr2nz1)=aq(i+nr2nz1)
    rmi1=rpi
    rmi2=rpi
750 continue
    call vtriz(fsing,nr2,nz2,2,1,dz,bc(iaz),tp,tc,tm,t0)
    call movlev(t0,saq,nr2nz2)
c
        set r boundaries of saq

```

```

      j=2
cdir\$ ivdep
      do 770 k=nr3,nr2nzi1,nr2
          saq(k)=arf2i(j)*(aq(k)-arf1(j)*saq(k+1))
          saq(k+nr1)=arf4i(j)*(aq(k+nr1)-arf3(j)*saq(k+nr))
          j=j+1
770 continue
c
c
c          =====
c          ALL DONE, clean up vacuum regions of both Aq and Bq
c          =====
c          clean up vacuum regions of saq and sq
780  if (ivc.ge.1) then
      if(nerdbly.ne.1) call cleanaq(saq,skey,sr,aq,tp,tc,tm,t0,dr,dz,
*   nr2,nz2,fsing,sar,saz,rg,iar,iaz,rmin,zmin,rmax,3hlaq,
*   skeyd,dval)
      if(nerdaly.ne.1) call cleanv(sq,skey,sr,bq,tp,tc,tm,t0,dr,dz,
*   nr2,nz2,fsing,sar,saz,rg,ibr,ibz,rmin,zmin,rmax,3h1bq)
      end if
      if(nerdbly.eq.1) go to 905
c
c
c          =====
c          Define B_r,B_z and u_eq from this new information
c          Remember: Sq=B_theta, Saq=A_theta
c          =====
800  continue
      iwhen=9
      if (rmin.gt.0.) go to 880
      rmi1=4.*dri
      rmi2=-4.*dri
      go to 885
880  rmi1=1./rmin
      rmi2=rmi1
885  do 895 i=2,nr1
          ks=i+nr2
          rm1=rg(i-1)
          rp1=rg(i+1)
          rp=rg(i)+drh
          rm=rg(i)-drh
          ri=1./rg(i)
          rr=rg(i)
          rpi=1./rp
          do 890 k=ks,nr2nzi1,nr2
              br(k)=-dzi2*(saq(k+nr2)-saq(k-nr2))
              bz(k)=ri*dri2*(rp*saq(k+1)+dr*saq(k)-rm*saq(k-1))
              ueq(k)=uiq(k)+vs(k)*cofp*
*                   (dris*(rp1*rpi*saq(k+1)-rr*(rpi+rmi1)*saq(k)+
*                   rmi1*rmi2*saq(k-1))
*                   +dzis*(saq(k+nr2)-2.*saq(k)+saq(k-nr2)))
890      continue
          rmi1=rpi
          rmi2=rpi
895  continue

```

```
c
c
c          =====
c          Set BC's before we return
c          =====
call bdyp(ueq,s,rmin,zmin,dri,dzi,nr2,nz2,t,13)
call bdyp(br,saq,rmin,zmin,dri,dzi,nr2,nz2,t,3)
call bdyp(bz,saq,rmin,zmin,dri,dzi,nr2,nz2,t,5)
call bdyp(saq,s,rmin,zmin,dri,dzi,nr2,nz2,t,16)
905 continue
call bdyp(sq,s,rmin,zmin,dri,dzi,nr2,nz2,t,4)

c
c
c          =====
c          Update Electron Temperature here
c          =====

call electt(subdt,itr,itx)
return
end
```

Bibliography

- [1] H. Alfvén and E. Smars. Gas insulation of a hot plasma. *Nature*, 188:801, 1960.
- [2] D. Anderson, M. Lisak, and H. Wilhelmsson. Anomalous heat transport through a cold turbulent plasma blanket. *Nuclear Fusion*, 19(11):1522-1528, 1979.
- [3] Dale T. Anderson, John C. Tannehill, and Richard H. Pletcher. *Computational Fluid Mechanics and Heat Transfer*. McGraw-Hill Book Company, 1984.
- [4] S. I. Braginskii. Transport processes in a plasma. In M. A. Leontovich, editor, *Reviews of Plasma Physics*, pages 205-311, Consultants Bureau Enterprises, Inc., New York, 1965.
- [5] R. L. Burton, S. A. Goldstein, B. A. Milko, D. A. Tidman, and N. K. Winsor. *Investigation of a Pulsed Electrothermal Thruster*. Technical Report N84-12227, GT Devices, Inc., 1983.
- [6] F. R. Chang and J. L. Fisher. A supersonic gas target for a bundle divertor plasma. *Nuclear Fusion*, 22(8):1003, 1982.
- [7] D. G. Fearn. *Electric Propulsion of Spacecraft*. Technical Report N83-28070, Royal Aircraft Establishment, 1981.
- [8] D. G. Fearn. *A Survey of Electric Propulsion Research and Development in the UK*. Technical Report AD-A024 498, Royal Aircraft Establishment, 1975.
- [9] D. W. Hewett. A global method of solving the electron-field equations in a zero-inertia-electron-hybrid plasma simulation code. *Journal of Computational Physics*, 38:378-395, 1980.

- [10] Yu. L. Igitkhanov, A. S. Kukushkin, and I. P. Stakhanov. A possibility of wall-protecting cold-plasma layer formation in a tokamak reactor. *Nuclear Fusion*, 18(3):415-420, 1978.
- [11] R. G. Mills. *A Fusion Power Plant*. Technical Report MATT-1050, Princeton Plasma Physics Lab, 1974.
- [12] M. Mitchner and Charles H. Kruger. *Partially Ionized Gases*. John Wiley and Sons, 1973.
- [13] Kim Molvig. Private communications.
- [14] D. W. Peaceman and H.H. Jr. Rachford. The numerical solution of parabolic and elliptic differential equations. *Society for Industrial and Applied Mathematics. Journal.*, 3(1):28-41, 1955.
- [15] Roger Peyret and Thomas D. Taylor. *Computational Methods for Fluid Flow*. Springer-Verlag, 1983.
- [16] Patrick J. Roache. *Computational Fluid Dynamics*. Hermosa Publishers, 1982.
- [17] L. Spitzer and R. Härm. Transport phenomena in a completely ionized gas. *Physical Review*, 89:977, 1953.
- [18] N. Yoshioka, N. Sogo, T. Miyamoto, M. Sato, and C. Obata. Gas-embedded z-pinch in a gas cylinder with deep density minimum on axis. *Plasma Physics*, 25(11):1199-1213, 1983.